

**Development and characterization of pore-blocking
small molecules against cholesterol-dependent
cytolysins as anti-virulence strategy**

Inaugural-Dissertation
to obtain the academic degree
Doctor rerum naturalium (Dr. rer. nat.)

submitted to the
Department of Biology, Chemistry, Pharmacy
of Freie Universität Berlin

by

Umer Bin Abdul Aziz

2023

The research for this PhD thesis was conducted from August 2018 until December 2022 at the Institute of Pharmacy, Freie University Berlin under the supervision of Prof. Dr. Jörg Rademann.

1. Reviewer: Prof. Dr. Jörg Rademann
2. Reviewer: Prof. Dr. Gerhard Wolber

Date of defense: 17- 07- 2023

Acknowledgment

I feel incredibly grateful and humbled to have had the chance to work on this intriguing project. To everyone who has helped me along the way, I would like to take this opportunity to express my sincere gratitude.

I want to profess my sincere gratitude to Professor Dr. Jörg Rademann for his invaluable guidance, support, and patience during my Ph.D. This research would not have been possible without his constant encouragement. I am deeply indebted to Prof. Dr. Gerhard Wolber and Dr. Marcel Bermudez for their inspiring computational work and insightful discussions that have helped to shape this work. I also want to express my gratitude to Prof. Dr. Gerhard Wolber for agreeing to be my second reviewer.

I want to acknowledge Dr. Christoph Arkona for his site-directed mutagenesis work, Thomas Rudolf for the chemical synthesis of inhibitors, and Ali Saoud for helping me out by splitting my workload over the course of his master's thesis. Your support, time and contributions were invaluable.

In addition, I owe a debt of gratitude to all former and current members of the AG Rademann family for their time-to-time ideas, assistance, and constructive criticism, as well as for upholding a pleasant working environment. Likewise, I am especially grateful to my practical course colleagues (Damian, Rebekka, Anna, etc.) for making breaking the mundane by lively discussions. I appreciate you all and have had a great time working with you all.

Last but not least, I want to sincerely thank my family and friends for their unwavering support and inspiration. I am especially grateful to my wife and kids, whose love and support have provided me with ongoing inspiration and strength. I would like to thank everyone for their encouragement and belief in me throughout this journey.

Declaration of Independence

I declare that my doctoral thesis "Development and characterization of pore-blocking small molecules against cholesterol-dependent cytolysins as anti-virulence strategy" has been written independently and with no other sources or aid than those cited. Moreover, I have not submitted this thesis in any other doctoral procedure.

X

Umer Bin Abdul Aziz

Summary

Cholesterol-dependent cytolysins (CDC) are acknowledged virulence factors of a wide range of pathogenic gram-positive bacteria like Streptococci, Clostridia, and Listeria etc. CDC selectively target membranes that contain cholesterol and induce pathogenesis in the host organisms by versatile mechanisms. Bacteria release CDC during an infection, which infuriate the infection and the treatment of infection becomes challenging with the contemporary regime of anti-infectives. The noxious responses of CDC include direct toxicity via pore formation, manipulation of cellular signaling to promote bacterial survival and evasion of the immune system. Worldwide, millions of deaths are associated with CDC like PLY, PFO, LLO etc. Therefore, CDC have been considered as a potential target for drugs. In the research of the last few decades, multiple natural and synthetic small molecules have been proposed as anti-toxins, however, due to lack of specificity, none of them were contemplated for clinical testing. Thus, to date there is no specific treatment available to counter CDC manifestations and the goal of this project is to develop and validate specific small molecules against CDC. PLY was selected as a prototype CDC for testing of small molecules. In our earlier work, a model of PLY-pore was developed to virtually screen half a million molecules from online databases that could block the oligomerization and ultimately pore formation of PLY. **Pore-Blocker-1 (PB-1)**, was the only molecule that actively inhibited PLY in a hemolysis assay and, thereon, its optimization led to the discovery of **PB-2** with ten times improved activity.

In this dissertation, **PB-1** and **2** were validated in the BLI assay. Cryo-TEM analysis showcased that **PB-2** prevented the PLY penetration in membranes of cholesterol-liposomes. By analyzing several closely related derivatives of **PB-2** the pharmacophore of inhibitors was identified, which enabled the effective alteration of scaffolds to produce **PB-3**, a more chemically stable and potent inhibitor of PLY. **PB-3** exhibited an IC_{50} of 3 μ M in the hemolysis assay and a K_D value of 256 nM against PLY in the BLI assay. Analogous potency of **PB-3** was observed in the LDH assay and cellular microscopy. **PB-3** was generated and quantified through the protein-catalyzed ligation of precursor fragments. The actual mechanism of inhibitors was unveiled by evaluating the activity of inhibitors against multiple PLY-mutants and in contrast to the virtually proposed mechanism of binding, a cysteine mutant of PLY suggested that **PB-3** might be binding to a cysteine in the membrane-binding domain of PLY. Then, BLI

and MS investigations of cysteine mutant PLY and wild type confirmed the cysteine-mediated reversible covalent interaction between **PB-3** and PLY. Afterwards, **PB-3** was observed barely active against other cysteine-proteases (PTP-1B and SARS-CoV2), confirming the increased affinity of **PB-3** toward PLY. **PB-3** blocked PLY in a bacterial infection-model assay, this experiment further affirms selectively of **PB-3** to PLY because the cell culture medium contained 13000-fold more free-cysteine than PLY. Finally, **PB-3** was examined against two further CDC, PFO and ILY. PFO is analogous to PLY and possesses a cysteine residue in the undecapeptide and when **PB-3** was tested, it was nearly 10 times more potent against PFO than PLY. Conversely, ILY is devoid of cysteine and **PB-3** was expectedly inactive against ILY. In the light of these results, we presumably consider **PB-3** as an inhibitor of cysteine-containing CDC.

Zusammenfassung

Cholesterin-abhängige Cytolysine (CDC) sind anerkannte Virulenzfaktoren einer breiten Palette pathogener grampositiver Bakterien wie Streptokokken, Clostridien und Listerien usw. CDC zielen selektiv auf Membranen ab, die Cholesterin enthalten, und induzieren die Pathogenese in den Wirtsorganismen durch vielseitige Mechanismen. Bakterien setzen während einer Infektion CDCs frei, die die Invasivität der Infektion erhöhen, und die Behandlung von Infektionen wird mit der derzeitigen Therapie mit Antiinfektiva zu einer Herausforderung. Zu den schädlichen Reaktionen von CDC gehören die direkte Toxizität über die Porenbildung, die Manipulation der zellulären Signalübertragung zur Förderung des bakteriellen Überlebens und die Umgehung des Immunsystems. Millionen von Todesfällen weltweit sind mit CDC wie PLY, PFO, LLO usw. verbunden. Daher wurden CDC als potenzielles Arzneimittelziel angesehen. Während der Forschung der letzten Jahrzehnte wurden mehrere natürliche und synthetische kleine Moleküle als Antitoxine vorgeschlagen, aufgrund mangelnder Spezifität wurde jedoch keines von ihnen für klinische Tests in Betracht gezogen. In unserer früheren Forschung wurde ein Modell von PLY-Poren entwickelt, um virtuell eine halbe Million Moleküle aus Online-Datenbanken zu Screening, die die Oligomerisierung und letztendlich die Porenbildung von PLY blockieren könnten. **Pore Blocker-1 (PB-1)** war das einzige Molekül, das PLY in einem Hämolyse-Assay aktiv hemmte, und seine Optimierung führte anschließend zur Entdeckung von **PB-2** mit zehnfach verbesserter Aktivität.

In dieser Dissertation wurden **PB-1** und **2** mit dem BLI-Test validiert. Die Cryo-TEM-Analyse zeigte, dass **PB-2** das Eindringen von PLY in die Membranen von Cholesterin-Liposomen verhinderte. Das Pharmakophor der Inhibitoren wurde durch die Analyse mehrerer eng verwandter Derivate von **PB-2** identifiziert, was eine effektive Veränderung der Gerüste ermöglichte, um **PB-3**, einen chemisch stabileren und stärkeren Inhibitor von PLY, zu entwickeln. **PB-3** hatte eine IC₅₀ von 3 µM im Hämolyse-Assay und einen KD-Wert von 256 nM für PLY im BLI-Assay. Eine ähnliche Wirksamkeit von **PB-3** wurde im LDH-Assay und in der Zellmikroskopie nachgewiesen. **PB-3** wurde durch die protein-katalysierte Ligation von Precursor-Fragmenten erzeugt und quantifiziert. **PB-3** wurde durch die Proteintemplat-unterstützte Ligation von Precursor-Fragmenten erzeugt und quantifiziert. Der wahre Mechanismus der Inhibitoren wurde durch die Auswertung der Aktivität der Inhibitoren gegen mehrere

PLY-Mutanten entdeckt. Im Kontrast zu dem virtuell vorgeschlagenen Bindungsmechanismus deutete eine Cystein-Mutante von PLY darauf hin, dass **PB-3** an ein Cystein in der Membran-Bindungsdomäne von PLY binden könnte. Anschließend bestätigten BLI und MS Untersuchungen der Cystein-Mutante PLY und des Wildtyps die Cystein-vermittelte reversible kovalente Interaktion zwischen **PB-3** und PLY. Im Anschluss daran wurde PB-3 als kaum aktiv gegen andere Cystein-Proteasen (PTP-1B und SARS-CoV2) identifiziert, was die erhöhte Affinität von PB-3 gegenüber PLY bestätigt. **PB-3** blockierte PLY in einem bakteriellen Infektionsmodell-Assay. Dieses Experiment bestätigt außerdem die Selektivität von **PB-3** für PLY, da das Zellkulturmedium 13000-mal mehr freies Cystein als PLY enthielt. Zum Schluss wurde **PB-3** gegen zwei weitere CDC, PFO und ILY, getestet. PFO ist analog zu PLY und enthält Cystein, und bei der Prüfung von **PB-3** wurde festgestellt, dass es fast zehnmal stärker gegen PFO wirkt als PLY. Umgekehrt ist ILY frei von Cystein und **PB-3** war erwartungsgemäß inaktiv gegenüber ILY. In Anbetracht dieser Ergebnisse halten wir **PB-3** vermutlich für einen Hemmstoff gegen Cystein-haltiges CDC.

Table of contents

LIST OF FIGURES	5
LIST OF TABLES	7
ABBREVIATIONS	8
1. CHAPTER 1: INTRODUCTION	11
1.1. Introduction	12
1.1.1. Cholesterol dependent cytolysins.....	12
1.1.1.1. Structure of CDC	14
1.1.1.2. Process of pore formation in CDC.....	15
1.1.1.3. Role of CDC during bacterial infection	20
1.1.1.4. Modulation of immune system by CDC	25
1.1.2. Introduction to CDC evaluated in this research project.....	29
1.1.2.1. Pneumolysin	29
1.1.2.2. Perfringolysin O	32
1.1.2.3. Intermedilysin	34
1.1.3. CDC as an anti-virulence drug target	35
1.1.4. Antimicrobial resistance.....	39
1.1.5. Aim of the project.....	40
2. CHAPTER 2: RESULTS AND DISCUSSION	42
2.1. Overview of the preceding research	43
2.1.1. Introduction the hemolysis assay	44
2.2. Synthesis and testing of pore blockers	46
2.2.1. Stability of PB-2.....	47
2.2.2. Identification of pharmacophore	50
2.2.2.1. Testing of multiple derivatives of PB-2 for optimization	54
2.2.3. Modification in the PB-pharmacophore	59
2.2.3.1. Discovery of PB-3.....	59
2.2.3.2. Diverse active derivatives of PB-molecules	62
2.2.3.3. Inactive derivatives of PB-molecules.....	66
2.2.4. Structure activity relationship and the pharmacophore	68
2.2.5. Analysis of PLY-mutant variants via hemolysis assay	70
2.2.5.1. PLY mutations in the oligomer-forming region	70
2.2.5.2. PLY mutations in the cholesterol-binding region.....	72
2.2.5.3. Selectivity of PB-molecules against PLY.....	75
2.2.6. Evaluation of PB-molecules with other CDC	78
2.2.6.1. Perfringolysin O	78
2.2.6.2. Intermedilysin	81
2.2.7. Summary	85
2.3. Biophysical evaluation of PB-molecules	87
2.3.1. Introduction to bio-layer interferometry.....	87

2.3.2. Evaluation of PB-1	88
2.3.3. Evaluation of PB-2.....	92
2.3.4. Evaluation of PB-3.....	96
2.3.5. Evaluation of pneumolysin mutations.....	100
2.3.6. Evaluation of binding between PB-3 and PFO.....	103
2.3.7. Investigation of aggregation via dynamic light scattering.....	106
2.3.8. Summary	107
2.4. Investigation of pore formation blockade in CDC by PB-molecules via cryo-transmission electron microscopy (cryo-TEM)	109
2.4.1. Summary	113
2.5. Investigation of protein-ligand complex via mass spectrometry	114
2.5.1. Native MS	114
2.5.2. Classical or denaturing MS	114
2.5.3. Summary	117
2.6. Cellular testing of PB-inhibitors in lung cells.....	118
2.6.1. Introduction to lactate dehydrogenase (LDH) assay	118
2.6.1.1. Analysis of PB-1	119
2.6.1.2. Analysis of PB-2	123
2.6.1.3. Analysis of PB-3	125
2.6.1.4. Analysis of PLY-C428A	127
2.6.2. Summary	129
2.7. Illustration of protective effect of PB-molecules via confocal laser scanning microscopy	130
2.7.1. Protective effect of PB-2.....	130
2.7.2. Protective effect of PB-3.....	131
2.7.3. Investigation of PB-3 in <i>Streptococcus pneumoniae</i> infection-model assay.....	133
2.7.4. Summary	136
2.8. Discussion	137
3. CHAPTER 3: EXPERIMENTAL SECTION	144
3.1. Experimental methods and procedures.....	145
3.1.1. Recombinant expression and purification of pneumolysin	145
3.1.2. Hemolysis assay.....	148
3.1.3. Quantitative analysis of protein-templated fragment ligation reaction	149
3.1.4. Kinetic analysis of inhibitors via bio-layer Interferometry	150
3.1.4.1. Data Acquisition.....	150
3.1.4.2. Data Analysis.....	152
3.1.5. Investigation of PB-3 binding to PLY and PLYC428A by BLI.....	157
Data acquisition	157
Data Analysis.....	157
3.1.6. Evaluation of binding between PB-molecules and PLY-mutants	158
Data acquisition	158
Data Analysis.....	158
3.1.7. Aggregation analysis via dynamic light scattering.....	159
3.1.8. Lactate dehydrogenase assay	159
3.1.9. Liposomes preparation	160
3.1.10. Protein-liposomes sample preparation for Cryo-TEM	161
3.1.11. Cryo-TEM investigation	163

3.1.12. Human lung cells protection from native PLY	164
3.1.13. Mitigation of <i>Streptococcus pneumoniae</i> infection.....	164
3.1.14. Live-cell microscopy	165
3.1.15. Protein-ligand complex investigation by MS.....	165
3.1.16. Chemical synthesis.....	167
3.2. Supplementary Information.....	179
3.3. References	198

List of figures

FIGURE 1.1. CDC ARE SELECTED ACCORDING TO THE GENETIC DISTRIBUTION OF BACTERIA.	13
FIGURE 1.2. A TYPICAL STRUCTURE OF A CDC.....	15
FIGURE 1.3. THE SHIFT OF CDC MODEL FROM EARLY TO LATE PREPORE.....	18
FIGURE 1.4. THE PORE FORMATION OF CDC.....	19
FIGURE 1.5. MECHANISMS OF MEMBRANE REPAIR AFTER CDC ATTACK.....	22
FIGURE 1.6. SIGNALING PATHWAYS ASSOCIATED WITH CDC.....	25
FIGURE 1.7. INFLAMMASOME ACTIVATION.....	27
FIGURE 1.8. CONCISE REPRESENTATION OF PLY-INDUCED TOXICITY IN DIFFERENT ORGANS OF THE BODY.	31
FIGURE 1.9. THE WORKFLOW OF THE PRIMARY WORK BEFORE START OF THE PROJECT.	40
FIGURE 2.1. STRUCTURE-BASED VIRTUAL SCREENING FOR THE IDENTIFICATION OF CDC INHIBITORS.	44
FIGURE 2.2. THE GRAPHICAL REPRESENTATION OF THE HEMOLYSIS ASSAY.	45
FIGURE 2.3. THE SYNTHESIS SCHEME OF PB-1 AND 2 VIA KNOEVENAGEL CONDENSATION.....	46
FIGURE 2.4. ANALYSIS OF LAB SYNTHESIZED PB-1 AND 2	47
FIGURE 2.5. THE ANALYSIS OF PB-2 STABILITY VIA LC-QTOF-MS.....	48
FIGURE 2.6. THE STABILITY OF PB-2 IN THE HEMOLYSIS ASSAY.	49
FIGURE 2.7. THE ANALYSIS OF PRECURSOR MOLECULES OF PB-2	51
FIGURE 2.8. THE FRAGMENT LIGATION REACTION FOR PB-2 GENERATION IN PRESENCE OF PROTEIN.	52
FIGURE 2.9. THE LEAD STRUCTURE OF PB-INHIBITORS AFTER INITIAL INVESTIGATION IS SHOWN..	53
FIGURE 2.10. DERIVATIVES OF PB-2	55
FIGURE 2.11. DERIVATIVES OF PB-2	56
FIGURE 2.12. DERIVATIVES OF PB-2	57
FIGURE 2.13. THE IC ₅₀ STABILITY OF PB-3 IN THE HEMOLYSIS ASSAY.....	60
FIGURE 2.14. THE PROTEIN-TEMPLATED FRAGMENT LIGATION TO PRODUCE PB-3	61
FIGURE 2.15. ANALYSIS OF PB-4	63
FIGURE 2.16. ANALYSIS OF PB-5	64
FIGURE 2.17. ANALYSIS OF PB-6	65
FIGURE 2.18. THE MODIFIED LEAD STRUCTURE WITH FIVE AND SIX MEMBERED RINGS.	69
FIGURE 2.19. THE ANALYSIS OF MUTATIONS FORM OLIGOMER-FORMING REGION.	71
FIGURE 2.20. THE ANALYSIS OF MUTATIONS FORM CHOLESTEROL-BINDING REGION.....	74
FIGURE 2.21. ANALYSIS OF REPORTED MICHAEL ACCEPTORS.....	76
FIGURE 2.22. THE ANALYSIS OF PB-3 AGAINST CYSTEINE-CONTAINING PROTEASES.	77
FIGURE 2.23. THE ACTIVITY OF PFO IN THE HEMOLYSIS ASSAY.....	79
FIGURE 2.24. THE ANALYSIS OF PB-MOLECULES AGAINST PFO.....	81
FIGURE 2.25. THE INACTIVITY OF ILY AGAINST SHEEP ERYTHROCYTES.	82
FIGURE 2.26. THE ACTIVITY OF ILY AGAINST HUMAN ERYTHROCYTES	83
FIGURE 2.27. THE ANALYSIS OF PB-MOLECULES AGAINST ILY.....	84
FIGURE 2.28. BIO-LAYER INTERFEROMETRY.....	87
FIGURE 2.29. THE RAW DATA OF PB-1	90
FIGURE 2.30. THE BINDING DATA OF PB-1	92
FIGURE 2.31. THE RAW DATA OF PB-2	94
FIGURE 2.32. THE BINDING DATA OF PB-2	95
FIGURE 2.33. THE RAW DATA OF PB-3	98

FIGURE 2.34. THE BINDING DATA OF PB-3 .	99
FIGURE 2.35. THE MUTATIONAL ANALYSIS OF PLY VIA BLI.	103
FIGURE 2.36. THE RAW AND BINDING DATA OF PB-3 AGAINST PFO.	105
FIGURE 2.37. THE ANALYSIS OF PB-3 VIA DYNAMIC LIGHT SCATTERING.	106
FIGURE 2.38. A HOMOGENOUS MIXTURE OF UNILAMELLAR LIPOSOMES, CONTAINING 70 % OF CHOLESTEROL AND 30 % OF PHOSPHATIDYLCHOLINE (DOPC).	110
FIGURE 2.39. THE CRYO-TEM ANALYSIS OF INHIBITOR.	112
FIGURE 2.40. DECONVOLUTED SPECTRA OF PROTEINS WITH PB-3 AND WITHOUT (AS CONTROL) IN DENATURING CONDITIONS.	116
FIGURE 2.41. THE REACTION MECHANISM OF THE LDH ASSAY.	119
FIGURE 2.42. SOLUBILITY OPTIMIZATION OF PB-1 .	121
FIGURE 2.43. CYTOTOXICITY ANALYSIS OF PLY WITH PB-1 .	122
FIGURE 2.44. CYTOTOXICITY ANALYSIS OF PLY WITH PB-2 .	124
FIGURE 2.45. CYTOTOXICITY ANALYSIS OF PLY WITH PB-3 .	127
FIGURE 2.46. CYTOTOXICITY ANALYSIS OF PLY-C428A WITH PB-3 .	128
FIGURE 2.47. DEMONSTRATION OF PLY-PROHIBITION IN CELLULAR INJURY IN A549 CELLS BY PB-2 .	131
FIGURE 2.48. PB-3 BLOCKING PLY IN A549 CELLS DEMONSTRATED BY MICROSCOPY.	132
FIGURE 2.49. PB-3 RESTRICTED CELLULAR DETERIORATION IN S.PN. INFECTION-MODEL ASSAY.	135
FIGURE 3.1. THE WORKFLOW OF THE BACTERIAL TRANSFORMATION.	146
FIGURE 3.2. WELLS OF AN ASSAY PLATE MARKED WITH CONTENT AND DESCRIPTION OF THE CONTENTS.	151
FIGURE 3.3. A DIAGRAM OF DATA ACQUISITION SOFTWARE WITH HIGHLIGHTED STEPS OF ASSAY DEFINITION.	152
FIGURE 3.4. ALL STEPS OF PROCESSING SECTION. IN THE SOFTWARE THOSE APPEAR AS VERTICAL LIST OF STEPS COMES AFTER ONE ANOTHER.	154
FIGURE 3.5. APPEARANCE OF ANALYSIS SECTION IN THE SOFTWARE IS AS VERTICAL LIST.	156
FIGURE 3.6. THE SCHEMATIC FLOW OF LIPOSOME PRODUCTION IN OUR LAB.	161
FIGURE 3.7. THE IMAGE SHOWS THE PROCEDURE OF BUFFER EXCHANGE.	165

List of tables

TABLE 1.1. PROMINENT DISEASE PROGRESSING CDC WITH THEIR PARENT SPECIES AND DISEASES.	21
TABLE 1.2. REPORTED INHIBITORS OF CDC IN PRECLINICAL STUDIES.	38
TABLE 2.1. LIST OF PB-2 DERIVATIVES.	58
TABLE 2.2. STRUCTURES OF MISCELLANEOUS PB-MOLECULES PURCHASED FROM SPECS.	67
TABLE 2.3. THE BINDING KINETICS OF PB-1 WITH STATISTICAL PARAMETERS OF GOOD CURVE FITTING.	92
TABLE 2.4. THE BINDING PROFILE OF PB-2 WITH STATISTICAL PARAMETERS OF GOODNESS OF FIT.	96
TABLE 2.5. THE BINDING KINETICS OF PB-3 WITH STATISTICAL PARAMETERS OF GOOD CURVE FITTING.	100
TABLE 2.6. THE BINDING KINETICS OF PB-3 WITH STATISTICAL PARAMETERS OF GOOD CURVE FITTING.	105
TABLE 2.7. COMPARISON OF DIAMETER INCREASE AND STANDARD DEVIATION.	107

Abbreviations

1

1,2-dioleoyl-sn-glycero-3-phosphocholine
DOCP, 169

A

absent in melanoma 2
AIM2, 34
AFM
atomic force microscopy, 25
alanine
A, 79
ALO
aerolysin, 31
antimicrobial resistance
AMR, 47
apoptosis-associated speck-like protein containing a
CARD / Pycard
ASC, 34
Aspartic acid
D, 79
association rate
kon, 103

B

beta mercaptoethanol
 β -ME, 156
bio-layer interferometry
BLI, 96

C

capsule locus
cps, 173
capsule-deleted mutant of *S.pn.*
D39 Δ cps, 142
cerebrospinal fluid
CSF, 38
chi-square
Chi2, 100
cholesterol recognition motif
CRM, 22
Cholesterol-dependent cytolysins
CDC, 20
c-Jun amino (N)-terminal kinases
JNK, 31
coefficient of determination
R2, 100
confidence interval
CI, 56

Cryo-EM
electron microscopy, 25
Cryo-ET
Electron tomography, 24
cysteine
C, 81

D

deubiquitinating enzyme cylindromatosis
CYLD, 31
dimethyl sulfoxide
DMSO, 55
dimethylformamide
DMF, 179
dissociation constant
KD, 100
domain 1
D1, 22
double mutant version
PLY-DM, 81
dynamic light scattering
DLS, 115

E

electron microscopy
EM, 25
endoplasmic reticulum
ER, 32
ESCRT-III
endosomal sorting complexes required for transport,
30
extracellular vesicles
EV, 36

F

fast protein liquid chromatography
FPLC, 156
fetal calf serum
FCS, 128

G

general secretory pathway
GSP, 40
glutamic acid
E, 79
glycine pair
GG, 22
Glycosylphosphatidylinositol

GPI, 22

H

Hanks' balanced salt solution

HBSS, 173

helical bundles

HB, 22

high performance liquid chromatography

HPLC, 158

High resolution electrospray ionization mass spectrometry

ESI-HRMS, 179

I

immobilized metal affinity chromatography

IMAC, 156

inhibitory concentration 50%

IC50, 56

interferon

IFN, 36

interleukin

IL, 31

intermedilysin

ILY, 24

isothermal titration calorimetry

ITC, 49

L

lactate dehydrogenase

LDH, 127

leucine

L, 81

liquid chromatography mass spectrometry

LCMS, 58

liquid chromatography-quadrupole time of flight-mass spectrometry

LC-QTOF-MS, 56

listeriolysin O

LLO, 20

Luria Broth

LB, 154

M

MAC-inhibitory protein

MAC-IP, 42

MAPK-ERK

MAPK-extra-cellular signal related kinase, 31

maximum response

R_{max}, 164

membrane attack complex

MAC, 42

micromolar

μM, 55

microvesicles

MV, 30

millimolar

mM, 55

Mitogen-activated Protein Kinase

MAPK, 31

molecular weight cut off

MWCO, 156

N

nanometer

nm, 97

nanomolar

nM, 55

nickel nitriloacetic acid

NiNTA, 97

NMR

nuclear magnetic resonance, 26

nucleotide-binding oligomerization domain-like /

NOD-like receptor family, pyrin domain-containing 3

NLRP3, 34

P

pathogen associated molecular patterns

PAMP, 31

perfringolysin O

PFO, 24

phage shock protein A

PspA, 38

phenylmethylsulfonyl fluoride

PMSF, 156

phosphate saline buffer

PBS, 54

pneumolysin

PLY, 21

pneumolysin and capsule loci-deleted mutant of *S.pn.*

D39ΔcpsΔply, 142

pore-blocker

PB, 52

post-translational modifications

PTMs, 39

protease activated receptor 1

PAR1, 44

protein kinase C

PKC, 38

protein tyrosine phosphate 1B

PTP1B, 85

R

rate of dissociation

k_{off}, 103

Reduced nicotinamide adenine dinucleotide
phosphate
NADPH, 36
revolution per minute
RPM, 169
room temperature
RT, 60

S

SDS
sodium dodecyl sulfate, 24
severe acute respiratory syndrome-corona virus 2
SARS-CoV2, 85
small ubiquitin like modifier
SUMO, 32
standard deviation
SD, 115
standard operating protocols
SOPs, 44
streptococcus
S, 139
Streptococcus pneumoniae
S. pn., 142
streptolysin O
SLO, 28
structure activity relationship

SAR, 49
Suilyisin
SLY, 29

T

tetramethyl-rhodamine methyl ester
TMRE, 173
thermal shift assay
TSA, 96
threonine
T, 81
Toll like receptor
TLR, 36
transmembrane hairpins
TMH, 22
transmission electron microscopy
TEM, 48
tumor necrosis factor α
TNF α , 31

U

undecapeptide
UDP, 22
unfolded protein response
UPR, 32

1. Chapter 1: Introduction

1.1. Introduction

A cell is commonly known as a building block of life. It is an independent entity in single-celled organisms, whereas in multicellular organisms it serves as a basic functional unit. A partially permeable phospholipid membrane demarcates cells from the external environment.¹ The membrane has evolved to perform basic cellular tasks like sustaining viable gradients, transport of material, protection of the internal environment, etc.¹ These functions are imperative for the survival of cells and, ultimately organisms. Therefore, the importance of a membrane is elemental and if the cellular membrane is disrupted, the cell loses its integrity due to the imbalance of the internal environment, leading to death.²

1.1.1. Cholesterol dependent cytolysins

Downstream the evolutionary pathway, pathogenic organisms have developed agents that cause membrane disturbances as their defensive manifestation.^{3,4} These agents include a wide array of products like chemicals, peptides, toxic proteins, etc., released by the organisms to erupt the host membrane.³⁻⁶ Cholesterol-dependent cytolysins (CDC) are a family of pore-forming toxins which is a perfect depiction of membrane-targeting agents. CDC have been known since 1890 as hemolytic toxins of gram-positive bacteria,⁶ however, in 1939, the relevance of cholesterol in their activity was established while investigating *Streptococcus pyogenes*⁷. The family CDC is named after cholesterol due to the fact that these are equipped with a unique feature of engaging membrane-cholesterol for anchoring the membranes and making lytic pores.^{5,8} Hence, CDC attack only eukaryotic membranes and are harmless against species of their kingdom.⁹ To date, more than 50 species of different bacteria have been identified to produce CDC and a wide majority of them are gram-positive with a single exception of gram-negatives.^{5,8-11} The individual name entitled to a protein/toxin is according to its parent species.⁹ The concise taxonomic classification of a few chosen CDC, for instance, can be observed in **Figure 1. 1**.⁵

The pathogenicity of CDC is not restricted to pore formation rather these are multifaceted toxins and have been widely recognized to enhance disease progression exponentially.¹²⁻¹⁵ CDC are effectively utilized by the bacteria for their survival within the host and CDC promote colonization, proliferation, and escaping the immune system.¹²⁻¹⁴ For instance, listeriolysin O (LLO), a CDC from *Listeria monocytogenes*,

efficiently bypasses human phagocytic activity and contributes to the invasiveness of infection.¹⁶⁻¹⁸ Similarly, pneumolysin (PLY), in *Streptococcus pneumoniae* infection, boosts bacterial colonization and evades the immune response by multiple mechanisms.¹⁹⁻²¹ A succinct overview of pathogenesis associated with CDC will be described later in the chapter.

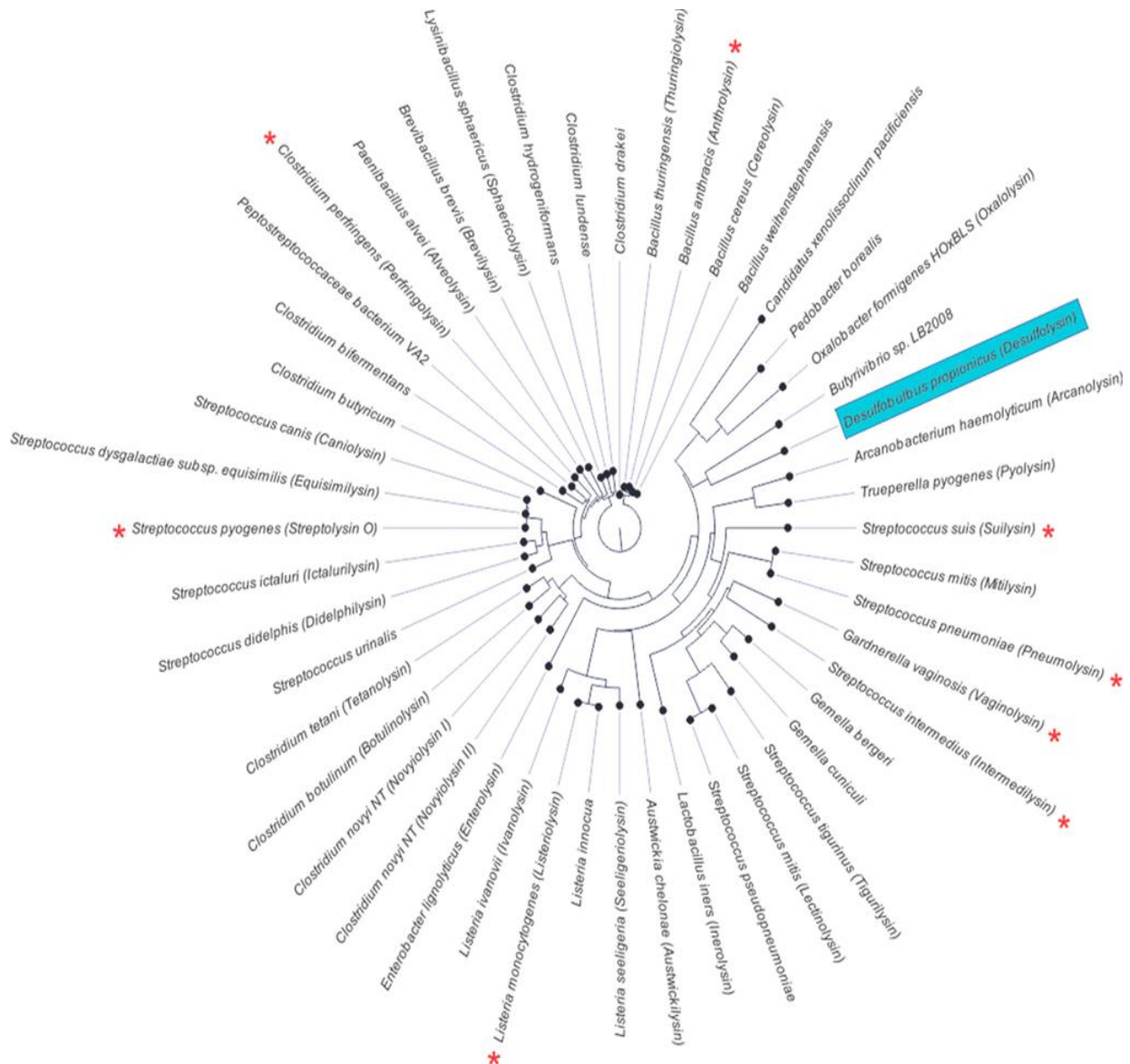


Figure 1.1. CDC are selected according to the genetic distribution of bacteria. Asterisk indicates toxins which have known crystal structure. Blue box represents gram-negative toxin.⁵

1.1.1.1. Structure of CDC

Crystal structures of around ten CDC have been reported and they show analogous structures with minor modifications.²²⁻²⁹ The structural homology among CDC is between 40 to 75%.^{5,30} A typical structure of a CDC can be narrowed down to four domains. The domain 1 (D1) is in direct connection to D2 and D3. Whereas D4 is present at the bottom and bridged with only D2, which enables the extension in length of the structure (115 Å).²⁸⁻³⁰

The structures of CDC contain predominantly β -strands and they have been known as β -pore-forming toxins as well.^{9,15} D1 consists of seven adjacent β -sheets surrounded by α -helices.^{5,22,31} D2 acts as a tensile connection between D1 and D4, and is also composed of parallel β -sheets.^{28,30} D3 is made up of five β -sheets (β 1 to 5) surrounded by two α -helical bundles (HB-1 and HB-2).^{11,30,31} During pore formation, HB-1 and HB-2 undergo transfiguration to transmembrane hairpins (TMH1 and TMH2), which infiltrate the membrane.^{24,28,31} Moreover, an additional profound motif is present between β 4 and β 5 of D3.¹⁰ It is a glycine pair (GG) that has acknowledged effects on CDC-oligomerization.^{10,23,31}

The insertion of CDC into the membrane occurs via D4 and therefore, it is of chief value and hence has been exclusively studied.^{32,33} D4, as a common feature of CDC, contains four loops at the base and these loops link the parallel β -sheets.^{29,30} Loop 1 has a principal pair of amino acids (threonine and leucine) that is common among CDC,³² however, the number in the sequence is different in each CDC, e.g. in PLY T459 & L460 and in PFO T490 & L491^{24,31} The T-L pair recognizes cholesterol embedded in the membrane and hence it is known as cholesterol recognition motif or CRM.^{5,30,32} In the majority of CDC, CRM directly binds to cholesterol leading to penetration into the membrane. In contrast, a few CDC, like ILY and VLY, have evolved to stick to the membrane via the CD59 receptor, which is a glycosyl-phosphatidylinositol (GPI)-anchored human cell-surface receptor.^{26,27,34,35} Thereafter, the CD59 facilitates interaction between toxin and membrane-cholesterol via CRM.^{26,27} Thus, CD59 mediation makes these CDC specific against humans, though their membrane anchorage still counts on CRM.^{34,36}

Similarly, another critical and conserved motif in D4 is the undecapeptide (UDP).³⁷ As the name implies, it is a sequence of 11 amino acids and is available at loop 4.³⁷ Unlike

CRM, UDP is not identical among CDC and may possess exquisite differences in amino acids between CDC.^{5,30} Typically, a UDP motif contains two or three tryptophan and, therefore, in some studies, it is referred to as a tryptophan-rich loop.^{23,24} UDP mediates hydrophobic interactions between proteins within membranes and serves to anchor them.^{5,30,37} Additionally, multiple studies have shown that UDP is involved in the allosteric activation of D3 during the conversion of pre-pore to pore.^{5,37} Further detailed analysis of the structural transitions is available in the description of pore formation.

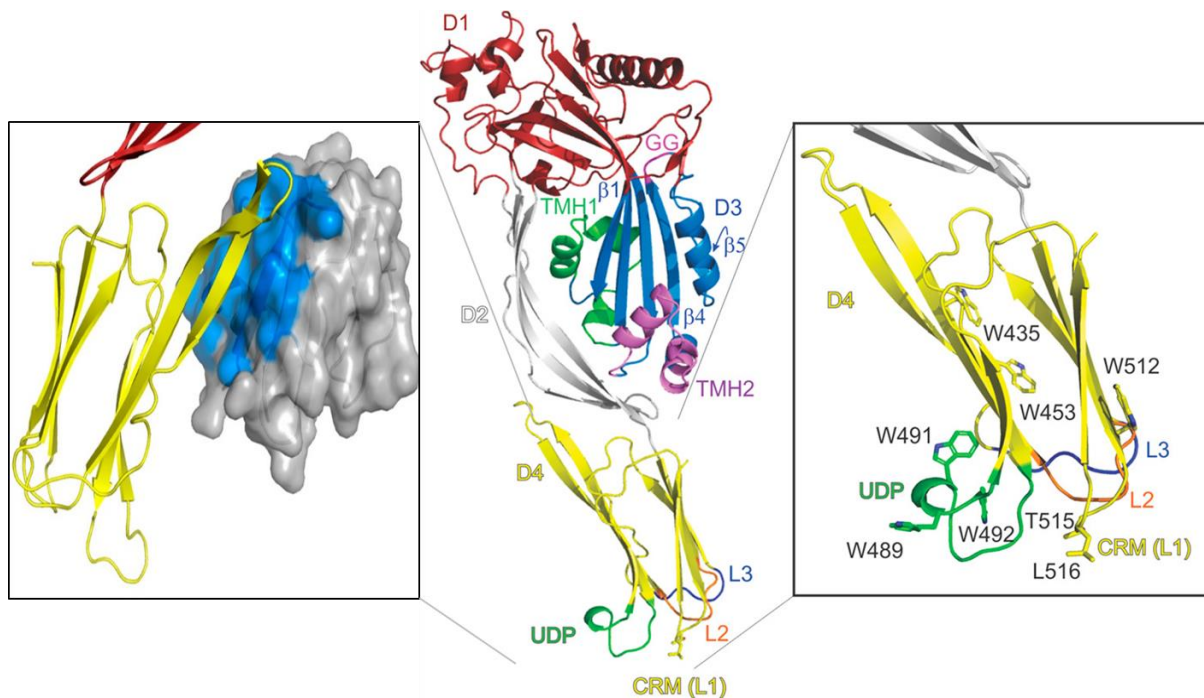


Figure 1.2. A typical structure of a CDC.

Every domain is distinctively colored and highlighting characteristic motifs, e.g., TMH, GG motif, etc. Right side: closer look of D4 engaging with CD59 receptor in ILY. Left side: D4 of PFO exhibiting loops, CRM and UDP.^{23,27,30}

1.1.1.2. Process of pore formation in CDC

The pore formation is a highly intricate process and, so far, poorly understood.^{15, 30,38-40} The crystal structures of numerous CDC have been thoroughly investigated and furthermore, pore formation on cholesterol liposomes has been exhibited with various toxins, yet some mechanistic details of pore formation are still missing.^{11,25,28,29,33} Here, the multistep pore formation is explained stepwise according to state-of-the-art information.

Membrane entry of CDC. Initial membrane anchorage of CDC relies on capturing the 3- β -hydroxyl moiety of cholesterol via CRM³² except for CD59-controlled CDC.²⁷ Even a minute difference in the structure of cholesterol, e.g., in lanosterol or stigmasterol, etc., has been proven to cause a significant reduction in the membrane binding ability of CDC.^{5,41} CRM identifies cholesterol in the membrane and further leads to penetration of loops 2, 3, and UDP into the membrane.^{30,37} In contrast, in the case of CD59-controlled CDC, a β -strand in D4 of CDC attaches to a GPI-anchored CD59 receptor, which further mediates membrane insertion involving CRM and UDP.^{26,27} Once a monomer is fastened perpendicularly to the membrane, it begins to form dimer with adjacent monomers via transitory interactions.²⁸

Oligomerization. The next critical step toward pore formation is oligomerization. The precise trigger for oligomerization is not yet clear.⁵ It is presumed that random diffusion leads to the dimerization of monomers²⁸ and furthermore, investigation of PLY,⁴² PFO,³¹ LLO²² and ILY²⁶ unveiled interfacial connections between adjacent monomers, especially, tryptophan of UDP interacts with threonine of the next monomer.^{28,42} Dimerization assists to structural changes in D3 and D4 domains of the protein, which further propagates to a circular arrangement of oligomers.^{5,43,44}

Cryo-ET reconstructed oligomer models of CDC have displayed a high level of organization between monomers to generate ring-shaped oligomers.^{28,42} Similarly, these cryo-ET models and other independent mutagenic studies have disclosed that certain amino acids, for instance, W165 in PFO, E151 in PLY, D205 in PLO, etc., are essential for producing oligomers.⁴⁵ These mutations stall the oligomerization partially or completely or interfere with the circular distribution of monomers.^{45,46}

Prepore complex. The circular oligomers form a prepore complex before detaching the patch of the lipid bilayer. The prepore formation is an inherent attribute of CDC and can be fulfilled by a ring or circular arrangement of oligomers.⁴⁵ A linear oligomer or even a dimer cannot constitute a prepore complex. Moreover, it is a complicated process that is further, in some studies, divided into different stages, like early prepore and late prepore, and once a prepore state is established, it does not accept further monomer to be a part of it.^{28,30,47} Based on structural transitions, early prepore assembly is flexible, delicate, and can collapse in slightly harsh conditions, whereas late prepore is a rigid, stable, and even SDS-resistant structure.^{5,47}

From the monomeric perspective, in early prepore assembly the average size of monomers ($\sim 115 \text{ \AA}$),³⁰ according to the assessments of CDC by various methods (AFM, Cryo-EM), remain unchanged, which then, implies that the vertical configuration of protein is still intact and D3 is away from the surface of the membrane.^{11,22,30,42} However, immediately thereafter, the early prepore structure experiences subtle structural shift and becomes stable and even heat-resistant. This stage is referred to, as per PLY- investigation, late prepore.²⁸ The precise mechanism that leads to the conversion from early to late prepore is still ambiguous and poorly understood. Nevertheless, a distinct feature of late prepore is the significant reduction in the elongated length of protein ($\sim 40 \text{ \AA}$).^{5,28,30} This occurs due to a 90° bend in the configuration of D2 that minimizes the gap between D3 and the membrane.³⁰ GG at the D2-D4 interface is apparently responsible for the structural shift of D2.^{5,30} The helical bundles (HB1 and 2) of D3 are still in shape and slightly above the membrane surface.^{28,30,43}

The preserved UDP has been known to allosterically trigger the disengagement of D2 and D3, which in turn leads to a set of structural adjustments in both domains.^{37,45} These phase-shifting structural configurations are simultaneous in neighboring monomers as well and eventually, a prepore structure is produced, comprising an average between 30 to 50 monomers.^{28,45}

Like UDP, there is a conserved GG pair in D3 of CDC that acts as a fulcrum in rotating $\beta 5$ sheet away and routing the path for $\beta 4$ to engage with the $\beta 1$ sheet of the adjoining monomer.^{30,45} Mutational studies of PFO exhibit that Y181 of $\beta 1$ and F318 of $\beta 4$ in the neighboring monomer interact via π -stacking, and likewise, E183 in $\beta 1$ is electrostatically connected to K336 ($\beta 4$) in the adjacent monomer.^{30,43,46} These strong interactions are another apparent cause of the detachment of α -helical bundles (HB1 and 2) of D3 from D2.^{28,30} Hence, the HBs become free and prepared to descend into the membrane. This association of β -sheets continues as a chain throughout the oligomeric ring as a kind of domino effect.^{30,44} The different stages of prepore complex formation have been captured during the investigation of CDC via crystal structure, electron microscopy (EM), atomic force microscopy (AFM), etc., and their transitions from one stage to another could be prevented by specific site-mutations, engineered disulfide bridges and temperature as well.^{5,28,30,31,45,46}

Since CDC share an analogous structure, in-depth analysis of a few CDC (PFO, SLO, PLY, LLO, etc.) has been found in conformity with a broader picture. However, some key interactions may differ among different CDC during the prepore formation, e.g., E183 and K336 are critical for PFO and absent in PLY,^{24,28,48} and vice versa D168 is critical for PLY and not available in PFO.^{24,28,31}

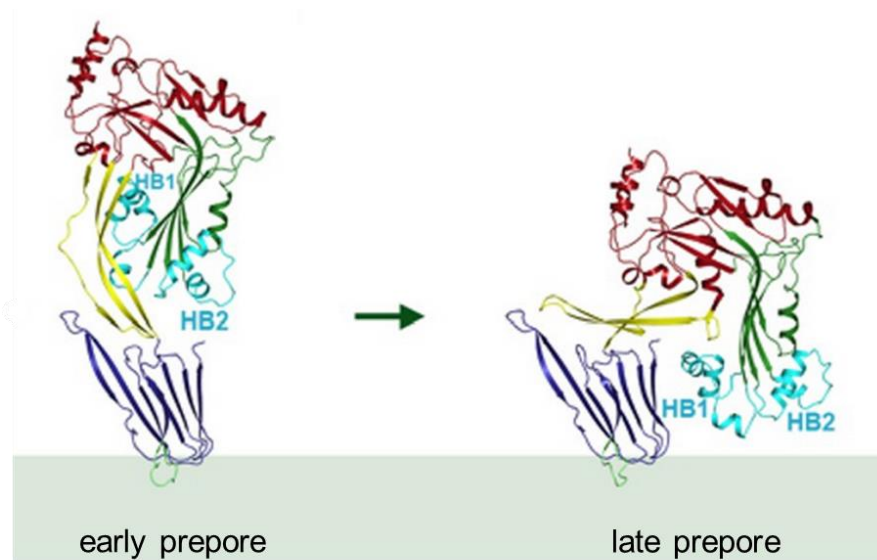


Figure 1.3. The shift of CDC model from early to late prepore. Exhibiting alteration in vertical structure of D2 and unfolding of HB1 and 2.²⁸

Pore formation. In this final step, a major transformation occurs within D3. The ductile HB1 and 2 of D3 lose their integrity and are remodeled into membrane penetrating β -strands.^{30,42} The source of energy required for pore formation is elusive to date and remains a scientific challenge.^{5,9} The discarded chunk of lipid bilayer during pore formation has an area of $\sim 200,000 \text{ \AA}^2$, which is significantly huge in comparison to the backbone peptide and hydrogen bonds of TMHs.^{5,15} Multiple opinions are circulating within the scientific community concerning the mysterious energy of pore formation. One of the relatively new assessments is based on the Cryo-TEM analysis of PLY, which suggests that the area of the membrane is not physically removed, rather lipids are pushed away, but still in contact with the membrane.^{28,49} This is a plausible explanation pertaining to energy. In contrast, the data obtained via other methods, e.g., solid-state NMR, AFM, EM, etc., imply that actual pores have been produced on cholesterol-containing vesicles.⁵⁰⁻⁵² Still, nothing is conclusive and further high-resolution examination is needed.

So far, it has been established that TMH1 and 2 infiltrate the membrane at an acute angle ($\sim 20^\circ$) while facing the hydrophobic side toward the membrane phospholipids and the partly hydrophilic side toward the lumen of the pore.^{28,42,48} The polar or charged inside strengthens the pore. For instance, in PLY, alternate negative and positive charge distributions on the surface of the pore and ionic interconnections, e.g., salt bridges between D168 and E170 and K271, are present among adjacent β -strands. Such aspects are critical for the stability of the pore.^{28,30}

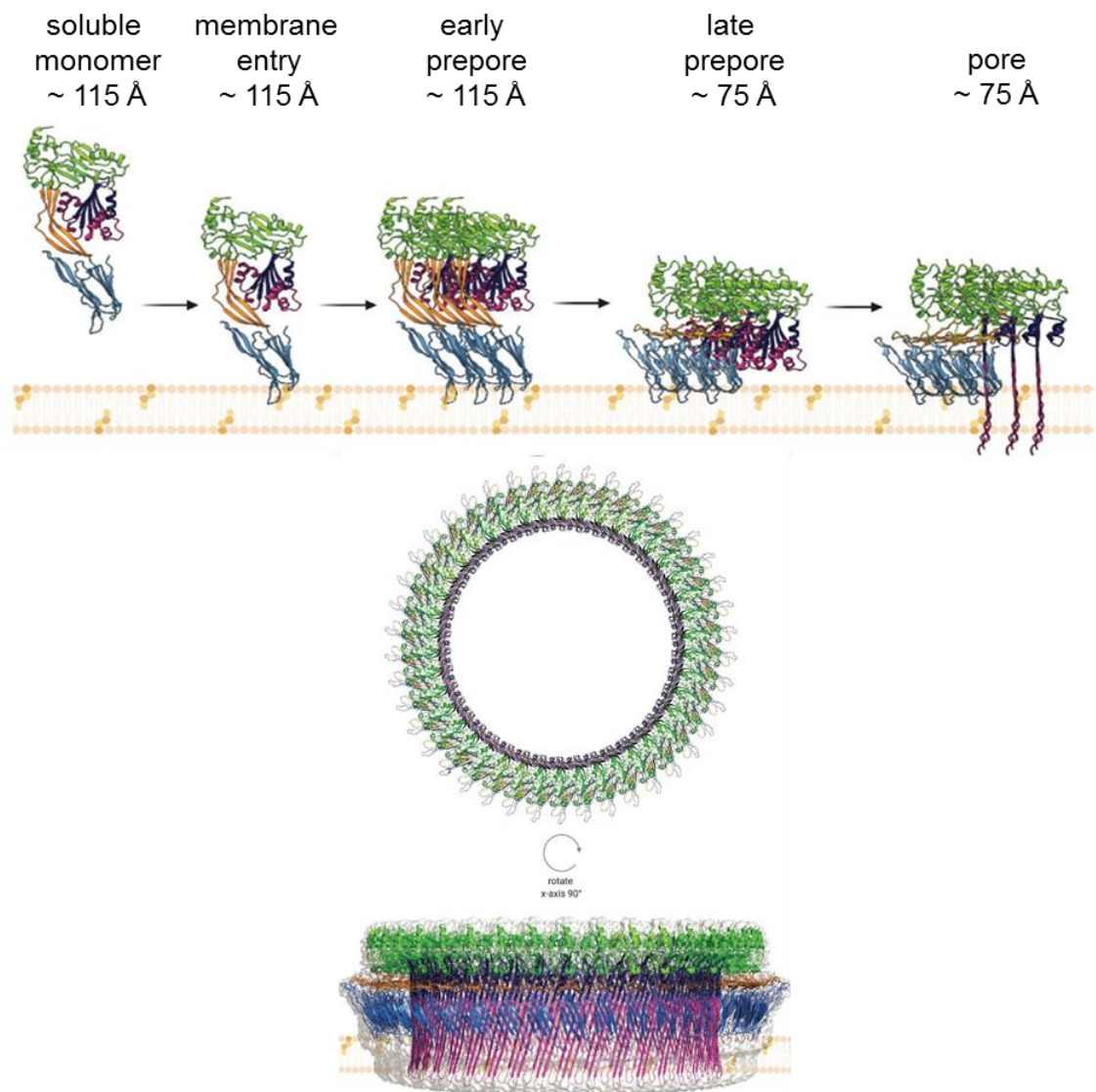


Figure 1.4. The pore formation of CDC. Common model of CDC highlighting different stages during pore formation from two different perspectives.³⁰

1.1.1.3. Role of CDC during bacterial infection

CDC are predominantly produced by gram-positive bacteria and several among them are known to cause diseases ranging from mild infections to life-threatening disorders. Common pathogenic species such as *Clostridia*,^{53,54} *Listeria*,^{16,55} *Streptococci*,^{25,56-59} etc., are known to express CDC and the role of CDC pertaining to virulence within the disease caused by these bacterial species has been extensively investigated. So far, there is an ample amount of evidence available about the fatal role of CDC in the exacerbation of infection.^{5,8,9,14,15} For instance, *Streptococcus pyogenes* is responsible for pharyngitis, fasciitis, cardiomyopathy, streptococcal toxic shock syndrome, etc., and all reported clinical isolates of *S. pyogenes* release streptolysin O (SLO).⁵⁸ When investigated in the SLO-deleted infected mice model, the virulence of *S. pyogenes* was significantly reduced.^{60,61} Likewise, *Streptococcus pneumoniae* is a causative agent of bacterial pneumonia, otitis, meningitis, sepsis, etc. and the CDC produced by *S. pneumoniae* is pneumolysin (PLY).²⁰ The PLY-deficient mutant of *S. pneumoniae* has been found as significantly less virulent in mice.^{62,63} Similarly, the data of *S. intermedius*, *S. suis*, *Listeria monocytogenes* and *Clostridium perfringens* convincingly prove that CDC belonging to each bacteria are the vital agents for the progression of diseases caused by these organisms.^{14,29,34,54,64} Therefore, CDC have been recognized as a common stringent virulence factor among bacteria.^{5,30} **Table 1.1** shows a few important diseases which are aggravated under the influence of the CDC.

In parallel to the pore formation, CDC activate numerous cellular pathways in the host, however, the response from the host against CDC may vary according to the cell-type and concentration of CDC.¹⁴ Certain cells are more susceptible to CDC than others, for example, CDC are lethal toward erythrocytes because they lack a nucleus and, therefore, possess the minimal ability to reconstruct ruptured membranes.^{65,66} On the other hand, CDC are more than 200 times better tolerated by immune cells in comparison to erythrocytes, e.g., neutrophils and macrophages.^{67,68} Similarly, regarding concentration, CDC stimulate necroptosis of host cells at lytic concentrations.^{69,70} Whereas, CDC may turn on various signaling pathways at sub-lytic concentrations that lead to complex interplay and modulation of the natural host immune reaction, eventually benefiting bacterial survival.^{14,20}

Table 1.1. Prominent disease progressing CDC with their parent species and diseases.

Bacterial specie	CDC	Diseases
<i>Streptococcus pneumoniae</i>	Pneumolysin (PLY)	Bacterial pneumonia, meningitis, otitis, etc.
<i>S. pyogenes</i>	Streptolysin O (SLO)	Septic shock, fasciitis, cardiomyopathy, pharyngitis, etc.
<i>S. intermedius</i>	Intermedilysin (ILY)	Brain abscess
<i>S. suis</i>	Suilysin (SLY)	Septicemia
<i>Listeria monocytogenes</i>	Listeriolysin (LLO)	Miscarriage, meningitis, etc.
<i>Clostridium perfringens</i>	Perfringolysin O (PFO)	Gas gangrene

Membrane repair subsequent to the formation of pores by CDC. In the event of membrane rupture in mammalian cells, a natural repair mechanism is activated.⁷¹⁻⁷³ Previously, it was proposed that endocytosis of toxin was a repair mechanism.⁷⁴ However, recent studies revealed that endocytosis is downstream of repair to restore cellular homeostasis by removing inactive toxins and the first stimulus for initiation of membrane healing is the Ca^{2+} influx.^{67,74} After investigations of multiple CDC, three major repair mechanisms have been reported. These include clogging, patch repair, and intrinsic repair.¹⁴ Clogging is a process of recruiting healing proteins, like annexins, at the site of a CDC pore in the form of latticework.⁷⁵⁻⁷⁸ Patch repair is attributed to resealing of the damaged plasma membrane by the fusion of internal vesicles, such as endosomes and lysosomes.^{14,75} Intrinsic repair is the most thoroughly investigated phenomenon among repair mechanisms. It has been demonstrated for many CDC like SLO, ILY, PFO, PLY, etc.^{14,67,79,80}

Intrinsic repair is characterized by the detachment of small lipid-area of the membrane containing the toxins-pore in the form of microvesicles (MV).^{67,79} The process of

removal of MV is known as shedding and is controlled by the Endosomal Sorting Complex Required for Transport III (ESCRT-III) machinery.^{79,81,82} Intrinsic repair is stimulated by the oligomerization of toxins.⁷⁹ The rate of shedding and the size of MV may fluctuate among different cell types, e.g., macrophages shed smaller MV than other cells.⁷⁹ Similarly, it depends on toxins as well, for instance, more shedding with PFO has been observed than SLO.⁸³ The shed MV consist of a mixture of lipids, prepores and pores of toxin, GPI-anchored proteins, and repair proteins such as annexins and ESCRT-III.⁸¹ Later, these MV manipulate the defense system of the host.¹⁴

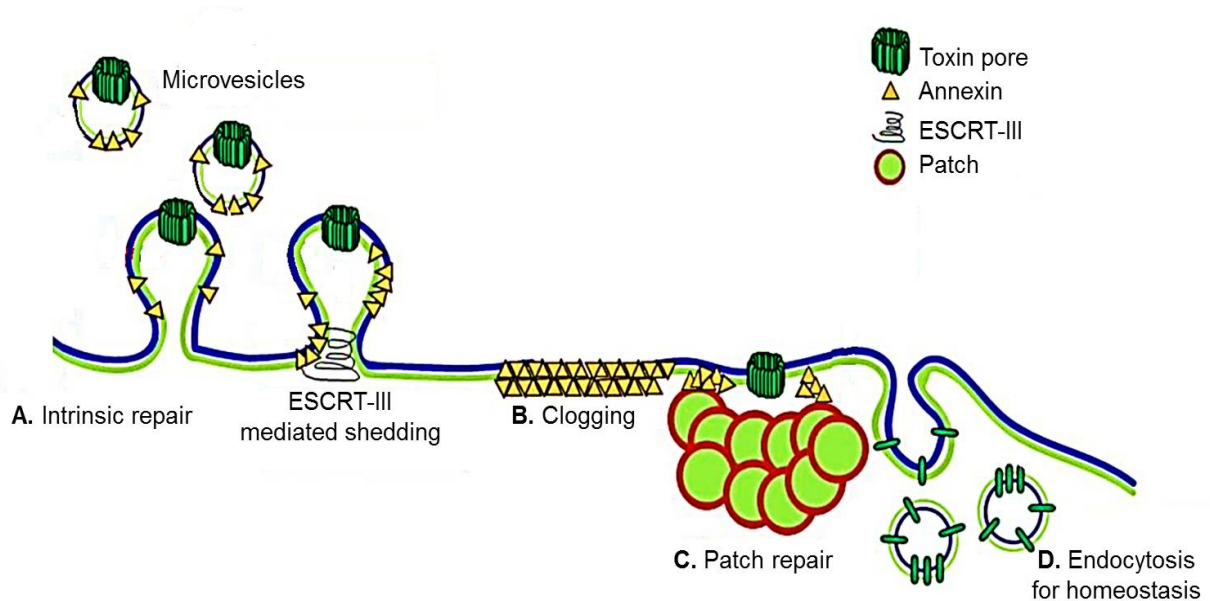


Figure 1.5. Mechanisms of membrane repair after CDC attack. **A.** Intrinsic repair. **B.** Clogging. **C.** Patch repair. **D.** Endocytosis.

CDC enhance programmed cell death. In addition to direct lysis, CDC are known inducers of programmed cell death, however, CDC assisted programmed cell death lacks apoptotic pathways. Instead, CDC induce cell death by programmed necrosis or necroptosis, autophagy, etc.^{2,8,9,14,30} By inducing programmed cell death directly or indirectly, CDC will intensify the complexity of infection and difficulty in treatment.^{5,20,40} One of the most common mechanisms of cell death under the influence of CDC is pyroptosis, especially in macrophages.^{84,85} Pyroptosis is stimulated by the activation of inflammasome,⁸⁶ deeper description about inflammasome are available in the immune system effects of CDC. Similarly, mitochondrial damage has been inflicted by numerous CDC (LLO, SLO, PLY, etc.).^{55,87-89} SLO and PLY have been reported to

reduce the membrane potential of mitochondria, resulting in ischemic cell death.^{87,88} Whereas, LLO affects cellular metabolism by transiently fragmenting the mitochondrial network and thus killing the cell.⁵⁵

In contrast to mutual mechanisms, activation of autophagy is variably noticed for CDC.¹⁴ For example, the experimental data of *C. elegans* exhibited that LLO has induced autophagy,¹⁶ whereas, in the same organism, SLO is unable to trigger autophagy.⁹⁰ The reason for this diverse behavior is elusive and further investigations might provide a better understanding of CDC.

Activation and manipulation of cellular signaling pathways by CDC. Intoxication of cells with CDC activates mitogen-activated protein kinase (MAPK) pathways, which generally monitor cellular physiologic functions including differentiation, migration, growth, and survival.⁹¹ MAPK pathways become active on stimuli such as growth factors, stress, cytokines, etc.⁹¹ Therefore, in the case of CDC, there has been a debate whether the activation is caused directly by CDC intoxication or indirectly through ionic flux (Ca^{2+} influx and K^+ efflux) or via DAMPs / PAMPs (danger/pathogen associated molecular patterns).^{91,92} CDC can stimulate all three MAPK pathways.¹⁴ However, the activation of the p38 pathway has been reported more frequently for CDC, like ALO,^{93,94} PLY,^{92,95} LLO,⁹⁶ VLY,^{93,97} SLO,⁹⁸ etc. Nevertheless, the downstream signaling of p38 includes recovery of K^+ after depletion, and production of pro-inflammatory cytokines, like tumor necrosis factor α (TNF α), interleukin (IL-1 β , IL-6 and IL-8), etc.^{93,97,99} The downstream protective effects of p38 are challenged by CDC like PLY, which neutralizes p38 by activating the deubiquitinating enzyme cylindromatosis (CYLD).¹⁰⁰ CYLD blocks p38, and the aftermath is increased vascular leakage leading to edema and acute lung injury in the case of pneumococcal pneumonia.^{20,100} Another pathway of MAPK is c-Jun amino (N)-terminal kinases (JNK) and it is also activated by PLY.¹⁰¹ JNK stops mucin release in *S. pneumoniae* infection.^{20,101} Mucin has a critical protective role in case of soft tissue infections, thus the stoppage of mucin production means better survival of the pathogen.^{14,101}

The third pathway, MAPK-ERK (extra-cellular signal related kinase), also known as, the MEK-ERK pathway is activated by CDC, such as ALO⁹⁴ and LLO^{96,102,103}. In the case of *L. monocytogenes* infection, MEK activation through Raf by LLO occurs to be

protective toward cell, however, on the other hand, the intracellular pathogen *L. monocytogenes* takes this as an opportunity to invade the cell.¹⁰²⁻¹⁰⁴

An ancillary consequence of CDC-mediated MAPK activation that occurs in the endoplasmic reticulum (ER), is the activation of unfolded protein response (UPR).^{14,105} UPR is a stress-induced feedback that causes the ER to increase the release of protein chaperones within the cytosol.¹⁰⁵ UPR could annihilate the cell if the stress is not reduced.^{14,105} Hence, it has shown better survival for *S. pyogenes* and *L. monocytogenes*.¹⁰⁶ UPR has been shown to assist cardiomyopathy post-bacterial infection.^{14,105,107}

CDC, like LLO, can also directly bind to the ER and deteriorate the cell via high intracellular calcium levels.^{108,109} ER has a low concentration of cholesterol (~5% mol.), but this is sufficient for CDC, like LLO, which is packed in vesicles and enters the cell via endocytosis, attacking the membrane.^{108,110} LLO impairs the ER membrane, leading to the release of calcium from an intracellular depot of ER.^{108,110} The calcium release typically enhances cellular repair via actin remodeling. However, an elevated concentration of calcium within cells is toxic.⁷⁷

Moreover, post-translational modifications occur in the cells under the influence of CDC.¹⁴ Modification of histone, ubiquitination and SUMOylation (small ubiquitin like modifier) are stimulated by CDC, yet in a cell-specific manner.^{110,111} Take the example of LLO, which affects ubiquitination in HeLa cells but cannot replicate the same in macrophages.¹¹⁰ Anyhow, numerous CDC alter ubiquitin and ubiquitin-like proteins and impair the E2 SUMO ligase Ubc9 after potassium efflux following membrane rupture, which ultimately boosts the infection.^{14,112} CDC are found to be involved in histone modifications, like dephosphorylation of Ser10 in histone H3 and deacetylation of histone H4.^{113,114}

Beyond intracellular adaptations, CDC are known to disturb the host vasculature. It is not only critical for the dissemination of bacterial infection but also regarding the migration of immune cells. PLY is notorious for the spread of pneumococcal infection via vascular infiltration.^{20,115} Similarly, ALO interrupts gap junctions⁹⁴ and PFO could cause vasoconstriction that leads to an impact on blood pressure.¹¹⁶ Additionally, PFO can impede neutrophil migration to the site of gas gangrene.⁵⁴ Likewise, SLO¹¹⁷ and

PLY¹¹⁵ have both been shown to restrict the migration of neutrophils. Furthermore, SLO has enhanced effects on platelet aggregation and eventually promotes microvascular occlusion that further blocks the migration of immune cells.^{14,88}

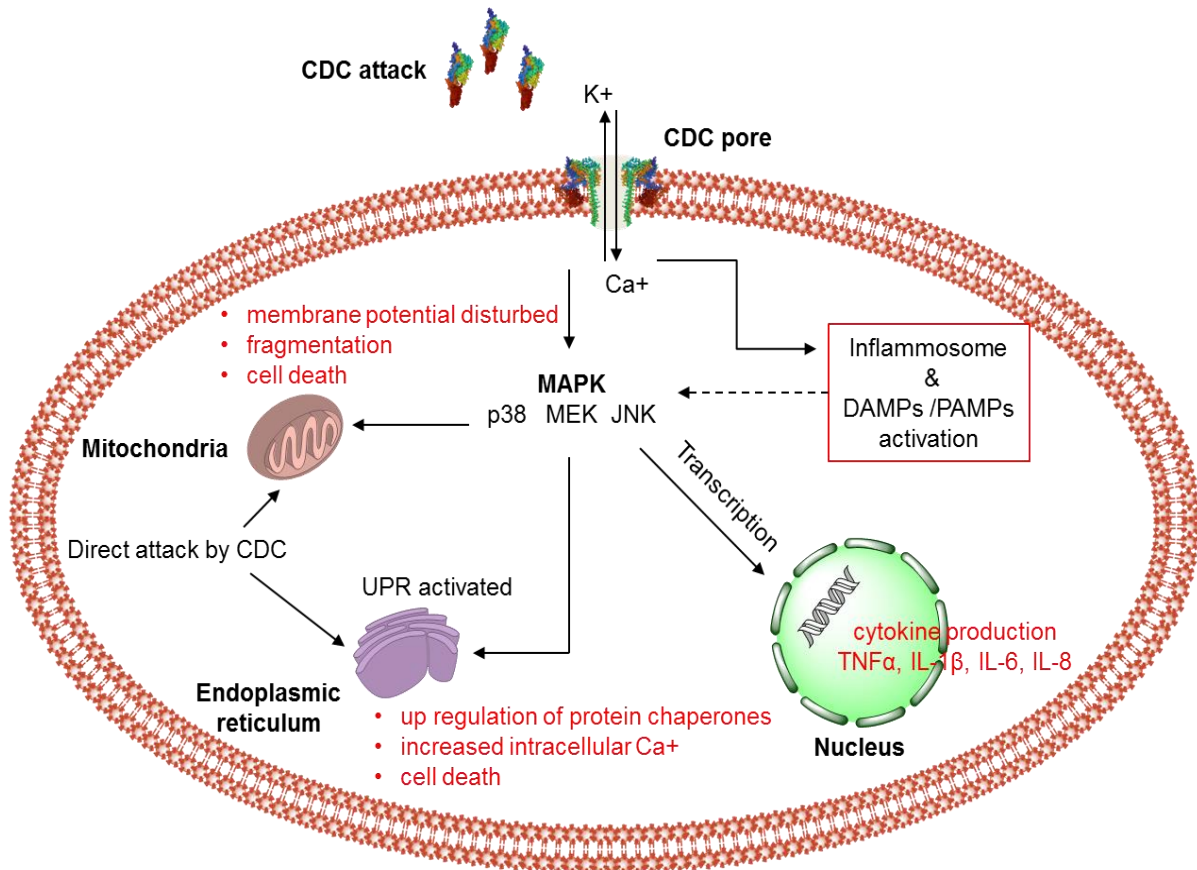


Figure 1.6. Signaling pathways associated with CDC. Ionic flux is produced after membrane rupture. If the cell survives lysis, various cellular mechanisms are triggered. Membrane pores activate inflammasome and DAMPs / PAMPs. Meanwhile, ionic flux activates MAPK pathways. MAPK pathways have multiple outcomes, ranging from pro-inflammatory cytokine synthesis to UPR activation, etc.¹⁴

1.1.1.4. Modulation of immune system by CDC

CDC are exceedingly detrimental to the host and their aforementioned effects are mutual among different types of cells in the body. However, when it comes to the immune system, the observed patterns of eluding the immune cells by CDC have been phenomenal in terms of creating a conducive environment for pathogens.^{5,20,30} Attenuation of the immune system is a peculiar feature of CDC that has been reported for multiple CDC.^{5,14} The natural immune response involves the recruitment of immune

cells such as neutrophils,^{69,70,117,118} macrophages,^{12,68,119,120} etc., to the site of infection after receiving the signals of infectious invasion within the body. CDC attack these immune cells and interfere with their protective actions including phagocytosis, cellular healing/repair, etc., via various ways and eventually trivialize the natural immune response. The following are some important immune-compromising manifestations of CDC.

Inflammasome mediated cell death. An inflammasome is an intricate intracellular multiprotein-oligomeric structure that is a component of the innate immune response and responsible for inflammatory cell death or pyroptosis.⁸⁶ CDC readily activates inflammasome by damaging the membrane.^{13,18,115,121-123}

Inflammasome could be activated in two ways under CDC attack, directly by potassium efflux during pore formation or indirectly by bacterial DNA or mitochondria DNA.^{121,124,125} Inflammasome includes repeating units of a sensory pattern-recognition receptor that recruit and oligomerize a protein ASC (ASC: apoptosis-associated speck-like protein containing a CARD/Pycard) and then, each ASC unit further combines with the inflammatory caspase (caspase 1, 4 or 5 in humans).^{86,126}

The sensory pattern-recognition receptor that initiates inflammasome is called NLRP3 (NLRP3: nucleotide-binding oligomerization domain-like/NOD-like receptor family, pyrin domain-containing 3) in case of direct activation via potassium efflux.^{115,121} In the case of indirect activation by bacterial or mitochondrial DNA, it is AIM2 (absent in melanoma 2).^{124,127}

Pyroptosis or inflammatory cell death occurs when NLRP3 or AIM2 triggers ASC for recruitment and activation of caspase.^{86,124,128} Thereafter, caspase-1 cleaves the cytosolic pore-forming toxin gasdermin D, leading to membrane disintegration and ultimately cell death.¹⁴ Meanwhile, apart from cell death, pyroptosis is responsible for the maturation and release of pro-inflammatory cytokines like HMGB1, IL-1 β , and IL-18, which stimulate the migration of further immune cells.^{86,126}

Although inflammasome is generally considered a favorable immune response for the host by limiting the shelter of pathogens within damaged cells.^{86,126} However, CDC take utmost benefit from the removal of immune cells. Hence, the reduction in the number of immune cells weakens the host defense, amplifies the opportunity for CDC to target other cells, and spreads infection throughout the host.^{12,123}

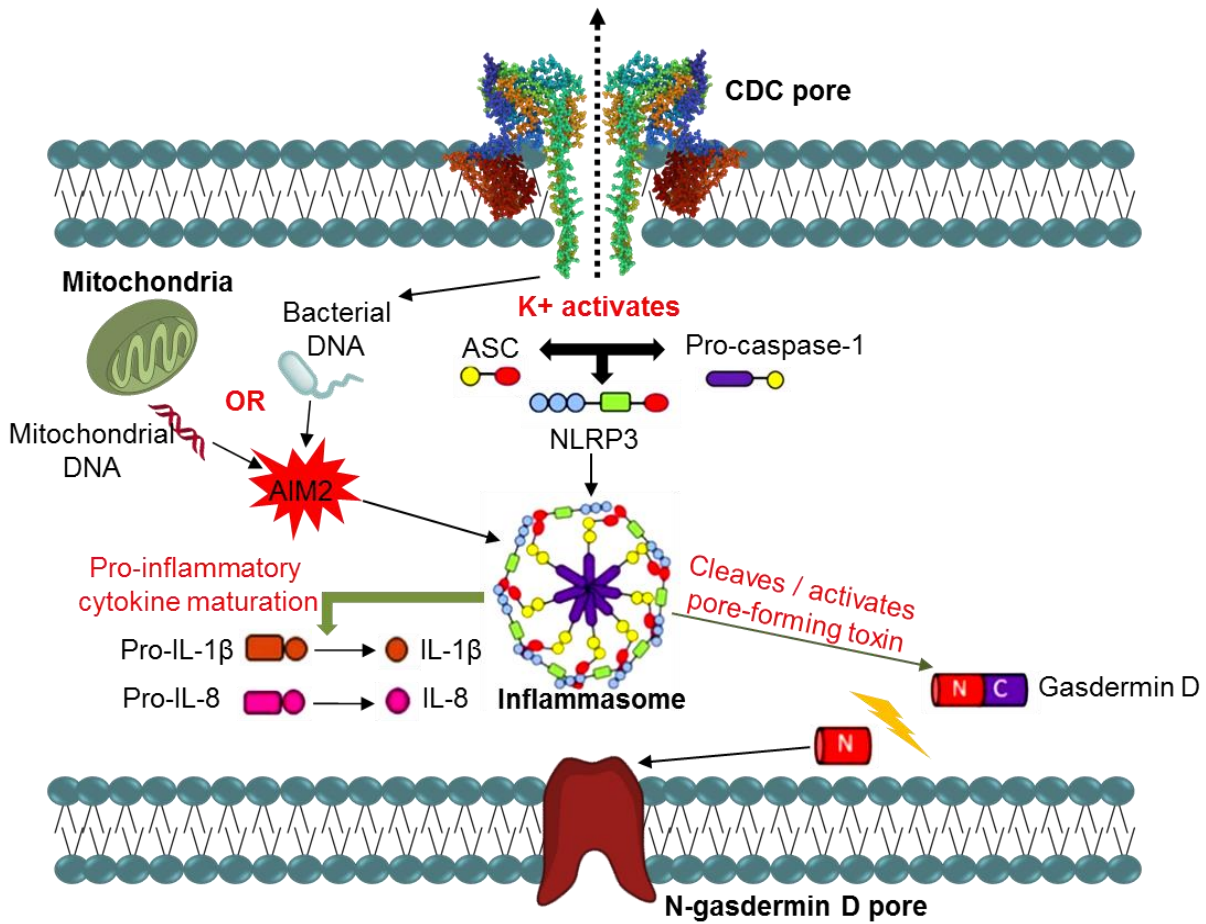


Figure 1.7. Inflammasome activation.

In immune cells, e.g., macrophages by CDC. Potassium efflux turn on the NLRP3 inflammasome. CDC can indirectly activate AIM2 inflammasome by bacterial DNA or mitochondrial DNA. After activation of inflammasome, caspase-1 controls pro-IL-1 β , pro-IL-18, and gasdermin D and thereafter, the N-terminus of gasdermin D produces pores that enables cytokine release and pyroptosis.^{14,86}

Evasion from phagocytosis. Another clinical attribute of the innate immune system is phagocytosis. It is characterized by the internalization of pathogens via engulfment that leads to the formation of a phagosome, which later fuses with a lysosome within the cytosol to exterminate pathogens.¹²⁹ Phagocytosis is typically operational when pathogens are greater than 0.5 μm and is performed by cells like macrophages, neutrophils, and dendritic cells.^{14,129}

CDC-secreting pathogens are known to escape phagocytosis and the prime example of such a kind of immune evasion is LLO.^{110,130-132} The survival and spread of *L. monocytogenes* infection is chiefly dependent on LLO-mediated phagocytic

escape.^{130,133} LLO dents the integrity of the phagosome by interfering with its ionic flux and eventually promoting bacterial survival.¹³⁴ Furthermore, LLO^{16,120,130,135,136} and PFO^{122,137,138} prevent the generation of extra oxygen by inhibiting NADPH oxidase in a phagosome that is required for production reactive oxygen species.¹⁴ However, not all CDC escape phagocytosis by identical mechanisms, for instance, SLO^{60,139,140} has been reported to hinder the engulfment of pathogens, whereas PLY¹⁴¹ and PFO¹³⁸ interfere with the acidification of the phagosome.

Similarly, some gram-positive bacteria have evolved to release extracellular vesicles (EV) to circumvent phagocytosis and eventually immune system. EV contain bacterial virulence factors, including CDC.¹⁴² The membrane of EV lacks cholesterol and constitutes phosphatidylglycerol and cardiolipin, thus, CDC can be effectively stored.¹⁴³ Immune cells are allured toward EV bypassing bacteria and during phagocytosis, EV release virulence factors in the cytosol.¹⁴⁴ The molecular details of the mechanism of EV are yet to be unveiled and hopefully, future studies will provide a much deeper analysis.⁵

Inhibition of cytokines. CDC enhance cytokines production and secretion in normal cells,^{120,141,145,146} however, conversely, in the case of immune cells, CDC inhibit the production of cytokines via multiple mechanisms.^{12,14,147} In the case of PLY, an indirect effect on the inhibition of cytokines has been reported.^{147,148} PLY interferes with the maturation of dendritic cells and, as a result, the production of interleukins (pro-IL-1 β , IL-8, and IL-12p70) is reduced.^{12,147,148} Likewise, PLY has been reported to block cytokines via interaction with the mannose receptor CD206, which is widely available on the surface of skin cells immune cells.¹⁴⁸ The detailed mechanism is still not clear and further investigations are ongoing. PLY-mutated version of *S. pneumonia* has exhibited no reduction in cytokines.¹⁴⁹⁻¹⁵¹ Likewise, investigations of PFO and SLO have shown significantly reduced production of TNF α .^{12,14} Whereas, CDC-deleted strains of bacteria have exhibited increased TNF α generation.^{12,14} Moreover, SLO interferes with the production of IL-8 and neutrophil-extracellular-trap by blocking the respiratory burst in neutrophils.¹⁵²

Meanwhile, the intrinsic repair mechanism of membranes also accounts for reduced cytokines.^{103,153} Shedding MV include lipids, repair proteins, toxins and immune receptors like IFN γ R1 and TLR4.^{79,154} The toxin-loaded MV damage the integrity of

immune receptors, consequently decreasing the signaling for cytokines.^{5,14,21} Despite the intensive investigations on CDC, many pathways are still obscure and future analysis might provide a better understanding.

1.1.2. Introduction to CDC evaluated in this research project

The pathogenic role and importance of CDC for the prolongation of a bacterial infection are indisputable in light of the evidence produced earlier. The timeframe allotted for this research is relatively short. Hence, it will be immensely challenging to evaluate each reported toxin in a narrow window of time. Therefore, only three toxins from CDC were chosen. The preference was not arbitrary, toxins were selected on the basis of a rational criterion. It includes their clinical relevance, investigative analysis, and availability.

CDC have two distinct groups, direct cholesterol binding and CD59-mediated binding toxins.^{8,9,15,27} The direct cholesterol binding group is predominantly bigger and comprises 90 % of all CDC,^{8,15} thus two members of this group were chosen, PLY and PFO. These were preferred because of their lethal capabilities during a diseased state and the amount of mechanistic details present in previous studies, and in addition, both share homologous conserved motifs, e.g., UDP.^{24,137} Alongside, ILY was chosen as a representative from human CD59-mediated CDC.³⁴

1.1.2.1. Pneumolysin

Streptococcus pneumoniae is one of the prevailing bacteria and it is frequently known as the cause of bacterial infections like pneumonia, meningitis, otitis, sepsis etc.^{56,59,155} Although there is a plethora of antibiotics and vaccines available against pneumococcus, yet the morbidity associated with diseases is considerably high worldwide.^{19,156-158} One of the vital reasons for the fatal nature of pneumococcus disease is PLY.^{19,20} It is composed of 471 amino acids and has been found in nearly all of the detected serotypes (> 100) of pneumococcus.^{23,24,123} It shares up to 70 % of homology with other CDC and is functionally analogous as well.^{123,159,160}

PLY exhibits a rare attribute, i.e., it lacks a secretory signal.¹⁹⁻²¹ It means that PLY is discharged into the host when a bacterial cell undergoes lysis, either autolysis or antibiotic-mediated lysis.¹⁹⁻²¹ Moreover, PLY stays inside the host after the removal of bacteria and causes damage at a cellular level. Therefore, conventional antibiotics are apparently ineffective against PLY.^{19,21} This atypical feature makes PLY one of the

most lethal toxins among CDC and thus, it has been regarded as a potential drug target.¹⁹⁻²¹ PLY is probably the foremost investigated toxin due to its noxious nature.

Contribution of PLY in the pathogenesis of infections. PLY has been defined as a determinant factor to distinguish between mild, chronic, and lethal infections in mice.^{70,149,151,161} Many effects of PLY are common among CDC and have been discussed earlier. Here, only distinctive effects of PLY are addressed according to the disease.

In the case of meningitis, discharge of PLY impairs the integrity of CSF by deteriorating the ependymal cells lining in the ventricles of the brain, and, as a consequence, ciliary frequency and flow of CSF are affected.^{162,163} Likewise, human brain models have shown PLY-induced loss of tight junctions and endothelial damage that ultimately favors the progression of bacteria across the blood brain barrier.^{164,165} Furthermore, PLY amplifies the severity of meningitis by stimulating glutamate discharge from astrocytes that is responsible for glutamate-dependent toxicity.²¹ PLY-deleted strains have shown significantly reduced virulence in meningitis.^{85,166}

Meanwhile, in otitis media, PLY, in combination with another virulence factor of pneumococcus, PspA, can induce hearing loss.¹⁶⁷ PLY-deficient bacteria have shown reduced biofilm generation and rapid recovery, which proves the deleterious role of PLY in a middle ear infection.¹⁶⁸

In bacterial pneumonia, an acute lung injury is a common outcome of the release of the platelet activating factor (PAF) by PLY and thereafter, downstream signaling of PAF stimulates phosphatidylcholine-specific phospholipase C and protein kinase C (PKC) leading to increased vascular resistance and pulmonary vasoconstriction.^{115,169-171} While, in parallel, pro-inflammatory mediators released by PLY cause an increase in vascular permeability and edema, which aggravate the injury.^{20,115,171} Furthermore, pore formation in the tracheobronchial, lung and alveolar epithelial cells worsens the condition, eventually advantageous for bacterial colonization and proliferation.^{161,167,172,173} PLY-containing bacterial strains have shown substantial biofilm formation within the respiratory tract in comparison to the mutated ones.^{149,174}

Next, the evidence of PLY involvement in acute cardiac events is sizeable.¹⁰⁷ PLY-pores may induce myocarditis and cardiomyopathy.^{107,175} Moreover, PLY triggers

cardiac troponins and those are signature markers of cardiac injury.^{107,175} The cardiotoxicity is dependent on the pore-forming ability of PLY, non-pore-forming and PLY-deleted mutants have not shown elevated enzymes.^{149,175} PLY activates the complement system that prolongs cellular survival and eventually bacteria shelter as well.¹⁷⁶ Triggering complement cascade could possibly escape opsonization and ultimately phagocytosis of bacterial cells.^{174,177} Similarly, recently it has been revealed that PLY regulates post-translational modifications (PTMs) of the relative abundance of histone in macrophages and shunts the expression of TNF α and IL-6.^{148,178} To conclude, PLY interplays in numerous cellular stages for the survival, dissemination and pathogenesis of pneumococcal infection.

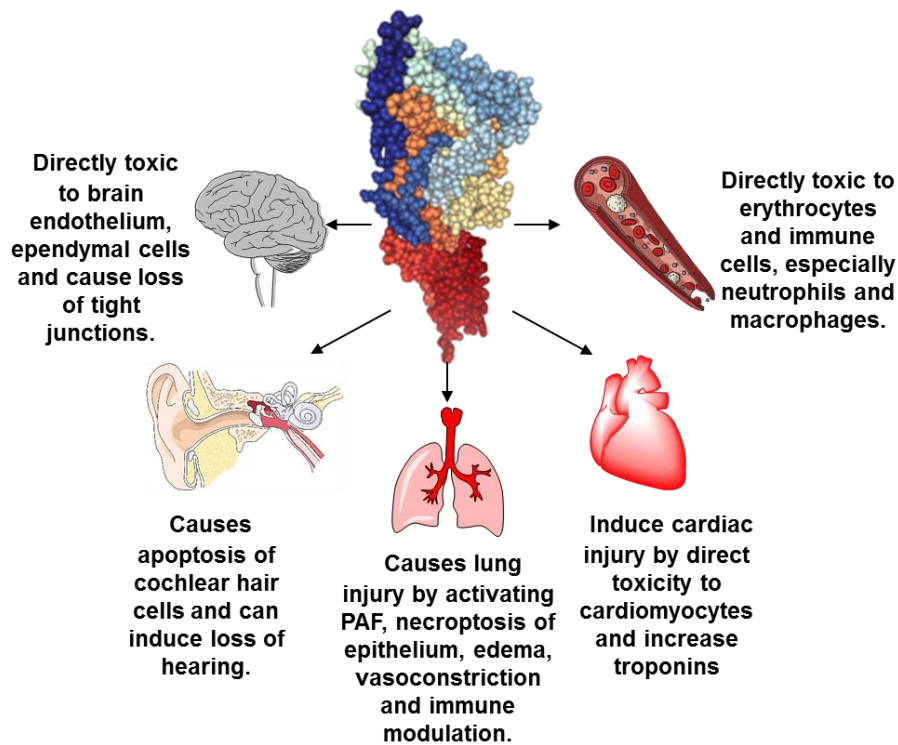


Figure 1.8. Concise representation of PLY-induced toxicity in different organs of the body.

1.1.2.2. Perfringolysin O

PFO is produced by *Clostridium perfringens*, a gram-positive anaerobic bacterium that is a common cause of food poisoning, gas gangrene, and other infections.⁵⁴ PFO is composed of 500 amino acids which is divided into signal peptide (1-28) and chain sequence (29-500).¹³⁷ The signal peptide assists in the transport of PFO outside the cell. PFO is excreted via the general secretory pathway (GSP), which is a mutual carrier for the transport of proteins across the bacterial membrane.^{137,179} The GSP detects the signal peptide of PFO and facilitates the toxin movement out of the cell, cleaving the signal peptide and only the chain sequence arrives in the bacterial extracellular environment.¹⁸⁰

The membrane binding ability of PFO is exclusive in regard to the availability of cholesterol.^{31,137} PFO can only engage to free-cholesterol or accessible-cholesterol, i.e. cholesterol molecules that are not tangled with sphingomyelin or other lipids and enzymes or proteins.¹⁸¹ It further means that only 33 % of the membrane cholesterol is available for PFO binding. Furthermore, the process of pore formation is afflicted in PFO due to the lipid microenvironment.¹⁸¹ It has been noticed that the formation of the pore is sluggish in PFO as compared to other CDC (SLO).^{31,137,181}

Pathogenesis in gas gangrene. *Clostridium perfringens* contains multiple virulent toxins (α , β , ϵ , etc.), some of them are encoded on the extra chromosomal plasmids and not present in all strains.¹⁸² However, the gene (pfoA) of PFO is coded on the central circular chromosome.^{137,182} Thus, it is present in nearly all known strains and is a potent virulence inducer during gas gangrene. The pathological feature of gas gangrene is leukostasis, which has been augmented by PFO.^{181,183} It limits the migration of leukocytes by impairing the chemotactic movement and morphology of neutrophils, which ultimately leads to vascular leukostasis and prohibits the transfer of immune cells to the site of infection.¹⁸⁴ The morphological impairment of neutrophils includes inhibition of cytoskeletal polymerization that occurs under the influence of PFO.^{31,137,184} Similarly, PFO has been known to increase the expression of adhesion proteins on leukocytes, as a result, adhesion between leukocytes and endothelial cells is escalated and further infuriates gas gangrene.^{182,183} The impact of deteriorated vasculature is not localized to the site of gas gangrene and it further propagates toward systemic effects including increased blood pressure and subsequently, cardiac

load.^{14,182} This effect does not occur because of direct cardiotoxicity but an indirect effect, however, the detailed mechanism is unclear so far.^{14,137}

Synergistic effect of PFO and alpha-toxin. The alpha-toxin (α -toxin) is a zinc metallo-phospholipase that requires zinc for its activation.¹⁸⁵ It is homologous to phospholipase C and therefore can hydrolyze phospholipids. α -Toxin disengages cholesterol from sphingomyelin and provides more free cholesterol to PFO.^{182,185} It has been observed in transgenic animal models of gas gangrene that the presence of α -toxin intensifies the toxicity of PFO and vice versa.¹⁸⁶ The myonecrosis of tissue presumably relies on α -toxin, however, an alliance of PFO and α -toxin accelerates the tissue necrosis.^{184,187} PFO promotes the survival of *C. perfringens* by directly interfering with the phagocytosis of macrophages and by NLRP3-mediated inflammasome activation at the early stages of the disease. Meanwhile, α -toxin escalates necrotizing actions.^{122,137,138}

Similarly, both PFO and α -toxin work in tandem for the progression of disease at a later phase. Impairment of vasculature and thrombosis takes place during gas gangrene by a combined effort of α -toxin and PFO.^{183,186,187} PAF is activated by α -toxin and PFO increases leukocyte adhesion proteins.¹³⁷ Hence, aggregates or clumps of platelets and leukocytes are formed and adhere to the endothelial lumen of the blood vessels, eventually manifesting thrombosis, which minimizes blood flow.^{188,189} Moreover, the occlusion in vessels diminishes immune activity by preventing the migration of immune cells and promoting edema.^{137,182,188}

The combination of PFO and α -toxin is lethal beyond humans. They are responsible for the disease progression of necrohemorrhagic enteritis in cattle, which accounts for 5-10% of mortality in diseased animals.^{187,190,191} Complications of necrohemorrhagic enteritis include vasocongestion, inflammation, and hemorrhages in contrast to myonecrosis, thrombosis and reduced blood flow during gas gangrene.¹⁹¹ The opposite actions in the pathogenesis of disease have been poorly understood and often related to the difference in phenotype.^{182,187,191} Nevertheless, the synergistic effects of PFO and α toxin are established and supposed to be the principal cause of virulence of *Clostridium perfringens*.^{187,191}

1.1.2.3. Intermedilysin

ILY is a CDC that belongs to *Streptococcus intermedius*, a gram-positive bacterium that is a common cause of dental abscesses, brain abscesses, and other infections.¹⁹² Unlike other CDC, ILY is strictly dependent on the human CD59 receptor for membrane attachment and that feature makes ILY a human-specific pathogen.^{26,36} Interestingly, CD59 receptor is the only membrane receptor that inhibits the membrane attack complex (MAC) and it acts by inhibiting C8 and C9 components of the complement system.¹⁹³ Thus, it protects the cell from MAC and called MAC-inhibitory protein (MAC-IP).²⁶ ILY and other CD59-mediated CDC have seemingly evolved and specialized the cytotoxic capacity against humans.^{30,97} However, there is an example of CDC, VLY, which has an intermediate binding mechanism. It can bind the membrane with CD59 and also directly to cholesterol, but with slightly reduced affinity.^{26,97} Nevertheless, to execute the pore formation, ILY or any other CD59-mediated CDC always needs cholesterol after membrane binding.⁸ In addition to subtle changes in the mechanism of membrane binding, ILY possesses multiple differences in the homology of D4, e.g., the UDP of ILY lacks cysteine and tryptophan.^{5,30} These amino acids are critical in terms of activity in many other CDC.

S. *intermedius* infections and role of ILY. The common biosphere of *S. intermedius* is the oral cavity of humans.¹⁹² It is generally non-pathogenic in a wide range of the population. However, it has been occasionally found to cause diseases like bacteremia and abscesses in organs like liver, brain, and lung. In 20% of *S. intermedius* infection patients, a previous dental procedure has been reported and it is often considered the biggest risk factor.¹⁹⁴ However, so far, there have been no mechanisms reported of how suddenly bacteria become pathogenic after a dental procedure. Additionally, alcoholism, diabetes, cancer, surgery, etc., are minor risk factors. A total of 101 cases of *S. intermedius* associated abscesses have been reported from 1996 to 2019 across 24 countries and 8% of total cases proved to be lethal.^{192,194}

ILY-expressing strains of the bacterium are capable of causing abscesses or bacteremia because high levels of ILY have been detected in most of the cases of *S. intermedius* infection.^{26,192} Experimentally, ILY-mutated strains have shown no cytotoxicity in human cells.¹⁹⁵ ILY enhances biofilm and eventually bacterial colonization.^{36,195} Bacteria secrete hydrolytic enzymes which take care of pus formation and ILY further activates the immune response which aggravates the

disease.^{26,36} Overall, the molecular insights of ILY-induced pathogenesis have not been unveiled. Most of the experimental data suggest direct toxicity.^{26,36,195} Further intensive studies are required to get deeper information on this topic.

1.1.3. CDC as an anti-virulence drug target

CDC have been under the limelight for over a century for their pore-forming ability. However, the cellular implications of CDC other than pore formation have been underestimated until the recent investigations of a few decades that have provided a hefty amount of data which have elucidated the critical role of CDC during bacterial infection.^{5,8,9,12,14,43} The meticulous analysis of CDC-carrying pathogenic organisms has exhibited that CDC contribute to the invasiveness of infection exponentially.^{5,8,12,14,30} Primarily, CDC promote bacterial survival and colonization within the host tissues via direct toxicity, and then, at a secondary level, CDC salvage bacteria by baiting the immune system.^{5,8,30} Therefore, CDC have been classified as the potential virulence factors of their respective bacterial organism. The plexus created by CDC within the host is perplexing and the molecular insights of various atrocities have already been described, whereas numerous mechanisms of deleterious actions are still to be uncovered, thus, there is still more to come.^{5,8,30}

Antimicrobial agents have been effectively treating infections for almost a century. Today, a wide range of antimicrobial agents are available to combat infections caused by pathogenic organisms, but other problems like resistance to antibiotics, health facilities, malpractice, etc., have emerged.¹⁵⁷ However, neglecting all these issues and strictly considering the treatment of CDC possessing pathogens, data suggest that despite the availability of antibiotics, the treatment has been consistently complex because of the detrimental actions of toxins, resulting in high rates of morbidity and mortality. A few noteworthy examples of mortality connected to CDC-pathogens include *S. pneumoniae* (circulates PLY), that is responsible for more than a million deaths annually.^{19,21,196} Likewise, *S. pyogenes* (circulates SLO), which is the cause of half a million deaths every year,^{60,152,197} and *L. monocytogenes* (circulates LLO), which account for the death of 15-20% among all infected patients.¹⁹⁸⁻²⁰⁰ These numbers clearly suggest that conventional antibiotics do not suffice and therefore, CDC require ancillary agents as adjuncts to antibiotics to curtail infections and save precious lives.

Evaluation of current and reported strategies to counter CDC. CDC are an ongoing challenge for healthcare providers as well as researchers. Consider the hospital settings, physicians encounter CDC-mediated impairment in several severe infections such as pneumonia, gas gangrene, liver abscess, sepsis, etc. Unfortunately, there are no official protocols or SOPs on how to control/manage CDC-associated pathogenesis in an invasive bacterial infection. The treatment protocol is customized according to an individual case and depends on several factors like disease condition, age, response to medication, etc.¹⁹ However, a generic plethora of available medications is considered for intervention.^{5,19,21} It includes antibiotics,¹⁵⁶ anti-inflammatory,²⁰¹ cholesterol synthesis inhibitors,²⁰² platelet aggregation blockers,^{203,204} and additional symptomatic relief medicines.²⁰³ Surgery is a rare way to block infectious spread, e.g. in gas gangrene, abscess, etc.¹⁸³

Since most of the CDC belong to gram-positive, therefore, antibacterial agents like penicillin, macrolides, clindamycin, vancomycin, etc., are applied for infection.²⁰⁵ Typically, to counter CDC, medicines like hydrocortisone for inflammation,²⁰¹ statins for decreasing cholesterol biosynthesis,²⁰² aspirin or PAR1 blocker for reducing thrombosis,²⁰⁴ etc., are given in combination with antibiotics. The universal efficacy of these combinations has not been established and that is why there are no consensual guidelines. The figures mentioned earlier concerning the lethality or the mortality connected to CDC-bearing infections are after the use of these medications. Hence, these medicinal agents are not adequate to give a cure.

In parallel, CDC have been addressed by the scientific community as a serious health concern. Pathogenic CDC like PLY, PFO, LLO, SLO etc., are highly toxic and widely accepted individual drug targets, have been investigated intensively and tested individually. Pre-clinical studies have proposed numerous inhibitors against individuals, as well as multiple pathogenic CDC. However, excluding few exceptions, most of them have not even been considered for clinical evaluation.

The proposed inhibitors include plant-based molecules,^{41,160,206} biologicals^{35,207,208} and synthetic products.^{209,210} But, polyphenolic compounds such as flavonoids, tannins, etc., either extracted from Chinese herbs or green tea or any other plant, constitute a predominant ratio among recommended anti-CDC agents.²¹¹ However, these molecules lack experimental evidence of specificity toward toxins and, in contrast,

polyphenols have shown association with multiple proteins and drug-targets for cancer, aging, etc.^{211,212} Hence, it is implausible that polyphenols could be considered for clinical evaluation. Similarly, cholesterol and related plant steroids have shown inhibition of many CDC in the pre-clinical investigation. Since cholesterol is an essential component of membranes, imbalance of cholesterol can lead to metabolic disorders. Thus, the therapeutic value of cholesterol or related compounds is not convincing. Despite this, a cholesterol-containing liposome-based approach to sequester toxins has been in clinical trials and so far, a dose-dependent effect has not been achieved.²¹⁰

Likewise, biologicals have been attempted to alleviate CDC toxicity. Immune serum from rabbit has shown attenuation of VLY.³⁵ Antibodies from murine source have effectively debilitated PLY, PFO and SLO in pre-clinical studies.^{207,213} Furthermore, a pneumococcal vaccine containing PLY toxoid has proceeded into the phase II trials, but due to lack of additional protection from the disease, further development has been terminated.²¹⁴ A compact review of molecules proposed as anti-toxin agents is available in the **Table 1.2**.

Table 1.2. Reported inhibitors of CDC in preclinical studies.

Anti-CDC/ toxin agent	CDC/ toxin	Category/ source	Clinical status
Acacetin ^{198,215}	LLO and PLY	Polyphenols	Not evaluated
Allicin ²¹⁶	SLO	Organosulfur	Not evaluated
Amentoflavone ^{217,218}	PFO and PLY	Polyphenols	Not evaluated
Apigenin ²¹⁹	PLY	Polyphenols	Not evaluated
Baicalein ²²⁰	LLO	Polyphenols	Not evaluated
Betasitosterol and other sterols ^{41,160}	PLY	Phyto-steroids	Not evaluated
Cal02, novel liposomal antitoxin ²¹⁰	PLY	Cholesterol based vesicle	Under evaluation
Chrysin ²²¹	LLO	Polyphenols	Not evaluated
Engineered liposomes ²⁰⁹	SLO and others	Cholesterol based vesicle	Not evaluated
Ephedra sinicia ²²²	PLY	Chinese herb/ polyphenolic	Not evaluated
Epigallocatechin ²²³	PLY	Polyphenols	Not evaluated
Fisetin ²²⁴	LLO	Polyphenols	Not evaluated
Immune serum ³⁵	VLY	Rabbit source	Not evaluated
Juglone ²²⁵	PLY	Naphthoquinone	Not evaluated
Luteolin ²⁰⁰	LLO	Polyphenols	Not evaluated
Morin and Myricetin ²²⁰	LLO	Polyphenols	Not evaluated
Murine mAbs PLY4, PLY5 and PLY7 ²⁰⁷	PLY	Mice source	Not evaluated
Anti-PFO mAbs ²¹³	PFO and SLO	Immunogenic	Not evaluated
Naringenin ²²⁰	LLO	Polyphenols	Not evaluated
PLY-vaccine ²¹⁴	PLY	Immunogenic	In phase II
Piceatannol ^{208,226}	PFO	Polyphenols	Not evaluated
Quercetin ²²⁷	PLY	Polyphenols	Not evaluated
Shikonin ²⁰⁶	PLY	Polyphenols	Not evaluated
Verbascoside ^{228,229}	PLY and PFO	Polyphenols	Not evaluated

1.1.4. Antimicrobial resistance

In addition to CDC contributing pathogenesis, we have acknowledged another contemporary paramount healthcare concern regarding treatment of infectious diseases, i.e. antimicrobial resistance (AMR).¹⁵⁷ AMR has been evaluated as a legitimate threat for at least the last thirty years.¹⁵⁷ The consequences of AMR include increased morbidity and mortality rates, longer hospitalization, higher healthcare costs, and the potential for the spread of infectious disease. Bacteria implement genetic as well as phenotypic techniques to shield against antimicrobial agents.²³⁰ In cases of prolonged infections, e.g., CDC-involving infections, the microbial tendency to gain resistance is increased.²³⁰ Therefore, the contemporary regime of anti-infective drugs is at the risk of becoming obsolete due to AMR.¹⁵⁷ According to a recent report (2019-20), nearly 5 million people died due to infections caused by drug-resistant pathogens.²³¹ Almost 90 pathogens have been reported as resistant to a single or a combination of antimicrobial therapies.²³¹ Furthermore, problems such as antibiotic abuse, limited medical facilities and inefficacious polysaccharide vaccines can aggravate the situation, and thus, researchers are striving for better and more effective approaches to counter these threats.²³²

To address the issue of AMR, the spotlight of preclinical studies has been gradually moving toward anti-virulence strategies instead of developing new antibiotics.²³² The goal of anti-virulence therapy is to neutralize or inhibit the virulence factors produced by pathogens, rather than killing the pathogen.²³³ By this approach, bacteria face reduced stress toward the evolution of resistance and, in addition, it promotes microbial clearance relatively easily by the immune system or by antibiotics.^{232,233} Hence anti-virulence therapy is an innovative and promising approach to overcome limitations of conventional antimicrobial therapy. Multiple virulence factors are opted to be targets, e.g., toxins,^{21,233} adhesion proteins,²³⁴ quorum sensing,^{158,234} etc.

Here, we have chosen CDC as an anti-virulence target. Our goal is to develop a generic inhibitor of CDC that could effectively encompass most of the pathogenic CDC and could be applied as an adjunct to antibiotics in CDC-mediated infections. Thereby, prohibiting CDC-associated toxicity and promoting an efficacious eradication of infection presumably without a fear of developing bacterial resistance.

1.1.5. Aim of the project

The preceding discussion has established that disseminated CDC in a bacterial infection pose a significant threat to human health, necessitating urgent remedial action. Although prior research has proposed various measures to contain CDC, including small molecules, these remedies have exhibited notable shortcomings. Therefore, the aim of to develop small molecule inhibitors of CDC capable of efficiently preventing or minimizing CDC-mediated pathogenesis at a cellular level in bacterial infections. Starting from primary hits derived from a virtual screening (**Figure 1.9**), we wanted to validate hits biophysically and identify their active pharmacophore, optimize the activity, elucidate the binding site, understand the binding mode, and evaluation of their efficacy in multiple CDC.

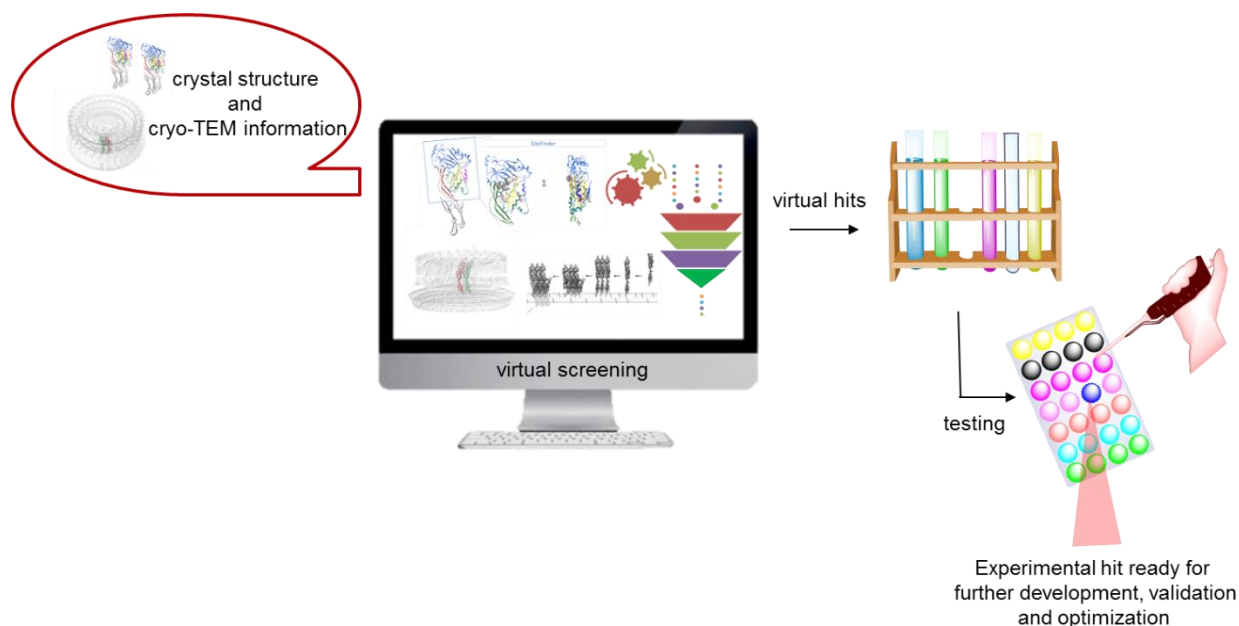


Figure 1.9. The workflow of the primary work before start of the project.

To achieve the objective of our study a collaborative effort is necessitated. The first crucial step in this study is the synthesis and testing of the active molecules. The biophysical validation will be followed after in vitro testing. There are several methods like ITC, BLI, mass spectrometry, etc., available in our lab, however, we need to establish a method according to the hydrophobicity of CDC and physiochemical properties of inhibitors. Then, in order to create more potent and chemically stable

inhibitors, it is necessary to identify the pharmacophore of active molecules. Our group labs are fully equipped with synthetic and analytic capabilities to develop a lead compound or series. Meanwhile, the testing of lead series establishes a structure activity relationship (SAR) in relation to the potency and stability of inhibitors that could be beneficial for further development of more potent inhibitors, if required. Thereafter, the realistic objective is the confirmation of the in silico suggested mechanism of the lead compound. The plan is to express multiple mutant versions of toxin (mutational analysis) and evaluate them against inhibitors to approve the proposed computational binding mode. Afterwards, the objective is to proceed toward the realm of cellular testing. The strategy is to analyze potent inhibitors against the wild toxin on human cell lines in cytotoxic and microscopic assays, and from there, only the successful inhibitors will be examined in an actual bacterial infection model assay. Finally, the potency and efficacy of the best inhibitors will be evaluated against multiple CDC by experimental testing.

2. Chapter 2: Results and Discussion

2.1. Overview of the preceding research

Here, a comprehensive review about the discovery of initial hits is provided, which served as a foundation in this project. It is known that CDC lack an established active catalytic site.⁵ Therefore, initially a typical CDC, PLY, which has been widely accepted as a drug target, was selected for the virtual screening.^{19,21} Cryo-EM maps of PLY-pores⁴² and the crystal structure^{23,24} were used by our collaborator Dr. Marcel Bermudez from the group of Prof. Dr. Gerhard Wolber to build a computational model of PLY. Subsequently, Dr. Bermudez employed the modelling tool SiteFinder to find a suitable binding site. After careful scrutinization, he selected a distinctive potential binding site within the prepore configuration of PLY-model, and the amino acids in that area were involved in the interfacial connections between the monomers. A small molecule apparently could prevent the oligomerization of the toxin by blocking this site, eventually the pore formation would also block. Thus, more than 500,000 small drug-like molecules from online commercial supplier libraries (Specs and Enamine) were virtual screened at the suggested binding site. Next, nearly 72,000 virtual hits were rescored and validated virtually and, finally, a best group of 10 diverse small molecules was chosen for in vitro testing. The molecules were purchased from Specs.

Multiple assays were considered to test the molecules, but only liposomal and hemolysis assays were customized and developed for screening of molecules. However, after an experimental comparison between the hemolysis and liposomal assays, the hemolysis assay was preferred for testing inhibitors. At first, two molecules demonstrated inhibition of PLY at concentrations $\leq 100 \mu\text{M}$. Unfortunately, one of the molecules had poor solubility and as a result, it was withdrawn from testing. Only one molecule, named **pore-blocker-1** or **PB-1** was contemplated for further testing and the IC_{50} value ($\sim 67 \mu\text{M}$) was calculated. Hereafter, the ability of **PB-1** to block the oligomer formation was evaluated in a liposomal-based assay involving 8% SDS-gel. **PB-1** hindered oligomerization at $25 \mu\text{M}$. Afterwards, **PB-1** was qualitatively validated in a biophysical (bio-layer interferometry) assay.

Next, to optimize **PB-1**, structural derivatives of **PB-1** were thoroughly searched online in the library of Specs. Finally, six suitable structural analogs of **PB-1** were purchased and tested. Only one showed a potency by almost 20 times increased and was named **PB-2**. Here, in this project, **PB-1** and **2** served as the starting points.

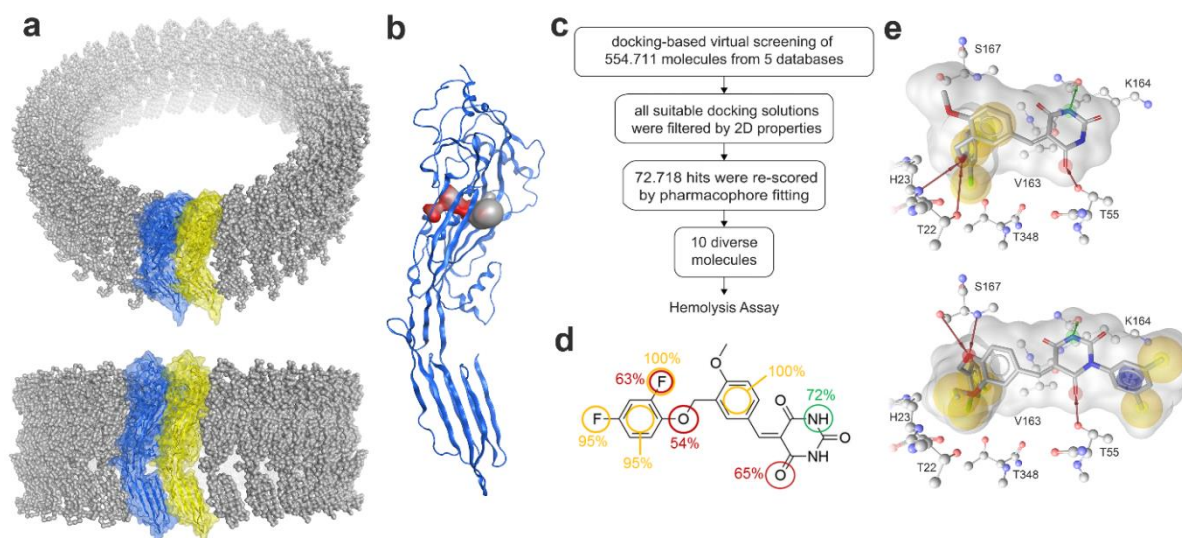


Figure 2.1. Structure-based virtual screening for the identification of CDC inhibitors. **a.** CDC (PLY) dimer was built by fitting crystallographic data (PDB entry: 4ZGH)²³ into a cryo-EM map⁴² (PDB entry: 2BK2).²⁴ **b.** The identified potential binding site is shown as surface. **c.** Virtual screening workflow resulting. **d.** PB-1 with interaction frequencies from 250 ns of MD simulation. Yellow indicates lipophilic contacts, hydrogen bond acceptors and donors are shown in red and green, respectively. **e.** Proposed binding modes of PB-1 (above) and PB-2 (below) the color code is the same as in (d), aromatic interactions are shown as purple disk. (This figure is provided by Dr. Marcel Bermudez)

2.1.1. Introduction the hemolysis assay

Hemolysis assay was used for initial testing of inhibitors. In this assay, defibrinated sheep erythrocytes were employed as substrate for CDC. Erythrocytes are extensively used in assays to determine toxicity of an agent.²³⁵ Erythrocytes rupture under the effect of CDC and release hemoglobin, which can be measured and quantified to determine the degree of hemolysis.²³⁵ In the presence of potential inhibitors of CDC, the discharge of hemoglobin was assessed and the efficacy of inhibitors was determined. The hemolysis assay is relatively easy to perform and does not require sophisticated cell culture techniques yet, results obtained via hemolysis assay are robust, reproducible and much closer to biological (in vivo) conditions in comparison to other in vitro assays like liposomal or fluorescence-based assays.

The native pore-forming activity of CDC considerably depends on the cholesterol content of the membrane²³⁶ and erythrocytes contain ca. 23% cholesterol in their lipid membranes.²³⁵ This feature of erythrocytes makes them ideal substrates for CDC and

hence the testing of CDC-inhibitors is best suited. The findings like IC_{50} or related inhibitory values obtained through hemolysis assay provide an estimate of inhibitor's concentration that could be used as reference value in further advanced biological and biophysical testing.

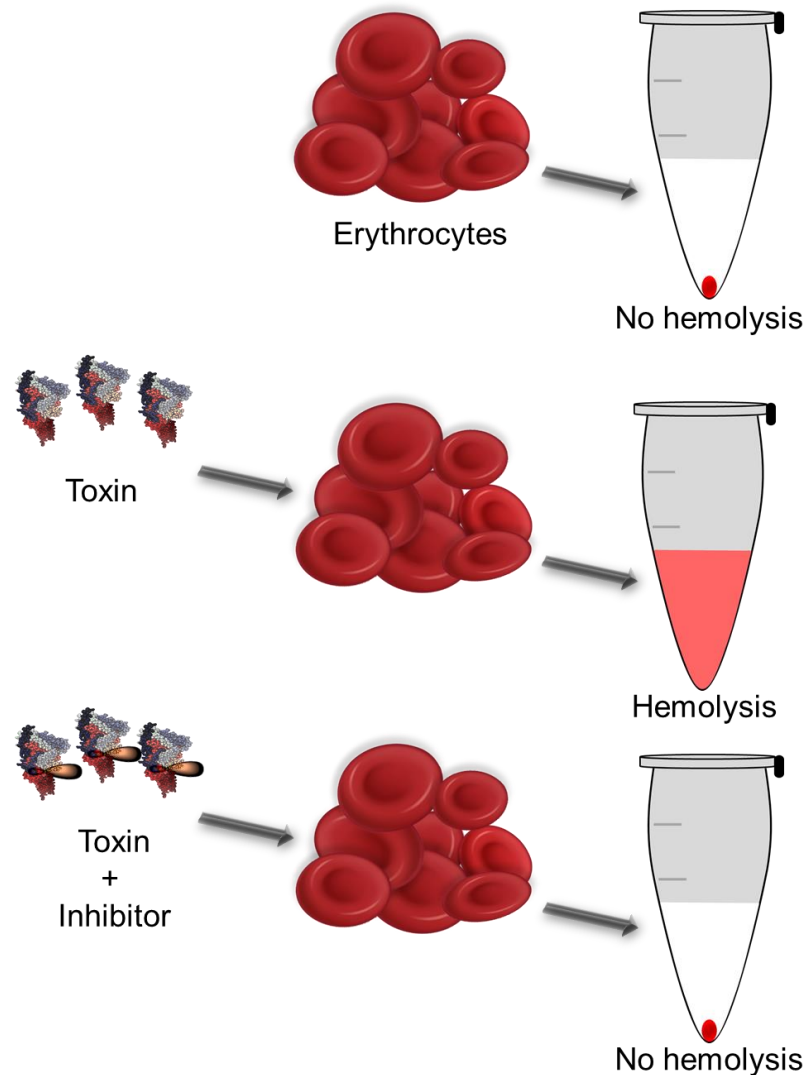


Figure 2.2. The graphical representation of the hemolysis assay.

Application of the hemolysis assay in this study was not limited to inhibitor testing alone, it was also customized to evaluate the stability of inhibitors in phosphate saline buffer (PBS). Additionally, the hemolytic activity of several native and mutated proteins was compared using erythrocytes.

2.2. Synthesis and testing of pore blockers

PB-1 and **2** were purchased from Specs in the previous work. IC_{50} values of **PB-1** and **2** were 67 and 3.2 μM , respectively. In this study, the research assistant in our working group, Thomas Rudolf, on request, re-synthesized **PB-1** and **2** in the lab. Furthermore, the contributions of Thomas Rudolf were not limited to **PB-1** and **2**; he was responsible for the synthesis of all PB-molecules, which are mentioned as 'synthesized' in this study.

PB-1 is a substituted 5-benzylidene-pyrimidine-2,4,6-trione and was synthesized through a Knoevenagel condensation of 3-(2,4-difluorophenoxy)methyl-4-methoxy-benzaldehyde with pyrimidine-2,4,6-trione (barbituric acid). **PB-1** was greatly soluble in DMSO (20 mM) and in PBS ($\leq 100 \mu\text{M}$). Similarly, **PB-2** was synthesized via the same Knoevenagel condensation method, however, in **PB-2**, the benzylidene substituents were modified to 4-(2,4-dichlorobenzyloxy) and 3-ethoxy and additionally, there was N-substitution of the pyrimidine-trione with 3,5-dimethyl phenyl. The solubility profile of **PB-2** was inferior to **PB-1**, as it dissolved in DMSO up to 3 mM and in PBS, it precipitated between 10-20 μM .

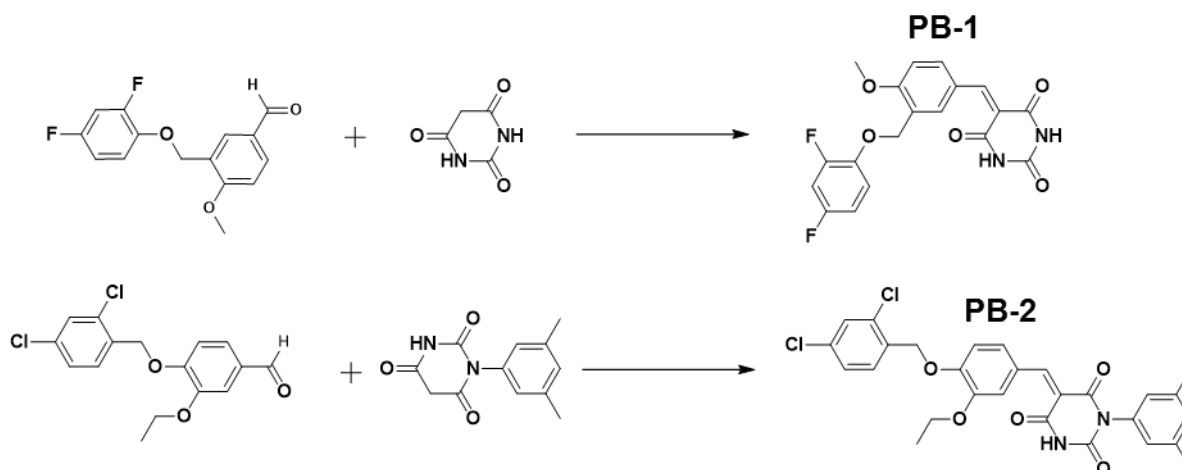


Figure 2.3. The synthesis scheme of **PB-1** and **2** via Knoevenagel condensation.

Both in-house synthesized molecules were tested in the hemolysis assay. In the assay, PLY (15 nM) was used according to the reported hemolytic activity,¹⁶⁰ and each inhibitor was analyzed at multiple concentrations against PLY, whereas, DMSO in PBS

was a negative control and 10% Triton-X was kept as a positive control. The assay-calculations were performed according to 1 ml of assay-volume.

The IC_{50} of lab synthesized **PB-1** in hemolysis assay was $38 \mu\text{M}$ with a 95% confidence interval (CI) and it was significantly better than the commercially purchased one. The lab-synthesized **PB-1** was the purer compound and, certainly for this reason, it achieved a lower IC_{50} . On the other hand, **PB-2** had exhibited an IC_{50} ($4.8 \mu\text{M}$) similar to earlier report activity of the commercial product. The modification of **PB-1** led to an approx. 10-fold increase in the potency of **PB-2**.

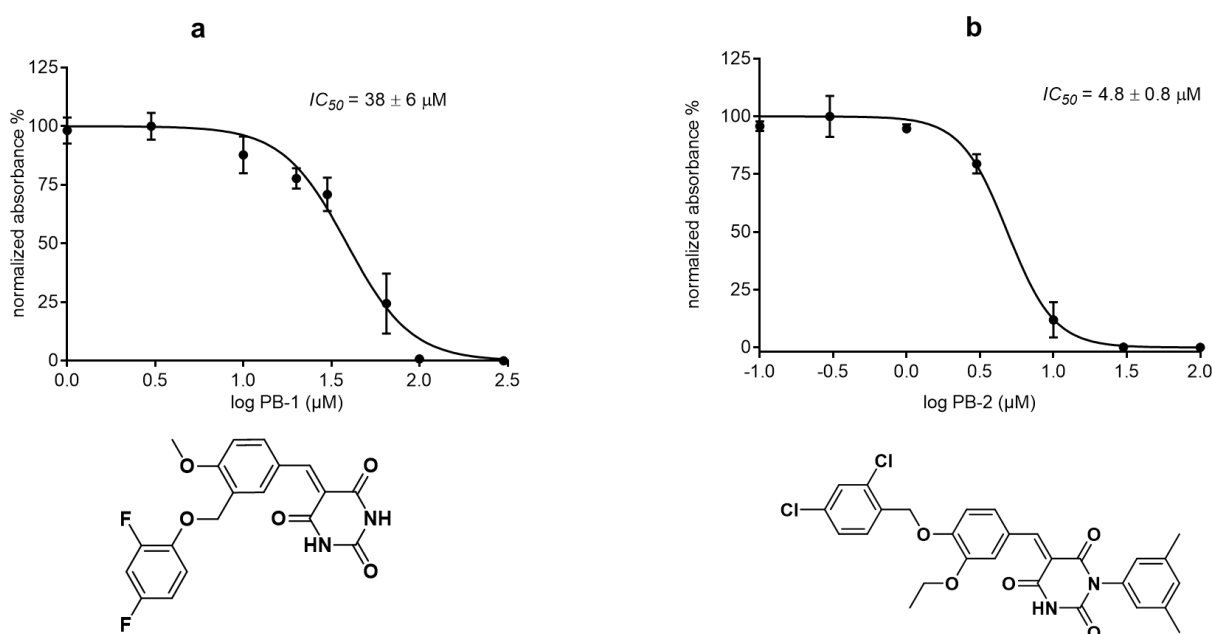


Figure 2.4. Analysis of lab synthesized **PB-1** and **2**.

a. The structure and IC_{50} of **PB-1**. **b.** The structure and IC_{50} of **PB-2**. (95 % CI, $n = 3$ and error bars represent \pm S.D.)

2.2.1. Stability of PB-2

PB-2 had an exceptional potency, however, while testing, a problem regarding efficacy of **PB-2** was detected. When **PB-2** was dissolved in PBS (dilution buffer in assay) in the absence of protein, and protein was added later in the assay, a significant decline in the potency of **PB-2** was observed. This effect was repeatedly observed, and it was ascertained that it was not an artifact. At that stage, it was assumed that **PB-2** might be hydrolyzed in PBS. To confirm this hypothesis, **PB-2** was analyzed using LC-QTOF-MS. The solubility of **PB-2** was limited in both PBS and DMSO (PBS: $10\text{--}20 \mu\text{M}$ and DMSO: $1\text{--}3 \text{mM}$), thus, it was analyzed at $10 \mu\text{M}$ in PBS with around 1% DMSO.

Samples of **PB-2** (10 μM) were analyzed in LC-QTOF-MS at $T = 0$ and at $T = 10$ min at room temperature. A significant degradation of **PB-2** was observed in samples after 10 min incubation in PBS. Unfortunately, the effect was not quantified in terms of molar concentration because due to degradation, the calibration curve of **PB-2** was nonlinear (Supplementary Information). However, the decrease of the peak area in the chromatogram was explicit and displayed in **Figure 2.5. a & b**. Moreover, the area under curve of the **PB-2** peak (10 μM) was quantified at $T = 0$, and $T = 10$ min. The decay of **PB-2** explained the significant decrease in activity. **PB-2** might have undergone retro-aldol reaction following the addition of a water molecule by a mechanism proposed in **Figure 2.5. d**.

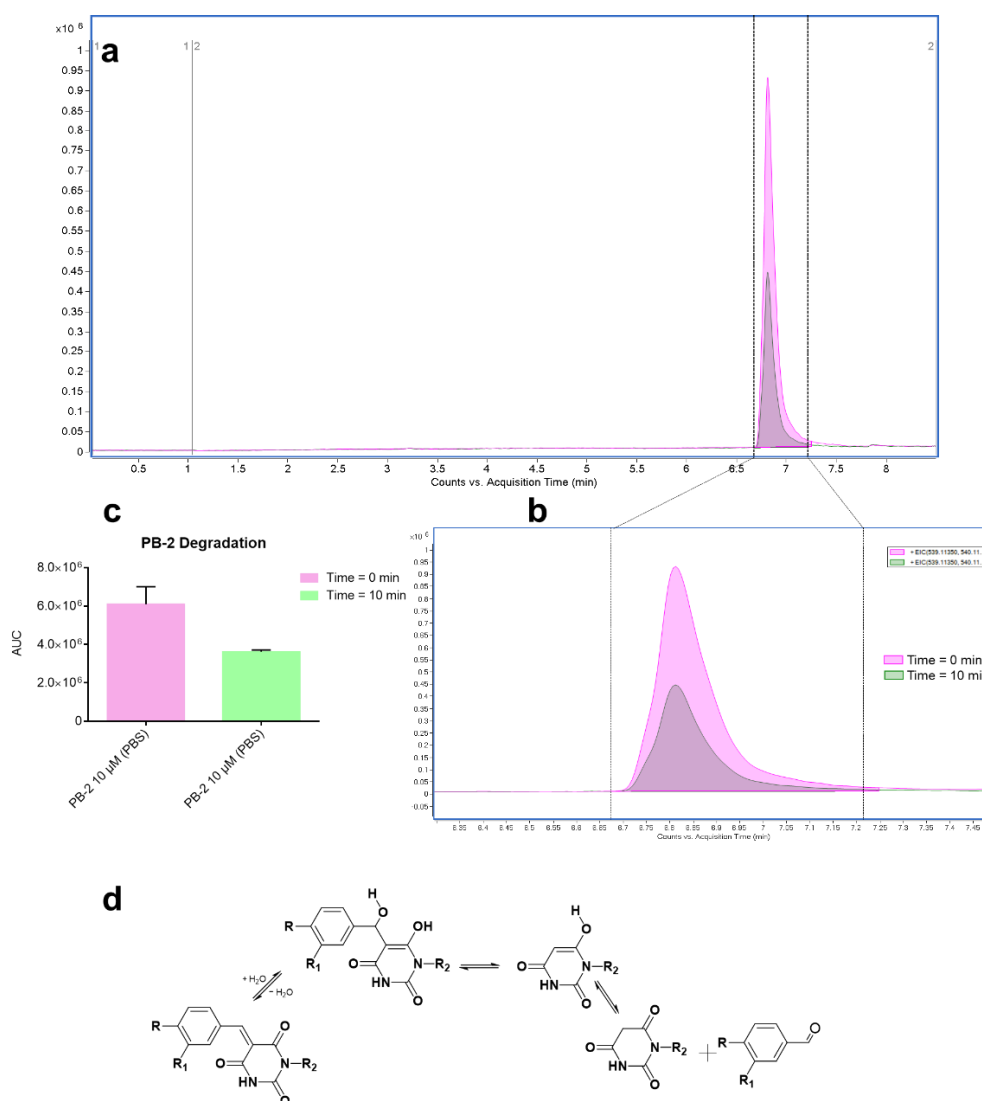


Figure 2.5. The analysis of **PB-2** stability via LC-QTOF-MS.

a & b. The chromatogram of **PB-2** showing decay after 10 min in PBS. **c.** The area under curve quantification of **PB-2** ($n=3$). **d.** Mechanism of **PB-2** degradation.

After confirmation of the stability problem via LCMS, it was decided that the hemolysis assay should be modified to assess the stability of molecules, because in the hemolysis assay much shorter time was required to estimate actual inhibitory potential of a molecule. Additionally, problems like limited solubility and poor ionization of molecules in LCMS could be by-passed.

Under standard conditions of the hemolysis assay, first PLY and then **PB-2** or any inhibitor was added to PBS, followed by an incubation of 10 min at 37° C and, thereafter, the mixture was treated with erythrocytes. Here, to analyze water stability of **PB-2**, two groups of samples were prepared. The first group was processed under standard protocol and, in the second, **PB-2** (alone) was pre-incubated for 10 min in PBS, afterward, PLY was added and, henceforth, the standard procedure was followed. As shown in **Figure 2.6.**, the second group had lost almost 80-90% activity and was unable to scavenge PLY effectively, like the first group. This result substantially suggested that only intact **PB-2** was capable of blocking PLY. Thereafter, the next task was to recognize the mode of reactivity of the inhibitor.

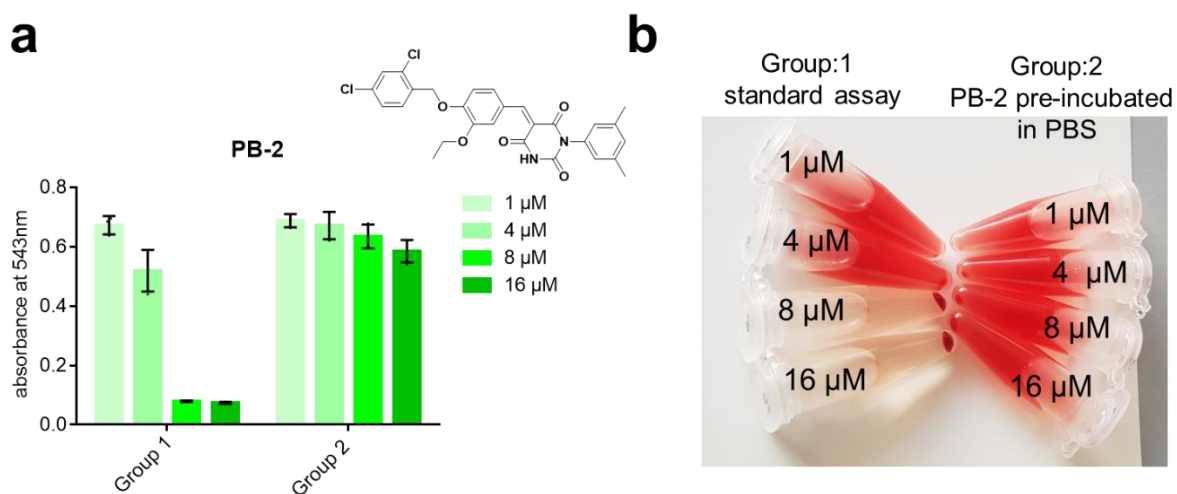


Figure 2.6. The stability of **PB-2** in the hemolysis assay.

a. The bar graph displaying quantitative decrease in **PB-2** potency. Group 1 = standard conditions and group 2 = **PB-2** pre-incubated in PBS ($n = 3$). **b.** Comparison of PLY-inhibition by **PB-2** at multiple concentrations in normal condition vs pre-incubation in PBS. In standard protocol, **PB-2** blocked PLY 100% at 8 and 16 μM whereas in pre-incubated conditions activity of **PB-2** declines significantly at same concentrations.

2.2.2. Identification of pharmacophore

The identification of the main reactive center of **PB-2** was mandatory to optimize the lead structure. However, after detection of the stability and solubility flaws, it became a priority. Therefore, the investigation was carried out stepwise.

Testing of PB-2.1, a close derivative of PB-2. A reduced version of **PB-2** was synthesized in the lab to elucidate the reactivity profile of **PB-2**. It was thought that the olefinic double bond of **PB-2** could be responsible for that reactivity and therefore it was saturated and **PB-2.1** was formed. The solubility of **PB-2.1** was significantly higher than **PB-2** (i.e., ~20 mM in DMSO and $\leq 150 \mu\text{M}$ in PBS). It was analyzed in the hemolysis assay up to 160 μM and was unable to inhibit PLY (**Figure 2.7 a**). The outcome of **PB-2.1** testing established the prime importance of the carbon-carbon double bond in the structure of **PB-2** regarding the activity of the molecule because the absence of this alkene bond had abolished the activity.

Testing of precursor fragments. **PB-2** consisted of two main fragments, an aromatic aldehyde, which was named **PB-2.2** and a pyrimidine-trione or barbituric acid fragment that is called **PB-2.3**. After confirming the degradation of **PB-2**, it was crucial to investigate the activity of precursor fragments. The evaluation of fragments individually against PLY can confirm that whether inhibition is caused by intact **PB-2** or any of the fragments are also involved in blocking PLY.

PB-2.2 was the first that had gone through the examination. The solubility of **PB-2.2** was excellent in DMSO ($> 20 \text{ mM}$) whereas in PBS it precipitated at $\geq 50 \mu\text{M}$. Hence, in hemolysis assay, a maximum 50 μM of **PB-2.2** was evaluated and it was unable to inhibit PLY (**Figure 2.7 b**). Next, the N-substituted barbituric acid fragment (**PB-2.3**) was tested. **PB-2.3** was equally soluble in DMSO and PBS ($> 5 \text{ mM}$). Thus, it was analyzed up to 160 μM in the hemolysis assay. Like **PB-2.2**, **PB-2.3** was also inactive against PLY (**Figure 2.7 c**). Hence, the aftermath of analyzing precursor fragments suggested that only intact **PB-2** was responsible for blocking PLY-induced hemolysis.

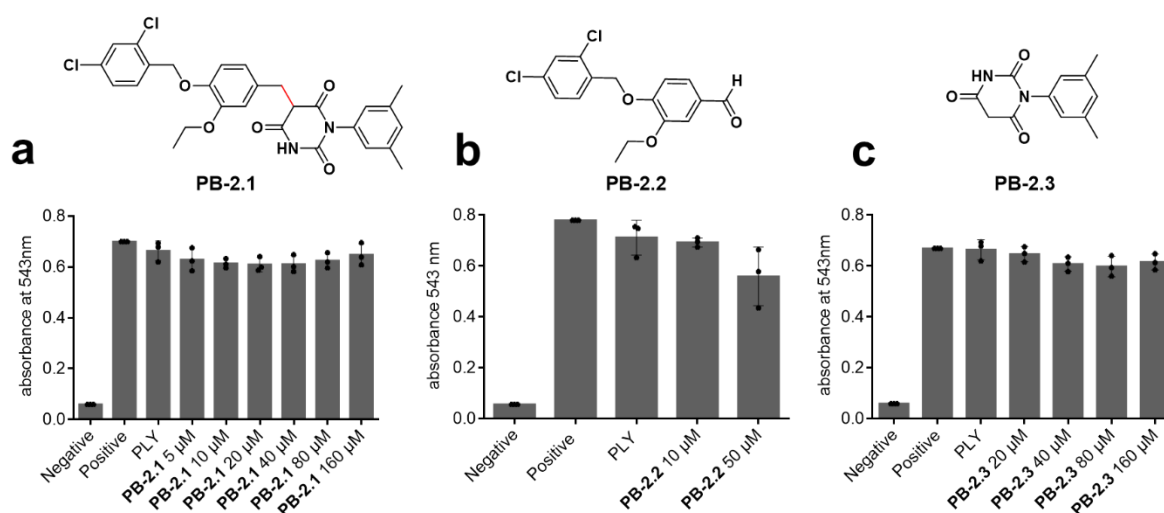


Figure 2.7. The analysis of precursor molecules of **PB-2**.

a. The structure of **PB-2.1** with reduced bond in red, and the result of hemolysis assay shows no inhibition of PLY by **PB-2.1**. **b & c.** The structure of **PB-2.2** and **2.3**. Moreover, both precursors are inactive as shown by graphs. (n=3)

Investigation of protein-templated fragment ligation. Protein-templated or catalyzed fragment ligation has been an established method in our lab and was performed with multiple protease targets.²³⁷ Here, the same concept was applied in the hemolysis assay. It was hypothesized that **PB-2.2** and **PB-2.3** would combine to form **PB-2** in the presence of PLY and, in the second step, **PB-2** would prevent lysis of erythrocytes. To investigate the protein-templation effect, 50 μM of both **PB-2.2** and **PB-2.3** were mixed in PBS 100 μl and incubated with PLY 15 nM for 1.5 h at room temperature (RT) $^{\circ}\text{C}$. **PB-2.2** and **PB-2.3** alone samples in PBS with PLY were kept as controls. After 1.5 h, the standard hemolysis assay (1 ml) was performed, and data were analyzed. The sample with both fragments and **PB-2.2** control sample exhibited inhibition of PLY. It was unclear from the data whether the inhibition induced was due to fragment ligation or alone by **PB-2.2**. In next back-to-back rounds of experiments, the concentration of **PB-2.2** was reduced to 25 μM and 10 μM respectively, yet, identical results were obtained i.e., both samples, the fragment-combination and **PB-2.2** alone, independently inhibited PLY (**Figure 2.8 a, b & c**). To sum up, there was not enough evidence to support the protein-templated fragment ligation. However, it was found that **PB-2.2** alone was active against PLY with slow reaction kinetics. Moreover,

the IC_{50} (~18 μM) of **PB-2.2** after longer incubation time (1.5 h) with PLY was calculated (Figure 2.8 d).

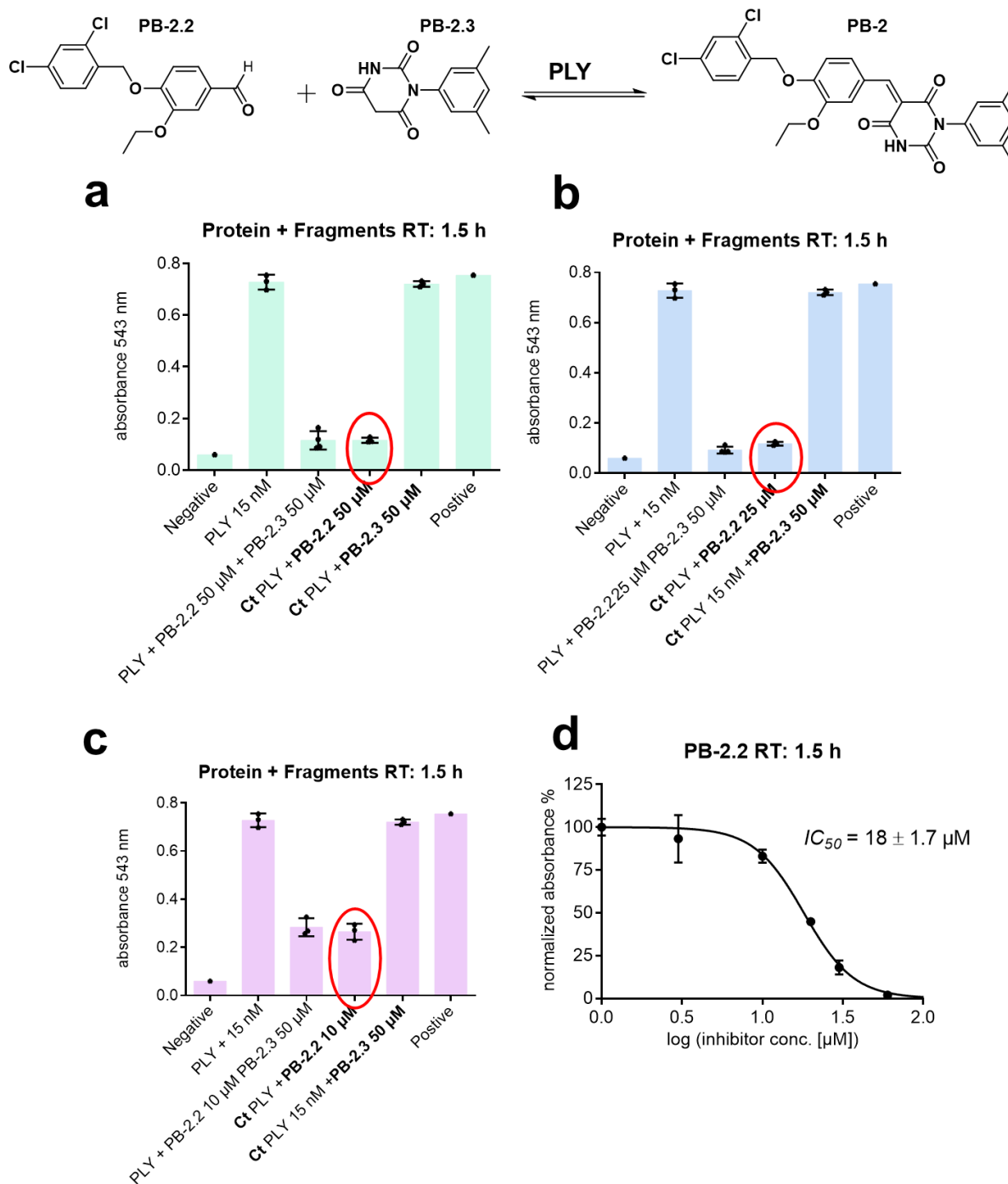


Figure 2.8. The fragment ligation reaction for **PB-2** generation in presence of protein. **a.** Protein-templated fragment reaction using 50 μM of **PB-2.2**. **b.** Protein-templated fragment reaction using 25 μM of **PB-2.2**. **c.** Protein-templated fragment reaction using 10 μM of **PB-2.2**. **d.** The IC_{50} (95% CI) of **PB-2.2** after 1.5 h of incubation with PLY. (n = 3)

The prudent investigation to this extent supported the identification of the reactive core of **PB-1** and **PB-2** that was responsible for the activity. In the light of the above-mentioned results, the lead structure of PB-molecules could be bisected into two parts in a broad perspective. The major part is 5-benzylidene-pyrimidine-2, 4, 6-trione, which is highlighted in red in the **Figure 2.9**. It possesses α , β -unsaturated carbonyl moiety that seems imperative for the inhibitory activity. The modifiable part includes N-substituent at pyrimidine and substituents at the benzylidene group. The modifiable group was in blue color (**Figure 2.9**). After recognition of the reactive center, the next critical step was to optimize the lead structure to achieve greater stability and efficacy. Thus, thereafter, a series of testing included structural variations in the substitution part of the lead compound.

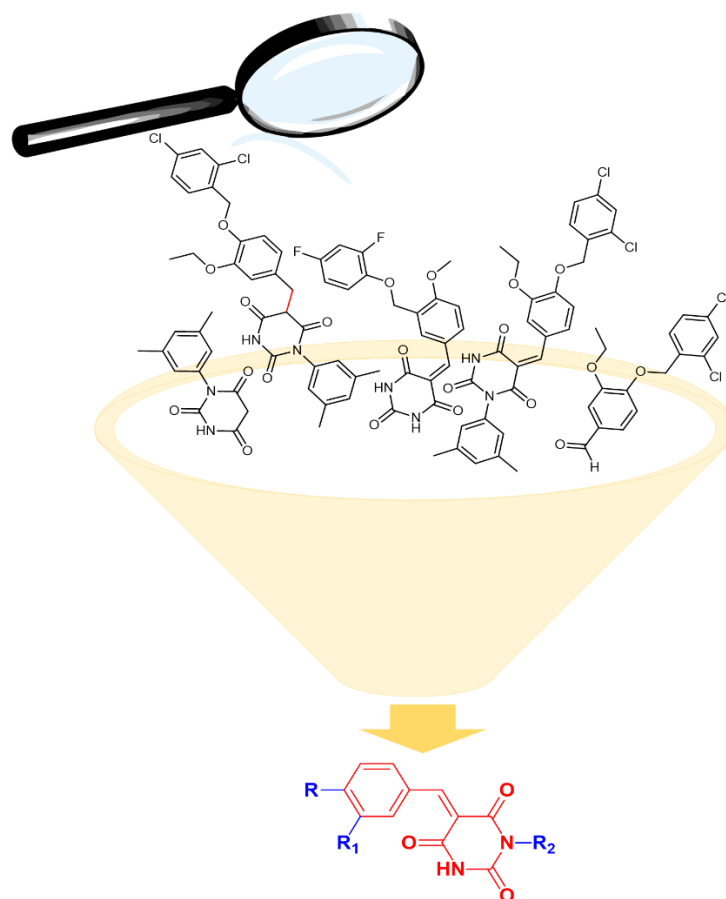


Figure 2.9. The lead structure of PB-inhibitors after initial investigation is shown. Red and blue denote corresponding critical and modifiable parts.

2.2.2.1. Testing of multiple derivatives of PB-2 for optimization

To improve the stability, solubility and potency of inhibitors, various spinoff versions of **PB-2** were synthesized in the lab. Ideas about derivatives of **PB-2** were presented to Thomas Rudolf, and he did all the synthesis.

It started with a truncated version of PB-molecules, **PB-2.4**. It was synthesized to observe the significance of big / small substituents at benzylidene group. In **PB-2.4**, benzylidene domain was shortened to 3-ethoxy-4-hydroxybenzylidene. It was a dark yellow powder and after inclusion of the hydroxy group in the molecule, solubility was significantly enhanced (20 mM DMSO and 1 mM PBS). Despite the high solubility, **PB-2.4** was highly instable in PBS and underwent discoloration, which was interpreted as degradation of molecule, because it was almost inactive when tested in the hemolysis assay. **PB-2.4** was evaluated up to 400 μM with slight to no inhibition of PLY. Hence, it was deduced from **PB-2.4** analysis that a larger substituent might be effective for the potency and water stability of the inhibitor.

Likewise, the importance of N-substitution at pyrimidine group was analyzed. A derivative, **PB-2.5**, was produced that lacked 3,5-dimethyl phenyl of barbituric acid residue. **PB-2.5** had slightly better solubility than **PB-2** in PBS ($\leq 25 \mu\text{M}$). The IC_{50} value of **PB-2.5** was 13 μM in the hemolysis assay. The potency was 2.5-fold decreased in this derivative. Thus, it was concluded that the N-substitution of pyrimidine-trione ring had a part in enhancing the inhibition of PLY.

The water stability of **PB-2.5** was also evaluated to observe the effect of 3,5-dimethyl phenyl removal from the barbituric acid part. The assay protocol to determine the stability of **PB-2.5** is the same customized hemolysis assay that is mentioned for the analysis of **PB-2**. Two experimental sets were prepared. The first set followed standard protocol whereas, in the second set, pre-incubation of **PB-2.5** in PBS for 10-15 min was performed before following the standard procedure. The final findings revealed no noteworthy improvement in the stability of **PB-2.5** and the inhibition was substantially decreased in the second set of samples.

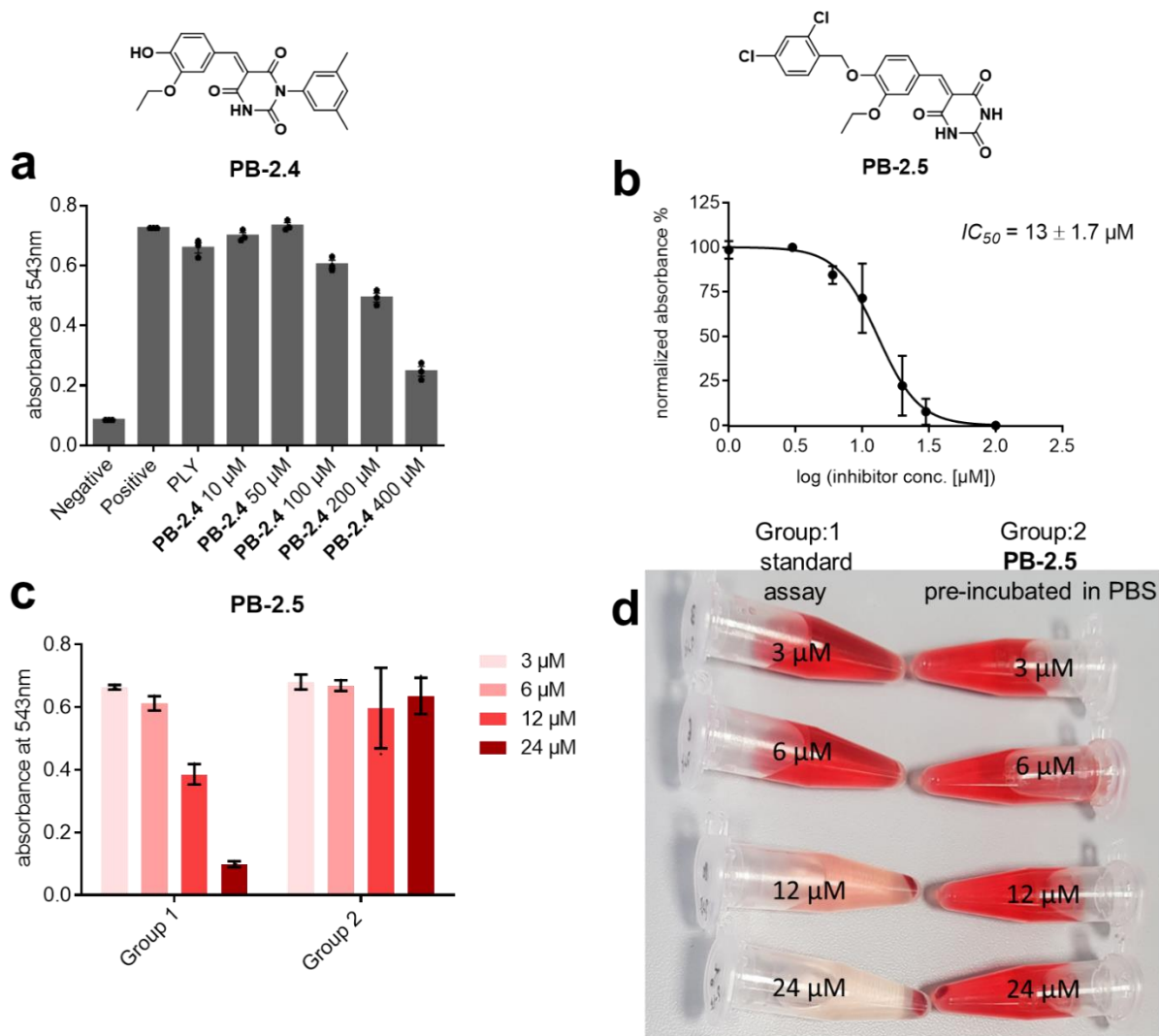


Figure 2.10. Derivatives of **PB-2**.

a. **PB-2.4** showed no inhibition up to 400 µM. **b.** IC_{50} (95% CI) of **PB-2.5** in standard hemolysis assay. **c** and **d.** Qualitative (comparison between two experimental sets) and quantitative data of **PB-2.5** water stability. ($n = 3$)

Afterwards, a new derivative of **PB-2** was synthesized, **PB-2.6**, and this time ethoxy substituent at position 3 of 5-benzylidene was removed and, at position 4 of 5-benzylidene, the 2,4-dichlorobenzyl oxy substituent was shrunk to 2,4-dichlorophenyl oxy. This alteration did not bother the solubility in comparison to **PB-2**, but the IC_{50} was doubled. Therefore, it appeared that 3-ethoxy had a slight influence on the potency.

Thereafter, **PB-2.7** was synthesized and involved the inclusion of 2,4-dichlorobenzyl oxy connection at position 4 of 5-benzylidene part and the methoxy group was added at position 3 of 5-benzylidene. After this modification, solubility was still the same but minor improvement in potency was observed in comparison to **PB-2.6**.

Next, **PB-2.8** was prepared and it possessed small changes. It was basically the same as **PB-2.7** but without ethoxy substituent at position 3 of the 5-benzylidene domain. The solubility of **PB-2.8** remained the same as previous derivatives, however, a loss of 4-fold activity was noticed (**Figure 2.11 c**). Thus, it was found that a substituent at position 3 of the 5-benzylidene domain was essential for the activity.

Moreover, **PB-2.9** was synthesized and lacks 3,5-dimethyl moieties at N-phenyl substituted of barbiturate part. The purpose was to investigate if there were any significant changes associated with these minor modifications. The solubility remained the same and the IC_{50} was doubled in comparison to the **PB-2**.

The stabilities of **PB-2.6**, **2.7**, **2.8** and **2.9** were analyzed in the hemolysis assay, and each of them showed degradation in PBS after 10-15 min pre-incubation in PBS. Finally, significant loss in the activity of inhibitors was observed. Thus, no improvement concerning stability was achieved.

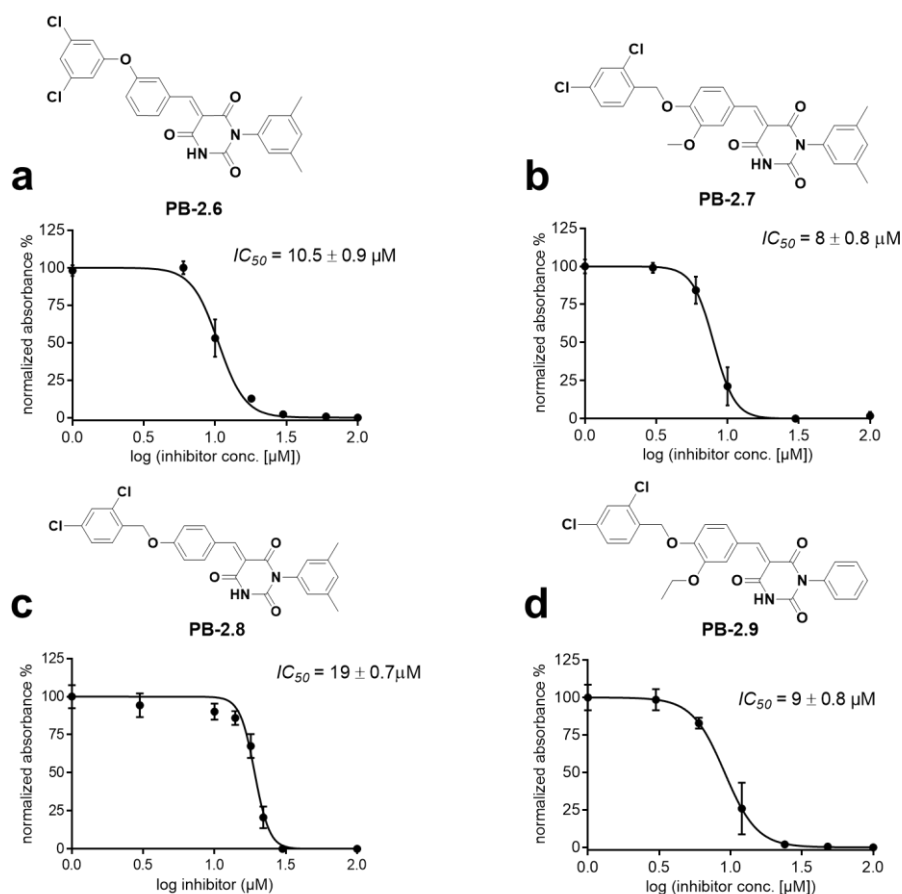


Figure 2.11. Derivatives of **PB-2**.

a. Structure and IC_{50} of **PB-2.6**. **b.** Structure and IC_{50} of **PB-2.7**. **c.** Structure and IC_{50} of **PB-2.8**. **d.** Structure and IC_{50} of **PB-2.9**. ($n = 3$ and 95% CI for IC_{50})

Furthermore, two more derivatives were synthesized, **PB-2.10** and **2.11**. In both derivatives, 2,4-dichloro moieties were removed from 4-benzyloxy-benzylidene part. Additionally, in **PB-2.10**, like **PB-2.9**, 3,5-dimethyl moieties were absent at N-substituted phenyl of pyrimidine-trione part. There was a major decrease in water solubility of both molecules that was observed after these minor alterations. Despite the rapid precipitation in PBS, action of **PB-2.10** and **2.11** was tested up to 40 μM in the hemolysis assay and no inhibition of PLY was noticed. It was not clear from the findings whether insolubility made molecules ineffective or removal of two chlorine atoms abolished the activity. Anyhow, substitution of chlorine was the chief cause of inactivity of molecules. The decisive role of chlorine substituents was a major discovery that could explicitly facilitate the development of further stable and potent derivatives.

One more critical derivative of **PB-2** was synthesized and, in this derivative, the closed pyrimidine-trione ring was replaced by malonamide. **PB-2.12** was synthesized by the condensation of aromatic aldehyde (**PB-2.2**) and malonic acid diamide. The water solubility of **PB-2.12** was excellent compared to all other derivatives, but in contrast, the activity of **PB-2.12** was significantly reduced with an IC_{50} value of 51 μM . Since, **PB-2.9** and **2.10** were inactive, and **PB-2.12** had high inhibitory concentration. Therefore, the aqueous stability of these molecules was not evaluated.

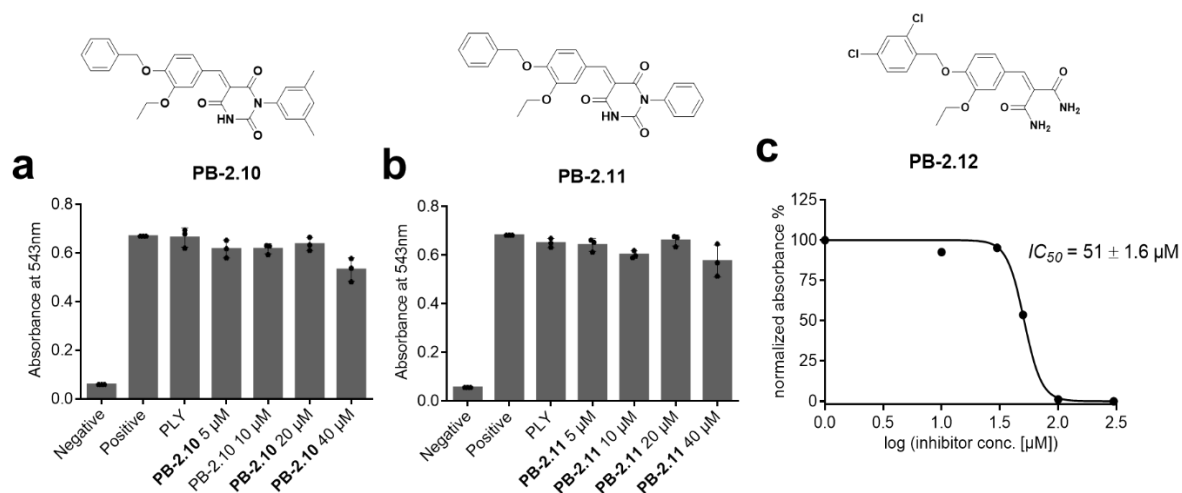
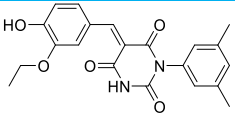
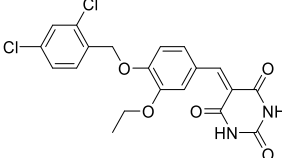
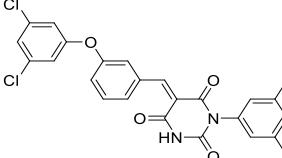
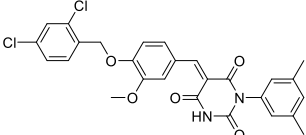
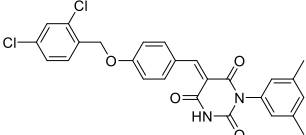
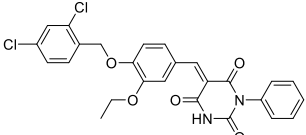
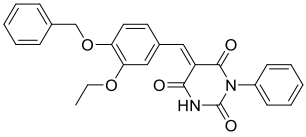
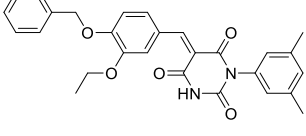
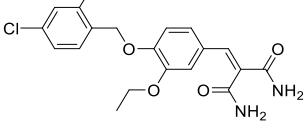


Figure 2.12. Derivatives of **PB-2**.

a. Structure and activity of **PB-2.10**. **b.** Structure and activity of **PB-2.11**. **c.** Structure and IC_{50} (95% CI) of **PB-2.12**. (n = 3)

Table 2.1. List of **PB-2** derivatives. Solubility and stability are mentioned in comparison to **PB-2**.

Name	Structure	IC_{50} (μ M)/ Activity	Solubility (PBS)	Stability (PBS)
PB-2.4		≥ 300	1mM	poor
PB-2.5		13	$\leq 25 \mu$ M	same
PB-2.6		10.5	10-20 μ M	same
PB-2.7		8	10-20 μ M	same
PB-2.8		19	10-20 μ M	same
PB-2.9		9	10-20 μ M	same
PB-2.10		not active	poor	N/A
PB-2.11		not active	poor	N/A
PB-2.12		51	$\leq 100 \mu$ M	N/A

2.2.3. Modification in the PB-pharmacophore

The experimental findings to this point provided pivotal insight into the structural activity relationship of PB-molecules, yet we were unable to develop a more stable and efficacious inhibitor than **PB-2**. Alterations in the benzylidene domain have revealed that electron-withdrawing moiety like chlorine or fluorine on 4-benzyloxy-benzylidene (**PB-2.10** and **2.11**) is compulsory because these groups reduce electron-density from the double bond and favors nucleophilic attack at this position. The withdrawal of chlorine or even its aromatic partner (benzyloxy) (in **PB-2.4**) has terminated the inhibitory activity, whereas with other modifications activity is retained, though it is reduced. Similarly, with N-substituted pyrimidine-trione, maximum activity was recorded whereas potency was significantly decreased when ring was exchanged with malonamide (**PB-2.12**), probably because malonamide was far less acidic in comparison to pyrimidine-trione and therefore, the double bond is more stable and less reactive toward nucleophiles.

Similarly, stability was analyzed for compounds that obtained $IC_{50} \leq 20 \mu\text{M}$, and among those structural variants (**PB-2.4** – **PB-2.9**), the water stability did not improve at all. The main objective to enhance water stability without compromising potency was not achieved with contemporary analogues of **PB-2**. Although **PB-2** has exhibited promising inhibition, but subtle stability of inhibitors is the fundamental requirement for more sophisticated (*in vivo*) analysis. Hence, onwards, it was decided to manipulate both critical parts of the lead structure, i.e., 5-benzylidene and pyrimidine-2, 4, 6-trione.

2.2.3.1. Discovery of PB-3

To modify the reactive center, benzylidenepyrimidine-2,4,6-trione, the benzene ring was the first choice to be replaced. The benzene ring of 5-benzylidenepyrimidine-2,4,6-trione presumably withdraws electron density from the alkene bond, which could apparently make the molecule susceptible to water attack. Therefore, an electron-rich aromatic system might prevent this problem and could possibly increase the stability of the molecules. With this aim, the online library of Specs was manually searched, and a derivative of **PB-2** was found that contained furan instead of benzene. Hence, that molecule was purchased and named **PB-3**. Later, **PB-3** was synthesized in the lab by a condensation reaction between 5-(2,4-dichlorophenyl)-furan-2-carbaldehyde and 1-(3,5-dimethylphenyl) pyrimidine-2, 4, 6 (1H,3H,5H)-trione. **PB-3** displayed an IC_{50} value of $3.1 \mu\text{M}$ in the hemolysis assay. It proved to be slightly superior to **PB-2** in

terms of potency and solubility in DMSO (~3-5 mM). However, the solubility in PBS was similar to **PB-2** (i.e., 10-20 μM).

Stability of PB-3. Next, the stability of **PB-3** was estimated according to the same hemolysis procedure stated for **PB-2**. In the first place, two groups were prepared, the standard group and the other with pre-incubation of **PB-3** in PBS for 10 min. Both were then analyzed and found that **PB-3** was entirely stable and no difference in the potency was observed between standard and pre-incubated groups. It was evident from the result that the stability of **PB-3** was exceptional among the molecules tested until that moment. Thus, the conditions were customized, and three groups were prepared with revised time intervals. The first group was treated under standard conditions, whereas as for the second and third groups, the pre-incubation time of **PB-3** in PBS before adding PLY was extended to 30 min and 2 h respectively. Finally, after evaluation of data, it was concluded that the potency of **PB-3** declined in the second and third groups. However, still significant activity of **PB-3** (80% in group 2 and 60% in group 3) was retained (**Figure 2.13 c & d**).

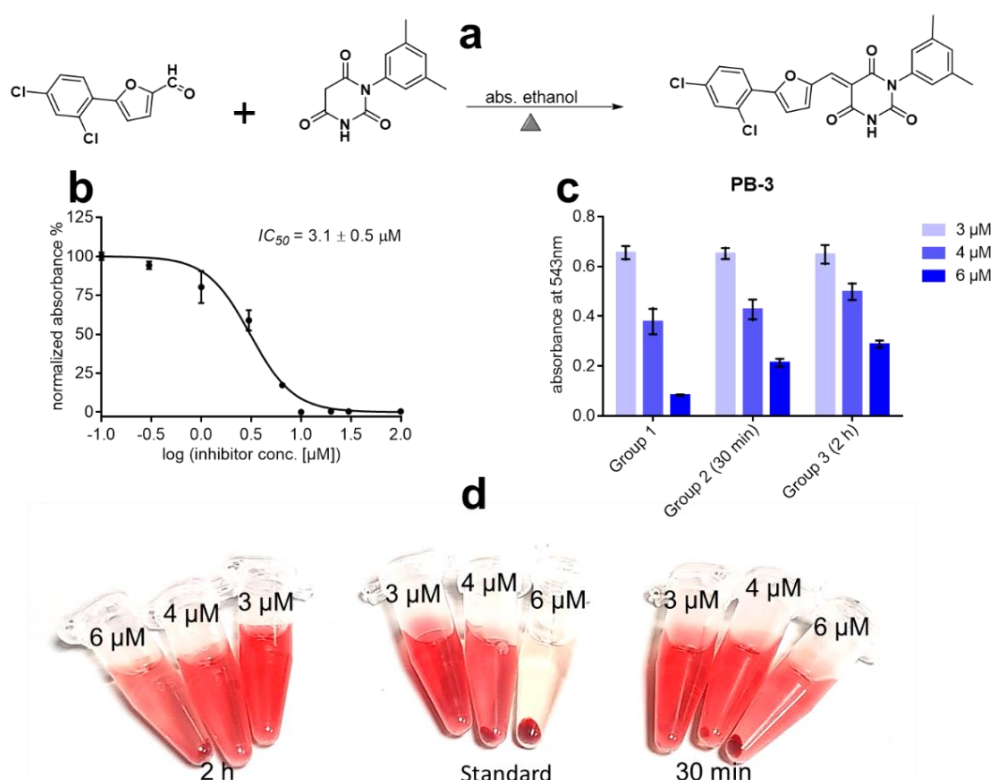


Figure 2.13. The IC_{50} stability of **PB-3** in the hemolysis assay.

a. Synthesis scheme of **PB-3**. **b.** Structure and IC_{50} (95% CI) of **PB-3**. **c & d.** Stability analysis of **PB-3**, Group 1: Standard assay, Group 2: 30 min pre-incubation and Group 3: 2 h pre-incubation and image for groups representation. (n = 3).

Protein-templated fragment ligation to generate PB-3. Next, the protein-templated fragment ligation approach was applied on PLY to form a bioactive inhibitor. Like **PB-2**, the ligation of fragments was first attempted in the hemolysis assay. The precursor fragments of **PB-3** (**PB-3.1**: 12.5 μM and **PB-2.3**: 50 μM) were incubated in PBS for 1 h in the presence of PLY (15 nM) at room temperature. **PB-3.1** and **PB-2.3**, alone samples were kept controls. Afterwards, the standard hemolysis assay was performed and around 50% inhibition of PLY was observed in the samples which contained both (**PB-3.1** and **PB-2.3**) fragments. The outcome might correspond to formation of **PB-3** in the presence of protein. Hence, furthermore, it was decided to quantify the effect of protein-templated fragment ligation via LC-QTOF-MS.²³⁷

The assay conditions in LC-QTOF-MS were different from the hemolysis assay. Samples of **PB-3.1** (50 μM) and **PB-2.3** (100 μM) together with 5 μM protein, and without protein, were analyzed from 0 to 7 h (420 min). The formation of **PB-3** was detected only in protein containing samples and it reached saturation after almost 3.5 h. The molar concentrations of **PB-3** were calculated by using a calibration curve of **PB-3** on Graphpad Prism. Finally, the values of **PB-3** were plotted against time using a one phase association equation [$Y=Y_0 + (c_{\text{max}}-Y_0)*(1-\exp(-k*x))$]. Here, the plateau was 795 nM, which is also the maximum concentration c_{max} , and the reaction half time ($t_{1/2}=\ln 2/k$) was ~ 20.5 min.

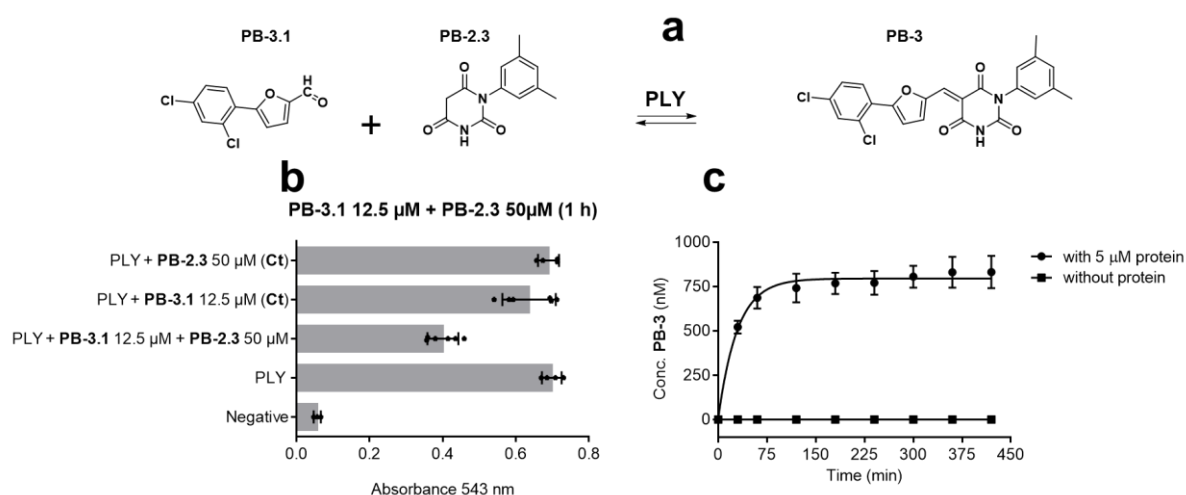


Figure 2.14. The protein-templated fragment ligation to produce **PB-3**. **a.** The workflow of fragment ligation. **b.** The fragment ligation analysis in the hemolysis assay ($n=3$). **c.** The quantitative analysis of protein-templated fragment ligation ($n=3$).

To conclude, the replacement of benzene ring by an electron-rich furan proved to be successful and **PB-3** emerged as the best inhibitor in terms of potency and stability. **PB-3** was adequately potent and stable to be pursued for advanced testing. However, it was decided to continue the alteration of the pharmacophore and test further new molecules. It would provide a better understanding of the reactivity profile, which could then be used to optimize the lead compound at later stages of testing.

2.2.3.2. Diverse active derivatives of PB-molecules

In order to utilize time effectively, once again the online library of Specs was revisited. This time, the pyrimidine-2,4,6-trione part was chosen for modification instead of the benzylidene moiety. A derivative of PB-molecules with a five membered (pyrazolidine) ring was selected, **PB-4**. It contained the benzylidene part that was similar to **PB-2.7** but the pyrimidine-2, 4, 6 (1H, 3H, 5H)-trione ring was replaced by five membered 1-(4-fluorophenyl) pyrazolidine-3,5-dione. The pyrazolidine-3, 5-dione is less acidic than barbituric acid and, hence, the electron density on the alkene bond would be increased and eventually the molecule might survive hydrolysis.

PB-4 was purchased and when initially tested in the hemolysis assay, it displayed inhibition of PLY comparable to **PB-3** and the IC_{50} value calculated was 3.2 μ M. In terms of solubility, **PB-4** had significantly better solubility than **PB-3**, both in DMSO (5-10 mM) and in PBS. It was observed soluble in PBS up to 100 μ M at room temperature.

The next step was the stability analysis of **PB-4**. The aqueous stability was evaluated according to the previously mentioned hemolysis protocol. **PB-4** was like **PB-3** active after 10 min pre-incubation in PBS. Therefore, in the case of **PB-2**, two sample groups were prepared, the first was standard one and the second had pre-incubation of **PB-4** for 1 h in PBS. **PB-4** was still actively inhibiting PLY in the second group samples, i.e., after 1 h pre-incubation. However, a reduced potency (3-4 folds) was detected in comparison to group 1 (standard group). Thus, to sum up, **PB-4** was undeniably better than **PB-2** concerning potency, solubility, and stability, whereas, **PB-3** superseded **PB-4** in regards to potency and stability. As **PB-4** had excellent solubility, therefore, it could be considered as an alternate to **PB-3**, if anyhow, **PB-3** failed to prevail in advanced experimentation.

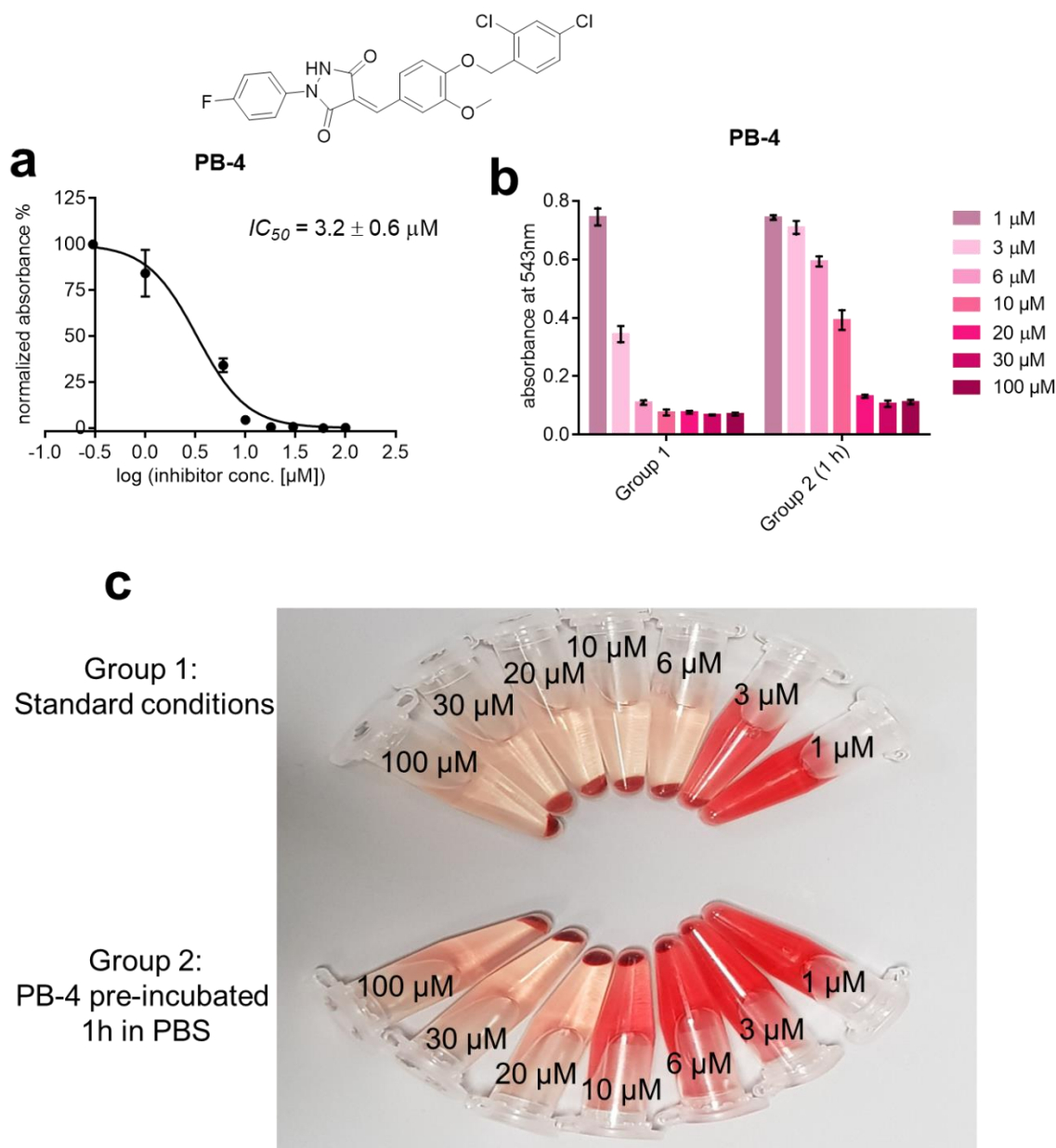


Figure 2.15. Analysis of **PB-4**.

a. Structure and IC_{50} (95% CI) of **PB-4**. **b.** **PB-4** stability results, Group 1: Standard assay, Group 2: 1 pre-incubation. **c.** The hemolytic representation of stability of both groups. ($n = 3$)

After **PB-4**, another derivative of PB-molecules was purchased from Specs and it had possessed changes in both parts, i.e. benzylidene and pyrimidine-trione parts. **PB-5** contains, similar to **PB-4**, the pyrazolidine-3,5-dione ring, however, without fluorine. On the other hand, the substituents of benzylidene underwent major modification and were changed to 4-(3-(4-chlorophenoxy)propoxy)-benzylidene. The solubility of **PB-5** was better than **PB-3** and comparable to **PB-4**. However, the potency of **PB-5** in the hemolysis assay was 3-fold more than **PB-3** and **4**. The IC_{50} of **PB-5** was 9.2 μM .

When the stability of **PB-5** was investigated in the hemolysis assay, it was found identical to **PB-4**. Two groups of **PB-5** samples, one standard group and the second 1 h pre-incubated group, were investigated. In the second group, the inhibition of PLY was detected (**Figure 2.16 b & c**), though the loss of half of the **PB-5** activity was observed. In conclusion, the stability of **PB-5** was comparable to **PB-4** and inferior to **PB-3**.

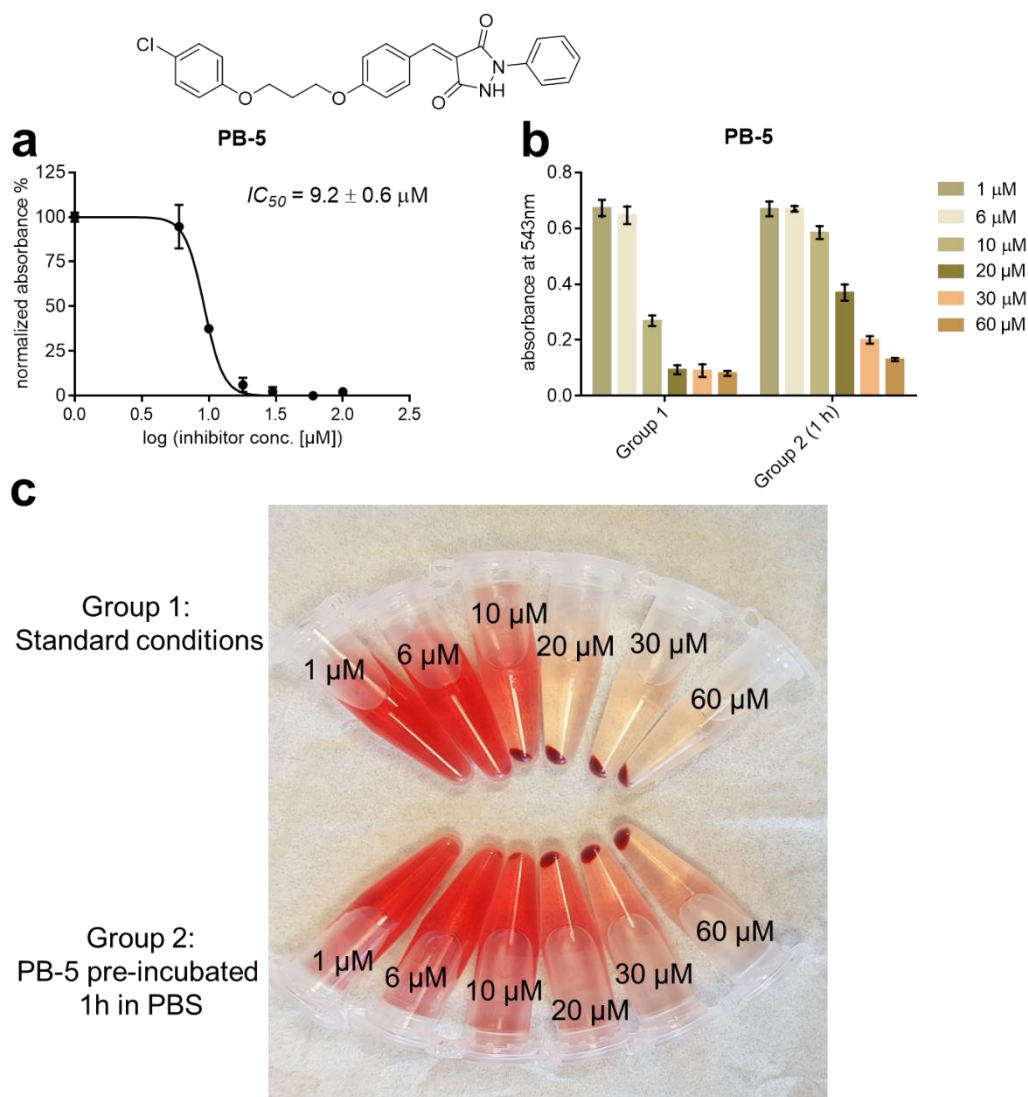


Figure 2.16. Analysis of **PB-5**.

a. Structure and IC_{50} (95% CI) of **PB-5**. **b.** **PB-5** stability results, Group 1: Standard assay, Group 2: 1 pre-incubation. **c.** The hemolytic representation of stability of both groups. (n = 3)

Thereafter, another derivative was chosen and purchased from Specs. This molecule, **PB-6**, shared the same pyrazolidine-ring part with **PB-5** but it had different benzylidene substitutions. **PB-6** contained 4-(3, 4-dichlorobenzyl)-oxy as benzylidene substituent.

The solubility profile of **PB-6** was identical to **PB-4** and **5**. **PB-6** was active in the hemolysis assay, but it showcased an abnormal Hill coefficient as shown in the IC_{50} curve of the **Figure 2.17. a**. A surge (5% to 100%) in activity of **PB-6** was observed between 6 to 10 μM concentrations, at 6 μM 5-7% inhibition of PLY was detected and at 10 μM 100 % PLY was inhibited. This kind of abnormal Hill slope indicate deviation from 1:1 binding model and requires further investigation of **PB-6**. Since **PB-6** was not a top listed inhibitor, therefore, further investigation to reveal its atypical inhibitory pattern was withdrawn. Regarding stability, **PB-6** was analyzed in the same assay with identical groups and pre-incubation interval of **PB-4** and **PB-5**. Finally, it was found that **PB-6** possessed equivalent stability to **PB-4** and **5**.

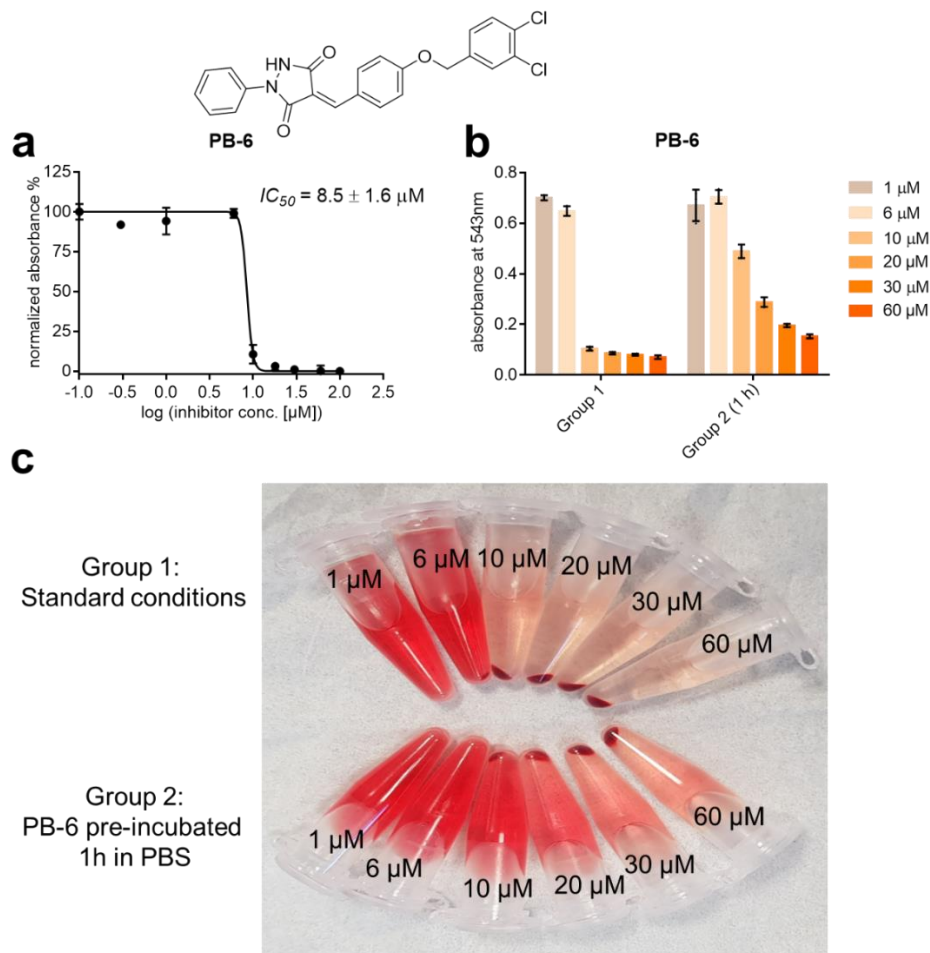


Figure 2.17. Analysis of **PB-6**.

a. Structure and IC_{50} (95% CI) of **PB-6** (abnormal “Hillslope = 13.07”). **b.** **PB-6** stability results, Group 1: Standard assay, Group 2: 1 pre-incubation. **c.** The hemolytic representation of stability of both groups. (n = 3)

2.2.3.3. Inactive derivatives of PB-molecules

A diverse collection of derivatives of PB-inhibitors, which keep the same core structure, were purchased from Specs. The derivatization of PB-inhibitors was successful in many ways. It enabled us to achieve a better lead compound (**PB-3**) that has better potency and stability. Nevertheless, success was not always the case. Multiple inhibitors were proven to be inactive. However, the structures of these inactive molecules provide thoughtful insights that could be used to optimize the lead compound.

The substitutions among these inactive molecules were diversified to explore the reactivity of PB-molecules. For convenience, these molecules were named **PB-7** to **11** (**Table 2.2**). The assorted substitution is the pragmatic way to note down the key scaffolds that affect the potency, solubility, and stability of PB-inhibitor. All these molecules exhibited excellent solubility in DMSO (10 mM) and PBS (100 μ M). Unfortunately, when these molecules were analyzed in the hemolysis assay, they were unable to inhibit PLY except **PB-7**, which started blocking PLY beyond 40 μ M. These observations were unique because each of them possessed the active core structure of PB-molecules. There was another possibility that these molecules were cytotoxic on their own, i.e., these were deteriorating the erythrocytes. If this was true, then in such a case, the inhibition of PLY could not be observed. Therefore, to rule out this possibility, all these five molecules were again tested in the hemolysis assay.

Starting from **PB-7**, each one of them was analyzed against erythrocytes individually. PLY was not included in these control experiments. These molecules (**PB-7** to **11**) were incubated with erythrocytes for 30 min at 37° C with shaking and then, afterwards, were spun down. No hemolysis in any of the samples was observed and it meant that none of the molecules were toxic to erythrocytes. Therefore, in conclusion, the experimental data implied that apart from the core structure, certain other features of the molecule are essential to inhibit PLY. Structures of inactive molecules along with only active molecule (**PB-7**) are available in the following **table 2.2**.

Table 2.2. Structures of miscellaneous PB-molecules purchased from Specs.

Compound	Structure	PLY-inhibition in the hemolysis assay (tested up to 100 μ M)
PB-7		active \geq 40 μ M
PB-8		inactive
PB-9		inactive
PB-10		inactive
PB-11		inactive

2.2.4. Structure activity relationship and the pharmacophore

In the quest of a more potent and stable inhibitor than **PB-2**, multiple discoveries regarding potency, solubility, stability, and reactive mechanism have been unveiled. The earlier presented lead structure (5-benzylidenepyrimidine-2,4,6-trione) has its own impact, but additionally numerous distinct features are found to be critical for the activity. The major observations explaining SAR are summarized in the following in the form of bullet points.

- The benzylidene group in PB-molecules is replaceable and, if replaced by a suitable group like furan-2-carbaldehyde in **PB-3**, it led to an increase in potency, solubility, and stability.
- The substitution of longer / branched group to benzylidene is critical for the inhibitor activity. The smaller substitutions appear to terminate the activity, as in case of **PB-2.4** and **PB-11**.
- Electron-withdrawing groups like chlorine or fluorine are compulsory for the activity and preferably, they should be on the longer substituent of benzylidene group. These group withdraw the electron-density from the double which assists the nucleophilic attack. Absence of chlorine / fluorine aborts activity of molecules; the prime examples were **PB-2.10** and **2.11**.
- Pyrimidine-trione, a six membered ring can be displaced with a five membered ring or an open chain amide, while retaining the activity and simultaneously improving stability and solubility of the molecule. When benzylidene-pyrimidine-trione was exchanged with benzylidene-pyrazolidine-dione in PB-molecules, the inhibitory activity was intact and significant increase in solubility and stability was observed e.g., **PB-4**, **5** and **6**. However, when open chain malonamide was applied in **PB-2.12** instead of a closed ring, a 12-fold reduction in potency was observed, though the stability and solubility were still enhanced.
- A single N-substitution of pyrimidine ring augments the potency and stability, whereas double N-substitution adjourns the activity of molecules e.g., **PB-8**, **9** and **10**.

The comprehensive evaluation of all components of PB-molecules regarding chemical and biological activity indicated that the fundamental reactivity in PB-compounds was due to α , β -unsaturated carbonyl moiety, but, at the same time, PLY was not blocked by multiple structural derivatives, which comprised of the α , β -unsaturated carbonyl

core. Therefore, it is evident from the data that the presence of above-mentioned critical characteristics combining with α , β -unsaturated carbonyl core makes molecules acceptable for binding to protein and eventually blocking it. In consideration to these functional insights, the lead structure of PB-compounds is slightly modified. Now, from the chemistry perspective, there will certainly be more room for investing in new ideas for the development of further more potent inhibitors, if required.

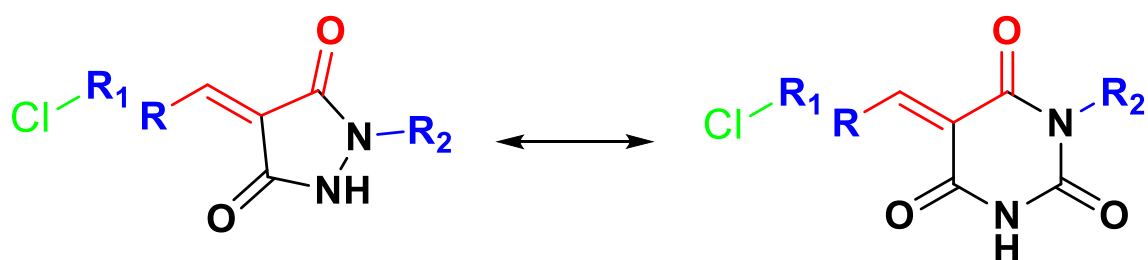


Figure 2.18. The modified lead structure with five and six membered rings. Red indicate the critical α , β -unsaturated carbonyl. The two ring (five or six member) are equally effective. R in blue denotes modifiable electron-rich aromatic substituent. R₁ represents extended aromatic substituent of R and "Cl" is the mandatory part of R₁. R₂ is the aromatic N-substitution of the ring.

The α , β -unsaturated carbonyl compounds commonly react via nucleophilic conjugate addition reaction e.g., Michael reaction²³⁸ and PB-molecules could act as Michael acceptors because there is a single cysteine available in the membrane binding domain of PLY.²³ In contrast, the probability of Michael reaction was minimal in consideration to the virtual screening proposed binding site (**Figure 2.1**). To resolve this contention concerning the reactivity mechanism, the mutational investigation of PLY was commenced.

2.2.5. Analysis of PLY-mutant variants via hemolysis assay

The pragmatic approach to figure out the actual binding site of PB-compounds on PLY was to construct and examine rational mutants of PLY. The amino acids for point mutations were chosen after reviewing the contemporary literature, inspecting the structure of PLY, and discussions with collaborators.

2.2.5.1. PLY mutations in the oligomer-forming region

The virtual binding site of PB-molecules was involved in the oligomerization of PLY. That is why, to begin mutational analysis, only those amino acids were chosen, which were involved or thought to be involved in the oligomer formation.

Aspartic acid at 205 (D205) in PLY was known to affect oligomer-formation.²³⁹ Hence, it was suggested by Dr. Christoph Arkona to modify D205 and investigate its influence on the activity of inhibitors. Therefore, aspartic acid was replaced by arginine.

The computational collaborator of this project, Dr. Marcel Bermudez suggested the next mutation in PLY, i.e. glutamic acid (E151). It was supposedly involved in oligomerization by forming salt bridge between adjacent monomers and it was in the proximity of the virtual binding-site of inhibitors. Activity of E151 in PLY was considered as a gateway for inhibitors to act. It was assumed that if the activity of PLY related to E151 was afflicted, then, it might influence the activity of inhibitors. Therefore, glutamic acid was exchanged for glutamine.

Dr. Christoph Arkona prepared the DNA of mutant proteins via site-directed mutagenesis protocol. Thereafter, Ali Saoud, a master student in our group, had expressed both mutant versions under supervision using our protein expression protocol. Meanwhile, PLY-D205A and PLY-E151Q were unable to release hemoglobin in the assay, which indeed confirmed their effect on oligomerization of PLY. Since there was no hemolysis, therefore, PB-molecules could never be tested against those variants of PLY in the hemolysis assay.

Afterwards, another amino acid T55 was mutually selected from the virtual binding site for investigation. T55 directly interacts with PB-molecules (**PB-1**, **2**, **2.5**, **2.6**, etc.) as per predicted binding site. Thus, T55 was replaced by alanine and PLY-T55A was expressed. Interestingly, unlike other mutants (E151Q and D205R) investigated up to now, PLY-T55A was active in the hemolysis assay and in fact, it was around three

times more active than PLY wild type. When **PB-1**, **2** and **3** were analyzed against PLY-T55A, each one inhibited the mutant version at an IC_{50} value lower than the IC_{50} for wild type PLY. The outcome indicated that the amino acid T55 had slightly increased the native hemolysis activity of PLY, but it was unable to upset the activity of PB-inhibitors.

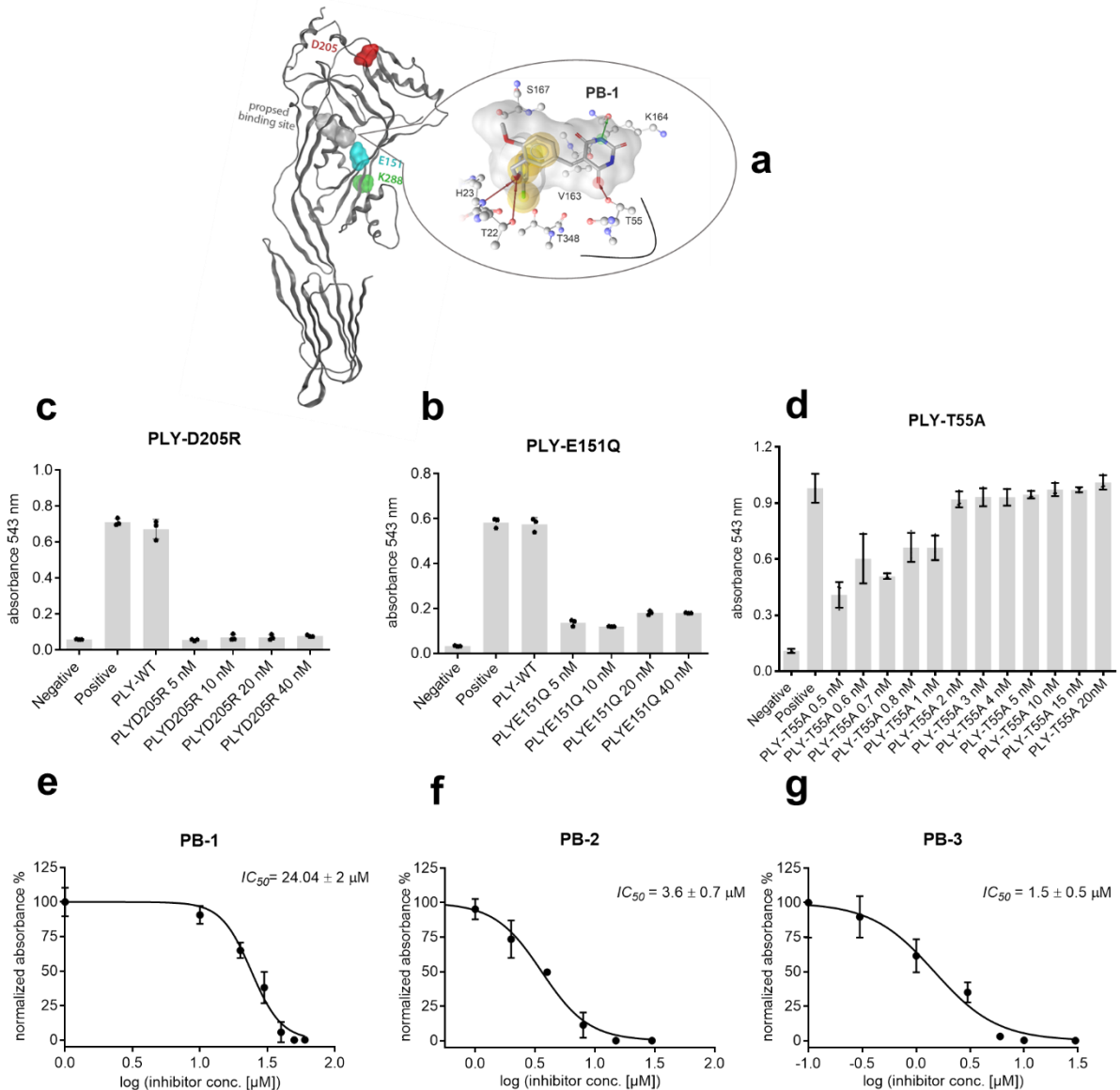


Figure 2.19. The analysis of mutations from oligomer-forming region.

a. The mutations from oligomer-forming region, D205: red, E151: cyan and K228: green (not prepared because away from binding site). The proposed binding site in grey and a zoomed view of **PB-1** with black highlighted interaction of T55. **b & c.** The comparison of the hemoglobin release between PLY-WT and variants (PLY-E151Q and PLY-D205R). **d.** Initial activity of PLY-T55A. **e, f & g.** IC_{50} (95% CI) of **PB-1**, **2** and **3** against PLY-T55A. (n=3)

2.2.5.2. PLY mutations in the cholesterol-binding region

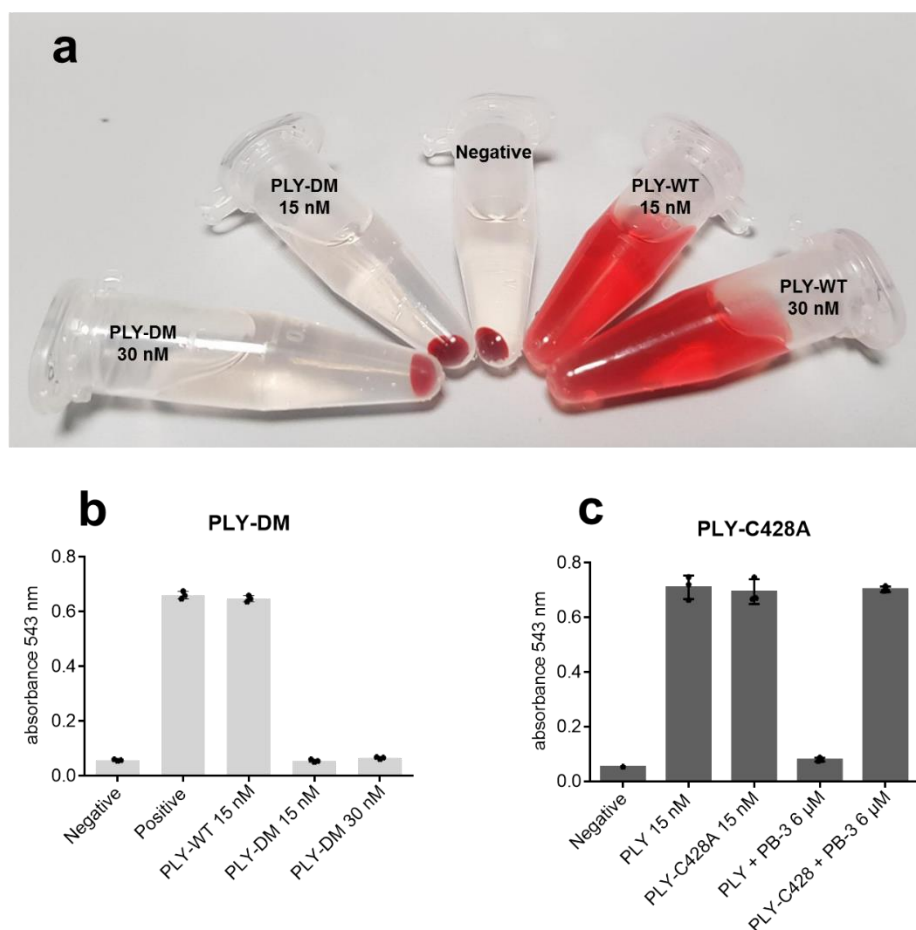
The evaluation of mutants of oligomer-forming region was not in accordance with the computational perspective. A couple of mutants were inactive and the active one showed no influence on binding of inhibitors. Thus, at that stage, mutations within the critical motifs of cholesterol-binding domain were considered. The cholesterol-binding domain contained at least two nucleophilic amino acids in the conserved motifs, e.g. threonine in the CRM and cysteine in the UDP.^{5,32} The core structure of the PB-inhibitors apparently favors a nucleophilic conjugation reaction. Therefore, it was plausible to investigate mutations of these amino acids.

To investigate cholesterol-binding domain, the first mutant was a known double mutant (PLY-DM). The amino acids of CRM that is a pair in loop L1 of D4, threonine (T459) and leucine (L460)¹⁶⁰, were exchanged by two glycine residues. It was known that PLY-DM was inactive in the hemolysis assay. So, the erythrocytes were treated with the recombinant PLY-DM up to 30 nM, and no hemolysis was detected as expected.

In the next mutant of PLY, the only cysteine at 428 in the UDP of PLY was replaced by alanine. PLY-C428A, a cysteine mutant of PLY, was acknowledged to retain hemolytic activity, which was comparable to wild type PLY.²⁴⁰ Hence, the direct influence of C428 on the activity of PB-molecules could be demonstrated. PLY-C428A was produced successfully and, in accordance with earlier studies,²⁴⁰ it exhibited hemoglobin release in erythrocytes that was nearly identical to PLY-WT and thus, the activities of best inhibitors were evaluated against PLY-C428A.

PB-1 was found to be inactive after analyzing up to 100 μM against PLY-C428A. While **PB-2**, which blocked 100% wild type PLY at 8 μM , was unable to inhibit PLY-C428A at same concentration. Afterwards, when the analysis was extended up to 30 μM , then, **PB-2** inhibited PLY-C428A beyond 15 μM and blocked almost ~90% of the toxin's activity at 30 μM . However, during the extended analysis, the precipitates of **PB-2** were observed because beyond 10 μM , **PB-2** became increasingly insoluble. Similar to **PB-2**, **PB-3** was unable to inhibit PLY-C428A. **PB-3** blocks ~100% PLY at 6 μM , whereas, same concentration of **PB-3** was feeble for PLY-C428A. Upon extended analysis, **PB-3** inhibited PLY-C428A with an IC_{50} of 11 μM but like **PB-2**, here, too, the precipitation of inhibitor was observed in concentrations beyond 10 μM .

The data obtained by investigation of PLY-C428A were a breakthrough and convincingly proved that C428 had a significant role in the potency of PB-molecules and subsequently had higher affinity for them. However, the activities of **PB-2** and **3** at higher concentration demanded a plausible interpretation. There could be two possible rationales for this behavior of inhibitors and either one of them could be legitimate. First, there is a probability that inhibitors could be engaging to additional binding sites, e.g., oligomerization site as proposed by the virtual screening. The second possibility might be the aggregation of inhibitors; small molecules with low solubility tend to precipitate after a certain threshold and these aggregates can block the toxin due to non-specific binding.²⁴¹ The complete ineffectiveness of **PB-1** is inclined toward the second explanation, however, at the current stage, it requires supplementary evidence. Nevertheless, the involvement of D4 cysteine in terms of the mechanism of PB-molecules is non-trivial.



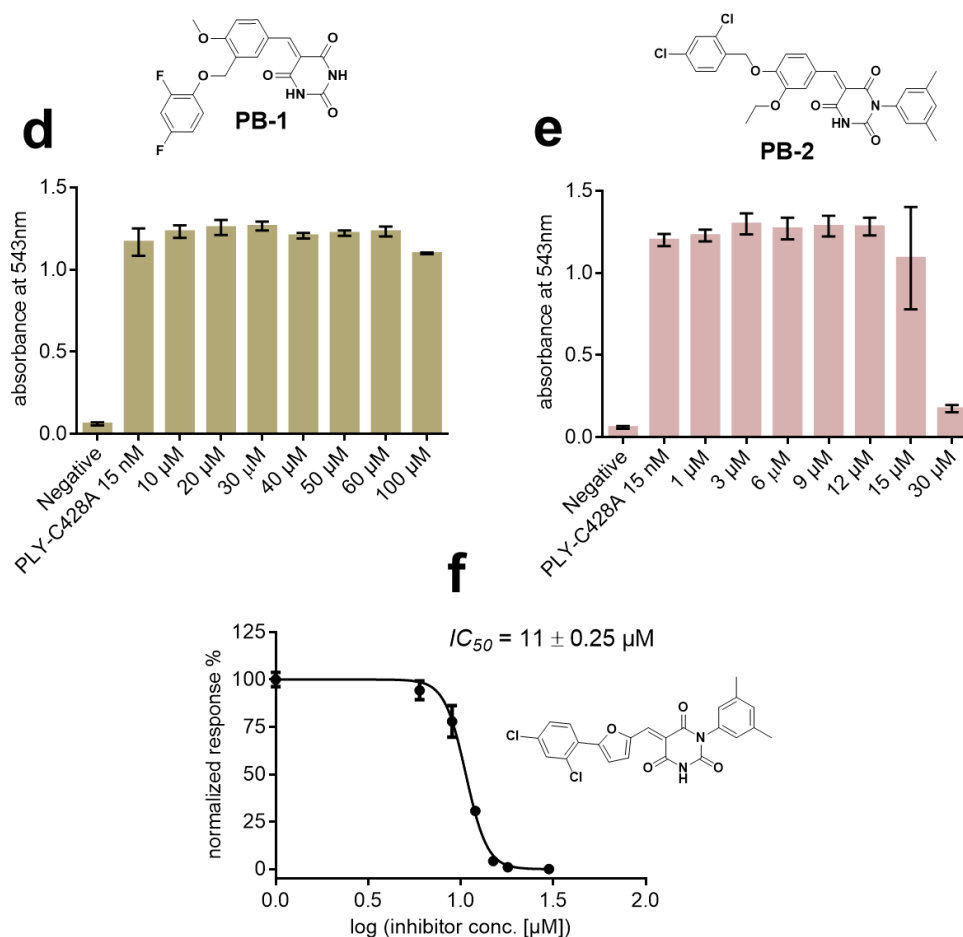


Figure 2.20. The analysis of mutations from cholesterol-binding region.

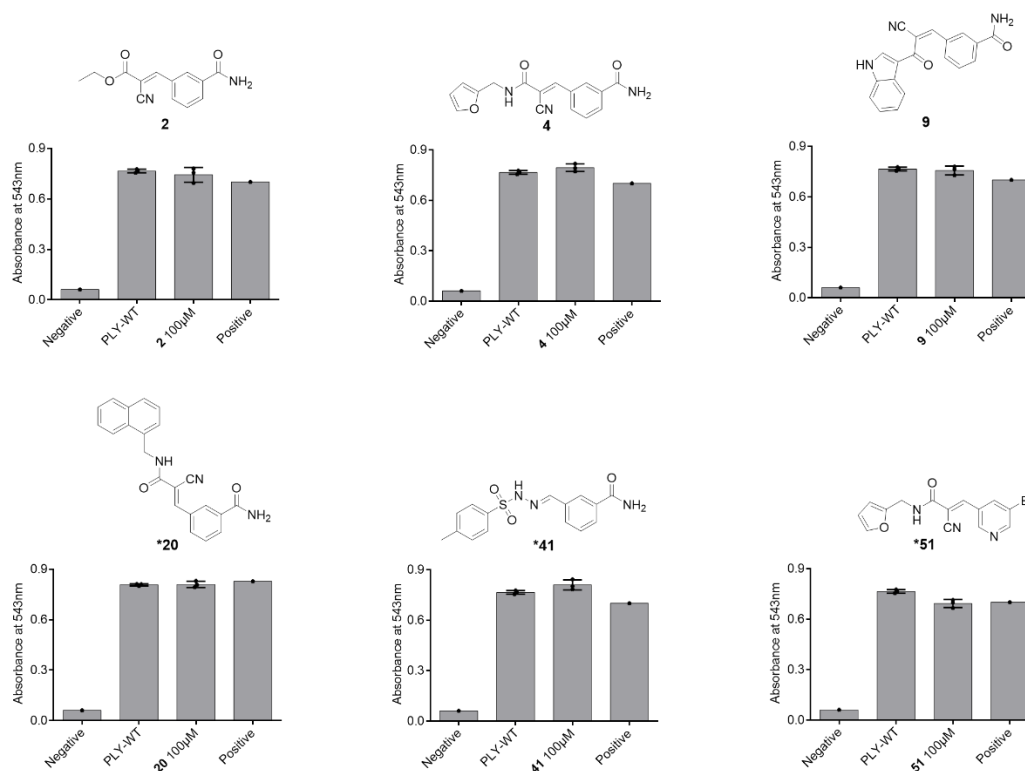
a. Inactive PLY-DM in the hemolysis assay. **b.** The graphical presentation of inactivity by PLY-DM. **c.** The activity comparison between PLY and PLY-C428A and simultaneously effect of **PB-3** (6 μM) on wild and cysteine-mutant proteins. **d.** Ineffectiveness of **PB-1** toward PLY-C428A. **e.** **PB-2** shows activity against PLY-C428A beyond 15 μM. **f.** IC_{50} (95 % CI) of **PB-3** measured against PLY-C428A (n = 3, error bar shows ± S.D.)

The information achieved after meticulous examination of mutants of PLY was of high value regarding validation of the binding site of PB-inhibitors. There are still some unanswered queries and to resolve them, supplementary analysis is advocated. The hemolysis assay did not confirm from the computational binding-mode perspective, and biophysical investigation of the mutants (PLY-E151Q, PLY-D205R, PLY-DM and PLY-C428A) would probably provide more insight regarding the engagement of inhibitors at the oligomer-forming site.

2.2.5.3. Selectivity of PB-molecules against PLY

The assumption implied by the SAR of PB-molecules is that inhibitors could react as Michael acceptors and, this hypothesis was supported by analysis of PLY-C428A and after ratifying the role of C428 in the potency of **PB-3**, the specificity of PB-inhibitors toward PLY was in question. Therefore, to affirm the selectivity of inhibitors against PLY, two plausible ways are conjectured. In the first way, PLY should be tested against other reported cysteine binding, electron-deficient olefines or Michael acceptors. Several molecules that are Michael acceptors were found inactive against PLY, e.g., **PB-2.4**, **2.10**, **2.11** and **PB-8** to **11**. However, to assure further, established Michael acceptors are going to be analyzed against PLY.²⁴² Moreover, in the second way, to rule out the possibility of non-specific activity, inhibitor must be assessed against proteins containing cysteine in the catalytic site. The lead compound, **PB-3**, was employed in second type of specificity analysis.

Testing of Michael acceptors against PLY. A compilation of cysteine chelating small molecules or Michael acceptors with diverse substituents previously established against enterovirus D68,²⁴² which contains active cysteine in the catalytic center, was available in-house. When these molecules were tested against PLY up to a concentration of 100 μ M, none of them was able to alleviate PLY.



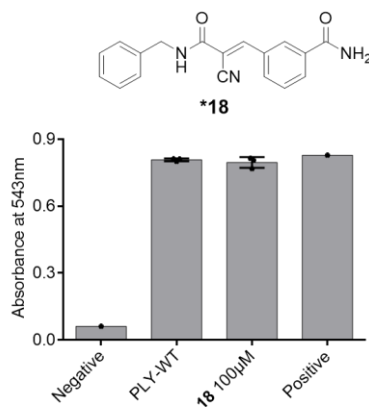


Figure 2.21. Analysis of reported Michael acceptors. Molecules are inhibitors of enterovirus D68 protease are inactive against PLY ($n \geq 3$, error bars represent \pm S.D, * means not published yet).

Analyzing PB-3 against two catalytic-cysteine containing proteins. To corroborate the specificity of **PB-3** against PLY, **PB-3** was tested against two in-house available proteins, PTP1b²⁴³ and SARS-CoV2²⁴⁴. Both proteins possessed cysteine in their active catalytic center.^{244,245}

My colleagues Markus Tiemann and Xinting Zhang conducted the testing on PTP1B and SARS-CoV-2 main protease in FRET assay.²⁴⁶ The activity range of **PB-3** is between 0.1 to 6 μ M against PLY and when the same activity range was employed on PTP1B and SARS-CoV-2 main protease, **PB-3** was found inactive. Thus, it was conclusive that **PB-3** was selective against PLY within that spectrum of activity. However, a crucial observation was made during both PTP1B and SARS-CoV2 testing, i.e. as the concentration of **PB-3** was increased, the solubility of **PB-3** in the assay buffers started declining and precipitates of **PB-3** became visible. Consequently, the precipitated-**PB-3** initiated blocking proteins. The precipitates of **PB-3** in the PTP1B assay buffer (50 mM MOPSO, 200 mM NaCl, pH: 6.5) started occurring after 15 μ M and in the buffer of SARS-CoV-2 main protease (100 mM HEPES and 1 mM EDTA) beyond 8 μ M. Therefore, it was inferred that **PB-3** at precipitating concentrations can induced non-specific inhibitions of enzyme.

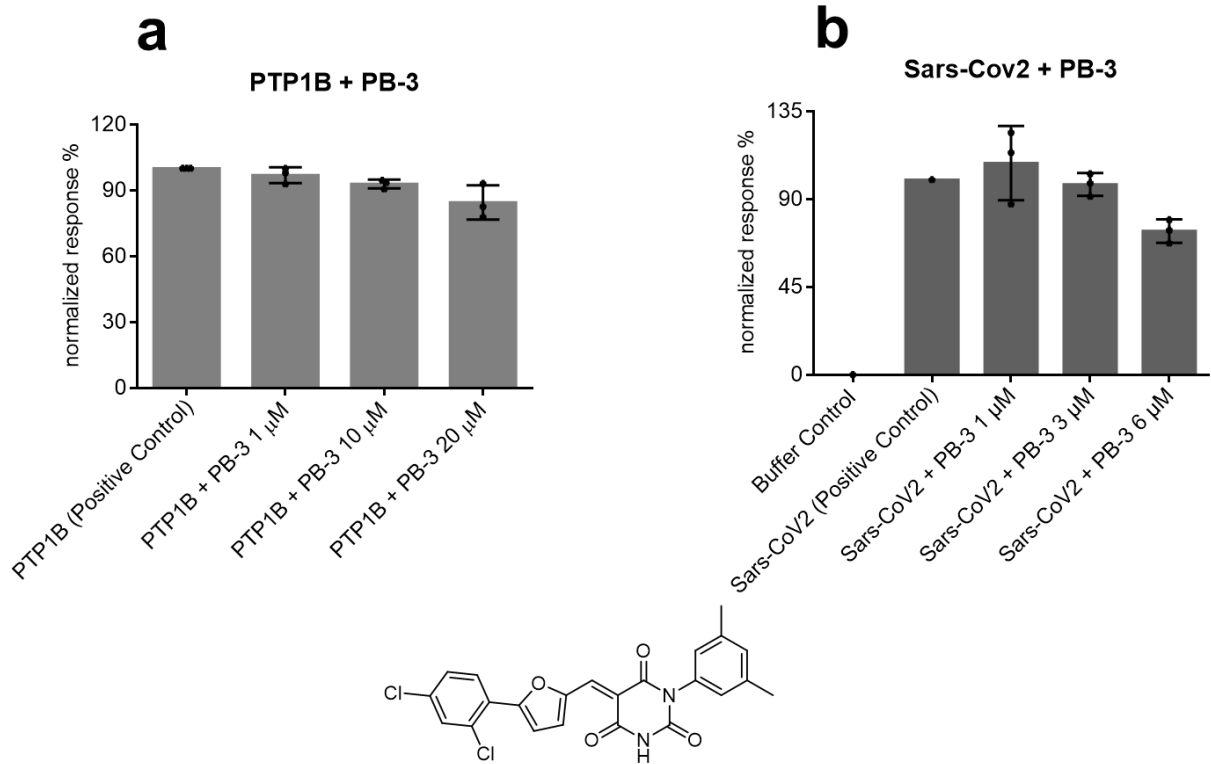


Figure 2.22. The analysis of PB-3 against cysteine-containing proteases. **a.** Testing result of **PB-3** against PTP1B. **b.** Findings after analyzing **PB-3** against **PB-3** ($n \geq 3$, error bars represent \pm S.D).

2.2.6. Evaluation of PB-molecules with other CDC

The aim of the project is to develop inhibitors, which could specifically and potentially block the detrimental effects of analogous CDC and to achieve the target, in the first phase, the potency and efficacy of pore-blockers (**PB**) have been successfully established in pneumolysin. The next rational stride forward would be the evaluation of PB-molecules against other CDC. As explained in the introduction, CDC are broadly branched into two categories. CDC of the first bind directly to membrane-cholesterol, whereas those of the second engages with other membrane proteins first. Both groups contain insidious molecular differences, thus, analyzing their response to PB-molecules would be intriguing and conceivably the findings could provide a better understanding of PB-molecules, particularly of their mechanism. Although PLY belongs to the group that interacts directly with cholesterol yet, to ascertain from the molecular perspective, one more member of the identical group must be analyzed and at least one member from indirectly cholesterol capturing proteins.

2.2.6.1. Perfringolysin O

Perfringolysin O (PFO) is the second CDC selected for evaluating the inhibitory potential of PB-molecules. PFO is sometimes refer to as theta toxin of the anaerobic bacterium *Clostridium perfringens*.¹⁸² As explained in the introduction, it belongs to CDC that interacts directly with cholesterol via CRM.³¹ It is structurally homologous to PLY and shares the identical UDP with a single cysteine.³¹ However, there is a subtle difference between PLY and PFO, i.e. the hemolytic activity of PFO relies on cysteine in the UDP and its mutation has been reported to produce a non-hemolytic version.¹³⁷ Like PLY, PFO exacerbate pathogenesis during the bacterial disease.¹³⁷ Here, PFO was expressed in the lab to endorse the activity of PB-molecules in CDC.

Native activity of PFO. PFO is more potent than PLY and kills erythrocytes at much smaller concentrations in the hemolysis assay.³¹ The established concentration range of PFO to induce 100% hemolysis was between 0.8–1 nM.³¹ Hence, at first, the native activity of PFO was analyzed on sheep erythrocytes before the evaluation of PB-molecules. The hemolysis under the effect of PFO was examined over a broad range (0.015–9 nM) and found that the activity of recombinant PFO was in conformity to reported values.³¹ Finally, 1 nM was chosen to investigate PB-molecules.

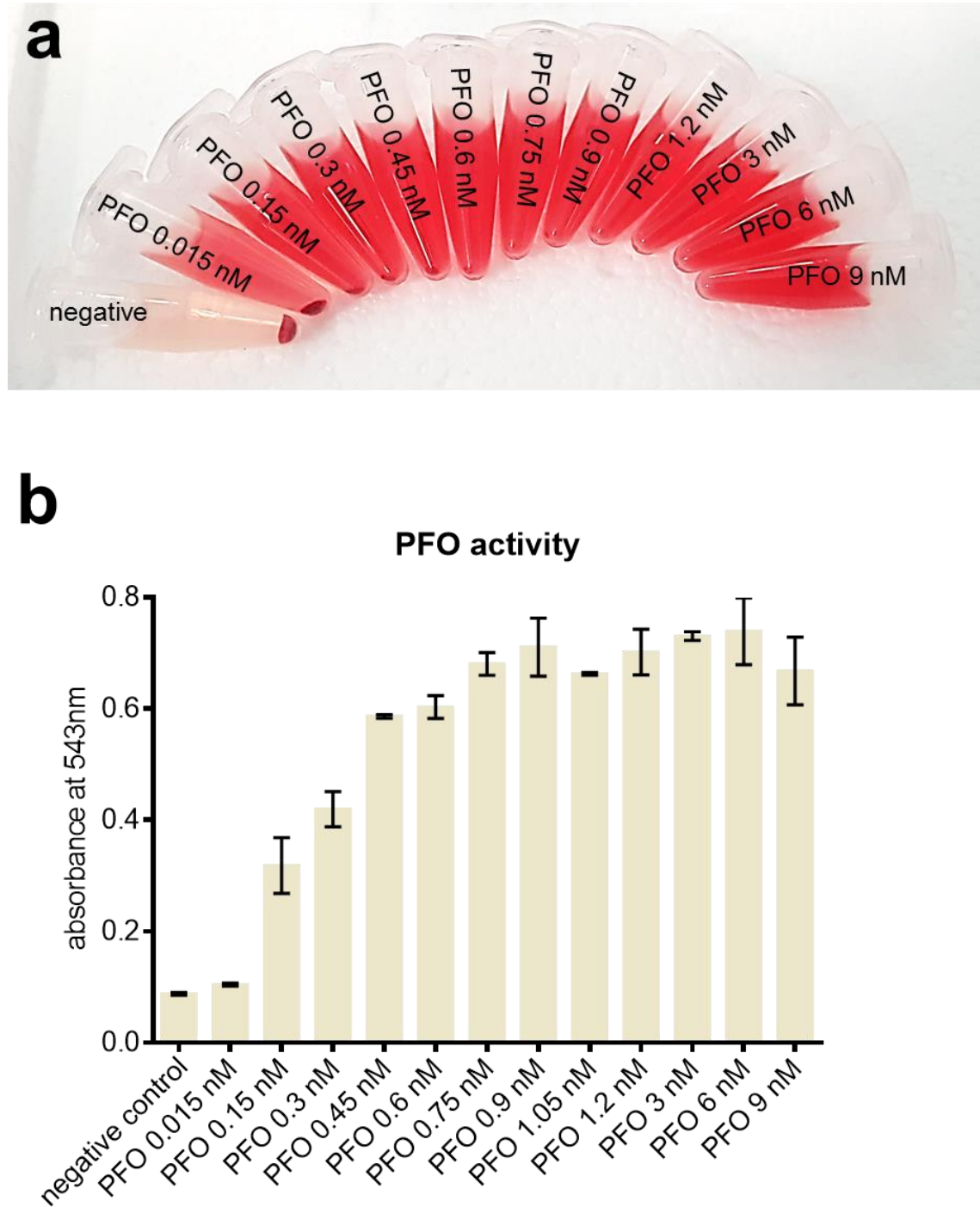


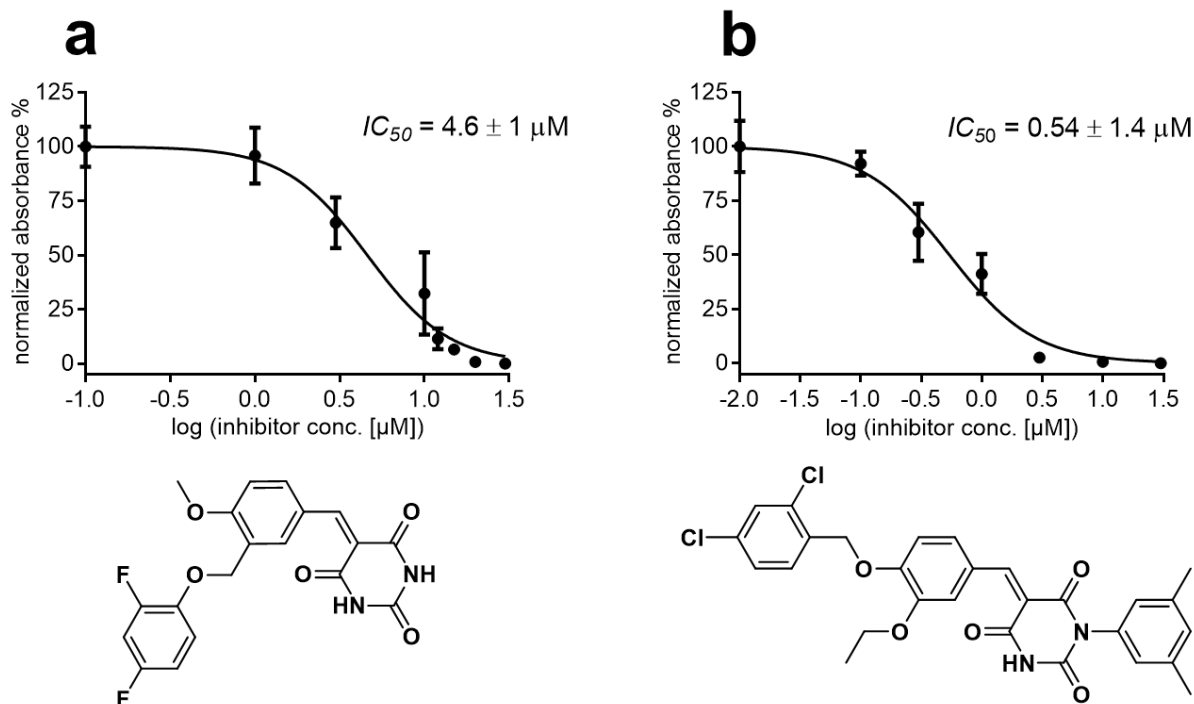
Figure 2.23. The activity of PFO in the hemolysis assay.

a. The hemolytic effect of PFO according to the increase in concentration, complete hemolysis starts at 0.75 nM. **b.** The graphical representation of the hemolysis (n = 3).

Testing PB-1 against PFO. **PB-1** has an IC_{50} of almost nearly 40 μM against PLY, hence, the same concentration range was adopted to counter PFO. Surprisingly, **PB-1** was noticed to be more potent against PFO than PLY and thus successfully blocked 100% PFO induced hemolysis at 20 μM . Later, the concentration range was reduced for determination of IC_{50} . It was calculated around 5 μM which is ca.10-fold potent in comparison to IC_{50} of **PB-1** against PLY.

Testing PB-2 against PFO. In the light of **PB-1** analysis against PFO, the concentration spectrum was broadened prior to testing. **PB-2** was evaluated within the 0.01-30 μM bracket and the IC_{50} was around 0.5 μM . Here, too, like **PB-1**, there was a significant improvement in the inhibitory potential of **PB-2** against PFO detected in comparison to PLY.

Testing PB-3 against PFO. The outlook of **PB1** and **2** result anticipates a lower IC_{50} from **PB-3** since it is an elite molecule among PB-inhibitors. The analysis window of **PB-3** for determination of IC_{50} against PFO was contained between 0.01-10 μM . In conformity to the expectations, **PB-3** stood out among PB-inhibitors with an IC_{50} value of 0.3 μM .



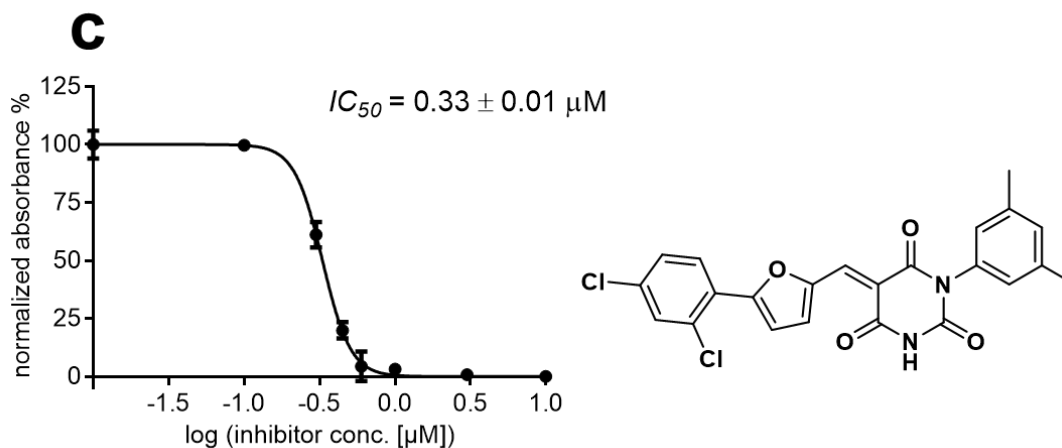


Figure 2.24. The analysis of PB-molecules against PFO.

a. It shows activity of **PB-1** against PFO. **b.** It represents inhibition of PFO by **PB-2**. **c.** It exhibits **PB-3** blocks PFO (95 % CI for all IC_{50} values, $n = 3$ and error bars represent \pm S.D.).

2.2.6.2. Intermedilysin

The toxin is named after *Streptococcus intermedius* and belongs to CDC. It is a fatal contributor of the pathogenicity induced by the bacterium.³⁶ Intermedilysin (ILY), as earlier explained, has been recognized as one of the few atypical CDC members which, in contrast to PLY and PFO, depends strictly on human CD59 membrane receptors for membrane binding of monomeric protein, followed by oligomerization.³⁴ Later, the initial structural alignment for prepore is also counted on CD59 receptor and soon afterward, CD59 is released at the membrane interface.²⁶ Next, the structural integrity of the prepore complex relies on the CRM and UDP, like in conventional CDC.²⁶ Aside from membrane sticking mechanism, ILY possess subtle variation in the UDP sequence, as it is devoid of a cysteine residue.²⁶

Here, in this study, the relevance of cysteine in the mechanism of PB-inhibitors has already been established during experimentation of PLY and PFO. After evaluating and affirming the efficacy and potency of PB-inhibitors in PLY and PFO, a member of CDC, such as ILY that lacks the cysteine, is a deliberated selection for investigating effect of PB-inhibitors. So far, the finding of PLY-C428A (a cysteine free mutant) has provided a succinct indication about the behavior of PB-molecules in the absence of cysteine and the outcome of ILY investigation would probably further signify the applicability of inhibitors.

Activity of ILY against sheep erythrocytes. Recombinant ILY was produced in the lab and after analytical validation, it was tested for the hemolytic activity against the sheep erythrocytes to confirm the activity of ILY. In the hemolysis assay, ILY was analyzed up to 60 nM with no appearance of any hemolytic activity. The result corroborated the fact that ILY depends on the human immune CD59 receptor for activity and, since sheep erythrocytes lacked them, no hemolysis was observed.^{26,36}

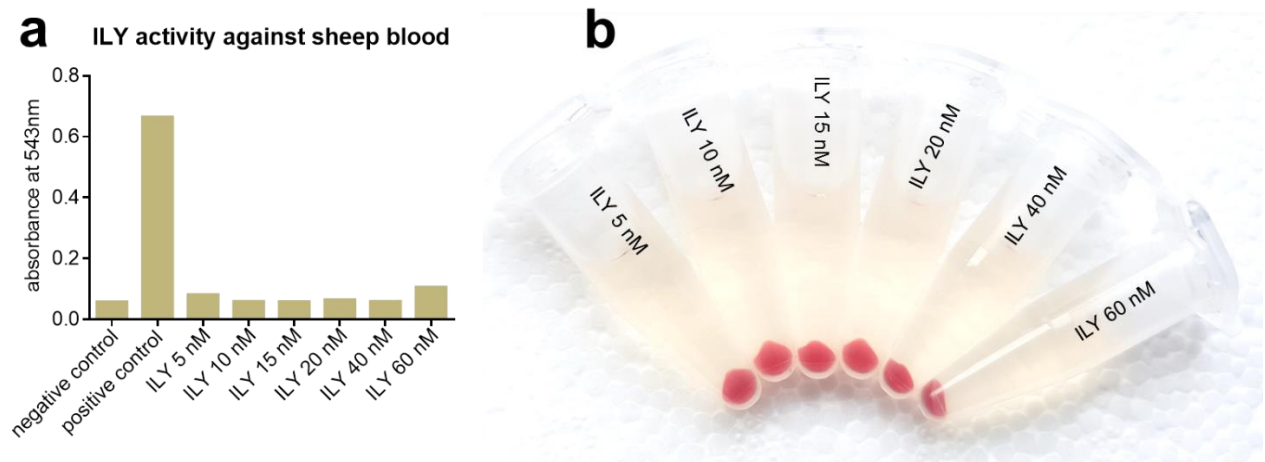


Figure 2.25. The inactivity of ILY against sheep erythrocytes.

a. The graphical representation of ILY activity where negative is only PBS and positive is 10% Triton-X. **b.** The visual exhibition of no hemolysis.

Activity of ILY against human erythrocytes. To analyze the native activity of ILY, human erythrocytes were isolated. Erythrocytes were extracted from fresh human blood and were washed 3x with PBS. Next, the isolated blood cells were used as substrate over a broad concentration range of ILY. The hemolysis assay applied for this purpose was the one that was already practiced in the lab.

The hemolytic activity of ILY on human erythrocytes has been known since decades.³⁴ Here, a similar effect of ILY was detected in the hemolysis assay. When ILY was tested starting from 0.1-10 nM, a gradual increase in hemolysis was observed. PBS was marked as negative control whereas 10% Triton-X was taken as positive control. The complete hemolysis of erythrocytes was observed after 3 nM, which was in accordance with the previously recorded values.³⁴ Thereafter, the concentration of ILY, 4 nM, was chosen to be used in the hemolysis assay for examination of PB-molecules.

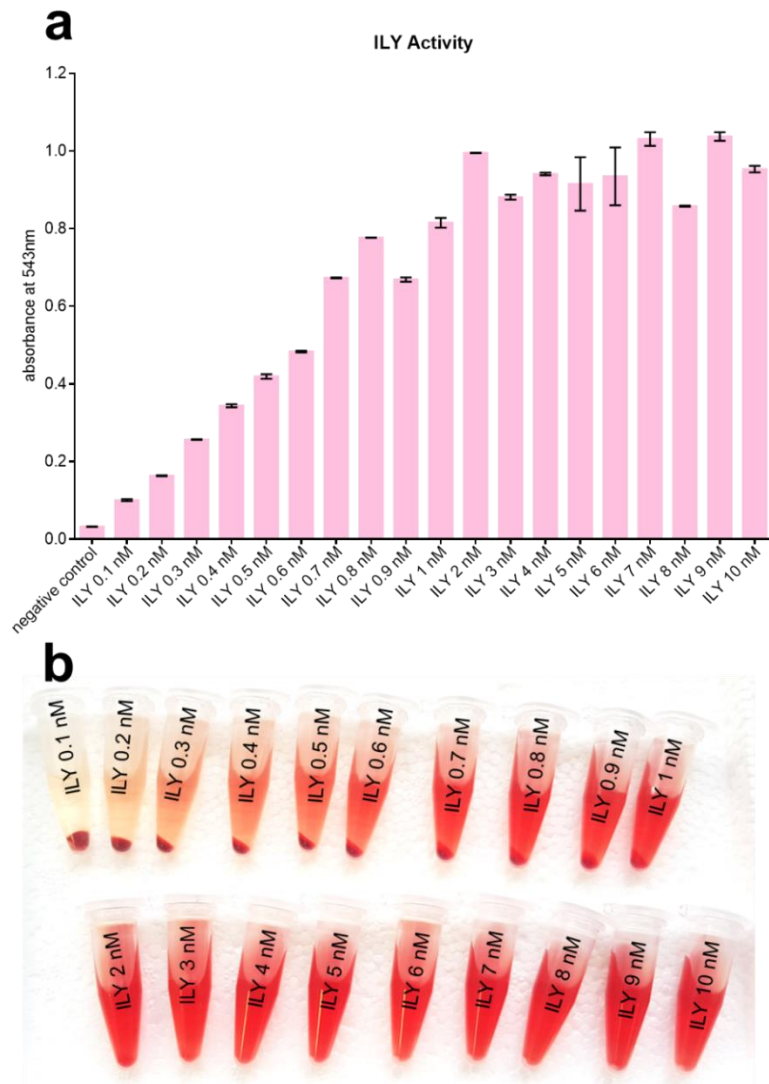


Figure 2.26. The activity of ILY against human erythrocytes

a. The graphical representation of ILY activity against human erythrocytes. **b.** The visual exhibition of the gradual hemolysis.

Testing of PB-1 against ILY. PB-1 was examined within an analysis window of 1-100 μM opposite to ILY. PB-1 was unable to completely stop ILY-mediated hemolysis. A slight inhibition of ILY was detected at $\geq 50 \mu\text{M}$ of PB-1 but it was still insufficient and, more importantly, did not lead to the absolute blockage of hemolysis. The experiment was conducted in triplicate like every other experiment, yet the result was identical. Therefore, it was confirmed that PB-1 was inactive in the hemolysis assay against CDC that are deficient in cysteine within UDP. The outcome of this experiment was in

conformity to the result of **PB-1** against PLY-C428A and further approved the essential role of cysteine.

Testing of PB-2 against ILY. When **PB-2** was analyzed against ILY, the earliest inhibition of hemolysis was detected at 10 μM and complete inhibition was observed at 15 μM . The IC_{50} was close to 11 μM . This outcome contrasted with the result of **PB-1**, which was inactive against ILY. Here, the apparent cause of inhibition could be precipitation of inhibitor yet, it requires complementary evidence.

Testing of PB-3 against ILY. **PB-3** showed results against ILY similar to those of **PB-2**. Like **PB-2**, inhibition started at 9 μM and IC_{50} was around 10 μM , which is marginally better than **PB-2**. Since **PB-2** and **3** have limited solubility, here too, the cause of inhibition could be the precipitation of the inhibitor.

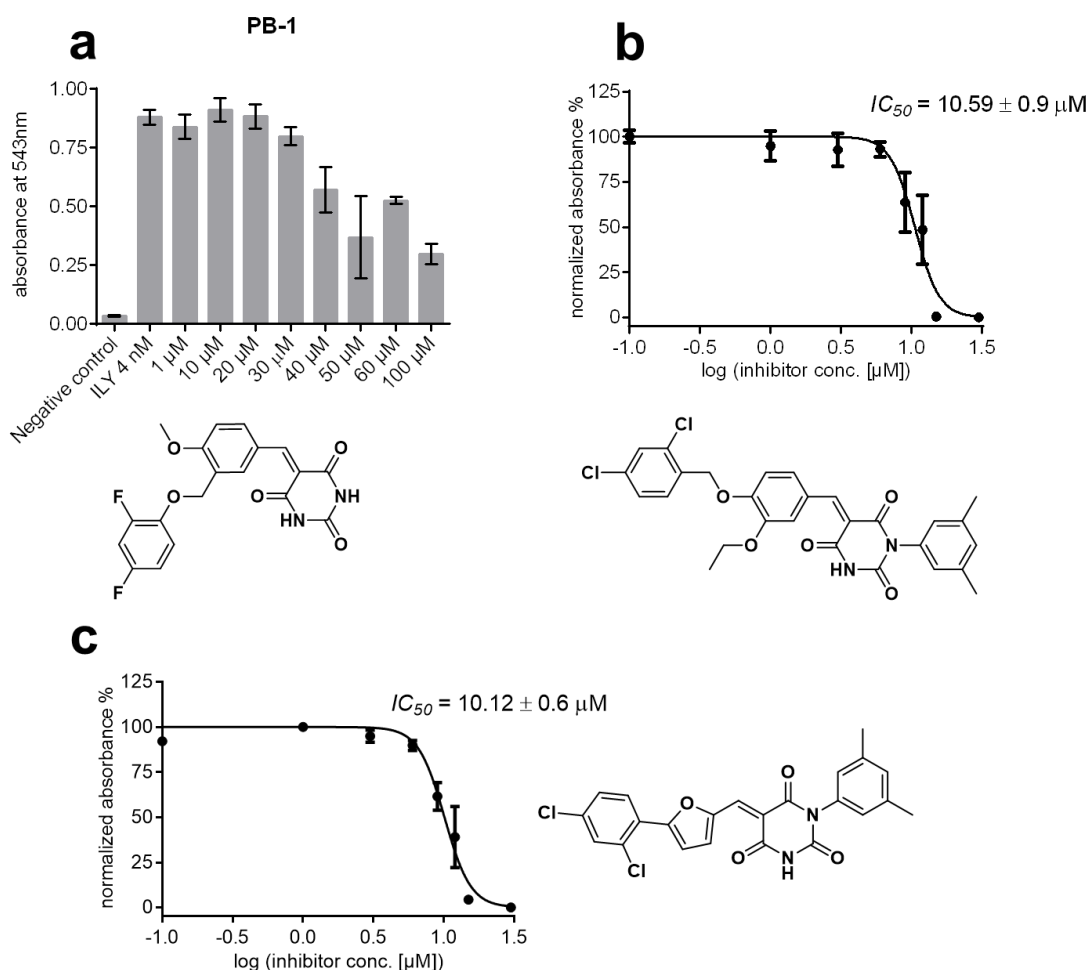


Figure 2.27. The analysis of PB-molecules against ILY. **a.** It shows activity of **PB-1** against ILY. **b.** It represents IC_{50} of **PB-2**. **c.** It exhibits **PB-3** IC_{50} (95 % CI for IC_{50} value, $n = 3$ and error bars represent \pm S.D.).

2.2.7. Summary

In continuation to our previous study, **PB-1** was a product of virtual screening that was actively hindering hemolysis mediated by a prototypical CDC, PLY. According to computational studies, **PB-1** was expected to block the oligomerization of PLY. Moreover, **PB-2** was an optimized version of **PB-1** with greater efficacy.

Here, in the current hemolysis testing, **PB-1** and **2** were re-synthesized in the lab and tested. During the testing, **PB-2** was diagnosed with instability in the assay buffer and meanwhile, the hemolysis assay was modified to estimate stability as well. The stability analysis led to the testing of precursors of **PB-2** (**PB-2.1**, **2.2** and **2.3**) that have demonstrated the specificity of intact **PB-2** against the target, as well as suggested the plausible reactivity of **PB-2**, i.e. via electrophilic 5-benzylidene-pyrimidine-2, 4, 6-trione. Later, multiple structural analogs of **PB-2** have been synthesized (**PB-2.4** to **2.12**) yet, unfortunately, none of them proved to be better than **PB-2**. At this point, the major structural shift has been executed by introducing a furan ring in place of the benzyl ring and **PB-3** is the product of structural scrutiny. **PB-3** supersedes **PB-2** with respect to stability and potency. Afterward, multiple attempts to design a better inhibitor than **PB-3** have been made via scaffold hopping (**PB-4** to **11**), however, none of them was superior to **PB-3**. Nevertheless, these new molecules have provided a valuable SAR.

In the hemolysis assay, the activity mechanism of PB-molecules was investigated via mutational analysis of PLY. From the viewpoint of the virtual binding mechanism, three mutant versions of PLY were produced for testing in the hemolysis assay and two of them were inactive in the hemolysis assay. Only, PLY-T55A was active in the hemolysis assay, but unfortunately it did not influence the activity of inhibitors. Next, two mutants mutated in the cholesterol-binding region were generated. The double mutant was inactive in the hemolysis assay and a cysteine mutant of PLY was capable of hemolysis. When PB-molecules (**PB-1**, **2** and **3**) were analyzed with PLY-C428A, it was convincingly established that C428 was critical for the efficacy of PB-molecules. Furthermore, it was presumed that PB-molecules interacted with cysteine in the UDP region of PLY (critical for membrane binding) via Michael addition reaction.

Afterwards, the specificity of PB-molecules as Michael acceptor was investigated and established in two ways. PLY was found active against assorted Michael acceptors

and none of them was able to inhibit PLY. Few of those molecules were reported Michael acceptors and inhibitors of a viral cysteine protease and others are in-house available molecules. In parallel, **PB-3**, the best among PB-molecules, was detected inactive at therapeutic concentrations, when tested against two protein targets (PTP1B and SARS-CoV-2 main protease) that contained cysteine in their catalytic domain.

Moreover, PB-molecules were evaluated in two different CDC, PFO and ILY. PFO shared identical UDP and membrane binding mechanism with PLY whereas ILY lacked cysteine in UDP and operates by a different membrane entry point. In the case of PFO, PB-molecules were observed to be significantly more potent than PLY. While in ILY, PB-molecules exhibited low to no activity (e.g., **PB-1**). The findings of PFO and ILY enhanced the argument concerning the activity of inhibitors via Michael reaction. However, at this stage, we suggested biophysical analysis to confirm the mode of activity.

2.3. Biophysical evaluation of PB-molecules

The biophysical evaluation of inhibitors is essential before applying advance testing on to the molecules. In our lab, multiple options are available to validate small molecules biophysically. It includes isothermal titration calorimetry (ITC), thermal shift assay (TSA), bio-layer interferometry (BLI), etc. After careful evaluation of these alternative methods, BLI was selected for the biophysical determination of protein-inhibitor interactions. PLY is a hydrophobic protein and can rapidly aggregate upon slight changes in buffer or even without a threshold concentration of glycerol in buffer. Therefore, BLI is well-suited system for such proteins because it is an open system and low concentration of protein is used in comparison to other methods and glycerol could be incorporated in the buffer, in short, there is plenty of room for customization of an assay.

2.3.1. Introduction to bio-layer interferometry

Bio-Layer Interferometry (BLI) is a biophysical method based enabling the detection, quantification, and kinetic analysis of molecular interactions between protein-ligand (ligand could be small molecule or protein) using a fiber-optic biosensor in real time.^{247,248} The biosensor comprises of two layers, first a biocompatible layer at the tip of biosensor and second an internal reference layer. In this technique, light passes through the biosensor and is reflected from the two layers of the biosensor. The detector records the optical interference patterns of reflected light beams and reports them in form of a sensogram.

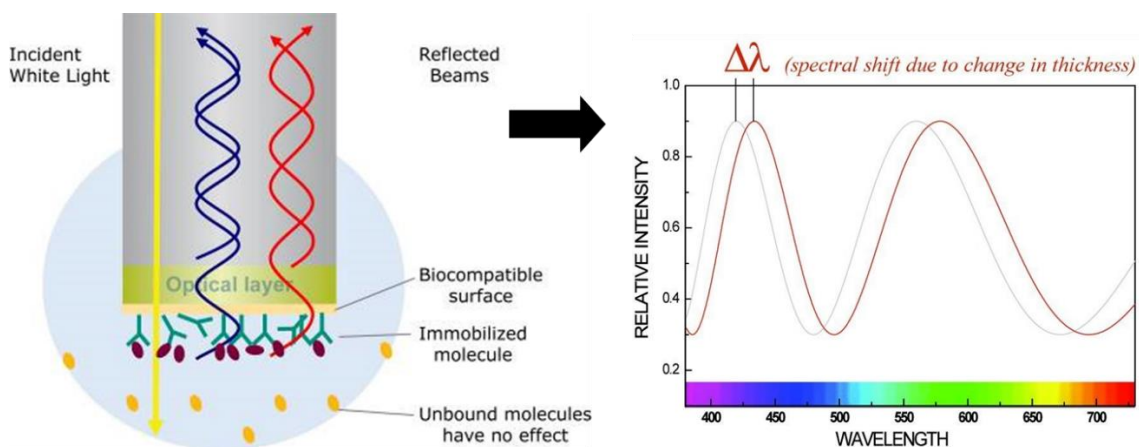


Figure 2.28. Bio-layer interferometry.

Representation of biosensor in presence of immobilized protein and ligand in accordance with thickness in bilayer and spectral shifts.²⁴⁸

A target protein is immobilized / loaded on the biocompatible layer of the biosensor and when it is dipped in an analyte solution, association / binding takes place between protein and analyte, and consequently an increase in the optical thickness of the molecular layer is observed. The thickness of layer leads to a shift in interference patterns on the spectrum and this spectral shift is interpreted as a change in wavelength. The change in wavelength is measured in the form of response (nm) on a sensogram. The data acquisition software in real time plots the interference patterns on a graph with time (s) on x-axis and response (nm) on y-axis and afterwards, the data analysis software is employed to determine the binding kinetics.

2.3.2. Evaluation of PB-1

There are various types of biosensors available for analyzing binding kinetics between ligand and protein. The interaction between **PB-1** and PLY was evaluated by utilizing Ni-NTA biosensors. Those were considered as the best option because NiNTA readily interacts with histidine tagged proteins and PLY contains 10x histidine at the N-terminus. Furthermore, NiNTA biosensors can be regenerated multiple times after the experiment. The experiment was executed in the following steps.

Biosensor soaking. Prior to the commencement of the machine, NiNTA sensors were calibrated by soaking for 45 min in the kinetic buffer.

Baseline. An initial stable baseline was established and observed in the kinetic buffer for 60 s. The baseline ensured that the sensor and the buffer did not interact with each other and were free of contaminants.

Loading. In this step, sensors were dipped into a 100 µg/ml solution of 10x histidine-tagged PLY for 400 s and protein was loaded onto sensors, which was observed in real time. The no-protein reference sensor was dipped in the buffer and subsequently no loading was noticed.

Inhibitor baseline. The loaded biosensors were dipped in 5 % DMSO containing buffer for 60 s. The same amount of DMSO was present in inhibitor (**PB-1**) containing solution for association. The inhibitor baseline validated that there was no interaction between sensors and DMSO.

Association. Next, loaded biosensors were soaked in solution containing **PB-1** for 120 s and the real time association was captured. The 5 % DMSO containing buffer was used as a no-inhibitor reference.

Dissociation. This step lasted for 200 s, sensors were moved in the buffer solution and **PB-1** dissociated from PLY. The dissociation of **PB-1** was detected on the sensogram.

The last three steps, i.e. inhibitor baseline, association and dissociation were repeated for each concentration and altogether four concentrations (20, 40, 80 and 160 μM) of **PB-1** were analyzed. The association continued to rise without reaching saturation with increasing concentrations of **PB-1** and could be clearly observed in the raw data (**Figure 2.29**). Meanwhile, an incomplete dissociation was noticed over the course of 200 s, especially for 80 and 160 μM of **PB-1**. This is atypical behavior for small molecules like **PB-1**, however, a strong or covalent interaction between protein and inhibitor could cause slow dissociation.^{242,249} Thus, it is presumed that the covalent interaction between **PB-1** and C428 of PLY was responsible for a stable protein-ligand complex formation and corresponding slow dissociation of **PB-1**. Moreover, the no-inhibitor reference had exhibited no association at all, whereas the no-protein reference had shown typical drifted signals which could be eliminated during data analysis.²⁵⁰

Once the experiment was over, the experimental raw data were transferred to data analysis software where the reference data were assigned and subtracted from the sample (**PB-1**) data. Then, the **PB-1** data were aligned according to the inhibitor baseline / dissociation (because both the same) for further evaluation.

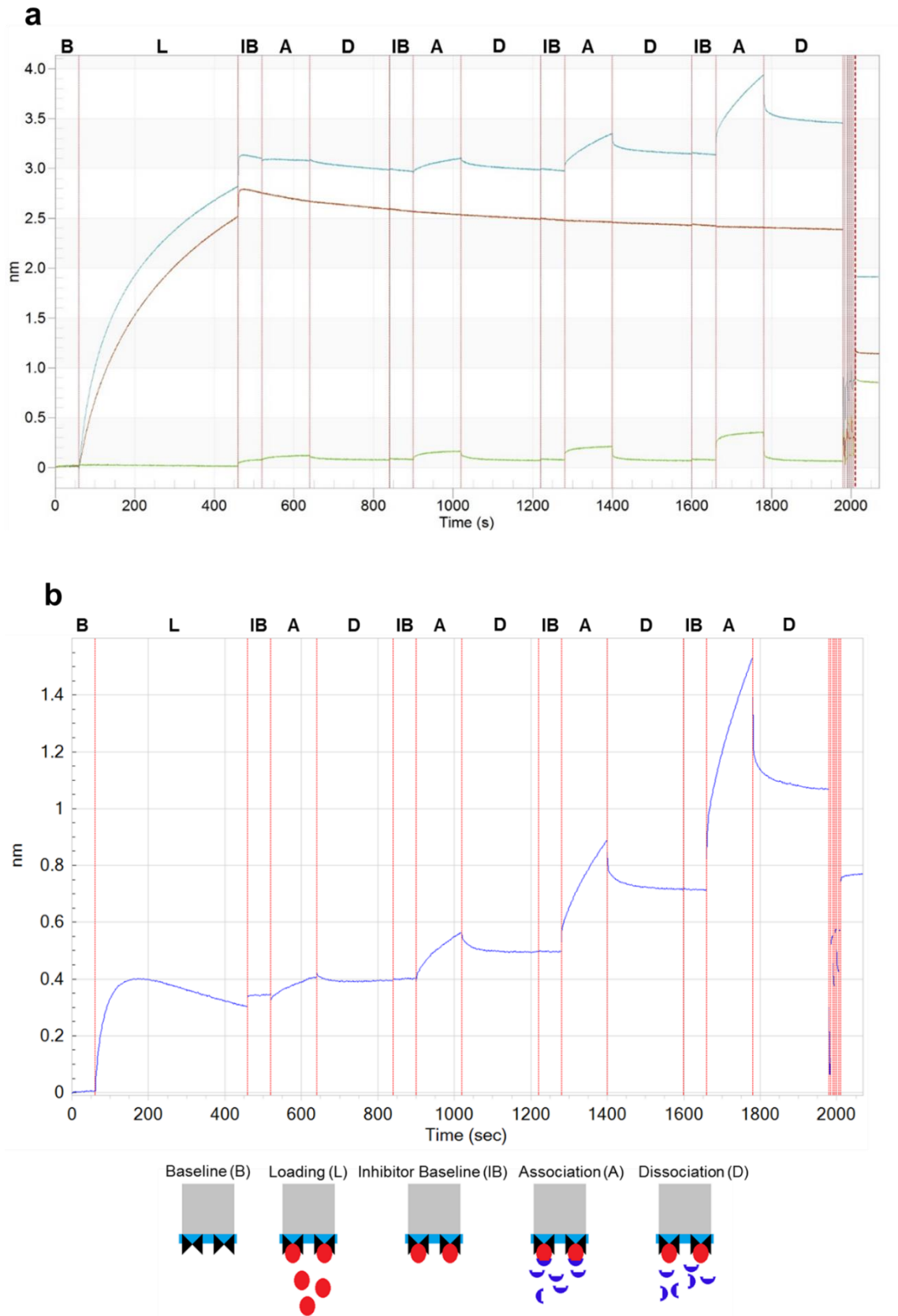
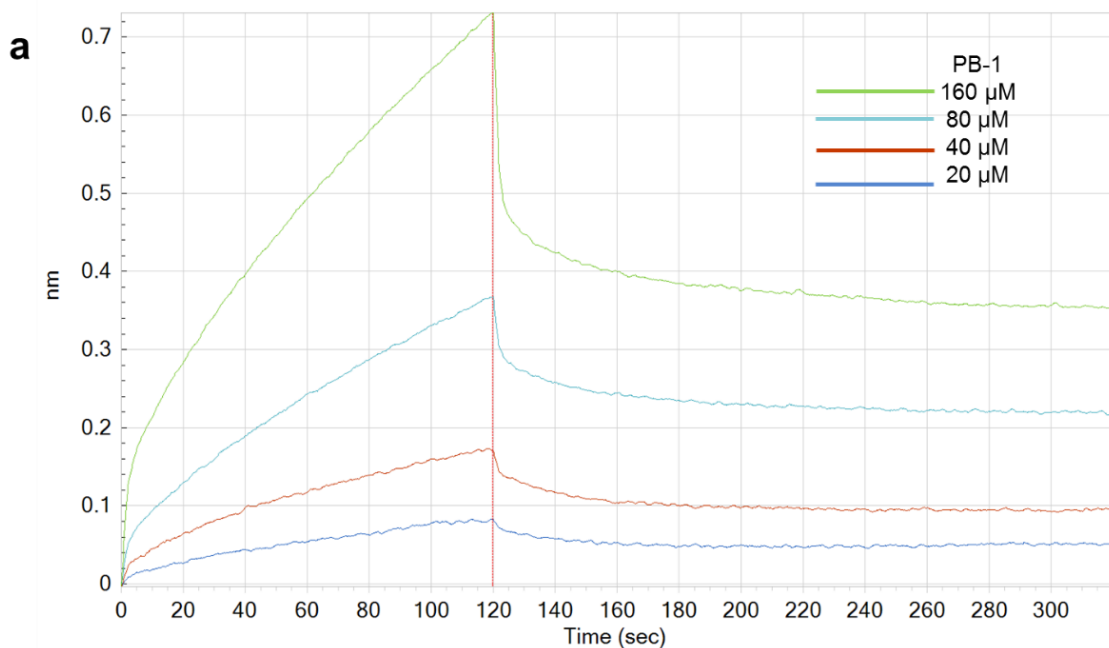


Figure 2.29. The raw data of **PB-1**.

a. The raw data displaying all steps of the experiment along with the label of sample and references. **b.** **PB-1** data after the subtraction of the reference data, exhibiting association with respect to concentration of **PB-1**.

To investigate the binding profile of **PB-1**, all concentrations were aligned in a single graph. The one-to-one (1:1) binding model was applied on that graph using the data analysis software and values were obtained. The binding data (association and dissociation curves) did not entirely fit into the one-to-one kinetic binding model and slightly deviated. In terms of statistical parameters, the chi-square (Chi^2) was 3.4423 and it indicates the error between the experimental data and fitted curves, closer to zero is regarded as better, and the coefficient of determination (R^2) was 0.8889, which denotes how better sample curves and fitted curves correlate and is regarded better when close to one. The variation between the binding model fitting and binding curves was probably due to the slow dissociation of **PB-1**. Typically, small molecules dissociate rapidly, and their binding is reversible,²⁵⁰ whereas in the case of **PB-1** there was limited dissociation due to a stable protein-ligand complex. The K_D value of **PB-1** was 85 μM (M), which is almost double the IC_{50} of **PB-1** calculated in the hemolysis assay. It is obvious that the discrepancy between K_D and IC_{50} was due to atypical binding, which led to improper fitting of the binding model. Furthermore, the k_{on} and k_{off} rates were found slow after calculation, their values are 52.3 ($\text{M}^{-1}\text{s}^{-1}$) and 0.00447 (s^{-1}) respectively. Additional details about the fittings and errors are available in the following **Figure 2.30.** and **Table 2.3.**



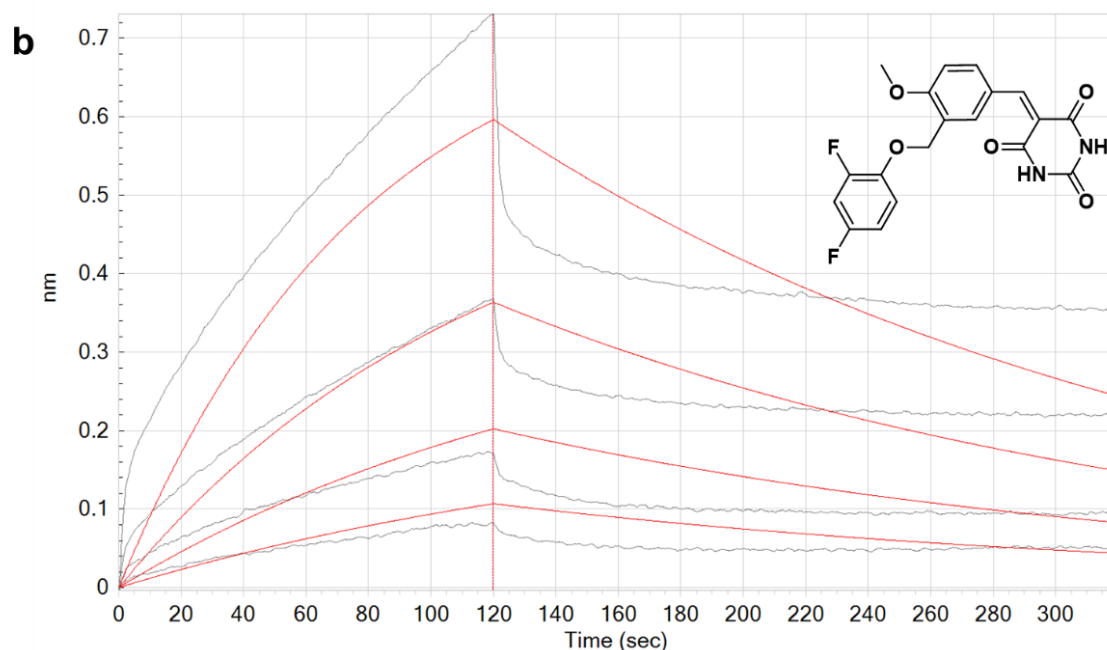


Figure 2.30. The binding data of **PB-1**.

a. Association and dissociation curves of **PB-1** concentrations. **b.** 1:1 binding model fitting data, red represents 1:1 model and grey indicates **PB-1** binding data.

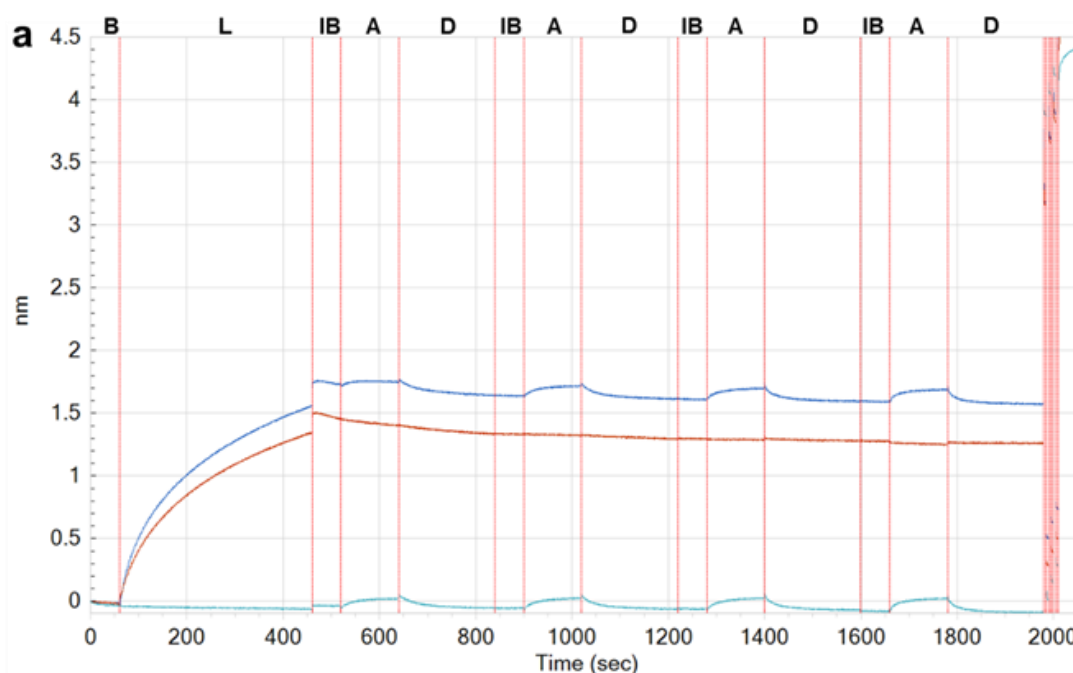
Table 2.3. The binding kinetics of **PB-1** with statistical parameters of good curve fitting.

Conc. (μM)	Response (nm)	k_{on} ($\text{M}^{-1}\text{s}^{-1}$)	k_{on} Error	k_{off} (s^{-1})	k_{off} Error	K_D (M)	K_D Error	χ^2	R^2
20	0.0806	52.3	2.97	4.47×10^{-3}	1.02×10^{-4}	8.56×10^{-5}	5.24×10^{-6}	3.4423	0.8889
40	0.1681	52.3	2.97	4.47×10^{-3}	1.02×10^{-4}	8.56×10^{-5}	5.24×10^{-6}	3.4423	0.8889
80	0.3536	52.3	2.97	4.47×10^{-3}	1.02×10^{-4}	8.56×10^{-5}	5.24×10^{-6}	3.4423	0.8889
160	0.7043	52.3	2.97	4.47×10^{-3}	1.02×10^{-4}	8.56×10^{-5}	5.24×10^{-6}	3.4423	0.8889

2.3.3. Evaluation of PB-2

PB-2 was investigated in a similarly designed layout to **PB-1**. All the major steps of the experiment, starting from the soaking of sensors down to the dissociation step were identical, except in this experiment, regenerated sensors were employed. Thus, the loading of PLY onto sensors was relatively reduced. Nevertheless, the loading was sufficient to conduct this experiment. Interaction of four concentrations of **PB-2** (1, 5, 10 and 20 μM) were analyzed with 100 μg of PLY immobilized on the NiNTA sensor.

The kinetic buffer was kept as a no-protein reference and baseline whereas a kinetic buffer with 5 % DMSO served as a no-inhibitor reference and inhibitor baseline. While in association with PLY, **PB-2** exhibited a concentration dependent increase in association and additionally, **PB-2** association achieved a saturated response in comparison to **PB-1**. When it comes to dissociation, a complete dissociation of each concentration of **PB-2** was observed during the dissociation step. Meanwhile, the no-protein reference had shown typical drift in signals,²⁵⁰ whereas the no-inhibitor reference had displayed neither association nor drifted signals. At the end of the experiment, the raw data were transferred to the data analysis software for evaluation. The stepwise raw data were captured and are available in **Figure 2.31 a**. Next, the no-protein and the no-inhibitor references were deducted from the data by the software and the reference subtracted view is available in **Figure 2.31 b**.



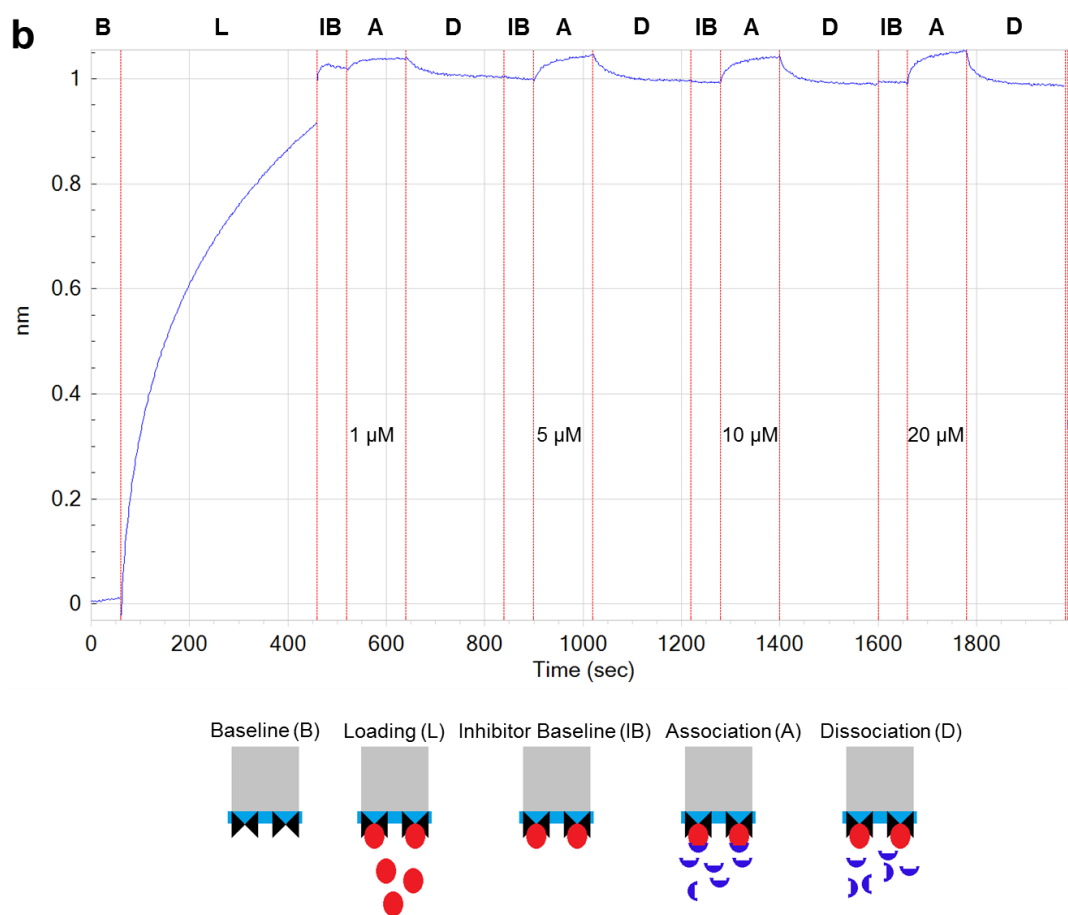


Figure 2.31. The raw data of **PB-2**.

a. The raw data including steps and labels of sample and references. **b.** **PB-2** data after the subtraction of the reference data.

Next, the binding kinetics of **PB-2** were calculated from the corresponding data. For this purpose, like **PB-1**, the association and dissociation steps for all concentrations of **PB-2** were rearranged according to the baseline and then one-to-one binding model was option selected on the data analysis software to generate fitting curves. The one-to-one model curves in red (**Figure 2.32 b**) fit well enough onto the binding data of **PB-2** in grey. The good fitting was further corroborated by calculated values of the chi-square (Ch^2) and the coefficient of determination (R^2), both values were 0.0954 and 0.8414 accordingly.

Moreover, the k_{on} and k_{off} rates of **PB-2** were 11400 ($M^{-1}s^{-1}$) and 0.0379 (s^{-1}) respectively, with errors within the acceptable range i.e. $\leq 10\%$. Both k_{on} and k_{off} rates were adequate and fall within the typical range of reversible small molecules. The common spectrum for k_{on} is between 10^3 to $10^6 M^{-1}s^{-1}$ whereas the accepted extend of k_{off} is with 10^{-2} to $10^{-5} s^{-1}$. The K_D value of **PB-2** was 3.3 μM (M) nearly same as the

IC_{50} of **PB-2** in the hemolysis assay. The curve fittings and binding profile are present in **Figure 2.32** and **Table 2.4**. To sum up, **PB-2** possesses much better binding kinetics in comparison to **PB-1**, which makes it superior inhibitor not just biologically but biophysically as well.

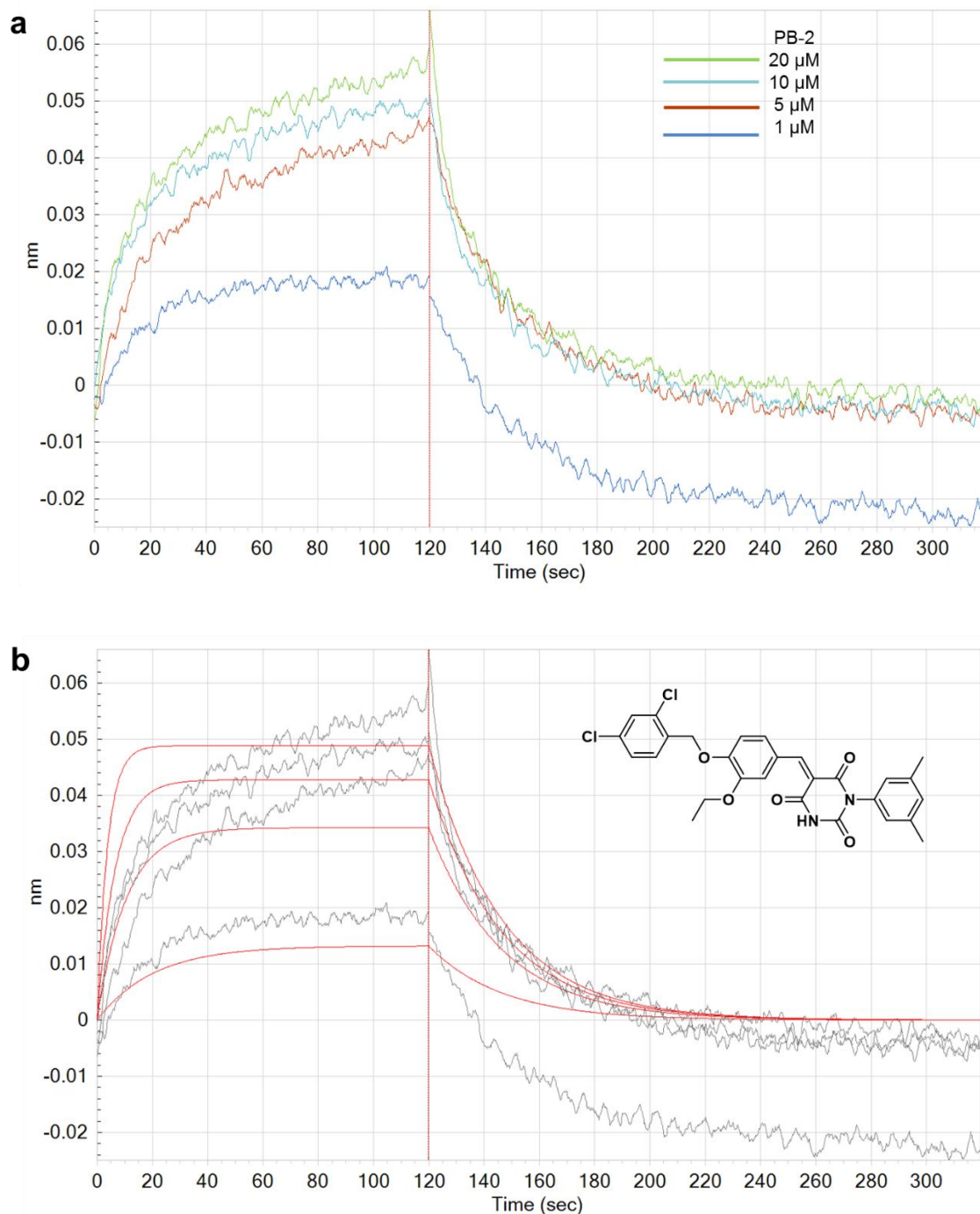


Figure 2.32. The binding data of **PB-2**.

a. Association and dissociation curves according to the concentrations of **PB-2**. **b.** 1:1 binding model fitting data and structure of **PB-2**, red lines are 1:1 model and grey for **PB-2** binding.

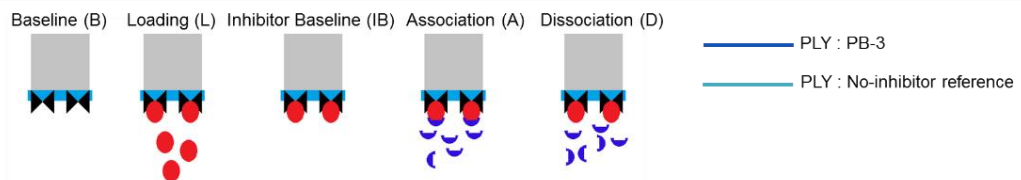
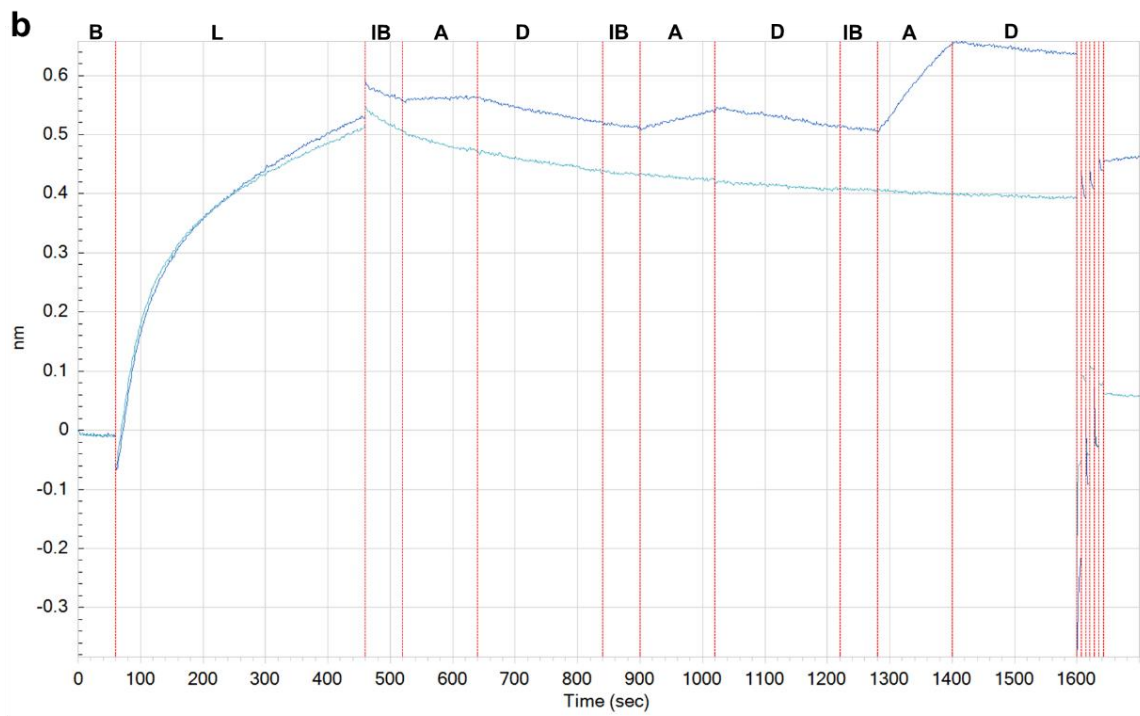
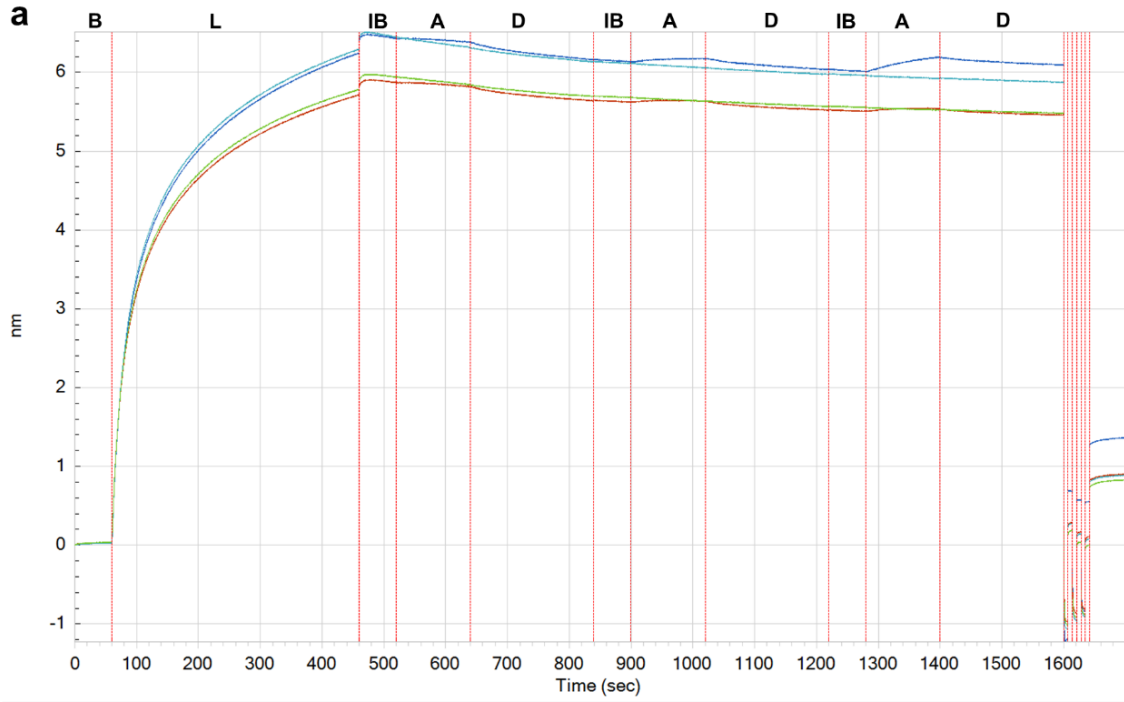
Table 2.4. The binding profile of **PB-2** with statistical parameters of goodness of fit.

Conc. (μM)	Response (nm)	k_{on} ($\text{M}^{-1} \text{s}^{-1}$)	k_{on} Error	k_{off} (s^{-1})	k_{off} Error	K_D (M)	K_D Error	Chi^2	R^2
1	0.0187	1.14×10^4	8.05×10^2	3.79×10^{-2}	1.61×10^{-3}	3.31×10^{-6}	2.72×10^{-7}	0.0954	0.8414
5	0.0434	1.14×10^4	8.05×10^2	3.79×10^{-2}	1.61×10^{-3}	3.31×10^{-6}	2.72×10^{-7}	0.0954	0.8414
10	0.0478	1.14×10^4	8.05×10^2	3.79×10^{-2}	1.61×10^{-3}	3.31×10^{-6}	2.72×10^{-7}	0.0954	0.8414
20	0.0558	1.14×10^4	8.05×10^2	3.79×10^{-2}	1.61×10^{-3}	3.31×10^{-6}	2.72×10^{-7}	0.0954	0.8414

2.3.4. Evaluation of PB-3

The analysis of **PB-3** was conducted through the identical experimental procedure and steps as for **PB-1** and **2**. Although the references of the system were optimized, e.g. the non-binding mutant PLY-C428A was used as a reference protein. Due to the presence of a reference protein, there were three reference sensors deployed, which were stepwise subtracted from the data and the binding profile was measured.

The experiment was executed in two rounds, during the first, 100 μg of each PLY and PLY-C428A was captured by parallel Ni-NTA sensors for 400 s, then the protein-captured biosensors underwent association and dissociation steps with three different concentrations (0.6, 1 and 6 μM) of **PB-3**. Meanwhile, in the second round, equal amount of protein-loaded on the biosensors were dipped stepwise in DMSO containing buffer as no-inhibitor references. **PB-3** displayed concentration dependent association to wild-type PLY and slow or weak dissociation whereas **PB-3** showed negligible to no association with PLY-C428A at any concentration. Since PLY-C428A was secured as reference here, thus, its data were subtracted and then PLY no-inhibitor reference was subtracted from the **PB-3** binding data.



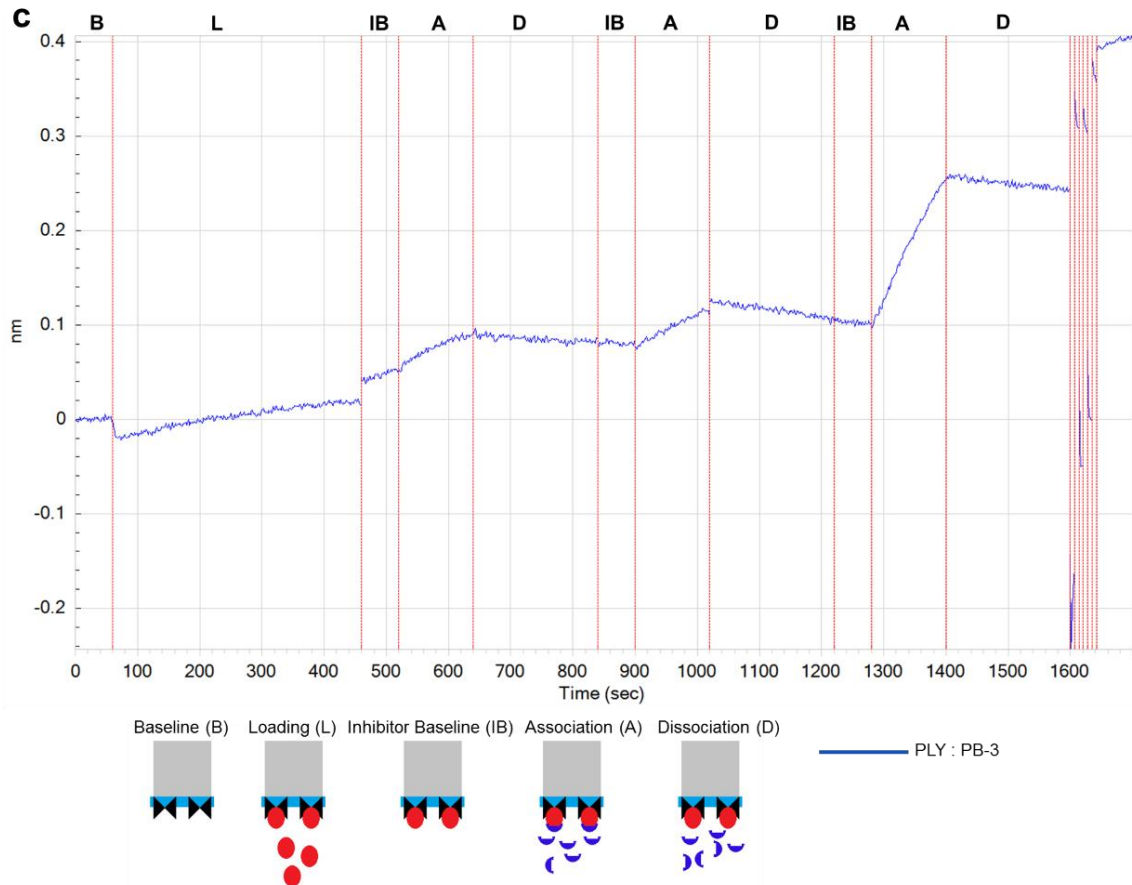


Figure 2.33. The raw data of **PB-3**.

a. The raw data of **PB-3** with references. **b.** The data after subtraction PLY-C428A references. **c.** The data after subtraction of all references.

The binding of **PB-3** pertaining to concentration was aligned according to the baseline with time on x-axis and response (nm) on y-axis (**Figure 2.33 a**). The 1:1 binding model was applied, and kinetics were calculated by using the data analysis software, revealing that **PB-3** had high on-rate ($1800 \text{ M}^{-1}\text{s}^{-1}$) and small off-rate (0.00046 s^{-1}). The K_D value of **PB-3** was $2.56 \times 10^{-7} \text{ M}$, or 256 nM (**Table 2.5**), which makes **PB-3** a tight binder. The curve fitting of **PB-3** was good and value of Ch^2 and R^2 were 0.1531 and 0.9346 respectively.

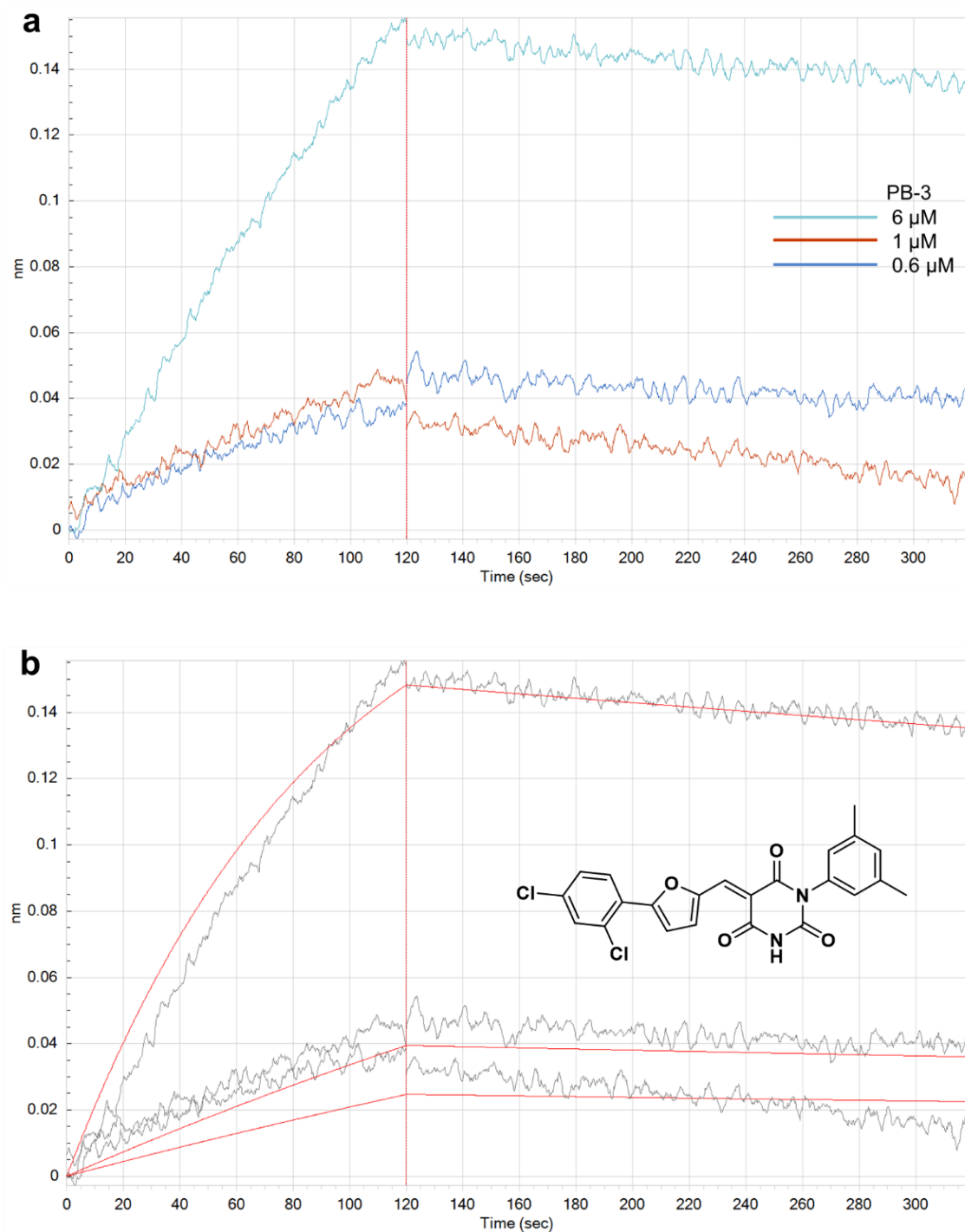


Figure 2.34. The binding data of **PB-3**.

a. Association and dissociation curves according to the concentrations of **PB-3**. **b.** 1:1 binding model fitting data and structure of **PB-3**, red lines are 1:1 model and grey for **PB-3** binding.

Table 2.5. The binding kinetics of **PB-3** with statistical parameters of good curve fitting.

Conc. (μM)	Response (nm)	k_{on} ($\text{M}^{-1}\text{s}^{-1}$)	k_{on} Error	k_{off} (s^{-1})	k_{off} Error	K_D (M)	K_D Error	Chi^2	R^2
0.6	0.0362	1.80×10^3	7.58×10^1	4.60×10^{-4}	7.96×10^{-5}	2.56×10^{-7}	4.55×10^{-8}	0.1531	0.9346
1	0.0458	1.80×10^3	7.58×10^1	4.60×10^{-4}	7.96×10^{-5}	2.56×10^{-7}	4.55×10^{-8}	0.1531	0.9346
6	0.1501	1.80×10^3	7.58×10^1	4.60×10^{-4}	7.96×10^{-5}	2.56×10^{-7}	4.55×10^{-8}	0.1531	0.9346

2.3.5. Evaluation of pneumolysin mutations

The objective of mutational studies was to understand and elucidate the mechanism of PB-inhibitors. As explained in the results of the hemolysis assay, five mutations of PLY were expressed, three of them belonged to the oligomerization domain whereas two were in the cholesterol-binding domain. Three mutant versions (two from oligomer region and one from cholesterol-binding region) were inactive in the hemolysis assay. Therefore, these three mutant-versions can only be analyzed in BLI assay that whether these bind to PB-inhibitors or not. In addition, PLY-C428A, which was active during hemolytic analysis and only **PB-3** blocked this mutant, also needs biophysical validation. Hence, the biophysical evaluation might serve as an opportunity to unveil the functional mechanism of PB-inhibitors.

Cholesterol binding of Pneumolysin-double mutant. PLY-DM contained known mutations of threonine (T459) and leucine (L460) in the cholesterol binding domain.³² PLY-DM was inactive in the hemolysis assay according to the expectations, so it was decided to further test PLY-DM in a qualitative manner before testing it against PB-molecules.

This was a control experiment to confirm that PLY-DM does not bind to cholesterol. The identical protocol of earlier experiments was utilized. Only the time for cholesterol baseline, association and dissociation steps was elongated to authenticate the qualitative binding. After the initial baseline, PLY-WT and PLY-DM (100 μg) were immobilized on the biosensors and a cholesterol baseline was established for 300 s.

The cholesterol baseline contained 5 % ethanol with kinetic buffer. Next, proteins were associated with cholesterol (5 μ M) for 300 s and then dissociated for 300 s as well. Similarly, no-protein and no-inhibitors references were treated in the same way. PLY-WT tethered with cholesterol whereas PLY-DM did not connect to cholesterol at all, which validated the absence of cholesterol engaging amino acids. When it came to dissociation, PLY-WT exhibited very weak dissociation. This occurred due to a fact that cholesterol is a tight binder of PLY-WT with a K_D value of 8 nM.¹⁶⁰

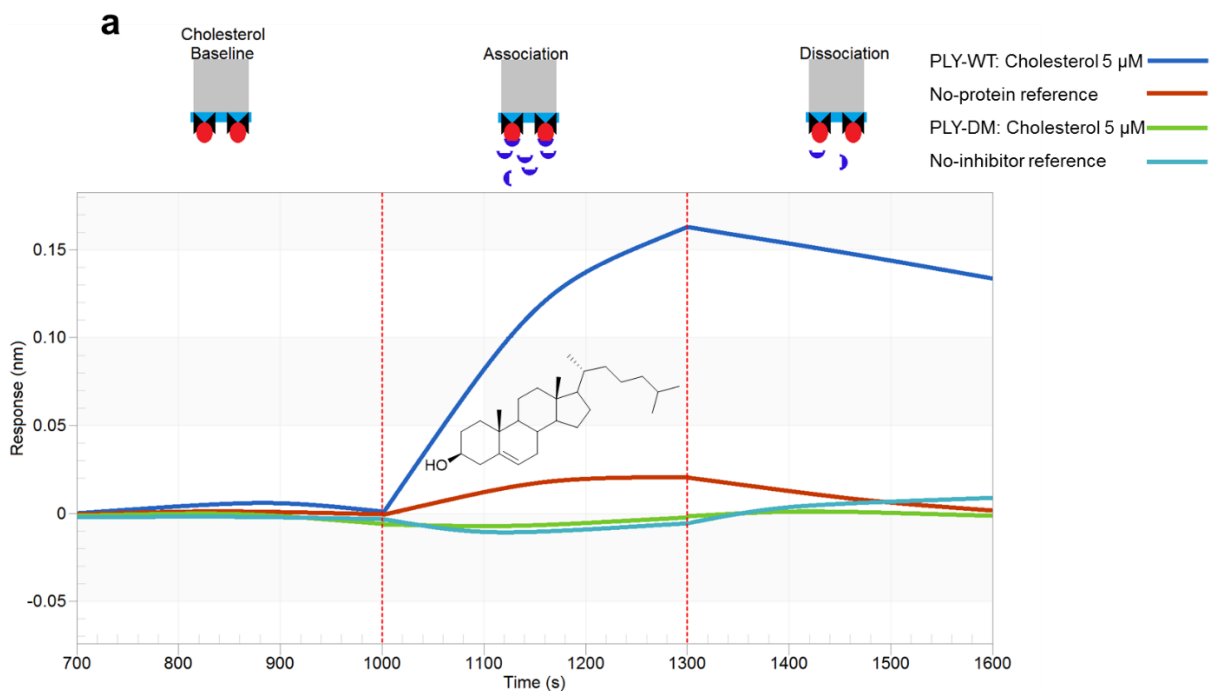
Qualitative evaluation of hemolytic inactive mutants of PLY. In addition to CRM-mutant (PLY-DM), two more mutant versions of PLY were inactive in the hemolysis assay. Amino acids, E151 and D205 belong to the oligomer-forming-region of PLY,²³⁹ and their mutant versions PLY-E151Q and PLY-D205R were expressed. The binding of these mutants toward **PB-2** was qualitatively examined via BLI. Ali Saoud, the master student of our group, performed these experiments independently with each mutant protein by customizing the same protocol mentioned in earlier experiments. The binding data points at 4 μ M with each mutant version were isolated from each experiment and joined in a graph with the aid of Graphpad Prism (software). Since conditions were similar, therefore, to make a comparison between qualitative-binding of proteins with **PB-2**, the data was aligned to the baseline. The binding between **PB-2** and PLY-WT was kept as a reference.

PLY-E151Q and PLY-DM showcased increased association toward **PB-2** than PLY-WT, whereas PLY-D205R demonstrated nearly the same binding as PLY-WT. The binding curve of all of them was reversible as complete dissociation was observed (**Figure 2.35 b**). In the light of the qualitative response by each mutant protein, it was obvious that **PB-2** was not interfering with the function of these crucial amino acids, and apparently did not seem to be involved in blocking the oligomer-forming region. However, oligomerization, as known from previous studies, is dependent on many other amino acids as well²⁸ and in this regard, further mutational analysis is an open door.

Qualitative comparison of PB-3 binding between PLY and PLY-C428A. PLY-C428A mutant belongs to the cholesterol-binding domain of PLY. Its role was recognized concerning the activity of PB-molecules during the hemolysis assay. However, **PB-3** had shown inhibition of PLY-C428A at higher concentration. Therefore,

it was critical to compare binding of **PB-3** with PLY-WT and PLY-C428A. PLY-WT and PLY-C428A were loaded on parallel biosensors and then immersed one by one in solutions containing 2, 4 and 8 μM of **PB-3**. Concentration beyond 8 μM exhibited atypical drift. Thus, the testing was performed up to 8 μM . The association of **PB-3** with PLY-C428A and PLY-WT was monitored in real time and the data was aligned according to the inhibitor baseline after completion of the experiment.

The association raw data for all three concentrations of **PB-3** against both proteins was transported to Graphpad Prism for comparative analysis. **PB-3** engaged to PLY-WT in a concentration dependent manner whereas it exhibited minimal binding to the mutant PLY-C428A (**Figure 2.35 c**). These findings suggested that PLY-C428A was not binding to **PB-3** and the inhibition of PLY-C428A by **PB-3** in the hemolysis could be an aggregation effect, however, it need further evidence of aggregation. So far, the data imply that C428 of PLY had significant higher affinity for PB-molecules as compared to PLY-C428A. Furthermore, it also suggested that **PB-3** binds to C428 via a covalent interaction.



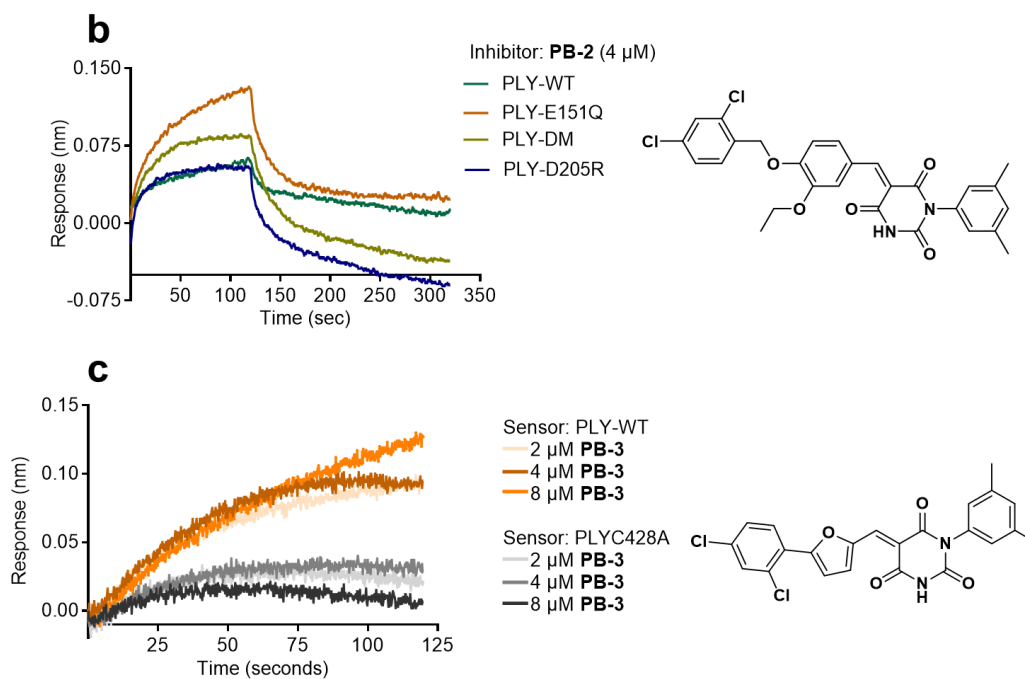


Figure 2.35. The mutational analysis of PLY via BLI.

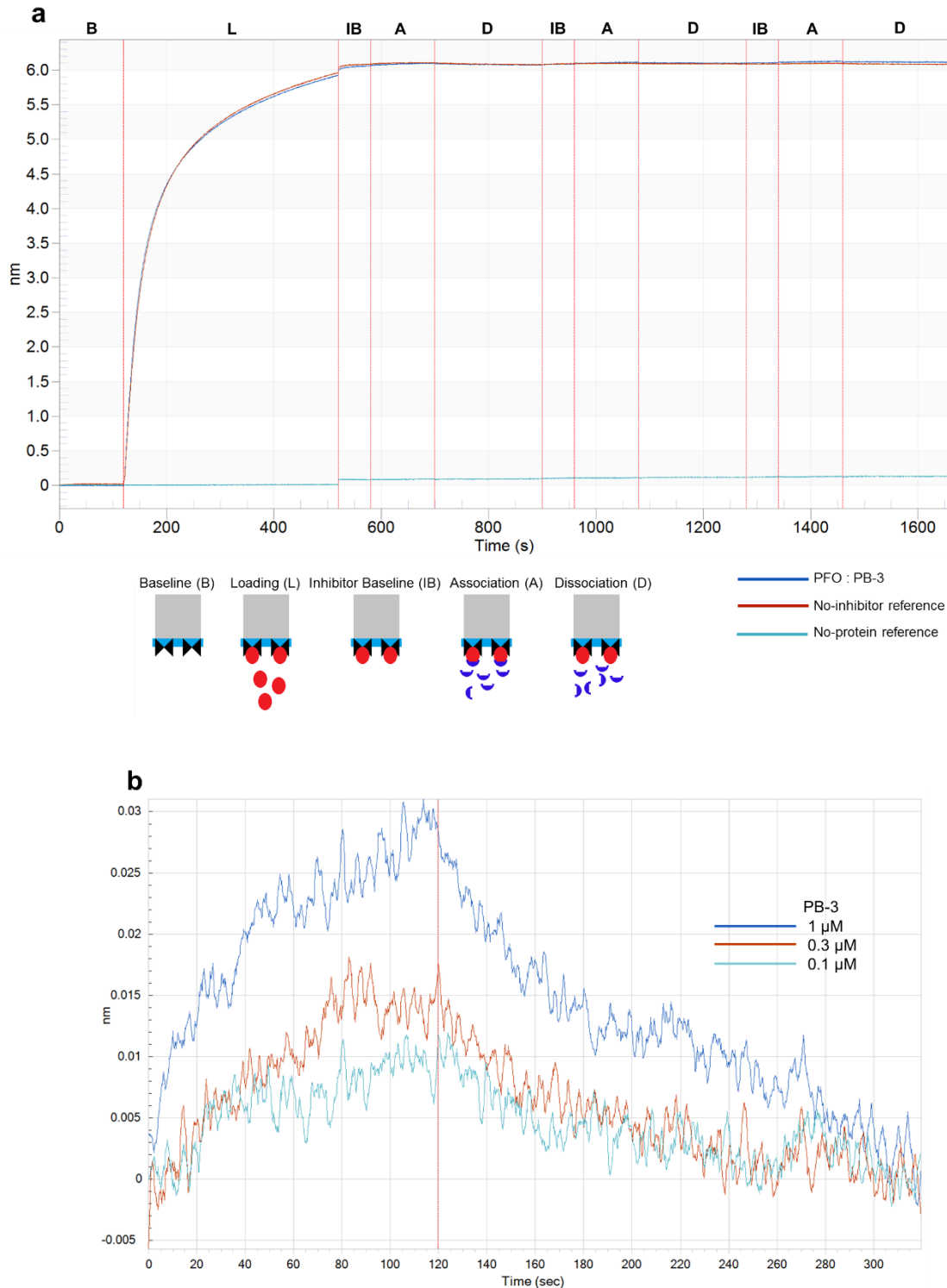
a. PLY-DM shows no association with cholesterol, whereas as PLY-WT binds tight with weak dissociation. **b.** Mutant-versions and PLY-WT interact with **PB-2** at 4 μM . **c.** **PB-3** binding comparison with PLY-C428A and PLY-WT.

2.3.6. Evaluation of binding between PB-3 and PFO

The affinity between **PB-3** and PFO was investigated via identical BLI protocol. PFO was like PLY, 10x histidine tagged, therefore NiNTA sensors were used for the protein immobilization. Two references, no-protein, and no-inhibitor references were employed. The no-protein reference sensor was soaked in kinetic buffer solution and then transferred to **PB-3** sample wells during the experiment. In contrast, the no-inhibitor reference sensor was loaded with PFO and afterward dipped in control wells containing kinetic buffer with 5% DMSO. PFO (100 μg) was immobilized on sensors for 400 s and then, one biosensor was immersed in one by one association and dissociation wells that contained three different concentrations (0.1, 0.3 and 1 μM) of **PB-3** and the adjacent no-inhibitor reference sensor was dipped in control wells. Likewise, in the case of no-protein reference sensor, the biosensor was dipped in buffer and afterward bathed in **PB-3** containing wells.

The raw data of experiment were transferred to data analysis software for quantification at the end of experimental procedure. Meanwhile, in data analysis, the references data were subtracted, and the remaining sample was aligned according to the dissociation.

Aligned concentrations of **PB-3** can be observed in the **Figure 2.36 b**. Later, the quantitative binding analysis of **PB-3** was acquired by applying the one-to-one binding model. The one-to-one model curves in red were efficiently fit onto the binding data of **PB-3** and the goodness of fitting could be assessed by values of the Ch^2 (0.0045) and R^2 (0.9111). The detailed quantitative report of binding kinetics between **PB-3** and PFO is available in the **Table 2.6**.



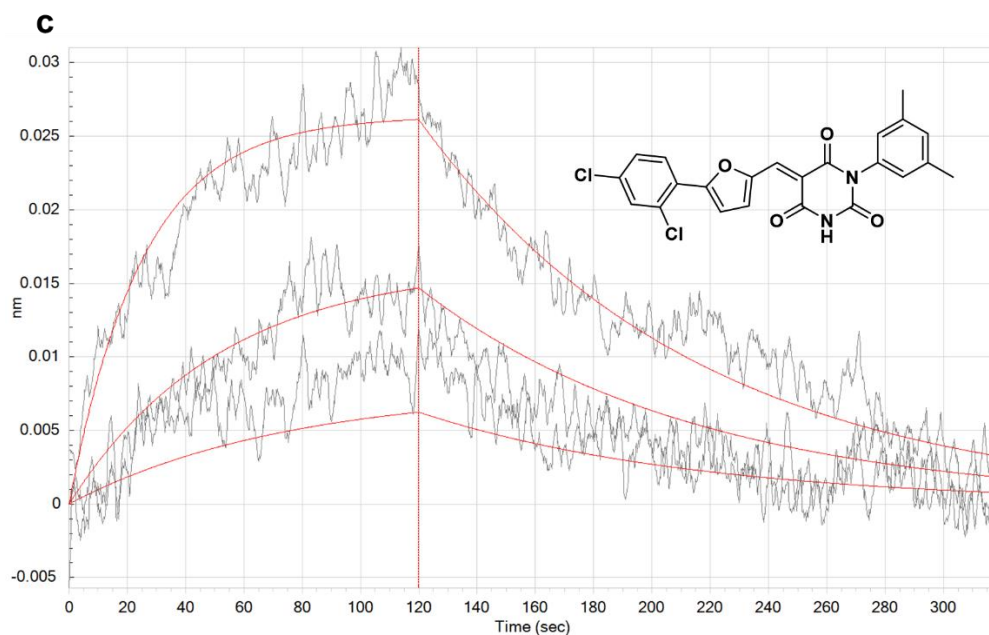


Figure 2.36. The raw and binding data of **PB-3** against PFO. **a.** The raw data of **PB-3** with references. **b.** Association and dissociation curves according to the concentrations of **PB-3**. **c.** 1:1 binding model fitting data and structure of **PB-3**, red lines are 1:1 model and grey for **PB-3** binding.

Table 2.6. The binding kinetics of **PB-3** with statistical parameters of good curve fitting.

Conc. (μM)	Response (nm)	k_{on} ($\text{M}^{-1}\text{s}^{-1}$)	k_{on} Error	k_{off} (s^{-1})	k_{off} Error	K_D (M)	K_D Error	Chi^2	R^2
0.1	0.0100	2.92×10^4	9.78×10^2	1.05×10^{-2}	1.78×10^{-4}	3.59×10^{-7}	1.35×10^{-8}	0.0045	0.9111
0.3	0.0137	2.92×10^4	9.78×10^2	1.05×10^{-2}	1.78×10^{-4}	3.59×10^{-7}	1.35×10^{-8}	0.0045	0.9111
1	0.0293	2.92×10^4	9.78×10^2	1.05×10^{-2}	1.78×10^{-4}	3.59×10^{-7}	1.35×10^{-8}	0.0045	0.9111

The calculated K_D value of **PB-3** with PFO is 359 nM, which is similar to its measured IC_{50} value in the hemolysis assay. More than three concentrations of **PB-3** were attempted but because of huge drift in the signal, it could not be considered in the evaluation of K_D . In addition, in the comparison of k_{on} and k_{off} rates of **PB-3** between PFO and PLY, it was noticed that **PB-3** exhibits relatively faster rates with PFO.

2.3.7. Investigation of aggregation via dynamic light scattering

The BLI findings indicate that there was no binding between **PB-3** and PLY-C428A. Thus, the inhibition of PLY-C428A and ILY at higher concentrations of **PB-3** was nonspecific binding of inhibitor.²⁴¹ **PB-3** can aggregate at higher concentrations, however, aggregates, if there are, between 10 to 20 μM were not visible. Therefore, to confirm aggregation, ascending concentrations of **PB-3** were evaluated via dynamic light scattering (DLS). In case of aggregating small molecules, the diameter of the aggregates is much bigger and it could be increased to several thousand nanometers, depending on the size of aggregates.²⁵¹

PB-3 was tested at four concentrations, it was dissolved in PBS from a DMSO stock solution, and the final amount of DMSO was $\leq 1.5\%$. **PB-3** exhibited a drastic increase in the diameter at 12 μM in comparison to 3 and 6 μM . Similarly, the standard deviation of samples were increased in proportion to diameter. The outcome of this experiment clearly suggested aggregation of **PB-3**. The mean diameter and standard deviations at each concentration is available in the following figure.

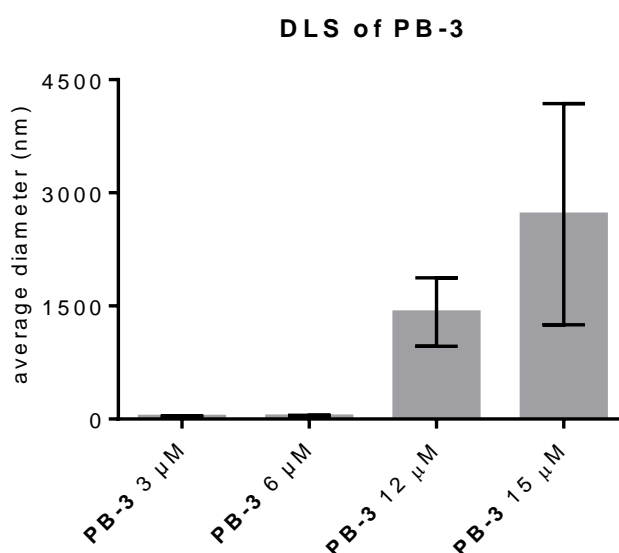


Figure 2.37. The analysis of **PB-3** via dynamic light scattering. **PB-3** shows aggregation at 12 and 15 μM ($n \geq 3$).

Table 2.7. Comparison of diameter increase and standard deviation. Four concentrations of **PB-3** are calculated by column statistics on Graphpad prism.

PB-3 concentration	Mean diameter (nm)	Standard deviation
3 μ M	36.33	1.528
6 μ M	40	11.27
12 μ M	1418	453.9
15 μ M	2717	1468

2.3.8. Summary

BLI is an appropriate method for biophysical evaluation of PB-molecules and CDC. The binding profile of three important inhibitors was calculated. Alongside, to predict the mechanism of PB-molecules, the analysis of different mutant proteins has provided critical information.

PB-1 was the first molecule that underwent BLI evaluation with PLY. **PB-1** has displayed a high non-saturating association and similarly incomplete dissociation. Consequently, the one-to-one model was not an ideal fit in case of **PB-1**. The calculated K_D value of **PB-1** was 85 μ M that is nearly two times of its IC_{50} (~40 μ M). The reason for this divergent value was the atypical binding and that occurred probably due to high drift or covalent interaction between **PB-1** and PLY.

PB-2 was the next inhibitor analyzed. It has not shown abnormally high signals for association and dissociation with PLY and, therefore, it has achieved a much better curve fitting and K_D (3.3 μ M). The K_D value, in the case of **PB-2** was slightly lower than its IC_{50} (~5 μ M). On the other hand, **PB-2** has been qualitatively examined with PLY mutants (PLY-E151Q and PLY-D206R), which have been effectively proved to stop oligomerization. **PB-2** presented a comparable association between PLY-WT and PLY mutants, and these findings establish that binding of **PB-2** with PLY does not depend on E151 and D206. Likewise, **PB-2** exhibited binding with PLY-DM and, hence, excludes the involvement of the cholesterol recognition motif in the binding mechanism.

Thereafter, **PB-3** analysis was commenced with the wild type and cysteine mutant version of PLY. PLY-C428A was employed as a non-binding reference protein in the binding kinetics of **PB-3** and PLY. **PB-3** flaunted a K_D value of 256 nM that was nearly 10-fold lower than its IC_{50} (~3 μ M). Additionally, **PB-3** displayed faster on and slower

off rates. **PB-3** showcased negligible binding with PLY-C428A in comparison to PLY-WT and decisively proved that C428 is a critical amino acid in binding of the inhibitor. This discovery is in accordance with the finding of the hemolysis assay. Afterward, the binding profile between **PB-3** and PFO was investigated. The analysis window of **PB-3** was selected between 0.1–1 μM , since at higher concentrations of **PB-3**, an abnormal drift of signals was recorded. The K_D value of **PB-3** obtained in this experiment is 359 nM, which is nearly identical to its IC_{50} ($\sim 0.3 \mu\text{M}$).

PB-3 was analyzed at various concentrations via DLS to investigate aggregation. **PB-3** showed aggregation at 12 and 15 μM , and indirectly substantiate that the residual activity of **PB-3** measured at higher concentrations ($\geq 10 \mu\text{M}$) is due to aggregation.

2.4. Investigation of pore formation blockade in CDC by PB-molecules via cryo-transmission electron microscopy (cryo-TEM)

Cryo-TEM is a form of transmission electron microscopy involving analysis of samples at cryogenic/very low temperatures.^{28,42} It has been more than a decade since the pore formation associated with CDC has been under investigation by employing cryo-TEM and this unveiled multiple mechanistic details of CDC.^{28,42,252}

Here, cryo-TEM was employed as a technique to investigate, how PB-molecules inhibit pore formation by CDC. Since CDC-induced pore formation in lipid membranes includes multiple steps, e.g. membrane entry, pre-pore, late pore formation etc.,²⁵³ these steps can be recognized by cryo-TEM.²⁸ Therefore, it was rational to analyze the influence of PB-molecules on pore formation by cryo-TEM and elucidate which step they hinder or at which stage there interfere with pore formation. This was a unique experiment because to date no one has reported any study of CDC-inhibitor investigated by cryo-TEM. PLY was used as archetypical CDC and **PB-2** was selected among PB-molecules to investigate the blockade of pore formation. To mimic the biological lipid membrane, cholesterol-containing liposomes were prepared according to previously reported studies.²⁰⁹

The assay was planned and designed in our lab and, at first, a protocol for preparation of liposomes was established, which was in accordance with the earlier reports.²⁸ Later, the samples were prepared for inspection under cryo-TEM. Ali Saoud, the master student of our group, prepared liposomes and samples under supervision. Dr. Christoph Böttcher at the Research Center of Electron Microscopy of Freie University Berlin executed Cryo-TEM and finally he and Dr. Kai Ludwig did cryo-electron tomography (Cryo-ET).

In principle, three categories of samples were prepared and optimized for cryo-TEM; liposomes only, PLY with liposomes and PLY + **PB-2** on liposomes. The size and concentration of liposomes were critical for the experiment. Thus, after various meticulous attempts, a suitable size (100 nm) and proper concentration of liposomes (2 mM) were selected. In the **Figure 2.38**, a homogenous distribution of 2 mM liposomes can be visualized with an average size of almost 100 nm.

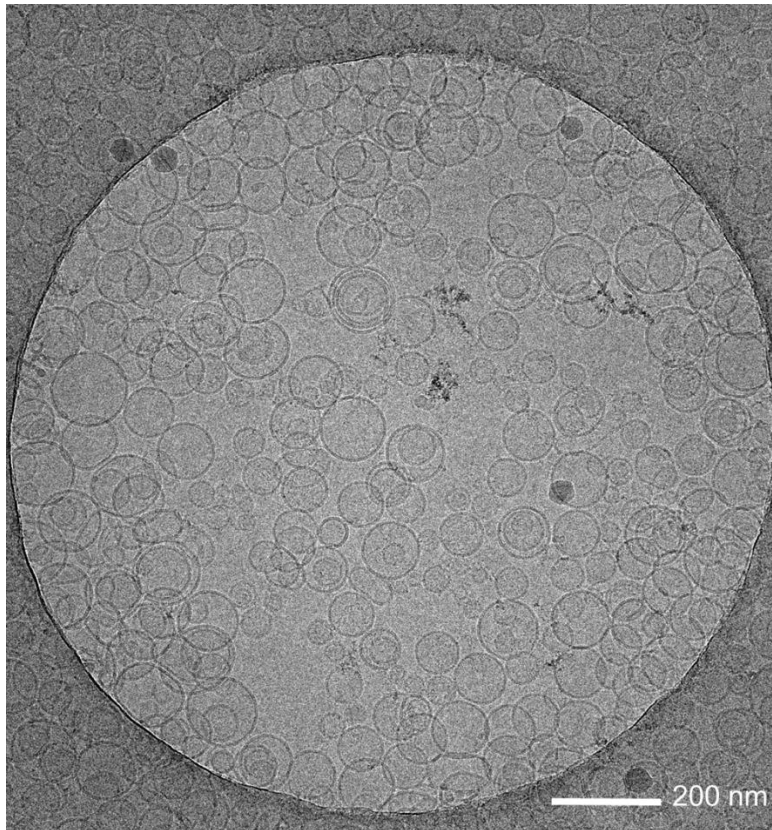
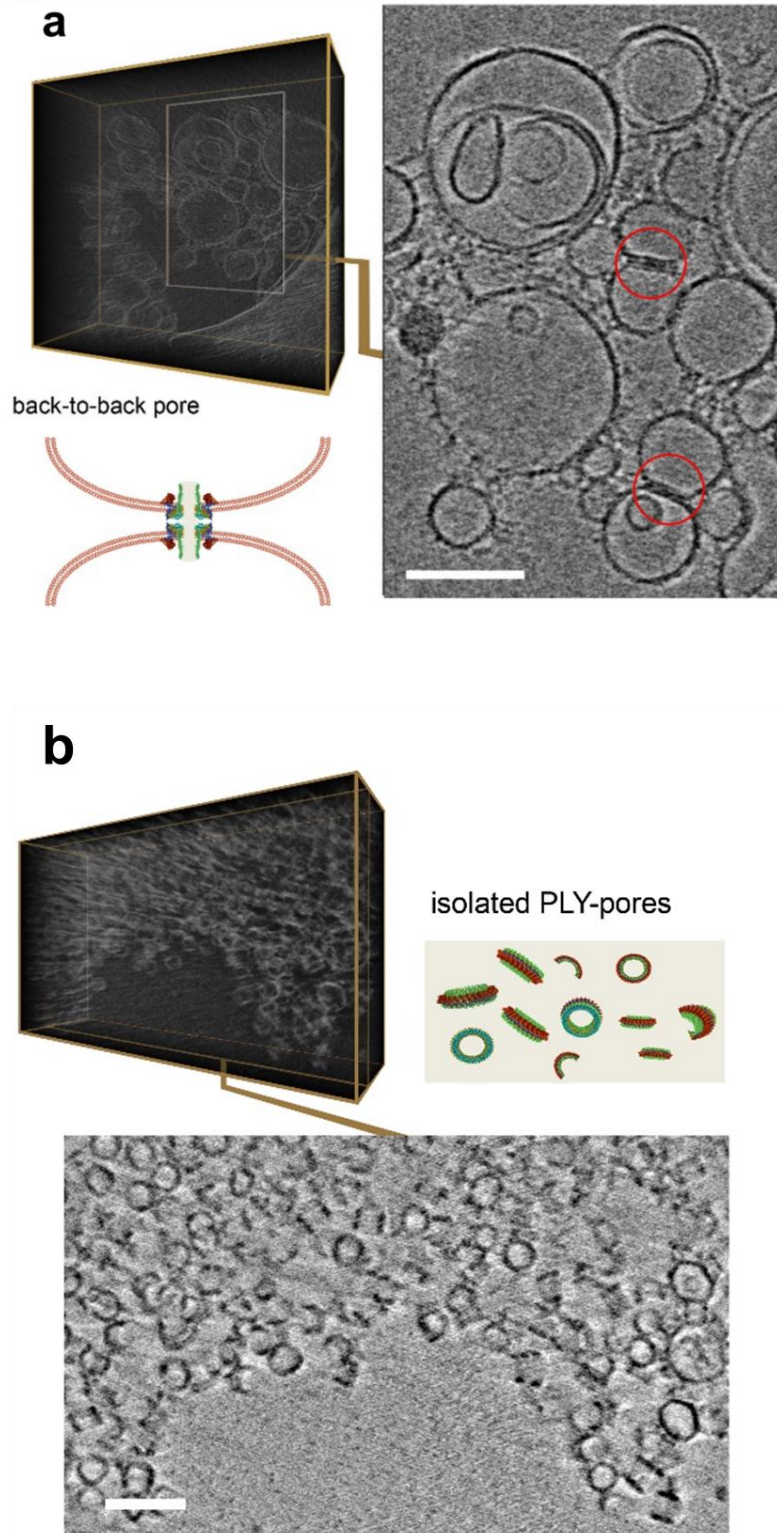


Figure 2.38. A homogenous mixture of unilamellar liposomes, containing 70 % of cholesterol and 30 % of phosphatidylcholine (DOPC).

Like liposomes, concentration of PLY was essential for an optimal outcome and it was observed that 1 mg/ml of PLY was sufficient to reveal the pores on liposomes without aggregation of protein. When PLY was added to liposomes, the formation of pores was observed and it was complementary to the previously reported studies.²⁸ In addition, clusters of liposomes were noticed because of protein-protein interactions between membrane-integrated protein of two adjacent liposomes. This phenomenon was named as back-to-back pore formation as highlighted in **Figure 2.39 a**.²⁵² Furthermore, liposomes were solubilized by using mild surfactant (Amphipol-35) and the oligomerized PLY-pores were exposed and captured. The tomogram of isolated PLY-pores generated via cryo-ET¹⁷³ is available in **Figure 2.39 b**.

If **PB-2** and PLY were pre-incubated before adding them to liposomes, there was no integration of protein on liposomal membranes observed and consequently back-to-back pore formation was absent. The liposomes were detected intact and were homogeneously distributed throughout the sample volume. PLY was blocked under

the influence of **PB-2** and aggregates of PLY were noticed and highlighted as free suspended particles in the same sample volume.



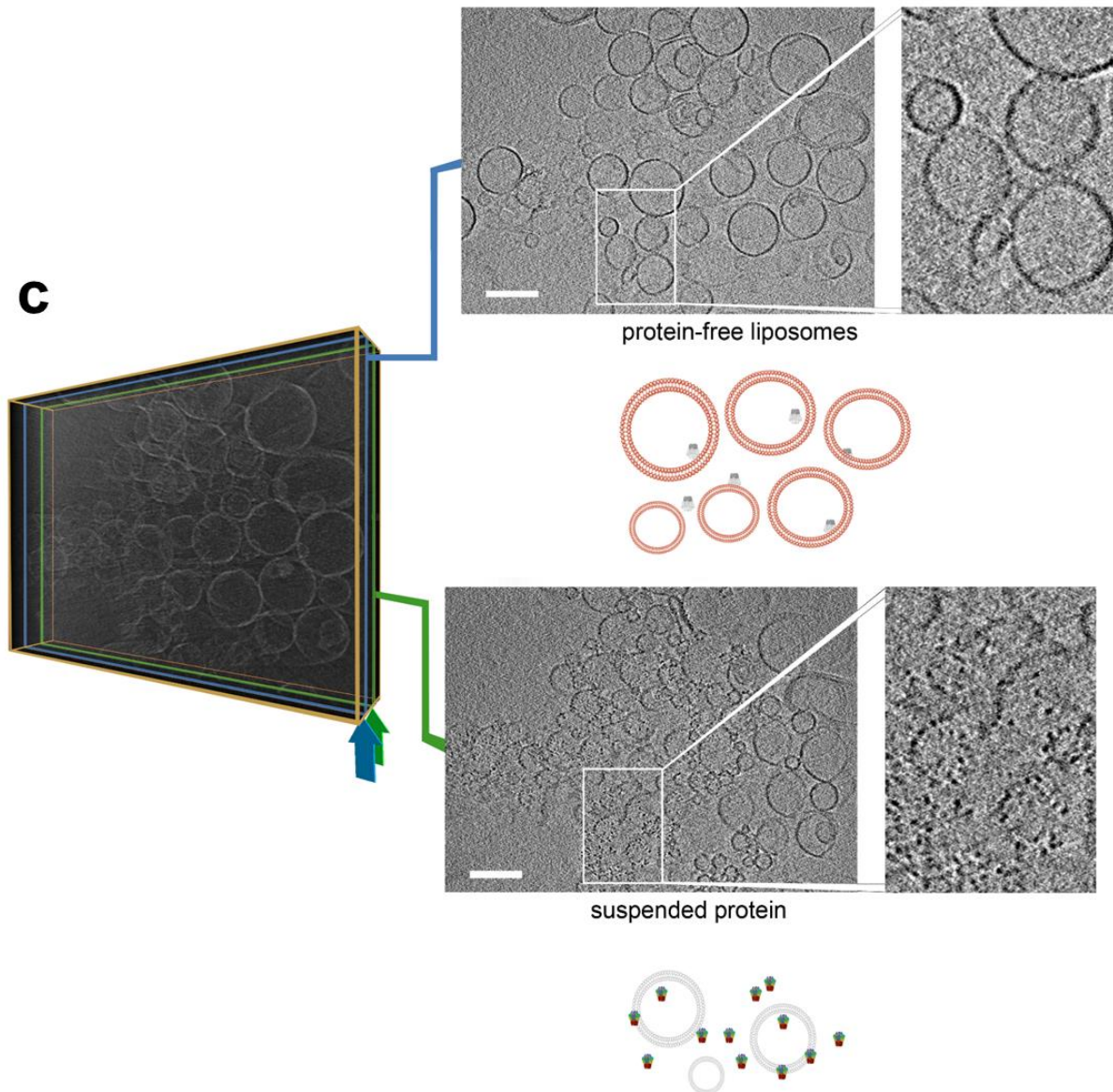


Figure 2.39. The Cryo-TEM analysis of inhibitor.

a. Cryo-ET of PLY treated liposomes sample: The left image is the reconstructed 3D volume (vortex presentation) of the sample and the right image is a section of central stack of 20 combined slices from 3D volume containing highlighted examples of PLY-induced back-to-back pore formation.²⁵² **b.** Cryo-ET of isolated PLY-pores: Top: Reconstructed 3D volume of solubilized liposomes. Bottom: Central accumulated stack of 20 slices from the 3D volume showing protein pores formed by oligomerization of PLY monomers in different orientation. **c.** Cryo-ET of PB-2 containing sample: A central stack of 20 accumulated slices (position corresponds to the blue frame in the 3D volume on the left) shows smooth vesicle membranes (top image and enlarged detail). A near-surface stack of 20 accumulated slices (position corresponds to the green frame in the same 3D on the left) shows suspended PLY particles not integrated in liposomal membranes. (scale bars shown in **a**, **b** and **c** correspond to 100 nm).

2.4.1. Summary

Cryo-TEM has been applied to visualize and demonstrate the mechanism of PB-molecules. **PB-2** was selected as a representative of PB-inhibitors. Such a method was not available for evaluation of CDC in

inhibitors, thus, the first challenge was the establishment of a protocol.

First of all, cholesterol-containing liposomes with a suitable size, i.e. 100 nm (avg. diameter), which are imperative for analysis of CDC, were successfully synthesized. Afterwards, the appropriate concentrations of toxin (1 mg/ml) and liposomes (2 mM) were aligned to detect the pore formation. Protein integration into the membrane of liposomes was detected and aggregation of liposomes due to protein-protein interaction was noticed as well. Moreover, isolated pores of PLY have been successfully captured by treating the sample of toxin and liposomes with Amphipol-35.

When the inhibitor (**PB-2**) was included in the sample of PLY and liposomes, the pore-forming ability of PLY was abrogated, and precipitates of insoluble protein were found suspended in the sample. Simultaneously, the liposomes were found widely distributed throughout the sample volume with no signs of protein aggregation. This outcome unveiled that in presence of the inhibitor (**PB-2**), PLY was unable to attack the membrane. Hence, this outcome implies that **PB-2** hinders the membrane-binding ability of PLY. Therefore, the probability that PB-inhibitors effect the oligomerization of the protein, as proposed in the computational studies, is minimal in the light of evidence provided by Cryo-ET.

2.5. Investigation of protein-ligand complex via mass spectrometry

Protein mass spectrometry was applied to investigate the inhibitor-protein binding. Since the role of PLY-C428A in terms of potency of PB-molecules, or more precisely **PB-3**, was established via hemolysis and BLI assays, a comparison of PLY and PLY-C428A with respect to binding **PB-3** would further substantiate the critical nature of the C428 mutation.

2.5.1. Native MS

The widely accepted scenario for analyzing the protein-ligand complex would be through native MS, however, in the case of PLY, it was dubious due to the presence of 50% glycerol in the buffer (20 mM MOPS, pH 8) of PLY. The hydrophobic nature of PLY compelled the addition of high percentage of glycerol to prevent precipitation. Nevertheless, to attempt MS under native MS conditions, buffers of both PLY and PLY-C428A were replaced with 10 mM ammonium acetate by a dialysis cassette. Despite the rigorous buffer exchange, when PLY was evaluated in native conditions, the MS spectra exhibited numerous additional masses that were still attached to the protein and corresponded to MOPS buffer salts, glycerol and a few were unknown (Supplementary Information). The protein (PLY) underwent aggregation in the ammonium acetate buffer, which was confirmed by the significant reduction of protein concentration after spinning.

2.5.2. Classical or denaturing MS

The masses of PLY and PLY-C428A were confirmed during the quality control of the protein expression in a buffer that contained acetonitrile-water in 1:1 ratio. Hence, there was an established robust method in our lab to record the deconvoluted protein spectrum. The major challenge was the stability of the protein-ligand complex in denaturing conditions.

A sample of **PB-3** and PLY, 6 μ M each, was prepared in acetonitrile-water and loaded on LC-QTOF-MS. A broad protein mass peak was obtained through deconvolution. The experiment was repeated twice and similar peaks were observed. In contrast, the protein without inhibitor (control) sample showed normal protein mass (**Figure 2.40 a**). Later, the prudent scrutiny of the peaks unveiled that the peak was starting in the

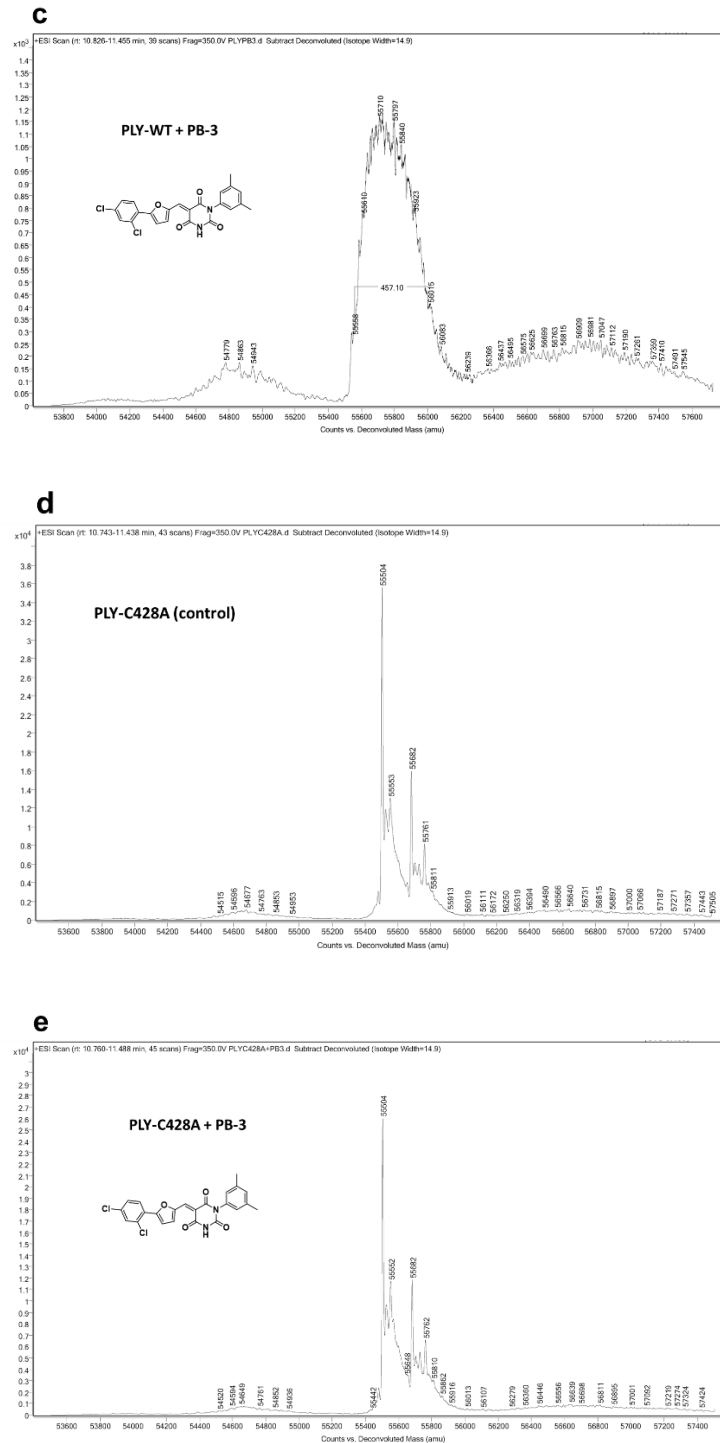


Figure 2.40. Deconvoluted spectra of proteins with **PB-3** and without (as control) in denaturing conditions.

a. PLY control sample, the main peak corresponds to exact protein mass. **b.** PLY with **PB-3** 6 μ M each, exhibit broadening of the protein-peak, which implies an instable protein-ligand complex that disintegrate partly during ion acceleration. **c.** The width of broad peak of protein-ligand complex is approx. same as the inhibitor mass. **d.** PLY-C428A control highlights protein mass peak. **e.** PLY-C428A with **PB-3** showcase identical spectra to control, and the main peak correspond to protein mass. The outcome suggests no binding interaction between PLY-C428A and **PB-3**. (Here, data are one of $n = 3$)

2.5.3. Summary

Mass spectrometry was adopted to investigate details of protein-inhibitor binding, especially in regard to binding between **PB-3** and PLY-C428A. Since **PB-3** showed activity against PLY-C428A in biological assays at higher concentrations, whereas in BLI, PLY-C428A was unable to engage PLY-C428A, this method had a critical value with respect to the cysteine mutant version of PLY.

The most preferred way to analyze protein-ligand binding is native MS, thus we have attempted analysis of the protein-inhibitor complex in native conditions. However, due to instability of proteins in the ammonium acetate buffer, analysis could not be executed under native conditions.

Next, classical or denaturing MS conditions were employed to investigate protein-inhibitor complexes. Peaks in the control sample of PLY and PLY-C428A were coherent, and the main peak of each spectrum corresponded to the protein mass. Whereas, when PLY and PLY-C428A samples with **PB-3** in a 1:1 ratio were analyzed, only PLY exhibited significant change in the spectrum, and PLY-C428A spectrum was detected as identical to PLY-C428A control.

Although the peaks in the PLY-**PB-3** sample were not clear and rather a broad peak was observed that started near protein mass and extends up to protein plus inhibitor mass on the spectrum. The inference made out of this anomalous peak was that, since **PB-3** interacts via covalent interaction with PLY, therefore, a stable complex of PLY-**PB-3** could be present in the sample when loaded. Afterward, it underwent partial disintegration during acceleration of molecular ions and consequently, massive ions were detected by the detector, which, after deconvolution, ranged between the PLY mass and PLY-**PB-3** complex mass.

2.6. Cellular testing of PB-inhibitors in lung cells

The advanced cellular environment was the next level of testing CDC inhibitors being more sophisticated and complex than the hemolysis assay. Inhibitors will be used to block a CDC/PLY in living cells, where the safety and efficacy will be analyzed. PLY is associated with fatal cellular and organ pathogenicity in lungs and other tissues during pneumococcal pneumonia.²⁰ Therefore, to validate the effectiveness of PB-inhibitors against the cytotoxic effects of PLY, immortalized human alveolar basal epithelial cells (A549-cells) were selected.²⁰⁶ The A549 cell line was a gift from our collaborator Prof. Dr. Andreas Hocke of Charite.

The lactate dehydrogenase (LDH) assay was chosen to estimate the PLY-induced cellular deterioration, out of numerous available cytotoxic assays. In cells, PLY-mediated pore formation leads to discharge of LDH in the extracellular fluid and, by quantification of released LDH, toxicity could be analyzed.

2.6.1. Introduction to lactate dehydrogenase (LDH) assay

Lactate dehydrogenase (LDH) belongs to the class of oxidoreductases. It is abundant throughout the body tissues and a non-specific marker in many pathological conditions such as liver disease, heart attack, cancers, infections etc. if found extracellularly.²⁵⁴

Concerning measuring cytotoxicity, the LDH coupled with enzymes provides a reliable colorimetric quantification. Since LDH is a cytosolic enzyme and when the plasma membrane damage under the influence of CDCs causes discharge of LDH,²²³ extracellular LDH can be quantified via coupled enzymatic reaction. LDH converts lactate to pyruvate and simultaneously NAD^+ is reduced to NADH, which subsequently reduces a tetrazolium salt (INT) to a red formazan product catalyzed by the enzyme diaphorase (**Figure 2.41**). Finally, the red formazan can be measured and quantified at 490 nm. The formazan dye obtained is directly proportional to LDH released into the medium, which is indicative of cytotoxicity.

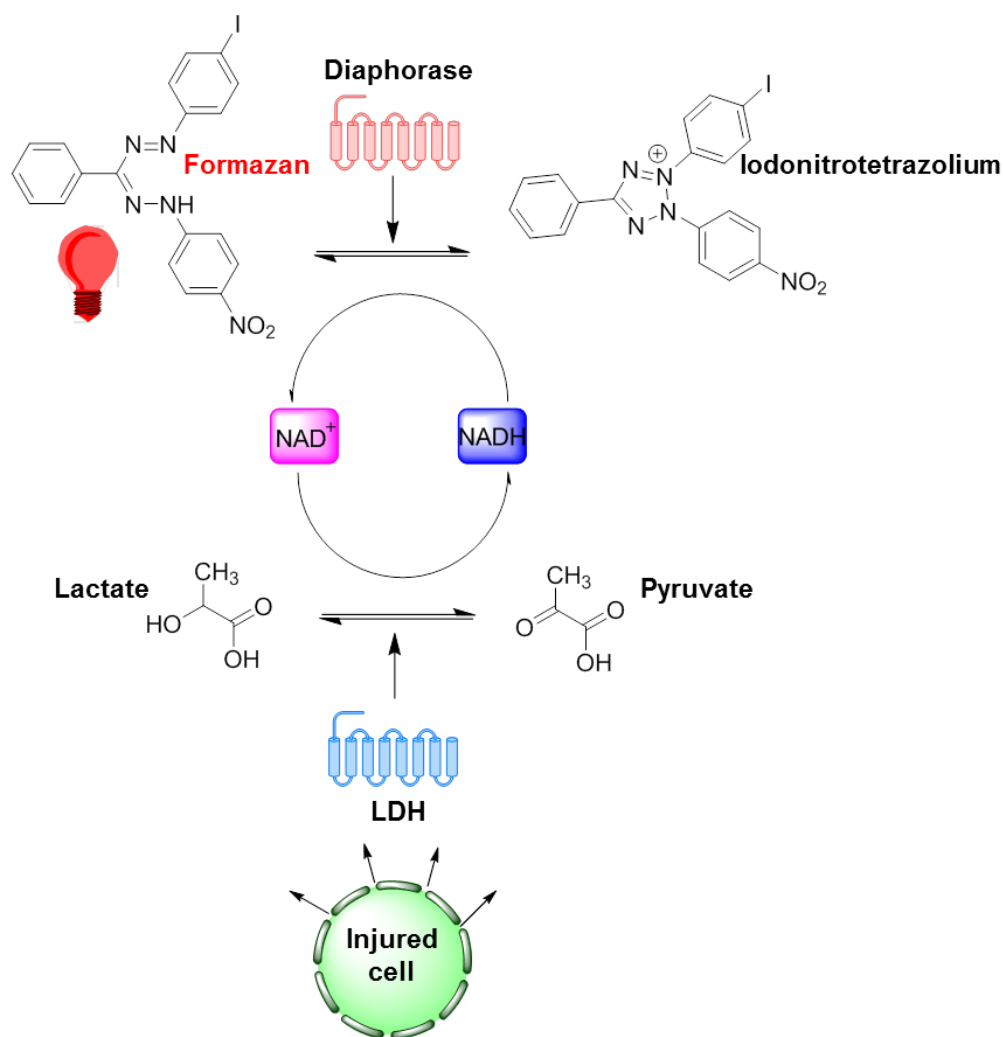


Figure 2.41. The reaction mechanism of the LDH assay.

2.6.1.1. Analysis of PB-1

The human alveolar basal epithelial cells were grown in a 96-well plate using Ham's F12 culture medium, including 10% fetal calf serum (FCS). Three concentrations (25, 50 and 100 μM) of **PB-1**, in the range of the previously known IC_{50} value, were chosen for inhibition of PLY. When tested for the first time, **PB-1** was incapable of blocking cytolytic effects of PLY at all concentrations. These findings were not anticipated, and the experiment was repeated with a modified layout. The experiment was altered using a 12-well plate instead of a 96-well plate because, with bigger wells, it was more convenient to observe cells under the microscope during the testing. Hence, the microscopic observation revealed that there were precipitates/aggregates in **PB-1** formed in all samples (**Figure 2.41 a**), whereas samples without **PB-1**, like the negative (only cells) sample and PLY sample, did not contain any precipitation. The outcome of

the microscopic intervention clearly suggested that **PB-1** was not soluble in the cell culture medium.

Solubility optimization. To enhance the solubility, a non-toxic and non-ionic surfactant polysorbate-20, commonly known as Tween-20 (0.05%)²⁵⁵ was included in the cell culture medium to dissolve aggregates of **PB-1**. It worked at first and the **PB-1** precipitates were solubilized in the medium. Consequently, **PB-1** displayed a time-dependent inhibition of PLY up to 1 h (Supplementary Information). However, after one hour, Tween-20 started damaging cells, thus, it could not be used further in the assay.

Next, PBS was added to the system to replicate the pre-incubation step of the hemolysis assay. Since PBS is a physiological buffer and does not harm the cells,²⁵⁶ PBS (10%) was introduced in the assay to enhance the solubility of **PB-1**. In this optimized protocol, all samples were pre-incubated for 10 min in PBS (i.e. 100 μ l = 10% of the assay volume) before pouring them into media containing cells. Unfortunately, this move did not prove beneficial and yet, there were still precipitates in the **PB-1** samples.

Later, the interplay of DMSO content within the assay was attempted. **PB-1** was soluble in DMSO up to 20 mM and was soluble in PBS as well. Keeping this as reference, the DMSO stock concentration of **PB-1** was adjusted to increase the final DMSO content of the assay. The DMSO stock solution of **PB-1** was reduced from 20 mM to 10 mM and a corresponding rise in the final DMSO content from 0.5 to 1%. In correlation, there was slight improvement detected in the solubility of **PB-1**. Hence, the stock concentration was further reduced to 5 mM and consequently the final DMSO increased to 2% and at this point, **PB-1** was completely dissolved in the medium at 100 μ M. The acceptable range of using DMSO in cellular assays is 3-5%, therefore, there is no harm in using 2% DMSO in the assay and as expected, A549 cells remained healthy with 2% DMSO in the medium. Cells along with the solubility comparison of **PB-1** between 0.5 and 2 % DMSO are displayed in **Figure 2.42 b**.

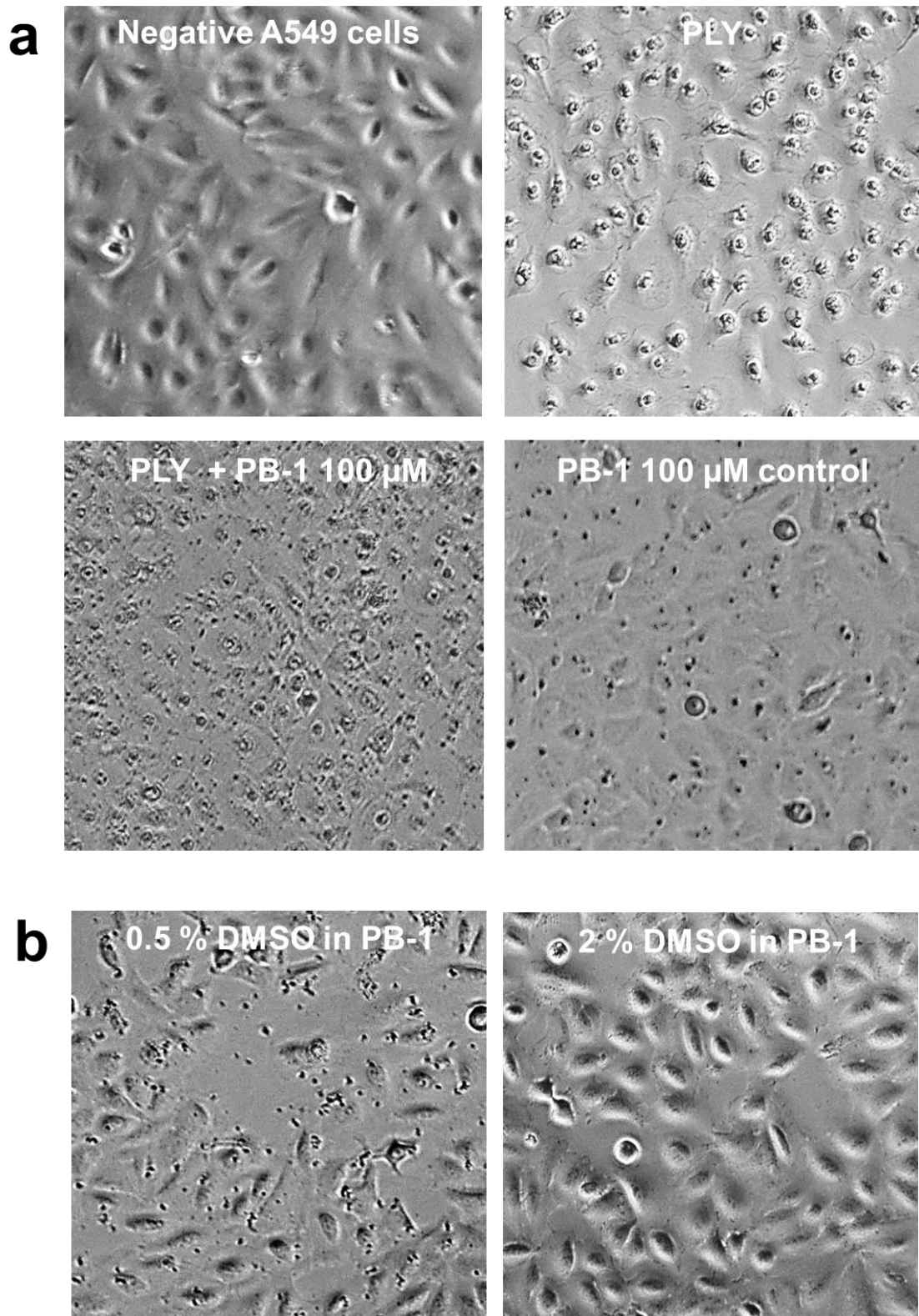


Figure 2.42. Solubility optimization of **PB-1**.

a. Human lung cells without solubility optimization, **PB-1** samples contain precipitates.
b. Cells with **PB-1** containing 0.5 and 2% DMSO, 2% DMSO sample is without aggregates (Micrographs are captured by EVOS FL digital imaging system).

After improvement of **PB-1** solubility, cells were seeded in the 12-well plate and once they achieved confluence, medium was replaced from 10% to 2% FCS. Samples of **PB-1** with PLY and PLY alone samples in combination with their respective controls were added to the cells after the pre-incubation in PBS. The controls included negative control/healthy cells, positive control was 5% Triton X-100 and the inhibitor control was **PB-1** (100 μM). The supernatants were aspirated after 4 h and 24 h, respectively, and cytotoxicity was analyzed. A concentration-dependent inhibition of PLY was shown by **PB-1** over the course of 24 h and at 100 μM more than 95% of the cytotoxicity of PLY was inhibited. In addition, micrographs of cells were captured after 24 h clearly showing necrotic cells and healthy cells (**Figure 2.43 c**).

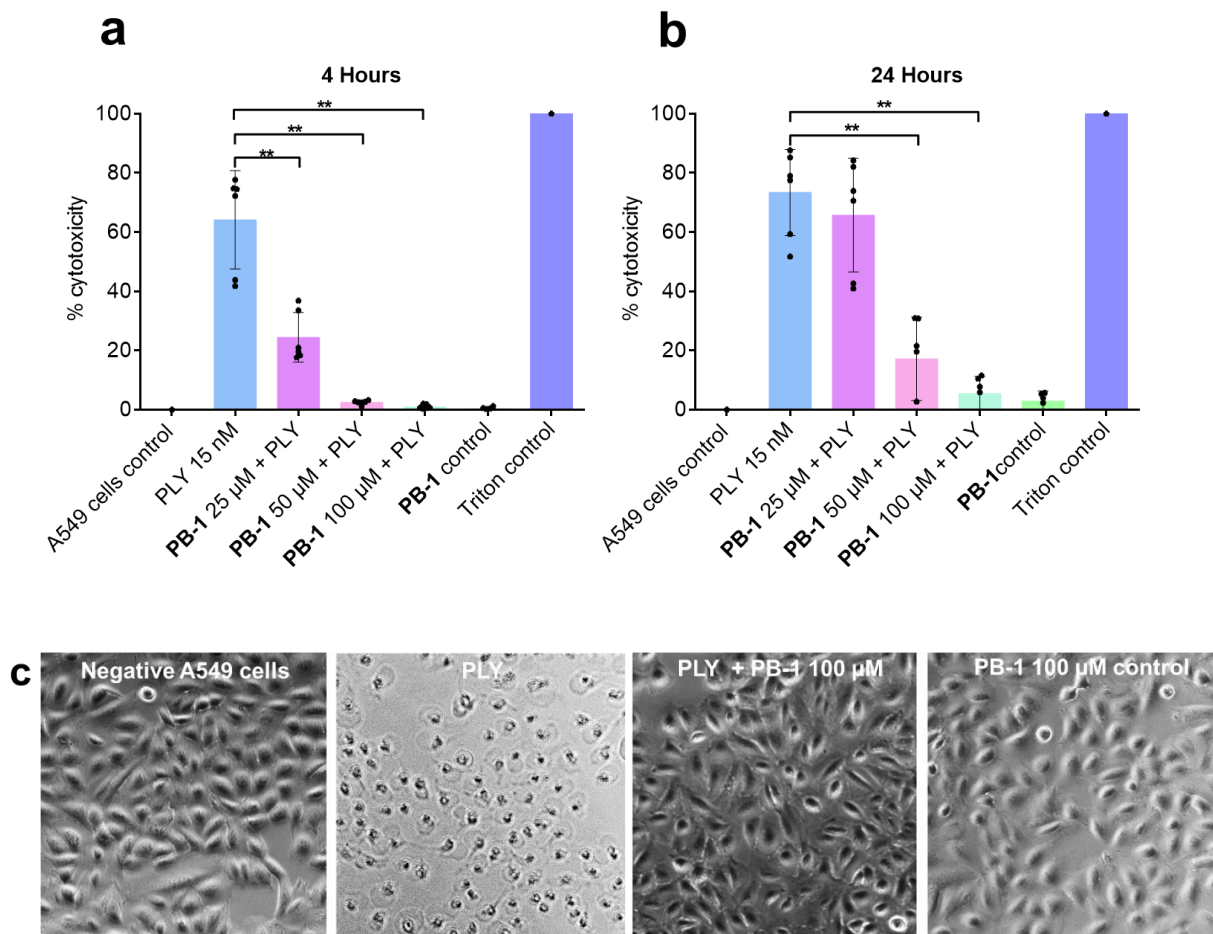


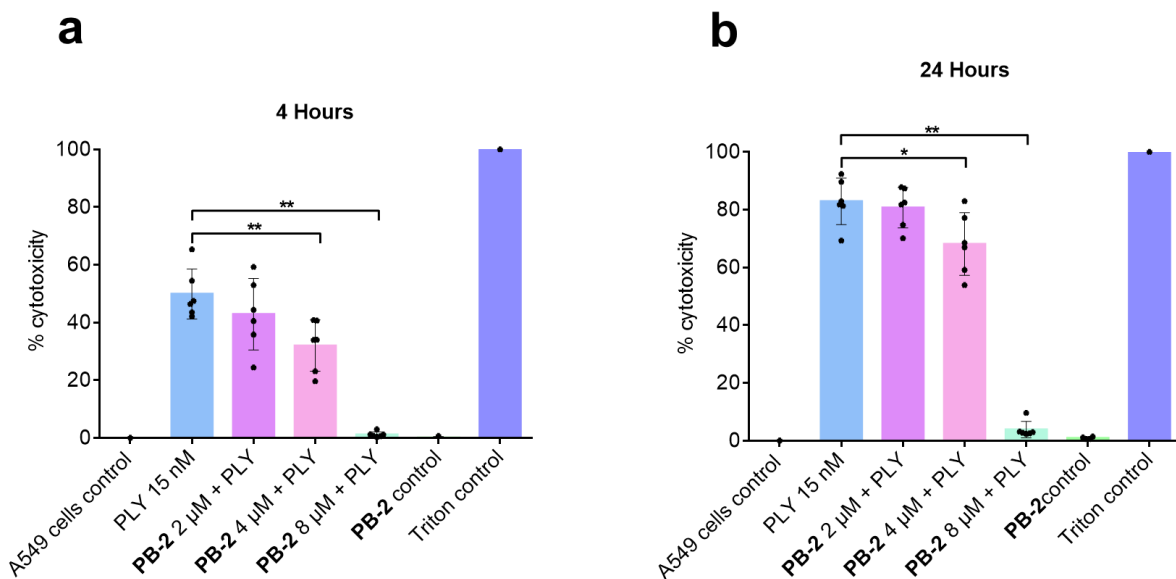
Figure 2.43. Cytotoxicity analysis of PLY with **PB-1**.

a and **b**. **PB-1** prevents human alveolar epithelial cells from PLY-associated impairment in a concentration dependent manner. Samples include controls (positive and negative), PLY alone and PLY with **PB-1** (25, 50 and 100 μM). Graphs quantify LDH release as percent-cytotoxicity after 4 h and 24 h. To evaluation statistical significance Mann Whitney test is applied ($n \geq 6$, $**p = 0.0022$ and error bars represent \pm S.D.). **c**. Micrographs showing healthy cells for negative, **PB-1** 100 μM + PLY and **PB-1** control samples.

2.6.1.2. Analysis of PB-2

The inhibitory potential of **PB-2** was validated via the LDH assay. It was tested against PLY in an order of ascending concentrations (2, 4 and 8 μM) using lung epithelial cells as a substrate. Like **PB-1**, the concentrations of **PB-2** chosen for analysis were roughly based on IC_{50} ($\sim 5 \mu\text{M}$) of **PB-2** in the hemolysis assay. The experiments were conducted on a 12-well plate, which was inspected under the microscope simultaneously. At the beginning of testing, it was detected under the microscope that **PB-2** was not able to dissolve in the cell culture medium. Therefore, similar to **PB-1**, this solubility problem was resolved by mimicking the pre-incubation in PBS step of the hemolysis assay. All samples of **PB-2**, PLY and their controls were incubated in 10% of PBS for 10 min at room temperature prior to adding them to the cells. The remaining experiment was completed according to the procedure mentioned for **PB-1**.

PB-2 was found to alleviate PLY-mediated cellular injury after 4 h and 24 h time intervals. The highest concentration of **PB-2**, i.e., 8 μM successfully reduced 95% of the LDH activity associated with cellular damage. The LDH activity of each sample was measured and plotted onto a graph by employing GraphPad Prism. Micrographs captured after 24 h were also in correlation to the calculated cytotoxicity showing that **PB-2** starting at 2 μM continued to protect the lung epithelial cells and at 8 μM almost 95% of LDH release was minimized.



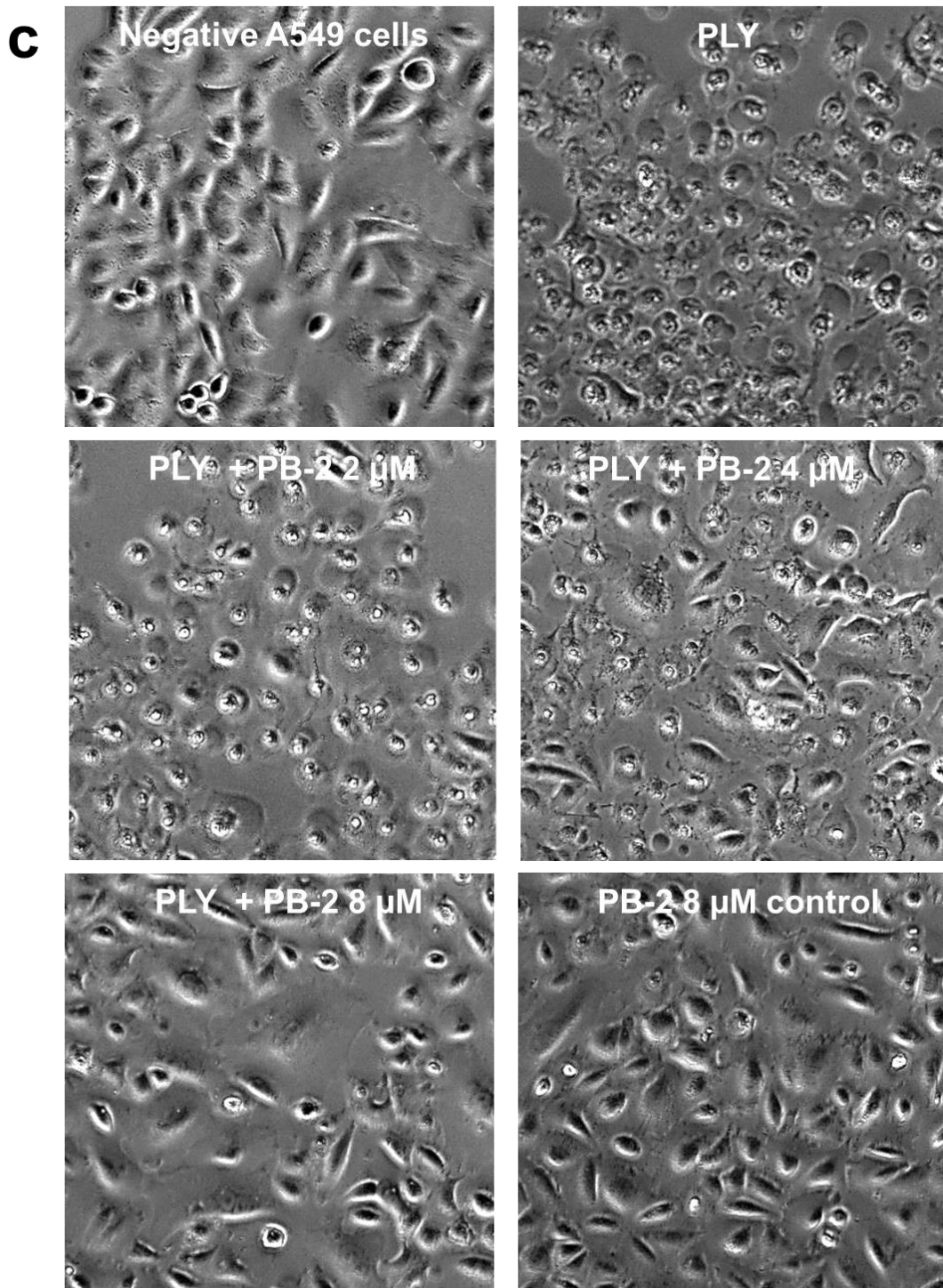


Figure 2.44. Cytotoxicity analysis of PLY with **PB-2**.

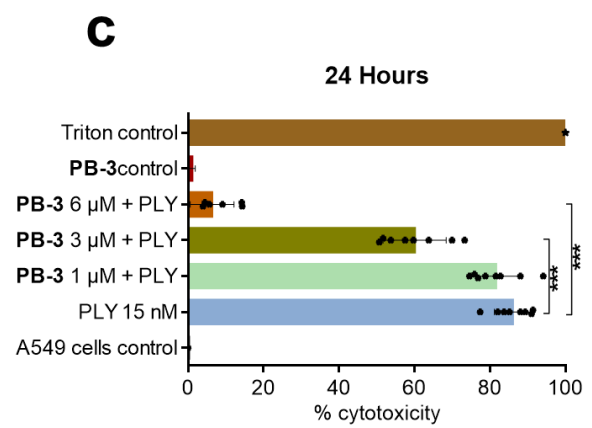
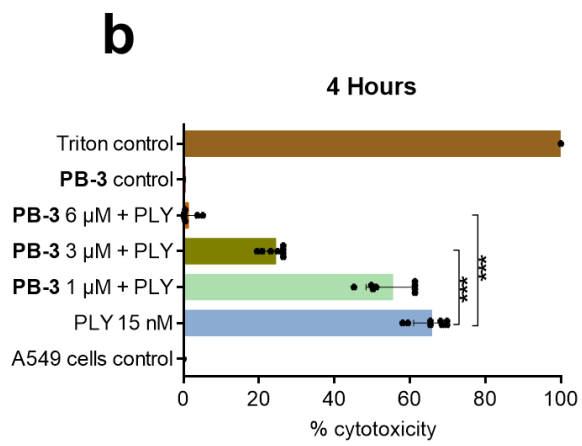
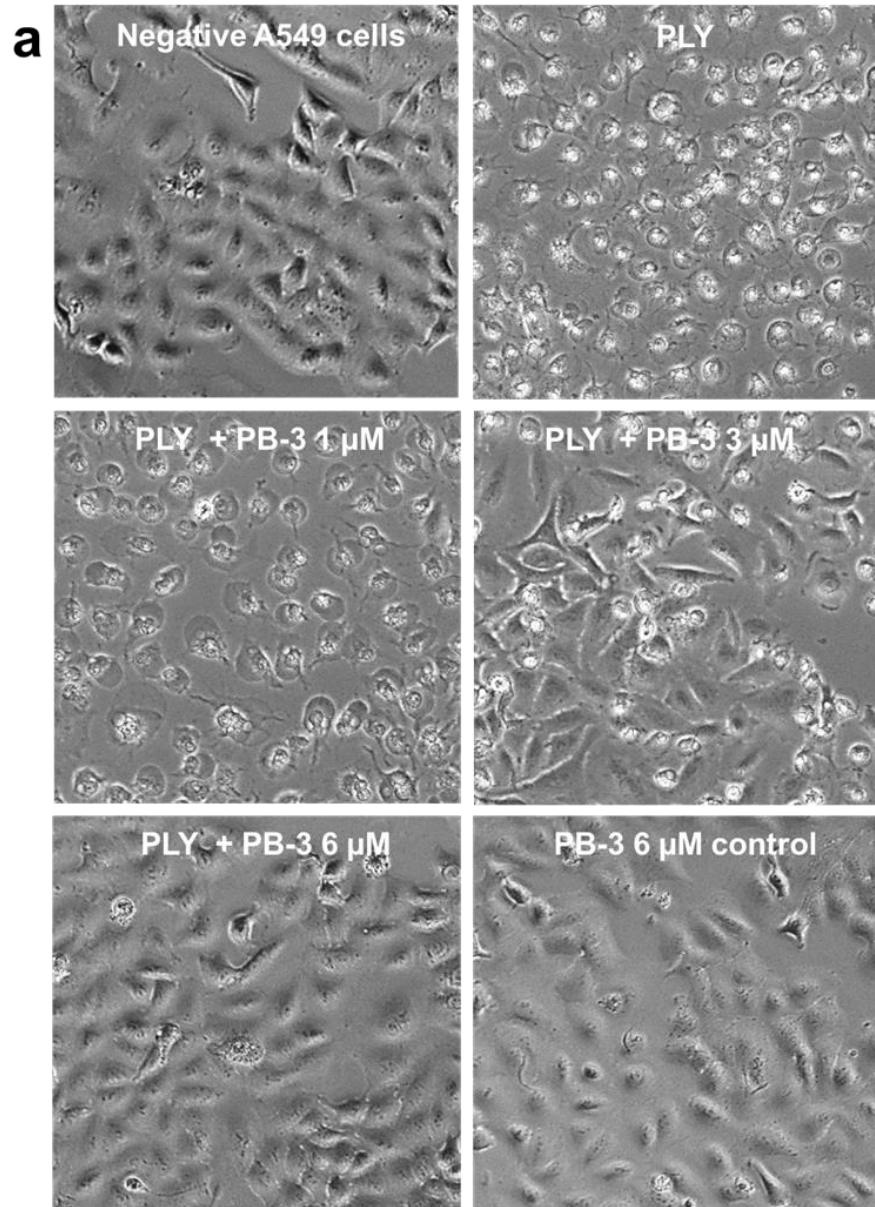
a. The LDH activity of **PB-2** samples with control samples after 4 h. **b.** After 24 h, the cytotoxicity graph showing highest inhibitory effects of **PB-2** at 8 μM . The statistical significance for both c and d, is calculated by Mann Whitney test ($n \geq 6$, $*p = 0.0411$, $**p = 0.0022$ and error bars represent \pm S.D.). **c.** Micrographs highlighting the protective effect of **PB-2** against PLY in an ascending concentration manner.

2.6.1.3. Analysis of PB-3

PB-3 is the best inhibitor among PB-molecules in the hemolysis assay. It was superior in terms of potency, stability in PBS, and solubility. Therefore, the solubility of **PB-3** was tested within the cell culture medium and it was discovered that **PB-3** was better dissolved in medium than **PB-1** and **2**. Although **PB-3** seemed soluble in the cell culture medium yet, in order to be consistent with **PB-1** and **2** experiments, it was decided to pre-incubate all samples, at least in two experiments, for 10 min in PBS. In this way, a difference, if there is any, could be observed between pre-incubated in PBS and standard LDH assay. Next, similar to **PB-1** and **2**, three concentrations of **PB-3** (1, 3 and 6 μM) were selected in connection to the IC_{50} ($\sim 3 \mu\text{M}$) in the hemolysis assay.

The standard protocol was followed in more than three experiments and the pre-incubation step was included in three experiments. The LDH release of all samples was determined first at 4 h and then after 24 h. **PB-3** inhibited PLY significantly at 3 and 6 μM and the LDH release was minimized more than 90% at 6 μM . There was no difference observed between the PBS pre-incubated experiments and standard experiments. In addition, micrographs were captured after 24 h and those were in perfect synergy with the cytotoxicity data and are shown in **Figure 2.45 a**. The cytotoxicity data were compiled and plotted using GraphPad Prism (**Figure 2.45 b & c**).

Stability of PB-3 in LDH assay. The stability of **PB-3** was determined by customizing the existing protocol of the LDH assay. As per findings of the hemolysis assay, **PB-2** underwent an immediate retro-Knoevenagel condensation in PBS with a significant loss in activity, however, **PB-3** appeared to be more stable than **PB-2** in the hemolysis assay. Thus, it was assumed that **PB-3** might exhibit a better stability in the LDH assay. Therefore, the stability of **PB-3** alone was investigated in the LDH assay by modifying the PBS pre-incubation step. **PB-3** (6 μM) was pre-incubated alone for 20 min in PBS. Then, PLY was added to the sample and the rest of the experiment was performed according to the standard protocol. The pre-incubated samples of **PB-3** were detected stable and active after pre-incubation alone for 20 min. This outcome further validated the superior stability of **PB-3**.



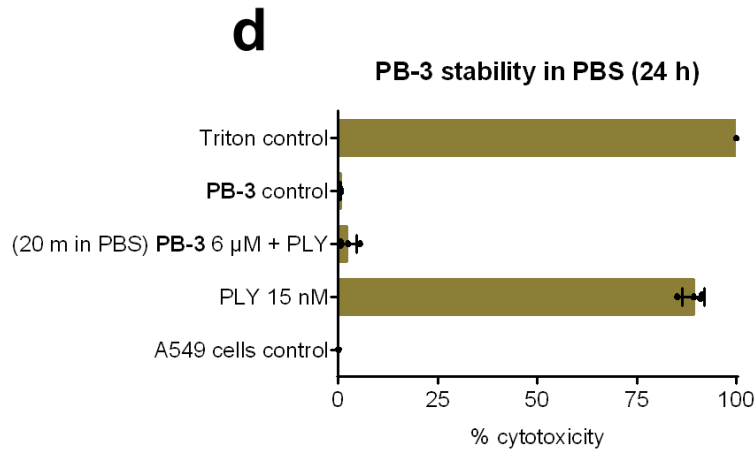


Figure 2.45. Cytotoxicity analysis of PLY with **PB-3**.

a. Micrographs display **PB-3** associated inhibition of PLY. **b.** The cytotoxicity data of **PB-3** after 4 h, showing significant inhibition at 4 and 6 μ M respectively. **c.** The LDH release after 24 h, the graph presents minimal LDH release at 6 μ M of **PB-3**. The statistical significance for both **c** and **d**, is calculated by Mann Whitney test ($n \geq 6$, $***p = 0.0002$ and error bars represent \pm S.D.). **d.** The stability of **PB-3** in PBS, **PB-3** (6 μ M) is active in the LDH assay after 20 min alone incubation in PBS, as shown by sample (20 min in PBS) **PB-3** 6 μ M + PLY. The data are determined after 24 h and $n \geq 3$.

2.6.1.4. Analysis of PLY-C428A

PLY-C428A was the only mutant of PLY that was active in the hemolysis assay and **PB-3** was unable to block PLY-C428A up to 10 μ M. However, if concentration of **PB-3** was increased, it inhibited PLY-C428A and at 16 μ M, nearly 90% of hemolysis was blocked. The activity of **PB-3** at higher concentration was thought to be an effect of aggregation. Since it was known that **PB-3** had limited solubility in PBS (10-20 μ M). Therefore, to validate these findings, PLY-C428A was further subjected to the LDH analysis. In the first three experiments, 6 μ M of **PB-3** was tested against PLY-C428A. All samples were incubated in cells for 24 h before calculating the cytotoxicity. **PB-3** was unable to block PLY-C428A.

Afterwards, the next round of experiments was conducted and **PB-3** was used up to 16 μ M against PLY-C428A. The cytotoxicity of samples was measured for 24 h. **PB-3** inhibited ~80% of PLY-C428A at 16 μ M. However, the micrographs of **PB-3** (16 μ M) were slightly hazy but the evidence of inhibitor aggregation was not conclusive, as it was in case of DLS experiment.

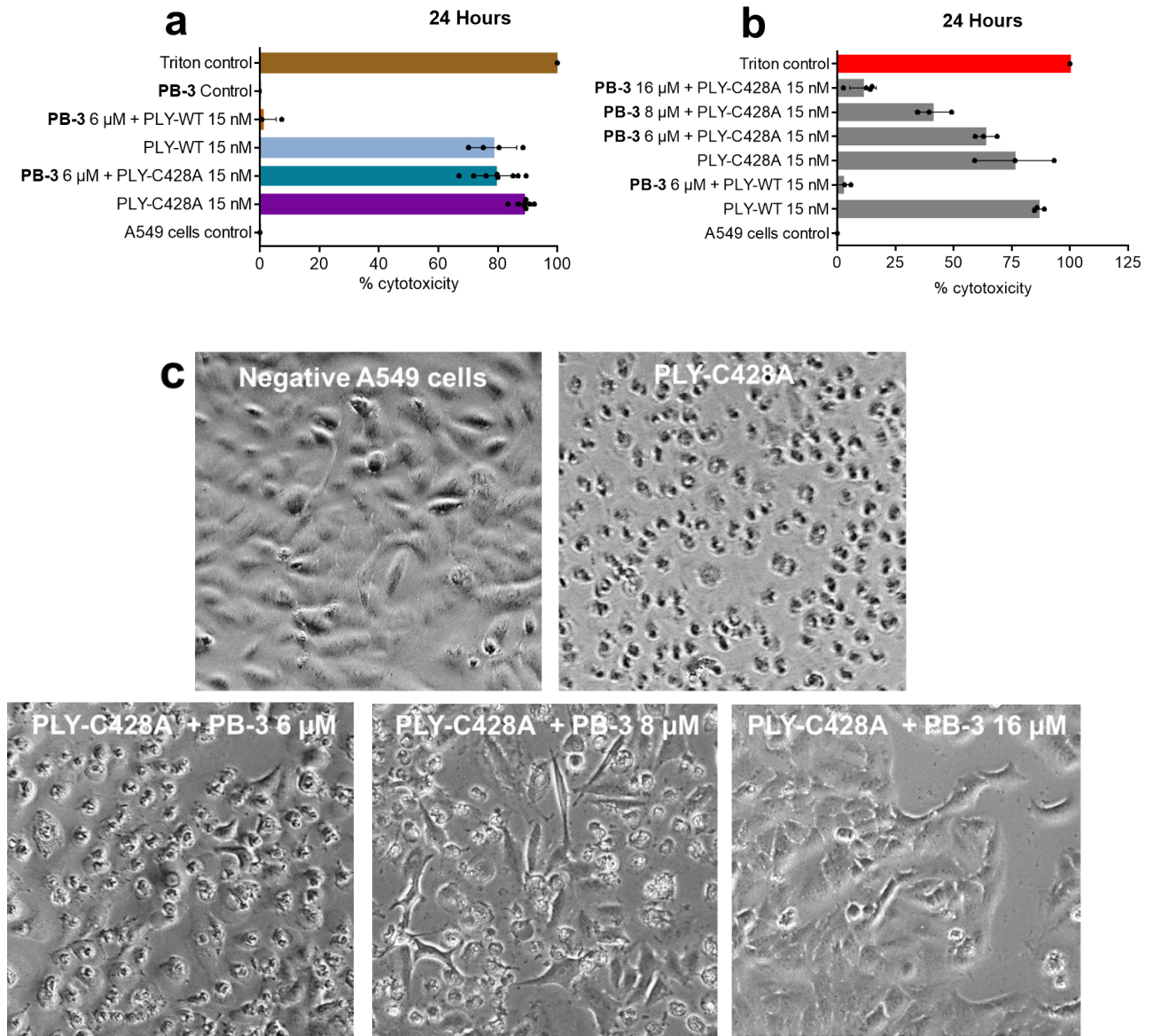


Figure 2.46. Cytotoxicity analysis of PLY-C428A with **PB-3**.

a. **PB-3** was unable to block PLY-C428A at 6 μ M, whereas completely block PLY-WT at same concentration ($n \geq 3$). **b.** Beyond 6 μ M, i.e. 8 and 16 μ M, **PB-3** inhibited PLY-C428A ($n \geq 3$). **c.** Micrographs highlight the inhibition of PLY-C428A under the effect of increasing concentration of **PB-3**.

2.6.2. Summary

LDH analysis is a well-suited method to quantify the damage induced by CDC. **PB-1** has been the first to be subjected against PLY. **PB-1** was unable to protect lung cells from PLY during the first couple of attempts. Later it was figured out that, due to solubility problems, **PB-1** was unsuccessful in blocking PLY. The solubility of the system was optimized by increasing the DMSO amount from 0.5 to 2% and in addition, by inclusion of a pre-incubation step of inhibitor and toxin in 10% PBS. Henceforth, **PB-1** inhibited PLY in a concentration dependent fashion up to 24 h. The concentration range (25, 50 and 100 μM) of **PB-1** was in relation to its IC_{50} (~ 40 μM) in the hemolysis assay. **PB-1** minimized PLY-mediated cellular toxicity $\geq 90\%$ at 100 μM and $\geq 50\%$ at 50 μM for a period of 24 h.

Moving forward, **PB-2** was the second inhibitor analyzed against PLY. Similar to **PB-1**, it was tested at three concentrations: 2, 4 and 8 μM and those were selected according to its IC_{50} (~ 5 μM). The DMSO content for analysis of **PB-2** was always $\leq 2\%$. Here, only the pre-incubation of inhibitor and toxin was a part of the assay protocol. **PB-2** has blocked $\geq 90\%$ of PLY-induced cytotoxicity at 8 μM and $\geq 50\%$ at 4 μM over a period of 24 h.

Afterward, the inhibitory potential of **PB-3** was inspected against PLY and PLY-C428A. **PB-3** was employed in three concentrations (1, 3 and 6 μM) and it exhibited excellent inhibitory potential by hindering $\geq 90\%$ PLY-induced toxicity at 6 μM and $\geq 50\%$ at 3 μM for 24 h. **PB-3** was better soluble amongst tested PB-molecules in the LDH assay and, therefore, it worked with and without the pre-incubation in 10% PBS step. The stability of **PB-3** was ascertained by pre-incubation of **PB-3** in PBS for 20 min prior to testing in the LDH assay. **PB-3** (6 μM) had prevented $\geq 90\%$ cellular damage after the 20 min pre-incubation in PBS and this was a substantial increment in molecular stability. While, when tested against PLY-C428A, **PB-3** was found not effective as against PLY. **PB-3** was unable to prohibit PLY-C428A at 6 or even at 8 μM . The inhibition of PLY-C428A was mainly detected at 16 μM of **PB-3**.

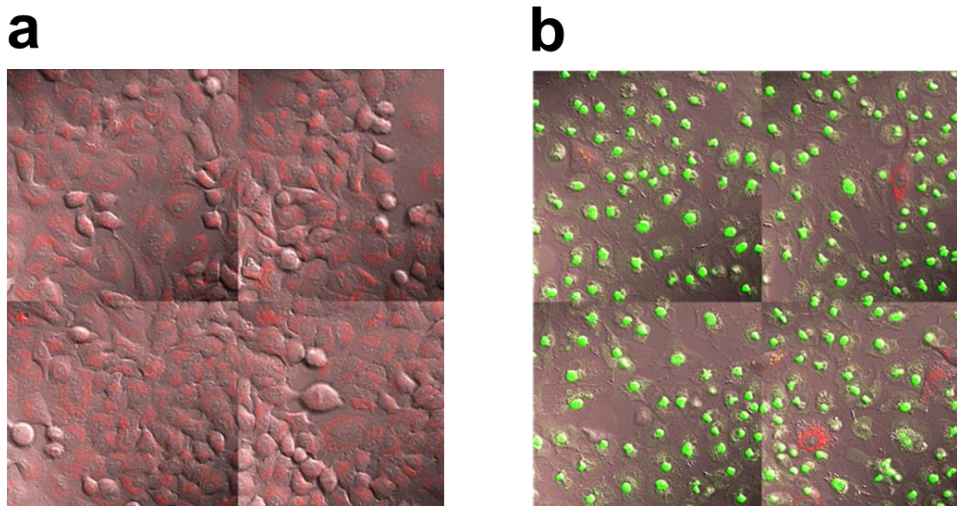
In addition to the quantitative values, the micrographs are captured for each inhibitor to further validate the results. There is always a correlation observed between the quantitative values and cellular morphology on micrographs.

2.7. Illustration of protective effect of PB-molecules via confocal laser scanning microscopy

Pneumolysin is the only CDC which lacks a secretion ladder for release.¹⁹ Nevertheless, when it is released from *S. pneumonia*, as explained in the introduction, it triggers cellular damage which could be observed via microscopy.²²⁵ Thus, in addition to cytotoxic quantification by LDH assay, the native effect of PLY and protective effect of PB-molecules on human lung alveolar cells (A549) was validated and illustrated by confocal laser scanning microscopy.

2.7.1. Protective effect of PB-2

PB-2 was the first inhibitor that was analyzed by confocal laser scanning microscopy. Cells were grown in 8-well chamber slides using Ham's F12 medium with 10% fetal bovine serum (FBS). Once cells were confluent, they were treated with tetramethylrhodamine methyl ester (TMRE) to determine the membrane potential of mitochondrial membranes. Later, healthy cells were loaded with fresh medium containing a marker substrate that detected the activity of capase-3/7 in case of apoptosis. Samples of PLY with and without **PB-2** (8 μ M) were analyzed overnight, healthy cells were marked as negative control and only **PB-2** (8 μ M) sample was considered as inhibitor control. According to the findings in **Figure 2.47**, **PB-2** was proven to be non-toxic as well as a potent inhibitor of PLY and it inhibited up to ≥ 90 % of the cellular damage caused by PLY. Dr. Maren Mieth in Charité performed these assays by employing our in-house synthesized **PB-2** and recombinant PLY.



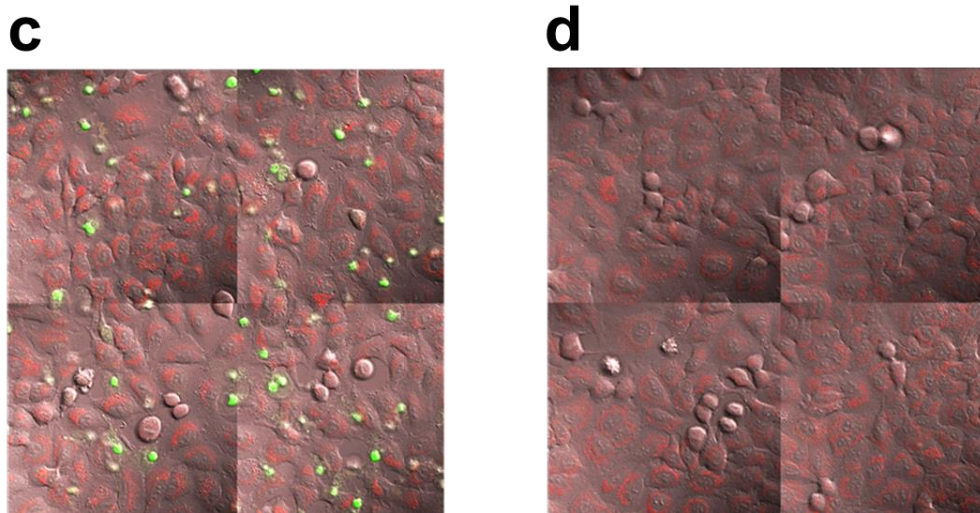


Figure 2.47. Demonstration of PLY-prohibition in cellular injury in A549 cells by **PB-2**. Red color indicates non-toxic mitochondrial dye (TMRE: tetramethyl rhodamine, ethyl ester), as indicative of healthy cells and a green color represents fluorescent substrate that notice the caspase-3/7 activity in apoptotic cells. **a.** Healthy cells as a negative control (24 h). **b.** Cells under the influence of PLY 15 nM show severe apoptosis (24 h). **c.** Cells treated with PLY 15 nM and **PB-2** 8 μM display survival of more than 90 % of cells, thus, signifies the activity of **PB-2** (24 h). **d.** Cells with only **PB-2** (8 μM) as a control, highlight that **PB-2** is inert toward cells (24 h). All micrographs were captured by Zeiss LSM780 confocal laser-scanning microscope after 24 h (data in a, b, c and d are one of $n = 3$).

2.7.2. Protective effect of PB-3

PB-3 was a next generation PB-molecule with improved efficacy and stability as per the hemolysis and the LDH assay. The experimental design to examine **PB-3** was identical to **PB-2**. When cells were prepared after determination of membrane potential and loading of green caspase-3/7 detection reagent for apoptotic cells, **PB-3** (6 μM) samples with PLY and without PLY as inhibitor control were loaded to cells. Consequently, PLY alone sample and medium only as negative control were poured into cells. All distinct samples were incubated for 24 h before investigating under microscope. Next day, microscopy data revealed that, indeed, **PB-3** was superior to **PB-2** and at only 6 μM , **PB-3** impeded cellular injury induced by PLY. As reported by **Figure 2.48 c.**, more than 95 % of the human lung alveolar epithelial cells withstood the detrimental effects of PLY. Like **PB-2**, Dr. Maren Mieth from Charité did the microscopic analysis of **PB-3** and we provided the recombinant PLY and stock solution of **PB-3**.

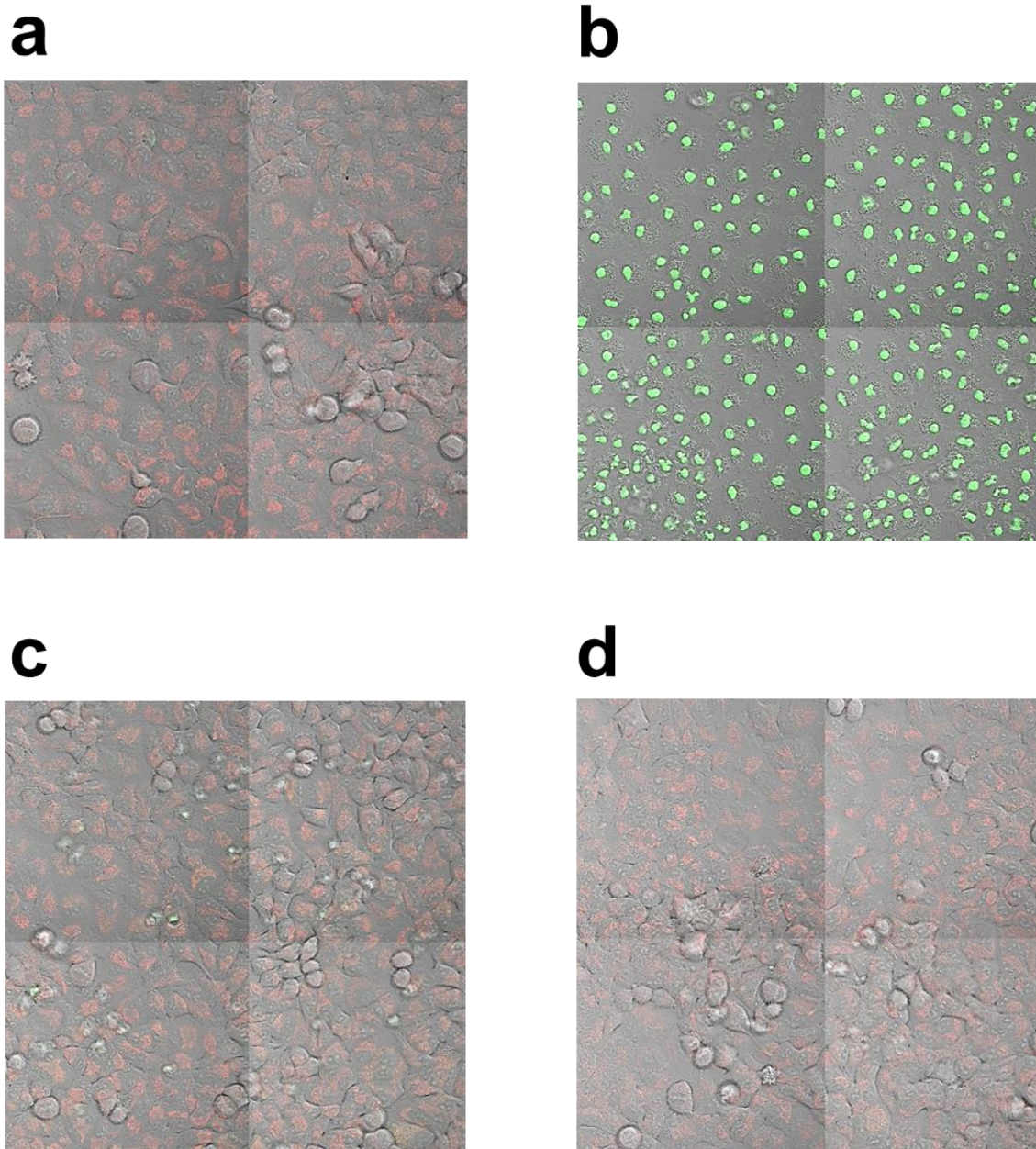


Figure 2.48. PB-3 blocking PLY in A549 cells demonstrated by microscopy. Red color denotes a mitochondrial dye (TMRE: tetramethyl rhodamine, ethyl ester) as indicative of healthy cells and green color represents fluorescent substrate peptide to show caspase-3/7 activity in apoptotic cells (data here represent one of $n = 3$). **a.** Healthy cells after 24 h. **b.** Apoptotic cells under the influence of PLY 15 nM after 24 h. **c.** PB-3 (6 μ M) blocks PLY and ≥ 95 % cells are living after 24 h. **d.** PB-3 has no effect on A549 cells after 24 h.

2.7.3. Investigation of PB-3 in *Streptococcus pneumoniae* infection-model assay

PB-3 was the triumphant inhibitor among PB-inhibitors. It was successful in the hemolysis, LDH, and microscopy assay, and in addition exhibited significant affinity for PLY (K_D : 256 nM) in the BLI assay. Therefore, the next rational advancement in the course **PB-3** pre-clinical studies would be to examine it in an actual bacterial infection.

To achieve this goal, D39 strain of *Streptococcus pneumoniae* (*S.pn.*) was chosen for analysis. At first, a capsule-deleted mutant (D39 Δ cps) of *S.pn.*^{89,123} was employed, since **PB-3** was specific against PLY and the capsule of *S.pn.* was one of the stringent virulence factors that cause cellular impairment. Therefore, the capsule locus (cps) was deleted in D39 *S.pn.* to ensure that PLY must be the cause of the observed cellular damage. Later, a pneumolysin and capsule loci-deleted mutant of *S.pn.* (D39 Δ cps Δ ply) was generated and marked as a control to assure that cellular toxicity was mainly dependent on PLY and cps. Besides the replacement of PLY by *S.pn.* infection, the rest of the experiment was conducted according to the previously mentioned protocol with identical indicators for living and dead cells.

Cells were infected with D39 Δ cps and D39 Δ cps Δ ply independently and after 16 h of incubation, nearly all cells of D39 Δ cps sample were dead, as recognized by the loss of the mitochondrial TMRE signal (red) and the abundance of caspase-3/7 signal (green). Whereas cells belonging to D39 Δ cps Δ ply sample were living as the TMRE signal was intact (**Figure 2.49**). Thus, it was confirmed that the cellular damage/death noticed in the D39 Δ cps sample was because of PLY only. Thereafter, **PB-3** (6 μ M) was added to cells with D39 Δ cps infection and after 16 h of incubation, noticeable cellular damage was observed, though it was not the same as in the case of D39 Δ cps alone. However, it was still considerable in comparison to the earlier results (hemolysis and microscopy assay) of **PB-3**. Here, the outcome of **PB-3** was not according to the expectation and needed a plausible explanation. One conceivable explanation would be that **PB-3** did not possess anti-microbial properties, thus it could block only PLY, not D39 Δ cps and, on the other hand, bacteria consistently produced PLY, which required more **PB-3** to counter. Therefore, in later experiments, **PB-3** (6 μ M) was added to the D39 Δ cps sample at regular time intervals, i.e. after each 4 h, up to 16 h, and when observed under microscope after 16 h, nearly all cells survived and there was no sign of apoptosis detected. Hence, it was evident by increasing the dosing

frequency of **PB-3** in the assay that bacteria continuously released PLY, which in turn needed a greater amount of inhibitor to be deactivated. In conclusion, **PB-3** successfully blocked the cellular injury associated with PLY in a pneumococcal infection-model assay. Dr. Maren Mieth performed the assay at Charité in her lab. Micrographs of samples and controls were captured after 16 h and can be seen in **Figure 2.49**.

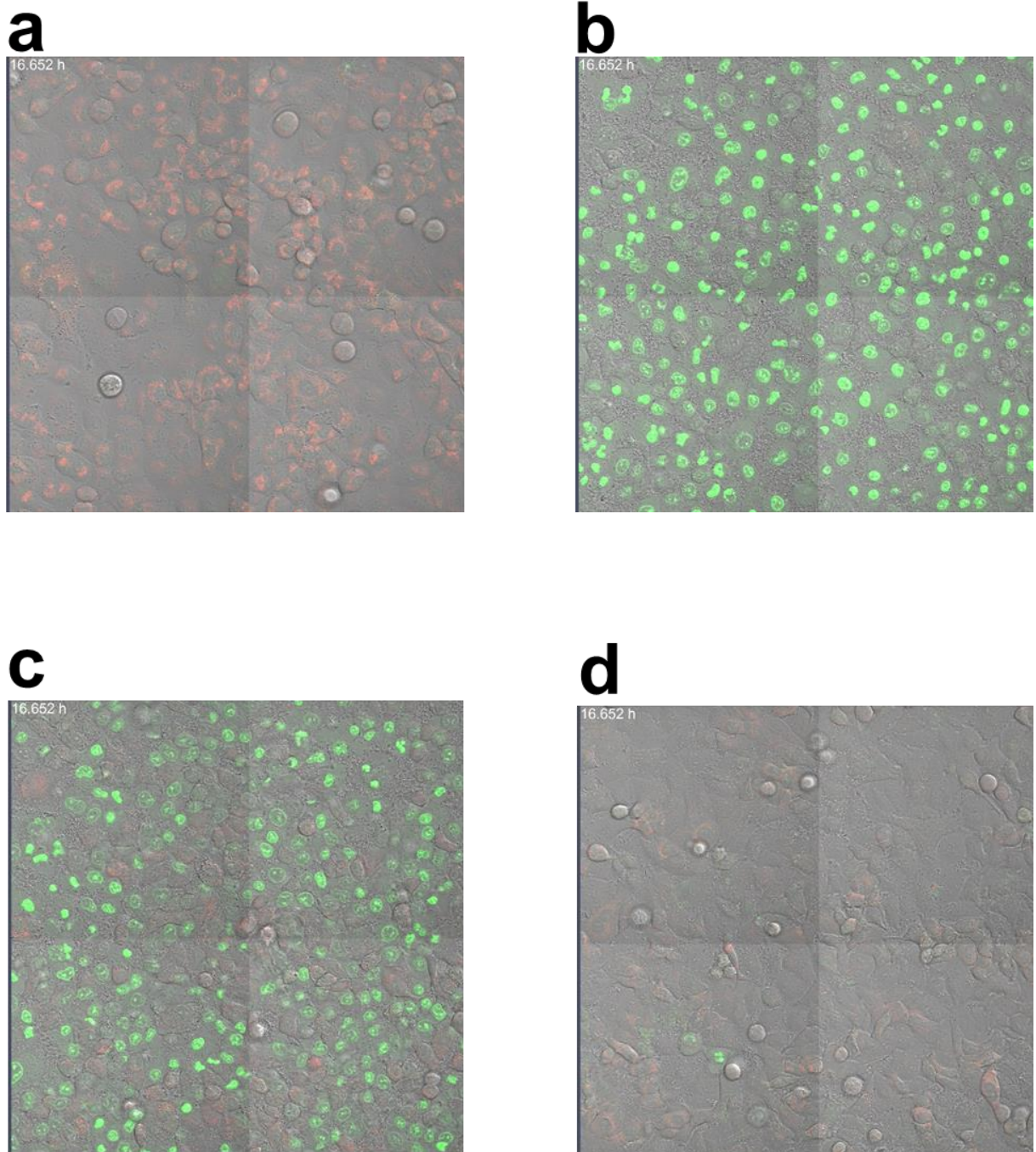




Figure 2.49. PB-3 restricted cellular deterioration in S.pn. infection-model assay. **a.** Healthy cells after 16 h. **b.** D39 Δ cps infected cells displayed cellular injury (16 h). **c.** D39 Δ cps infected cells with 1x-treatment of **PB-3** (6 μ M) exhibit cell-death after 16 h. **d.** D39 Δ cps infected cells with 4x-treatment of **PB-3** (6 μ M) after regular intervals prohibit cell death (16 h). **e.** D39 Δ cps Δ ply control, it represents that only PLY provokes the cellular injury.

2.7.4. Summary

The effect of PB-molecules has been shown by the hemolysis assay, LDH quantification and Cryo-TEM. This is a step forward and here, the potential of PB-molecules for abolishing the cytolytic capacity of PLY on human lung alveolar cells (A549) is demonstrated and ratified via confocal laser scanning microscopy.

PB-1 had a solubility problem and the highest IC_{50} among leading PB-molecules. Thus, it was pragmatic to skip **PB-1** for such an advanced analysis. Therefore, **PB-2** was the first inhibitor selected for microscopy. **PB-2**, at 8 μ M inhibited $\geq 90\%$ cytotoxic effects of PLY for 24 h in the presence of positive and negative controls. The effect is shown in **Figure 2.46 c**. Likewise, **PB-3** at 6 μ M, blocked $\geq 95\%$ of PLY-mediated injury and cells were survived for 24 h (**Figure 2.48 c**).

Next, **PB-3**, the chief inhibitor among PB-molecules, was subjected to the *S.pn* infection model assay. **PB-3**, when first applied in the assay, was not found potent at all, and only minor inhibition was noticed (**Figure 2.49 c**). Later, it was thought that since PB-3 was efficacious against only PLY and does not prohibit bacterial infection and within bacteria, PLY might have been continuously produced. Therefore, an additional supply of **PB-3** was required to counter the increasing production of PLY. Thus, **PB-3** (6 μ M) was supplied after every 4 h up to 16 h and cellular toxicity was reduced to almost none.

2.8. Discussion

Since the 19th century, cholesterol-dependent cytolysins (CDC) have been notorious as hemolytic toxins of gram-positive bacteria, and the increased exploration of this protein family in the last few decades has revealed that CDC are not merely pore-forming toxins, rather they activate intricate pathways of inducing pathogenesis and ultimately provoking disease progression in the host. Hence, CDC are stringent virulence factors of their respective organisms. The development of anti-virulence agents is an effective way of minimizing evolutionary stress on bacteria to acquire antibiotic resistance. Therefore, the aim of this study was to develop generic inhibitors of homologous CDC that could block their detrimental effects and could be added as an adjunct to antibiotics in invasive diseased conditions.

This research was an extension of our previous work in which small molecules from online database of Specs were virtually screened for an oligomerization-site of a prototypical CDC and an established drug target, PLY. **Pore-blocker-1** or **PB-1** was the name assigned to an active inhibitor from virtual screening. Afterwards, **PB-2** was structurally optimized and a 10-fold more active derivative of **PB-1**. Both **PB-1** and **2** were commercially purchased and exhibited an IC_{50} of 67 and 4 μ M, respectively.

The aim of this thesis was to synthesize and test active molecules and validate them biophysically. Then, recognize the essential pharmacophore of **PB-1** and **2**, and synthesize derivatives to obtain more potent and chemical stable inhibitors and to generate an SAR via testing of derivatives of the lead compound. Afterwards, the aim was the validation of the computational binding mechanism and to test the potent inhibitors in cellular assays against the native toxin and in a bacterial infection model assay. Finally, it was the goal to establish the activity of inhibitors in multiple CDC.

PB-1 and **2** were synthesized in the lab and demonstrated an IC_{50} of 38 and 4.8 μ M, respectively (**Figure 2.4**). The hemolytic testing at an early stage discovered that PB-molecules underwent degradation in the buffer and consequently their activity was reduced, later the degradation of **PB-2** was confirmed via LCMS, too (**Figure 2.5**). Meanwhile, the testing of **PB-2** precursors and a reduced analog (**PB-2.1**) have identified the reactive core of PB-molecules, which is an olefinic double bond (**Figure 2.9**). Thus, to develop more potent and stable inhibitors, multiple structural variants of

PB-2 were synthesized and tested, however, unfortunately, none of those was of better inhibitor than **PB-2** (**Table 2.1**). Besides the poor stability of **PB-2**, it blocked the activity of PLY $\geq 90\%$ in the cellular experiment quantified via LDH assay at 8 μM (**Figure 2.44**) and likewise, at the same concentration, the inhibitory potential of **PB-2** was confirmed in human lung cells by confocal microscopy (**Figure 2.47**).

Meanwhile, defining the mechanism by which PB-molecules inhibit PLY was another quintessential part of the project. To address this issue, first, two mutants of PLY from the view of the virtual-binding site (oligomer-forming region) were generated and expressed. As expected, those mutants are devoid of hemolytic activity as oligomerization is afflicted. However, in the BLI assay, those mutants were binding to **PB-2** equally to PLY-WT (**Figure 2.35**). Analysis of these two mutations from the oligomer-forming domain of PLY clearly confirm that PB-inhibitors were not binding to amino acids (E151 and D206) in the oligomer-domain. Thereafter, another amino acid (T55) of PLY, which according to the computational binding mechanism interacts directly with PB-molecules, was mutated and the protein (PLY-T55A) was expressed. This mutant version (PLY-T55A) was actively inhibited by the PB-inhibitors in the hemolysis assay (**Figure 2.19**). Therefore, in conclusion, the analysis of all three mutations from the oligomerization-domain suggested that PB-molecules might not be involved in hindering oligomerization.

Apart from mutational analysis, the mechanism of PB-inhibitors was investigated via Cryo-TEM. PLY-induced pore formation was detected on cholesterol liposomes, Cryo-ET unveiled membrane integration of PLY, and in addition, isolated pores were captured after the solubilization of liposomes. Whereas, in the presence of **PB-2**, precipitates of PLY were shown as free suspended and there was no sign of protein integration in membranes of liposomes (**Figure 2.39**). These findings decisively confirmed that **PB-2** had restricted the membrane binding ability of PLY. Otherwise, not pore formation but membrane binding must have been detected. A further inference can be made that PB-molecules do not interfere with oligomerization of PLY.

After achieving insights concerning the mechanism of PB-molecules, the optimization of **PB-2** was resumed. This time, a structural shift was triggered by displacing the benzene group of the reactive core of **PB-2** by a furan and eventually, **PB-3** was the product. **PB-3** proved to be far superior in stability and possessed an IC_{50} of $\sim 3 \mu\text{M}$

(**Figure 2.13**), which means it is more potent than **PB-2**. Similarly, **PB-3** was successfully synthesized by protein-templated fragment ligation and quantified via LC-QTOF-MS ($C_{max} \approx \sim 800$ nM) (**Figure 2.14**). Moreover, **PB-3** (6 μ M) illustrated protection from PLY by showing $\geq 90\%$ survival of cells via confocal microscopy and inhibiting $\geq 90\%$ LDH enzyme. **PB-3** showcased an affinity for PLY with a K_D of 256 nM, measured in the BLI assay (**Table 2.5**).

Concerning the binding mechanism of PB-molecules, the investigation of oligomer-forming domain mutants implies that PB-molecules do not block oligomerization of PLY and the cryo-TEM data exhibit that membrane entry of protein is restricted by PB-molecule. Therefore, in the next round of mutational analysis, the cholesterol-binding site mutants were evaluated for their involvement in the binding of PB-molecules. Two mutant versions of cholesterol-binding domain were created and expressed. The first one was PLY-DM that included mutation of both CRM amino acids. Like two (E151 and D205) oligomerization-domain mutants, it was also inactive in the hemolysis assay and exhibited binding to **PB-2** in the BLI assay (**Figure 2.35**). This outcome refers to no involvement of CRM in the activity of PB-molecules.

The second mutation of the cholesterol-binding site was a cysteine mutation (PLY-C428A). Cysteine (428) is part of a conserved (UDP) motif in CDC. Like CRM, UDP is critical for the membrane anchoring and pore formation abilities of the toxin. The pharmacophore of PB-molecules favors a nucleophilic addition reaction. Therefore, mutation of cysteine made perfect sense. PLY-C428A was expressed and was active in the hemolysis assay. After analyzing PB-molecules against PLY-C428A, **PB-1** was found inactive. Hence, it was conclusively proven that C428 was essential for the binding of PB-inhibitors and it may interact with PB-molecules via reversible covalent interaction.

The outcome of **PB-1** against PLY-C428A provided substantial evidence about the mechanism of PB-inhibitors yet, on the other hand, **PB-2** and **3** showed inhibition of PLY-C428A at higher concentration than PLY and the potency of both inhibitors was considerably reduced against PLY-C428A (**Figure 2.20**). **PB-2** inhibited PLY-C428A at 30 μ M and, IC_{50} of **PB-3** was increased from 3 μ M against PLY to 11 μ M against PLY-C428A. So, how did **PB-2** and **3** demonstrate residual activity? There may be additional binding sites for inhibitors.

Therefore, to investigate additional binding sites for **PB-3** in PLY-C428A, the BLI assay was customized to observe the binding of **PB-3** with proteins (PLY and PLY-C428A) on parallel sensors. However, there was a limitation because **PB-3** could be analyzed up to 8 μM in solution. If the concentration exceeded 8 μM , then, atypical high drift signals were detected. Hence, **PB-3** was used up to 8 μM . It was observed that **PB-3** was binding to PLY in a concentration-dependent manner, whereas with PLY-C428A negligible binding was observed over 2, 4 and 8 μM of **PB-3** (**Figure 2.35**). The outcome of the BLI assay indicated that **PB-3** had affinity only for PLY. Thus, the inhibition of PLY-C428A occurring at high concentrations of **PB-3** was probably due to the aggregation or precipitation, since both **PB-2** and **3** had the tendency to precipitate at higher concentrations. This assumption was further investigated, when **PB-3** was analyzed at multiple concentrations via DLS. At 12 and 15 μM , **PB-3** showed a drastic increase in diameter and in standard deviation among samples, which has been reported for aggregating molecules. Hence, these findings affirmed that the cause of residual activity was the aggregating effect of inhibitors (**Figure 2.37**).

Moreover, the (hemolysis and BLI) findings of PLY-C428A and the BLI data of **PB-3** with PLY suggested a covalent interaction between PLY and **PB-3**. Thus, we conducted supplementary investigation to validate the covalent interaction between wild type PLY and **PB-3**. The protein-ligand complexes were analyzed via mass spectrometry. The testing was attempted in native conditions, however, due to the hydrophobic nature of proteins, they were instable in ammonium acetate and other buffers of native MS. Thus, MS could not be conducted under native conditions. In contrast, the spectra of pure proteins were successfully obtained in denaturing conditions. The protein-ligand complex exhibited a broad peak that correlated to the PLY + **PB-3** mass in the sample. The broadening of peak probably occurred decomposition of the protein-inhibitor complex during acceleration of molecular ions in the mass spectrometer. In other samples like PLY control, PLY-C428 + **PB-3** and PLY-C428A control, there was only one main peak that corresponds to protein mass in each sample (**Figure 2.40**). These MS results implied that there was a reversible covalent interaction between PLY and **PB-3**. There are other methods, e.g. ITC and TSA, available in the lab to detect protein-ligand interactions. However, these methods cannot provide evidence for the nature of interaction, e.g. covalent or non-covalent. Additionally, due to limited solubility of inhibitors and the hydrophobic nature of

proteins, those methods would not be appropriate. PLY and its mutants require a threshold concentration of glycerol (50%) to be in stable and soluble form and experiments like ITC and TSA cannot be conducted with such high amounts of glycerol.

After establishment of the binding mechanism, the next major concern was about the specificity of PB-molecules toward PLY. Since PB-molecules react as Michael acceptor thus, there is a probability that these could bind to every available nucleophile, e.g. cysteine. This issue was resolved by testing **PB-3** against cysteine-containing drug targets available in the lab (PTP1B and SARS-CoV-2 main protease), and **PB-3** did not inhibited PTP1B or SARS-CoV2 at therapeutic concentrations of PLY (**Figure 2.22**). Furthermore, the specificity of **PB-3** was readily validated in the cellular experiments because the cell culture medium (Ham's F12) contained 0.2 mM of cysteine, i.e. > 13,000 fold cysteine than PLY and **PB-3** was effectively inhibiting \geq 90% of PLY at 6 μ M. Moreover, the selectivity of **PB-3** was also ascertained by employing assorted Michael acceptors (some of them are reported Michael acceptors against D68 protease) or similar electrophilic molecules against PLY, and none of the molecules has displayed inhibition of PLY (**Figure 2.21**). The details of specificity are available in the results section. Hence, like the efficacy, the specificity of **PB-3** has been convincingly proven. Therefore, we took a leap forward toward more advanced and sophisticated testing.

PB-3 was evaluated in an actual *Streptococcus pneumonia* infection model assay. In infected human lung alveolar cells, **PB-3** effectively neutralized PLY without aggravating the infection. However, a repeated dosing of **PB-3** (6 μ M after ca. 4 h) to counter PLY was required because the bacterial proliferation was not hindered, and bacteria can constantly produce the toxin (**Figure 2.49**). The infection-model assay data also indicate that **PB-3** is not an antimicrobial and only anti-PLY.

The importance of PLY as a drug target is well known as explained in the introduction and, so far, there is no specific cure available for the disease progression associated with PLY. Although, multiple natural products including polyphenolic compounds, plant steroids and other unspecific phytochemicals, etc., have been reported in the pre-clinical studies to possess anti-PLY properties yet, all of them were unable to produce sufficient evidence for specificity to PLY and in fact, on the contrary, most molecules have been known to effect numerous proteins and biological pathways. Thus, the

comprehensive investigation of PB-molecules, especially **PB-3**, in terms of potency, efficacy and specificity makes it a lead compound for a drug against PLY.

After obtaining assertive findings against PLY, next, PB-inhibitors were examined against other CDC. As per introduction, CDC have two broad branches: directly and indirectly cholesterol engaging, although both are pore-forming toxins. However, subtle mechanistic differences are present. Therefore, PB-inhibitors were expected to behave differently and likewise, we have chosen two toxins, PFO and ILY, one from each group. PFO is homologous to PLY and has an identical UDP and both belong to the directly cholesterol binding group, whereas ILY binds to the human CD59 receptor, and the UDP of ILY does not contain cysteine.

PB-inhibitors were observed more potent against PFO than PLY. **PB-1**, **2** and **3** have recorded IC_{50} values (5, 0.5 and 0.3 μM , respectively), which are 10-fold lower in comparison to PLY (**Figure 2.24**). The cause of elevated potency was not clear and future studies might address this query. Maybe blocking the UDP cysteine is much more crucial in PFO because cysteine is imperative for the activity of PFO and, unlike PLY, cysteine mutation in PFO has been known to lose hemolytic activity. Side by side, testing of PB-inhibitors against ILY provided different outcome than PFO and these results are somehow expected. **PB-1** was found inactive against ILY, whereas **PB-2** and **3** displayed IC_{50} beyond 10 μM (**Figure 2.27**). These findings were, in principle, similar to the outcome of PLY-C428A testing. In the case of PLY-C428A, we were able to produce adequate evidence that the activity of **PB-2** and **3** at higher concentration is due to precipitation of inhibitors. Therefore, in the case of ILY, apparently a similar mechanism to PLY-C428A seems to be the cause of inhibition.

To conclude, inhibitors against CDC or more precisely direct-cholesterol-binding CDC were developed, characterized, and validated by employing a dynamic and rational drug design approach. These inhibitors are unique in terms of activity and hold the intrinsic potential of binding specifically to cysteine within the UDP peptide of CDC and ultimately blocking the membrane entry of the toxin. Originally, the inhibitors were designed to engage CDC via oligomerization domain, however, in contrast, the mutational analysis and biophysical data are sufficient to show that inhibitors react via reversible covalent interaction with UDP-cysteine. Nevertheless, other than cysteine, there could be a remote possibility of interaction at the oligomer-forming-site but for

that, additional investigation is required. At the current stage, **PB-3**, the best of PB-molecules, has been effectively consumed to prevent PLY-induced cellular injury in the pneumococcal infection model. The effect of **PB-3** on CDC-activities other than pore formation, e.g. bacterial colonization, necroptosis, immune-modulation etc., are yet to be evaluated. Nevertheless, **PB-3** or a more stable and potent future analog has a potential to be a lead molecule or candidate for cure against CDC-induced pathogenesis. It could be effectively applied as an adjunct to antibiotics in treating severely diseased patients.

3. Chapter 3: Experimental section

3.1. Experimental methods and procedures

In this chapter, all the necessary methodological and technical details to reproduce the experiments of results and discussion chapter are available. In addition, the multiple software used for data analysis are also mentioned.

3.1.1. Recombinant expression and purification of pneumolysin

Established protocols of PLY expression were customized in this study.^{23,24,28} To synthesize PLY gene, a cDNA encoding the wild-type sequence of PLY was cloned between the NdeI and the XhoI site of the plasmid pET-19b (Novagen). The pET-19b plasmid possessed an ampicillin resistant gene and a 10-fold histidine tag. Mutants of wild type PLY were prepared with the wild type cDNA as template by standard site-directed mutagenesis protocols. Genes of PFO and ILY in separate pET-19b plasmids were purchased from BioCat GmbH.

Transformation and pre-culture. The in-house prepared or commercially purchased recombinant plasmids pET-19b containing the protein gene were transformed by heat shock into the BL21 strain of *E.coli*. The plasmid (1 μ l out of 1 μ g / μ l) and 50 μ l of *E.coli* were mixed and incubated on ice for 0.5 h. Afterward, the mixture was dipped in a temperature-controlled water bath (42 °C) for exactly 30 s. The heat shock caused the opening in the bacterial cell wall and led to the infiltration of the recombinant gene. Next, 950 μ l of sterile Luria Broth (LB) medium was added to the bacterial solution and incubated at 37 °C for 1 h. Later, 10 – 30 μ l of bacteria were spread on an agar plate containing ampicillin (100 μ g / ml) and incubated overnight. Another agar plate as a negative control was also incubated overnight and it contained *E.coli* without recombinant plasmid.

Bacterial colonies were observed only on the agar dish that comprised of the recombinant plasmid. Moving forward, the pre-culture was prepared by dissolving a single colony of the bacteria into 5 – 10 ml of LB medium with the aid of a sterile pipette tip. The LB medium was left in the incubator for overnight incubation at 37 °C. Next day, a glycerol stock solution of bacteria was generated by mixing 0.5 ml of bacteria with 0.5 ml of sterile 50 % glycerol solution in double distilled water. The glycerol stock solution is also known as mother culture and it had a benefit that the mother culture

could be stored at $-80\text{ }^{\circ}\text{C}$ for years and could be used for inducing growth of transformed bacteria, whenever required. The remaining bacteria in LB medium was used as pre-culture for the induction of bacteria, up to 5 ml of the pre-culture was capable of inducing growth in 2 L of LB medium. A simple workflow diagram of transformation can be seen in **Figure 3.1**.

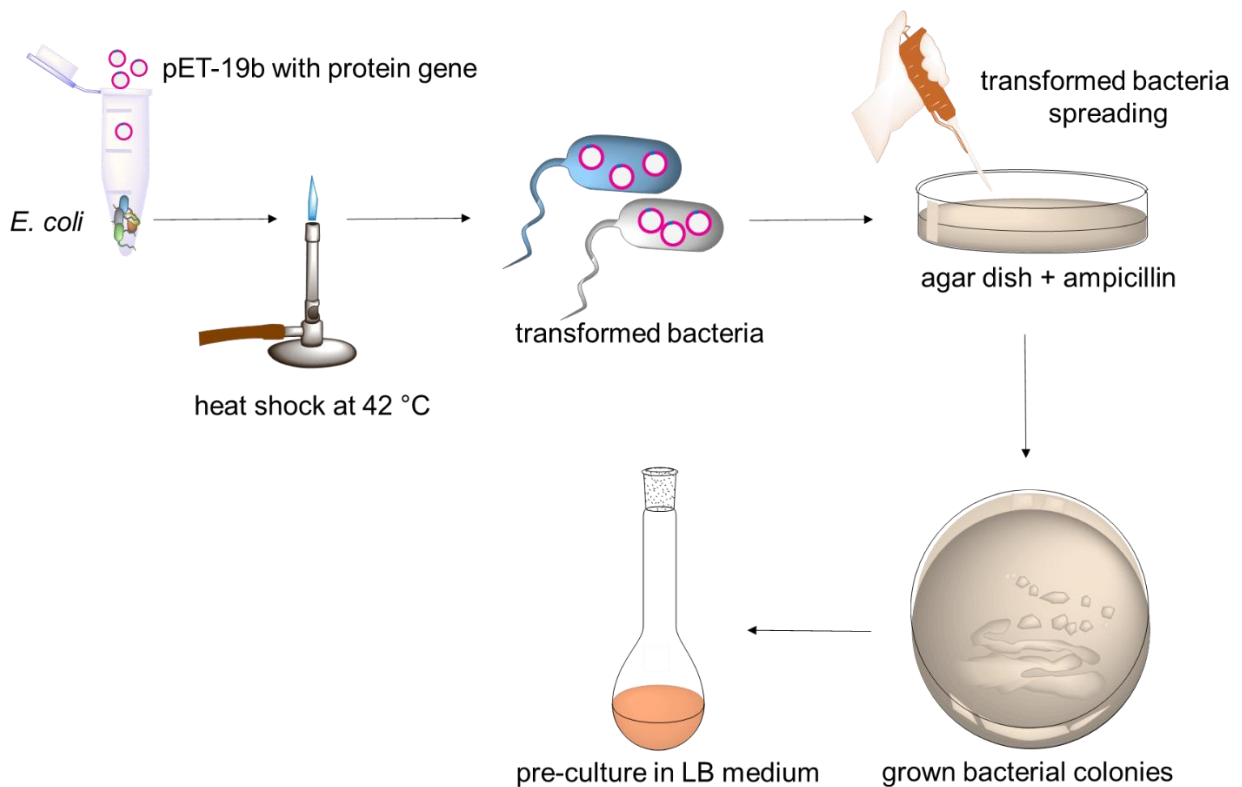


Figure 3.1. The workflow of the bacterial transformation.

Induction of bacteria. 1 ml of pre-culture was sufficient to induce growth in 200 ml of LB medium and according to this ratio, the bacterial growth was induced in LB medium at 37°C till the optical density of bacteria reached 0.8. At this moment, the temperature of the incubator was reduced to 25°C and 0.1 mM of isopropyl β -D-1-thiogalactopyranoside (IPTG) was added to bacteria and, then, the bacterial growth was further induced for 4 h.

Harvesting and lysis of bacteria. After induction, the bacteria was stored at $-20\text{ }^{\circ}\text{C}$ in the form of pellets, which were produced by centrifugation (4000 RPM) at $4\text{ }^{\circ}\text{C}$ for 0.5 h. Later, the bacteria was re-suspended in the buffer (25 mM Tris, 500 mM NaCl, 20 mM imidazole, 10 % glycerol, 2 mM β -ME and pH 7.2) containing 100 $\mu\text{g/ml}$

lysozyme for lysis. Bacteria were incubated for 1 h at 30 °C and then 100 µM phenylmethylsulfonyl fluoride (PMSF) was added and further incubated for 0.5 h in the ice bath. Afterward, the slimy bacterial solution while in the ice bath was additionally broken by 10 sonification cycles (75 % power of instrument) and each cycle lasted 20 seconds. Next, the cellular debris was removed in two spinning rounds at 4 °C and 16000 RPM for 20 min. In each round, new / clean centrifugation tubes were utilized to collect debris and after removal of the cellular trash, a protein-rich solution was obtained. Control samples were taken at each step of the process for the quality control of protein expression.

Purification via Ni-NTA column. During the first stage of protein purification, proteins are extracted by affinity chromatography or immobilized metal affinity chromatography (IMAC). Ni-NTA (Nikel-Nitrilio Triacetic Acid) agarose, a nickel charged affinity resin used to purify proteins. A 2 ml column of HisPur Ni-NTA Superflow Agarose was consumed to extract a single batch of protein. At first, the Ni-NTA column was equilibrated by buffer (25 mM Tris, 500 mM NaCl, 10 mM imidazole, 10 % glycerol, 2 mM β-ME and pH 7.2) and, next, the protein mixture was flushed steadily with a flow rate of 0.5 ml per minute through the column. Thereafter, the column was washed with the washing buffer (25 mM Tris, 500 mM NaCl, 25 mM imidazole, 10 % glycerol, 2mM β-ME and pH 7.2) and, finally, the protein was eluted by elution buffer (25 mM Tris, 500 mM NaCl, 300 mM imidazole, 10 % glycerol, 2 mM β-ME and pH 7.2). Samples for the quality control were reserved for pre and post column run.

Purification via size exclusion chromatography. ÄKTA pure, a FPLC instrument, was employed for advance purification of the protein. The instrument was calibrated with buffer (20 mM MOPS buffer, 5% glycerol and pH 8) and the eluted-protein sample was loaded. The protein was flowed on HiLoad Superdex 75 pg preparative size exclusion chromatography column and, at last, the protein containing fractions were pooled in an ice bath. The quality control samples were taken pre and post ÄKTA run.

Ultrafiltration and storage. The protein obtained via FPLC was ultra-pure, however, it was diluted in the buffer. Therefore, the protein was ultra-filtrated by MWCO: 30 kDa filter (Vivaspin 6 Sartorius) to increase the concentration of protein. The protein sample was centrifuged at 3500 RPM for 0.5 h at 4 °C. Later, the protein was aliquoted and glycerol was added to each aliquot in 1:1 ratio and, then, the concentration was

determined by NanoDrop One (Thermo Scientific™). Thereafter, the protein was shock-frozen in liquid nitrogen and it was stored at -80 °C.

Expression quality control. The quality of protein expression was analyzed by a 12 – 14 % SDS-gel. The controls, kept at different steps of expression and purification along with the final purified sample and protein ladder (Protein Marker VI prestained, PanReac Applichem, ITW Reagents, Spain) were examined on the SDS-gel. Since protein expression and purification is a lengthy, complicated process, thus, control samples at each step are critical for troubleshooting in case of any error. Furthermore, the purified protein sample was analyzed via LC-QTOF-MS for confirmation of mass and the detailed method is mentioned in mass spec analysis.

3.1.2. Hemolysis assay

CDC has been known for damaging erythrocytes since decades.^{7,131,257,258} The membranes of erythrocytes are sensitive upon rupture, release hemoglobin into the extracellular fluid and turn the fluid red, which can be measured using spectrometer.^{41,218} To analyze the hemolysis, defibrinated sheep blood was purchased from Thermo-Fischer Scientific and aliquoted under sterile conditions for later use.

Phosphate saline buffer (PBS) was selected as an assay and dilution buffer due to its physiologic and inert properties toward erythrocytes.²⁵⁶ The assay was bifurcated in two phases and in the first one, inhibitors were incubated with protein (toxin) and respective (positive and negative) controls. Whereas in the second phase, erythrocytes were added to the sample and further incubation was performed. In ILY, human blood was provided by healthy volunteer and erythrocytes were isolated and washed by PBS.²⁵⁹

Toxin/protein (12 - 18 nM or 0.5 - 1 µg / ml) alone was incubated for 10 min with shaking at 37°C in PBS as a protein control and the same concentration of protein was applied when investigating different concentrations of inhibitor with identical incubation conditions, i.e. 10 min with shaking at 37 °C. PBS alone and 10 % Triton X-100 samples were marked as negative and positive controls accordingly. In the next step, the blood cells (2.5 % of total assay volume or 25 µl when assay volume 1 ml) added to each sample and incubated for 10 to 15 min at 37° C with shaking. Thereafter, all samples were centrifuged at 9000 g for 1 - 2 min and, afterward, 50 - 100 µl of individual sample supernatants were isolated in a 96-well plate and absorption was measured at

543 nm in a spectrometer. The data were normalized via Graphpad Prism 6 (software) and bar graphs were plotted against different concentrations of inhibitors. To calculate IC_{50} values, concentrations of inhibitor were transformed to log values and “log (inhibitor) vs. normalized response- variable slope” curve fitting were applied using Graphpad Prism 6. The shelf life of defibrinated blood is up to 40 days, however, a slight variation in findings ($\leq 5\%$) was observed with an old batch of blood, i.e. after 2 weeks. Sometimes there could be variation while testing the same inhibitor among different batches of blood. Nevertheless, these variations were minor and always less than 5% when testing an inhibitor that had an activity range of under 10 μM .

3.1.3. Quantitative analysis of protein-templated fragment ligation reaction

First of all a calibration curve of **PB-3** was establish over 0.312 to 10 μM . To quantify the fragment ligation product, the fragments **PB-3.1** (50 μM) and **PB-2.3** (100 μM) were incubated with in PBS with PLY (5 μM) and without protein (control) at room temperature. The final DMSO concentration in samples was $\leq 7\%$ and, likewise, the final glycerol concentration was $\leq 3\%$. The samples were first analyzed after 0.5 h and, then, after each h up to 7 h. The fragments were dissolved into PBS from DMSO stock solutions and protein was dissolved from buffer: 20 mM MOPS, 50% glycerol with pH 8.

HPLC column: Zorbax eclipse plus C18 (1.8 μm 2.1 x 50 mm). HPLC parameters: injection volume: 1 μl , gradient: 0-8 min from 95/5 (A/B) to 5/95 (A/B), 8-9 min 5/95 (A/B), 0-1 minutes waste. The data was later analyzed by Agilent Masshunter Qualitative analysis v. 10.0 (software). The unknown values were determined via calibration curve of PB-3 by using Graphpad Prism. Next, the quantified values of product (**PB-3**) were plotted vs time and nonlinear regression one phase association equation was applied [$Y=Y_0 + (\text{Plateau}-Y_0) \cdot (1-\exp(-k \cdot x))$] using Graphpad Prism.

3.1.4. Kinetic analysis of inhibitors via bio-layer Interferometry

The Octet K2 system by FortèBio is available in our lab for determining interactions between protein-ligand (toxin-inhibitor) by BLI. The instrument is operated by “FortèBio Data acquisition 9” software that is available on the computer connected to the instrument. Meanwhile, there is a separate software “ FortèBio Data Analysis 9” only for analyzing the data after the completion of an experiment.

The Octet K2 includes two probes that move on a robotic arm and white light via light source (lamp) is transmitted through the probes. A pair of fiber optic sensors are lifted up via probes and transferred to a 96-well plate that contains samples for analysis. Here, the target protein (toxin) is immobilized on the surface of biosensors. Thereupon, in a series of steps, the target protein loaded sensors are transported one by one to wells containing multiple concentrations of the binding partner in solution. Hence, association and dissociation between the binding partner and the target protein is monitored in real time. The binding of molecules at the biosensor surface leads to changes in thickness of the binding layer. The optical interference is measured between reflected light waves to the spectrophotometer from an internal surface, and from the external interface between sensor and solution. These changes in interference can be quantified and used to determine kinetic rates of binding and dissociation.²⁴⁷ A specialized buffer, highly recommended for the kinetic analysis of small molecules, named kinetic buffer, was purchased from Pall ForteBio for the BLI assays. The kinetic buffer contained PBS, 0.1 % BSA, 0.02 % Tween 20 and 0.05 % sodium azide and it was always diluted to a 1:10 ratio in PBS before consuming in an assay. The biosensors were dipped in the kinetic buffer / assay buffer for 30 – 45 min ahead of the assay for the sake of calibration of sensors. Simultaneously, the Octet K2 instrument was switched on at least 0.5 h prior to the start of the experiment and the temperature was set between 25 – 30 °C. It helps the lamp to warm up and to minimize the noise and the drift of the optical signal during the experiment.

3.1.4.1. Data Acquisition

The FortèBio Data Acquisition 9 software was opened to create a layout for a new experiment. In the experiment wizard tab, “new kinetic experiment” was chosen and the assay layout was designed in subsequent steps. Each step of the experiment corresponded to an individual tab in the software.

Plate definition. All BLI analysis were executed only in black flat bottom 96-well plate. The first step in a new experiment included assignment of each well according to the material (protein, inhibitor, buffer and reagents) in the plate definition tab of the software. Wells were marked for buffer (baseline), load (target protein), reference (reference protein / buffer), inhibitor sample at different concentrations, wash (inhibitor baseline / dissociation), control (buffer control), neutralization and regeneration. The assignment of wells is available in the **Figure 3.2**.

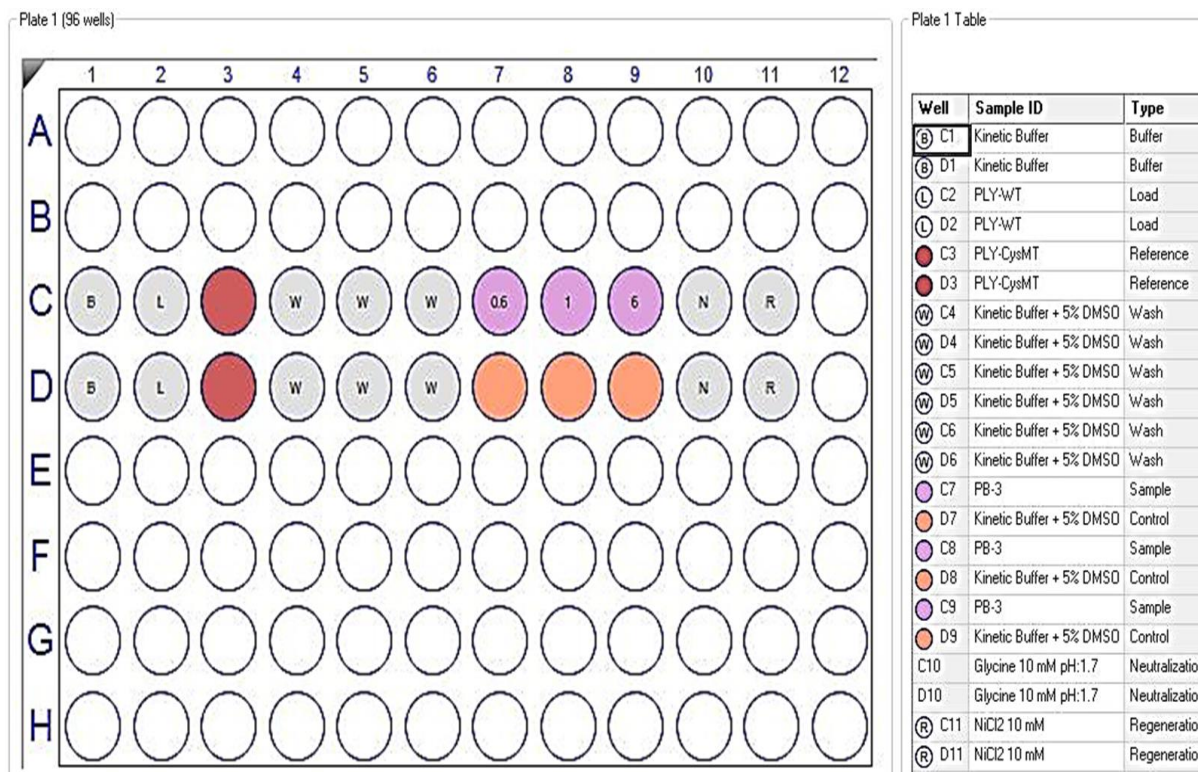


Figure 3.2. Wells of an assay plate marked with content and description of the contents.

Assay definition. Once wells were assigned, the assay layout was designed in the assay definition tab of the data acquisition software and to investigate binding profile, succeeding steps were selected and added to "Step data list" in the assay definition section. Steps included initial baseline, loading of target-protein and reference protein, inhibitor baseline, association, dissociation, neutralization and regeneration. Next, individual steps were assigned by a right-click on a column of the assay plate and click on "add assay step", then, a single step for the respective column was added to "Assay step list" area in the assay definition. Similarly, one by one steps were assigned to all the assay columns. After that, the sequence and timing of each step was confirmed. A clear workflow to define the assay is available in the **Figure 3.3**.

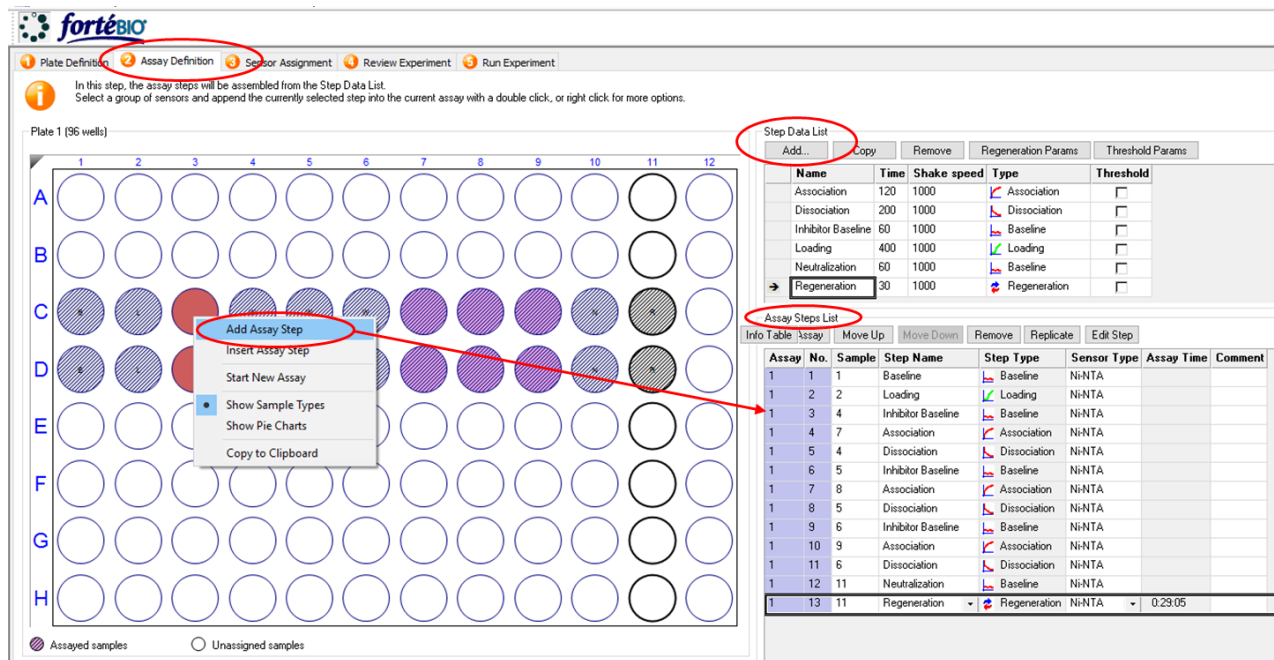


Figure 3.3. A diagram of data acquisition software with highlighted steps of assay definition.

Inhibitor baseline, association and dissociation were repeated for all concentrations of an inhibitor and thereafter, sensors were transported to the regeneration steps. To regenerate NiNTA biosensors, the first 60 s sensors were soaked in a 10 mM glycine solution with pH 1.7 to discard the molecular layer on the biocompatible surface of the sensors. Then, afterward, one by one, sensors were soaked in 10 mM NiCl₂ solution and in kinetic buffer (initial baseline solution) for 5 s each, and this cycle was repeated 3 times in order to regenerate nickel on the biosensors.

Sensor assignment, review and assay run. Next, the sensors were selected for the analysis. The location of sensor columns must be always analogous to the sample rows on the sample 96-well plate, e.g. if the sample rows were C and D of the 96-well plate, then, sensors must be selected from C and D rows of sensor tray. Thereafter, the whole experiment was carefully reviewed and finally “GO” button was clicked for assay run.

3.1.4.2. Data Analysis

After the completion of the assay, the raw experimental data were qualitatively and quantitatively analyzed by the FortéBio Data Analysis 9. This software had three tabs / sections for the detailed investigation of the data. Those include data selection, processing and analysis.

Data selection. In this section, the data generated during the experiment was available in the form of folders. After opening the desired folder, the data were available as experiment summary and sensor-assay. Here, the data were superficially reviewed, and sensors were selected only for the data, whose investigation were required. The nonessential data could be removed in this step by deselecting the respective sensors. The remaining data were shifted to processing.

Processing. This is the main section where formatting of the data takes place before the application of binding models. Henceforth, it is further divided into multiple steps and these steps, in the software, possess check bars, buttons and scroll bars for selection. In the following manner, our data were configured.

- **Step 1.** Data selection, at this step, unwanted wells or wells that were not involved in binding could be skipped for analysis, e.g. neutralization and regeneration wells. Additionally, sensors were labeled for either sample or reference.
- **Step 2.** Subtraction. During this step, the reference data were subtracted. In our experiments, double referencing was employed, therefore, the double reference option were selected for subtraction.
- **Step 3.** Align Y axis, for proper curve fitting, the axis of the data must be properly aligned. X axis is automatically aligned due to the parallel position of sensors, however, Y axis requires alignment. Thus, at this step, Y axis was assigned to a common reference point. According to the data, this common point could be set to baseline or association or dissociation, and the time range of the chosen step will be used to calculate an average and that average will then be set to zero on Y axis. To calculate K_D values in the experiments, Y axis were aligned to the baseline step using the entire time of the step.
- **Step 4.** Inter-step correction, during this step, any mismatching or abnormal drift caused by assay artifacts between two steps are corrected. It is not of chief importance and certainly could be skipped in the case of pertinent data. In our experiments, the inter-step correction step was aligned to baseline.

- **Step 5.** Process. This step includes Savitzky-Golay filtering button, checking this means avoiding high frequency signals, to minimize the signal to noise ratio. It is an optional step, however, it is recommended. In our BLI experiments, it was always checked.
- **Step 7.** View results, during this step, the data could be reviewed after selecting desired conditions in the processing section, and from here data are automatically transferred to the analysis section. The data could be viewed from different perspectives, e.g. sensor summary, report points etc.
- **Step 8.** In this step, the data could be saved for external use and the parameters of analysis could be saved for further analysis.

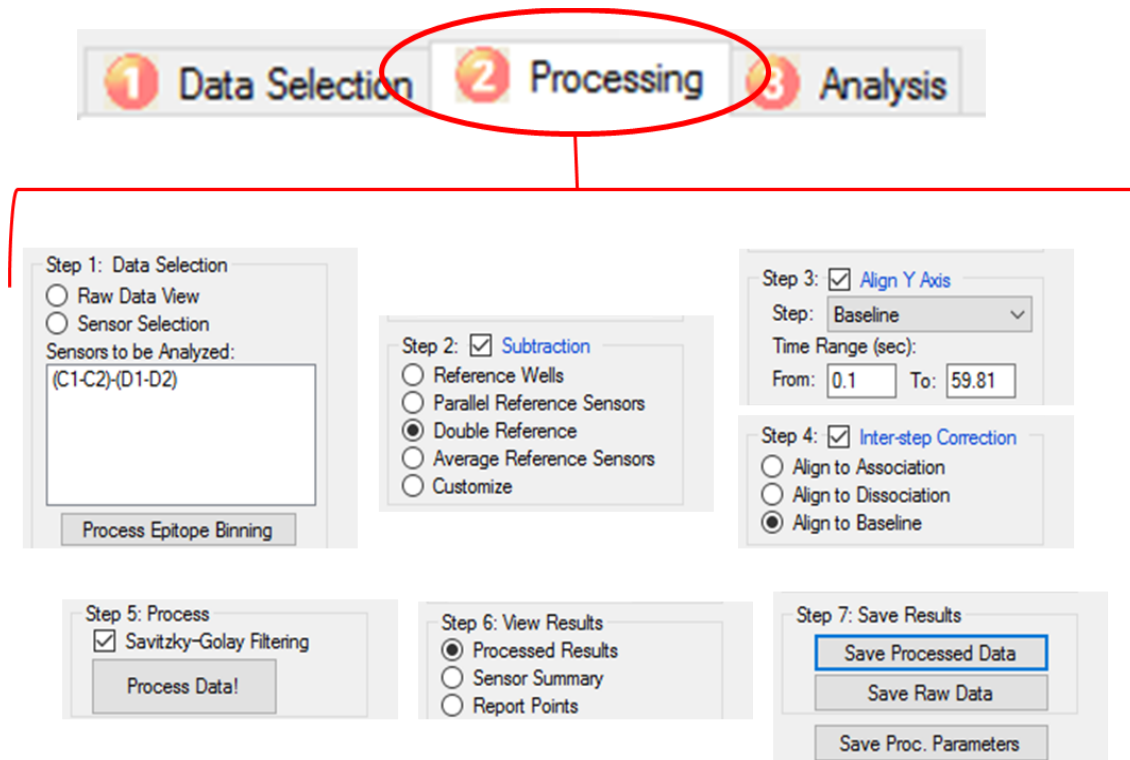


Figure 3.4. All steps of processing section. In the software those appear as vertical list of steps comes after one another.

Analysis. It is the most important section of the software that applies curves on the experimental data finalized by the processing section. The analysis section bifurcates into three main parts: curve fitting, steady state analysis and data export. These parts / steps carry numerous options for achieving quantitative values with minimum artifact. However, the options applied for investigating the binding profile of PB-molecules are the following.

1. **Curve Fitting:** This part of analysis broke down further into multiple small steps:
 - Step to analyze: In this step, association and dissociation were selected together for analysis.
 - Model: Here, the 1:1 model was picked for protein-ligand binding.
 - Fitting: Two kinds of fittings are available in this step; global and local. Local fitting is suitable for multiple inhibitors with a single concentration or it could also be applied to inhibitors with more than one binding site. Whereas, global fitting is perfect for multiple concentrations of a single inhibitor. Global fitting has two more options; 1st, group by sensor or color, and, 2nd, R_{max} linked or unlinked. Since PB-molecules were individually analyzed, therefore, global fitting was applied group by sensor and unlinked by R_{max} .
 - Window of interest: Here, the time of selected steps could be defined for curve fitting. In our data, the entire time of association and dissociation was selected for curve fitting. Hence, the button “use entire step times” was pressed and afterward “fit curves!” button was pressed to obtain the quantitative values (e.g. R_{max} (nm), k_{on} (1/Ms), k_{off} (1/s), K_D etc.) of inhibitor.
2. **Steady State Analysis:** This step could be performed when normal kinetic analysis is not possible, e.g. low affinity ligands, abnormal k_{on} and k_{off} rates etc. This option was avoided in the experiments because the normal kinetic analysis was sufficient to generate kinetic values.
3. **Data Export:** The final results and its various parameters are stored and exported in this step. Multiple options are available to include and exclude different parameters, values, images etc.

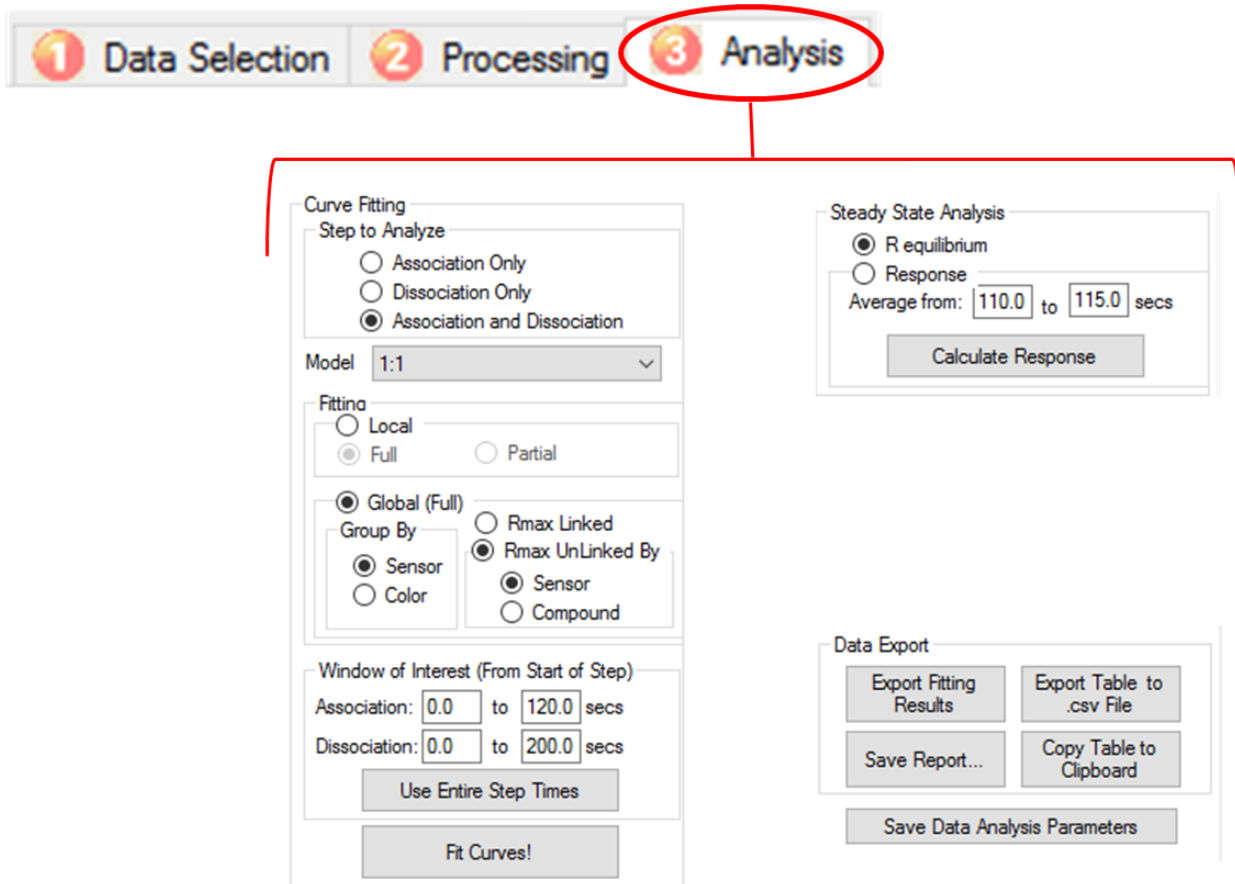


Figure 3.5. Appearance of analysis section in the software is as vertical list. In order to see details of each step and button read application note 14 of FortèBio.

3.1.5. Investigation of PB-3 binding to PLY and PLYC428A by BLI

To establish a difference of affinities between PLY and PLY-C428A toward **PB-3**, a customized BLI assay was developed. The assay was a qualitative comparison between PLY and PLY-C428A and it was examined on FortèBio Octet K2 system, and in accordance with the binding kinetics analysis, FortèBio NiNTA biosensors and kinetic buffer were subjected to use.

Data acquisition. After fulfilling the earlier explained prerequisites of the instrument and sensors (i.e. soaking of sensors in the kinetic buffer and switching on the instrument 0.5 h before the experiment), the data acquisition software was operated to design the plate for the experiment. Two adjacent rows were allocated, one for PLY and the other for PLY-C428A. Wells of the rows were assigned for baseline, load, sample with three different concentrations (2, 4 and 8 μM) and wash. Afterward, similar to the earlier explained method, the assay steps were defined. It included baseline, loading, inhibitor baseline, association and dissociation. The sequence and timing of each step was later added to the assay definition. Next, a pair of parallel sensors were selected in the sensor tray at an identical position to the sample rows on the sample plate. PLY and PLY-C428A each 100 $\mu\text{g/ml}$ were loaded onto adjacent biosensors and, according to assay definition, stepwise, soaked in wells containing different concentrations of **PB-3**.

Data Analysis. After the experiment, the data for both sensors were first selected in the processing section and then opened in the same section of the data analysis software for scrutiny. The assay data contained all steps in a defined sequence and this data was aligned to a common point on the Y axis. Thereafter, out of all steps, only the association step of both proteins with **PB-3** at 2, 4 and 8 μM was of critical importance for comparison. Therefore, the raw data of association steps were copied from the data analysis software and transferred to Graphpad Prism 6 (software). Here, the association of PLY and PLY-C428A with **PB-3** were plotted in a response vs time XY graph. Time (s) was plotted on the X axis whereas the response (nm) was plotted on the Y axis. The association of PLY and PLY-C428A with **PB-3** at different concentrations was distinguished by different colors which were explained in the legend of the graph.

3.1.6. Evaluation of binding between PB-molecules and PLY-mutants

The qualitative analysis of interaction between PB-molecules and PLY-mutant versions (PLY-D205R, PLY-E151Q, and PLY-DM) including PLY wild type was evaluated by BLI assay. FortèBio Octet K2 system, NiNTA sensors and kinetic buffer were employed in this experiment. Pre-wetting of biosensors in kinetic buffer and activating the Octet K2 system were imperative prior to commencing the experiment.

It was a complicated experiment to execute and was established in parts. To ensure consistency among the data, **PB-2** alone was chosen as a representative of PB-molecules for evaluation against all proteins. First, all the proteins were individually examined against **PB-2** under constant conditions. Then, the data acquired from those experiments were inspected and relevant data were combined to layout a qualitative comparison.

Data acquisition. As a separate experiment was commenced for each protein, therefore, the plate design for each experiment was identical. Two parallel rows were marked, one for sample protein and the other for reference / control wells. Wells were defined for baseline, load, sample with three different concentrations of **PB-2** (0.4, 4 and 40 μM) and wash. Thereafter, the assay steps were defined in a sequential manner. Steps started from baseline to protein loading, then led to inhibitor baseline, association and dissociation. The latter three were repeated for all concentrations of the inhibitor. Later, a pair of sensors, a sample and a reference, were selected according to the adjoining position on the sample plate. The concentration of proteins was 100 $\mu\text{g/ml}$ and it was constant throughout all experiments.

Data Analysis. After the initial selection, the raw data of each experiment was opened in the processing section. Here, the data of each experiment was aligned to a common point on the Y axis. Thereafter, the assay steps were discreetly reviewed and, afterward, the middle concentration of **PB-2**, i.e. 4 μM was chosen for comparison between all proteins. Hence, for each protein, **PB-2** association and dissociation at 4 μM were independently isolated and combined in a XY graph of Graphpad prism 6, where time (s) was shown on the X axis, and the response (nm) was available on the Y axis. The binding of PB-2 with each protein was highlighted by a different color which was available in the graph legend.

3.1.7. Aggregation analysis via dynamic light scattering

Multiple concentrations of **PB-3** were prepared in PBS by dissolving from DMSO stock solution. The total content of DMSO was always $\leq 1.5\%$. The particle size distributions were determined by placing 800 μl of sample in a glass cuvette into Nicomp nano Z3000 (Particle sizing system). Data was acquired by Software ZPW388 V2.16.

3.1.8. Lactate dehydrogenase assay

Lactate dehydrogenase (LDH) is widely present within most of the body tissues. LDH quantification is one of the most appropriate assays to quantify the cellular damage, especially in the case of CDC, because as soon as the target cell membrane is ruptured, the discharge of LDH is detected. To quantify LDH release, Pierce LDH Cytotoxicity Assay Kit was purchased from Thermo Scientific for 1000 reactions. It contained a lyophilized powder known as substrate mix and an assay buffer. The LDH reagent was prepared by gentle mixing of lyophilized powder in double distilled water (11.4 ml) and once the powder was dissolved, 0.6 ml of assay buffer was added. Afterward, this ready to use, light sensitive reagent was stored at $-20\text{ }^{\circ}\text{C}$ in the form of 5 ml aliquots in aluminum foil wrapped. Since freeze-thaw of LDH reagent was not advisable, thus, an aliquot was only one time use, though it was sufficient for a single 96-well plate.

To investigate the effect of an inhibitor in the LDH assay, the human alveolar epithelial cells (A549 cells) were grown in Ham's F12 medium complemented with 10% FCS (fetal calf serum). In most of the experiments, 12-well plates were used for cultivation of cells and cells were seeded according to 1×10^5 cells per well. In other experiments, 96-well plates were employed and in those the seeding cell count was $1\text{--}2 \times 10^4$ per well. The next day, Ham's F12 medium with 10% FCS was replaced by 2% FCS containing medium and wells were incubated for a further 24 h. Thereafter, toxin (15 nM) + increasing concentrations of inhibitors were incubated for 4 h and 24 h at $37\text{ }^{\circ}\text{C}$. Cells with media and 5 % Triton X-100 samples were kept as negative and positive controls, whereas toxin alone and inhibitor (highest concentration) alone samples were regarded as toxin and inhibitor controls respectively. The cellular supernatants of each sample were aspirated after the mentioned time slots and centrifuged at 2000 RPM for 10 min at $4\text{ }^{\circ}\text{C}$. Since only small amount of supernatants were required for LDH

quantification, the remaining supernatants could be stored in a freezer (-20 °C) as an experiment control and if some error or mistake occurred then, those could be reused.

The LDH reagent from the reaction kit was meanwhile thawed and then, in a 96-well plate, mixed with supernatant of each sample in 1:1 ratio, i.e. 50 µl of reagent and sample. The mixing of reagent and supernatant must be carefully performed and the bubble-formation should be avoided, otherwise it would be difficult to remove bubbles and it could interfere with the absorption. The mixture was incubated in the dark for 0.5 h and later, the absorption at 490 nm was measured in a microplate reader. The cytotoxicity data was collected in an excel file and the percentage cytotoxicity of an individual sample was determined by using the following formula:

$$\text{Cytotoxicity (\%)} = \frac{(\text{Experimental value} - \text{Negative control})}{(\text{Positive control} - \text{Negative control})} \times 100$$

Thereafter, the data were transferred to Graphpad Prism 6 and plotted in a bar graph. Moreover, Mann Whitney test was applied via Prism 6 to determine the statistical significance between two columns.

3.1.9. Liposomes preparation

Cholesterol and 1,2-dioleoyl-sn-glycero-3-phosphocholine (DOPC) containing liposomes were prepared in the lab by extrusion. Stock solutions of DOPC (25 mg/ml) and cholesterol (10 mg/ml) were prepared in chloroform. These solutions were stored in a glass-vial and flushed with argon and preserved at -20 °C for further use. Liposomes containing 30% of cholesterol were successful in mimicking the natural lipid membrane in reported studies.²⁸ Therefore, 70% DOPC and 30% cholesterol were mixed together in a round bottom flask with chloroform as a solvent. Afterward, the solvent was evaporated with the aid of a rotatory evaporator. The temperature of the rotatory evaporator was 40° C and the pressure was 475 mbar at the beginning, and it was gradually reduced to 0 mbar. Under these conditions, a thin film of dried lipids was formed in the round bottom flask. Thenceforth, the dried lipids were rehydrated by PBS buffer and the suspension was shaken (500 RPM) overnight in a closed flask at room temperature.²⁸ Next day, the overnight suspension was first shock-frozen in liquid nitrogen and immediately thawed at room temperature. Such a freeze-thaw cycle was repeated three more times. Afterward, a polycarbonate filter (100 nm) was installed in

the assembly of a manual extruder that was purchased from Avanti polar lipids, USA. The lipid suspension was then extruded in 25 cycles at room temperature over the 100 nm polycarbonate membrane to produce uni-lamellar vesicles.²⁸ These liposomes were characterized by dynamic light scattering (DLS) and the mean diameter of vesicles were measured, it was 101.7 ± 27.7 nm. Furthermore, the polydispersity index of liposomes was 0.074, at 23° C with an intensity of 300 KHz. Liposomes could be stored for up to one week, however, in cryo-TEM experiments, always fresh prepared liposomes were used. A general scheme of lab production of liposome is available in the following figure.

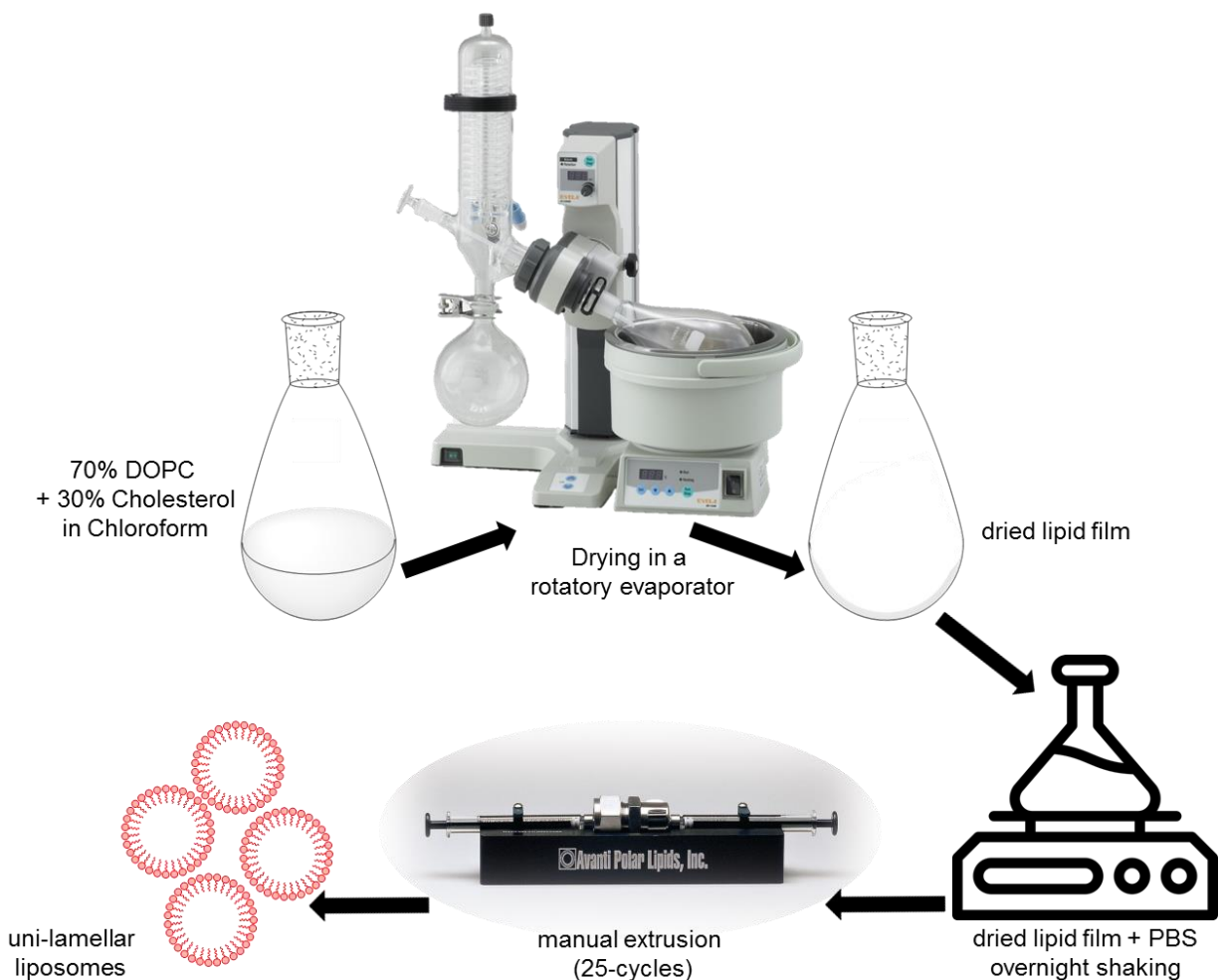


Figure 3.6. The schematic flow of liposome production in our lab.

3.1.10. Protein-liposomes sample preparation for Cryo-TEM

To investigate the inhibitor effect on pore formation of PLY, first, three types of samples were prepared. It included a liposomes only sample, a protein-liposomes sample and

a pre-incubated inhibitor-protein with liposomes sample. The liposomes were used as a control sample to check the quality and homogeneity of liposomes and to prepare this sample, 2 mM of liposomes (70:30 DOPC: Cholesterol) were incubated alone at room temperature with shaking for 1 h, then Cymal-6 (0.56 mM) was added to liposomes and incubation time with same conditions were extended for 10 min, thereafter, the sample was ready for application on to the Cryo-TEM grid.

In the case of protein-liposomes samples, liposomes (2 mM) were incubated with PLY (1 mg/ml) for 1 h at 37 °C with shaking. Then, after 1 h, Cymal-6 (0.56 mM) was added to the protein-liposomes mixture and a further 10 min incubated. At this stage, protein-liposomes samples were ready to be blotted on the Cryo-TEM grid. The protein-liposomes sample visualizes the pore formation under the influence of PLY on the membranes of liposomes.²⁵² However, in addition to the pore formation on the membrane of liposomes, isolated pores of PLY-oligomeric ring could be visualized, if liposomes are solubilized, and isolation of the PLY-pores required further treatment of protein-liposomes sample. Therefore, after cymal-6 incubation, the samples were further incubated with amphipol for 0.5 h.²⁸ Amphipol was added to the system in a 5:1 (w/w) ratio to PLY.(rf) Amphipol is a mild detergent and it was known to solubilize the liposomes without distorting PLY-oligomeric pore assembly, however, to detect the isolated pores in cryo-TEM detergents (cymal-6 and amphipol) must be withdrawn from the sample.²⁸ Thus, detergents were exchanged with PBS by a dialysis cassette (Slide-A-Lyzer® G2, Thermo scientific, USA). The buffer exchange was executed twice after 2 h and, then, after overnight, at 4 °C.

The direct effect of an inhibitor on PLY induced pore formation was analyzed by inclusion of **PB-2** as a member of PB-molecules. Hence, in an inhibitor-protein with liposomes sample, **PB-2** (100 µM) from a stock solution of DMSO was incubated with PLY (1 mg/ml) for 10 min in PBS with shaking at 37 °C. Thereafter, liposomes (2 mM) were added to the sample and incubated for 1 h in same conditions and, finally, 0.56 mM of cymal-6 was added and incubation extended for further 10 min. The DMSO content of the sample was always $\leq 5\%$.

3.1.11. Cryo-TEM investigation

Preparation of cryo-TEM-samples. Vitrobot™ Mark IV (Thermo Fisher Scientific) is an instrument designed to impart samples on grids. The Vitrobot was operated at 22 °C and at a relative humidity of 100%. In the preparation chamber of the Vitrobot a 4 µl sample was applied on a Quantifoil (R4/1 batch of Quantifoil Micro Tools GmbH, Jena, Germany) grid which was surface plasma treated for 60 s at 10 mA just prior to use. Excess sample was removed by blotting for 4 s, and the ultrathin film thus formed on the grid was plunged into liquid ethane just above its freezing point.

Imaging of cryo-TEM-samples. Vitrified samples were imaged with a Talos Arctica™ TEM (Thermo Fisher Scientific) at 200kV accelerating voltage and a primary magnification of 28k. Images were recorded by a Falcon III direct electron detector at full 4k resolution resulting in a pixel size of 0.373 nm/pixel. The defocus value was set to 4.9 µm.

Cryo-electron tomography. Vitrified samples were transferred under liquid nitrogen into a Talos Arctica™ TEM (Thermo Fisher Scientific, Hillsboro, Oregon; USA) at 200kV accelerating voltage employing a Volta phase plate in the back focal plane of the objective lens at a primary magnification of 28k. Image series in the tilt range of -64°/64° (2° tilt-increments) were recorded by a Falcon III direct electron detector at full 4k resolution resulting in a pixel size of 0.373 nm/pixel. The defocus value was set to -300 nm. A total dose of 180 e/Å² was accumulated on the specimen. The image stack alignment, 3D reconstruction and data processing were performed in the context of the FEI Inspect 3D software V4.3.

3.1.12. Human lung cells protection from native PLY

The human lung alveolar epithelial cell line A549 (ATCC, CCL-185) was cultured in Ham's F12 medium (Biochrome, Berlin, Germany) supplemented with 10% (v/v) fetal bovine serum (FBS; Capricorn Scientific GmbH, Ebsdorfergrund, Germany) and 2 mM L-glutamine (Invitrogen Life Technologies) at 37 °C and 5% CO₂. A549 cells were seeded in 8-well-ibidi-slides with a strength of 2.5×10^4 cells per well, after 24 h of incubation, the medium was changed to Ham's F12, 2% FBS. Next day, the membrane potential was determined by loading cells with 10 nM tetramethyl-rhodamine methyl ester (TMRE from Life Technologies) for 30 min at 37°C / 5% CO₂ and washing 3 times with Hanks' balanced salt solution (HBSS). Then, the medium was changed to Ham's F12 with CellEvent Caspase-3/7 Green Detection Reagent (Life Technologies). Cells were then, stimulated with 15 nM PLY (0.8 µg/ml), and with equal strength of PLY pre-incubated with inhibitor for 10 min (**PB-2**: 8 µM, **PB-3**: 6 µM). A sample of only cells in medium was marked as negative control and a sample of cells with inhibitor alone was reserved as inhibitor control.

3.1.13. Mitigation of *Streptococcus pneumoniae* infection

The human lung alveolar epithelial cell line A549 were seeded and grown, according to the earlier mentioned protocol of protection against native PLY experiment. In the second step, A549 cells were stained with TMRE and then, infected with the *S. pneumoniae*. D39 derived capsule locus (*cps*) deletion mutant D39Δ*cps* and the *cps*/pneumolysin double mutant D39Δ*cps*Δ*ply* cultured in Todd-Hewitt broth supplemented with 0.5% yeast extract (BD) to midlog phase using a multiplicity of infection of 1 in Ham's F12 medium supplemented with 2% FBS for 24h at 37°C/5% CO₂. One well was infected with D39Δ*cps* and inhibitor **PB-3** (6 µM) was added. Addition of 6 µM **PB-3** was repeated after every 4 h for 16 h.

3.1.14. Live-cell microscopy

Microscopy was performed on a LSM780 confocal laser-scanning microscope driven by Zen 2012 software using a 40x/1.2 NA C-Apochromat objective with 488 nm, 561 nm, and 622 nm excitation lines (Carl-Zeiss). To obtain clear micrographs, images of cells were captured in phenol red-free medium at 37 °C / 5% CO₂. Micrographs were taken after 24 h of incubation in case of native PLY-inhibitor experiment, and after 16 h in case of *S. pneumoniae* infection experiment.

3.1.15. Protein-ligand complex investigation by MS

Sample preparation for native MS. The buffer of PLY and PLY-C428A contained 50% glycerol (20 mM MOPS pH: 8, 50 % glycerol) because both are highly hydrophobic proteins and tend to precipitate rapidly in aqueous buffers without glycerol. On the other hand, glycerol containing buffer is not suitable for native MS analysis. Therefore, the buffer of proteins was exchanged to ammonium acetate buffer (10 mM ammonium acetate, pH: 6.9) using dialysis cassette (Slide-A-Lyzer® G2, Thermo scientific, USA) of MWCO: 2000 Da for 2 h, and again 2h and then, for overnight, at 4 °C. How buffer was exchanged is depicted in the **Figure 3.8**. Afterward, proteins were concentrated by using a filter of MWCO: 30,000 Da (Vivaspin 6 Sartorius) and concentration was measured by NanoDrop One (Thermo Scientific™). Proteins appeared soluble, however, these underwent precipitation / aggregation upon spinning and a significant reduction in potency was observed. It implied that proteins were unstable in 10 mM ammonium acetate, pH: 6.9 buffer.

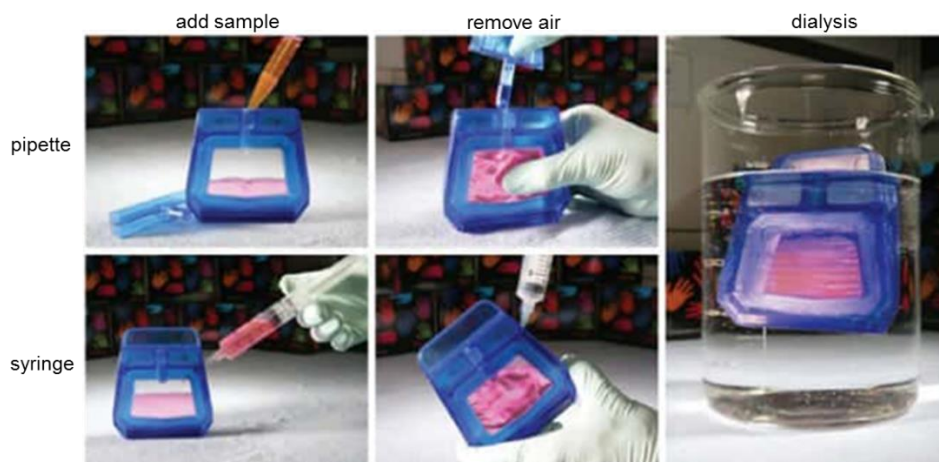


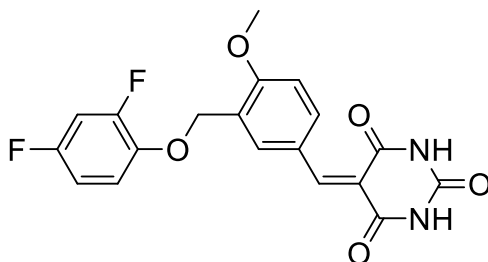
Figure 3.7. The image shows the procedure of buffer exchange.

Sample preparation for denaturing MS. The MS buffer for denaturing MS contained 50% acetonitrile and 50% water. A mixture of 1:1 ratio of protein to inhibitor (6 μ M, both) was prepared in MS buffer with a final volume of 20 μ l, samples contained up to 5% glycerol and up to 6% DMSO. In protein control sample, 6 μ M of protein were added to MS buffer containing 6% DMSO. All samples were loaded on 6550 iFunnel Q-TOF LC/MS (Agilent Technologies) after 2 to 5 min of incubation.

LC-QTOF-MS parameter and data analysis. 1 – 2 μ l of sample was used for analysis. The HPLC parameters: Jupiter C18- column (5 μ M, 300 Å, 3 x 250 mm) Phenomenex, injection volume: 1 μ l, gradient: 0-4 min 95/5 (A/B), 4-10 min from 95/5 (A/B) to 40/60 (A/B), 10-12 min 40/60 (A/B), 12-15 min from 40/60 (A/B) to 95/5 (A/B); QTOF parameters: fragmentor 350 V, nozzle voltage 2000 V, VCap 3500 V, 0-4 min waste. The final data was analyzed with help of Agilent MassHunter BioConfirm 10.0 Software. The deconvoluted spectra were integrated via maximum entropy-algorithm with no limited m/z-range.

3.1.16. Chemical synthesis

5-(3-((2,4-Difluorophenoxy)-methyl)-4-methoxybenzylidene)-pyrimidine-2,4,6(1H,3H,5H)-trione (PB-1)



3-[(2,4-Difluorophenoxy)-methyl]-4-methoxybenzaldehyde (139 mg, 0.5 mmol) was dissolved in 10 ml of absolute ethanol. Next, barbituric acid (67 mg, 0.525 mmol) was added to solution. The reaction mixture was heated for 4 h at 100 °C, and then cooled to room temperature. The crystals of product **PB-1** were filtered off, washed twice with ethanol, and dried in *vacuo*.

Yield: 170 mg (87%)

Melting point: 261 °C

¹H NMR (600 MHz, DMSO-*d*₆) δ [ppm] = 11.31 (s, 1H), 11.18 (s, 1H), 8.45 (s, 1H), 8.42 (d, *J* = 8.9 Hz, 1H), 8.24 (s, 1H), 7.30 – 7.26 (m, 2H), 7.21 (d, *J* = 8.9 Hz, 1H), 7.00 (t, *J* = 10.9 Hz, 1H), 5.11 (s, 2H), 3.94 (s, 3H).

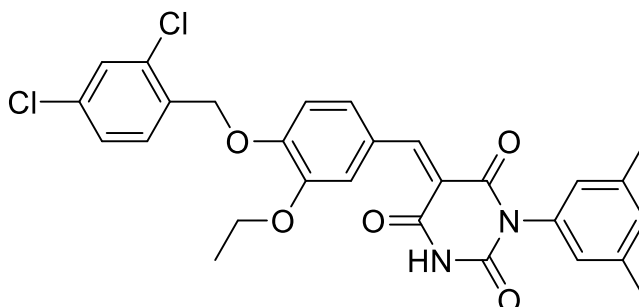
¹³C NMR (151 MHz, DMSO-*d*₆) δ [ppm] = 163.84, 162.11, 161.22, 156.71 – 154.76 (m), 154.59, 151.67 (dd, *J* = 247.0, 12.8 Hz), 150.20, 143.04 (dd, *J* = 10.8, 3.6 Hz), 137.90, 136.49, 124.91, 124.10, 116.46 (dd, *J* = 9.9, 3.0 Hz), 116.03, 111.04, 110.85 (dd, *J* = 22.4, 4.3 Hz), 104.86 (dd, *J* = 27.2, 22.4 Hz), 66.40, 56.19.

¹⁹F NMR (565 MHz, DMSO-*d*₆) δ [ppm] = -119.85, -129.36.

ESI-HRMS: [M+H⁺] calculated for C₁₉H₁₅F₂N₂O₅⁺: 389.0949 Da, found: 389.0944 m/z.

Elemental analysis: calculated for C₁₉H₁₄F₂N₂O₅: C=58.77%, H=3.63%, N=7.21%, found: C=58.98%, H=3.68%, N=7.25%.

(E/Z)-5-(4-(2,4-Dichlorobenzoyloxy)-3-ethoxybenzylidene)-1-(3,5-dimethylphenyl)-pyrimidine-2,4,6(1H,3H,5H)-trione (PB-2)



PB-2.2 (180 mg, 0.55 mmol) was dissolved in ethanol (9 ml) and water (1 ml). Next, **PB-2.3** was added to the solution which was heated under reflux until formation of precipitates. Further, ethanol (10 ml) was added and heated under reflux for 2 h. Yellow crystals were formed, which were filtered off and washed with ethanol and diethylether. Crystals were dried in high vacuum to furnish product **PB-2**.

Yield: 233 mg (79 %)

Melting point: 215 °C

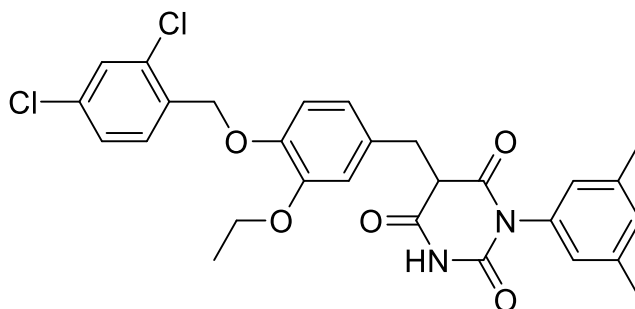
¹H NMR (500 MHz, DMF-*d*₇) δ [ppm] = 11.64, 11.56 (2s, 1H), 8.57, 8.41 (2s, 1H), 8.41, 8.30 (2s, 1H), 8.0-7.9 (m, 1H), 7.8 – 7.7 (m, 2H), 7.55 (m, 1H), 7.4 – 7.3 (m, 1H), 7.2-7.0 (m, 3H), 5.38, 5.36 (2s, 2H), 4.24 – 4.08 (2q, 2H), 2.33 (s, 6H), 1.43 – 1.30 (2t, 3H).

¹³C NMR (126 MHz, DMF-*d*₇) δ [ppm] = 164.28, 162.00, 156.65, 156.10, 153.23, 153.15, 150.85, 150.74, 148.28, 138.63, 138.60, 136.32, 136.09, 134.46, 134.20, 134.16, 133.84, 131.79, 131.62, 131.56, 131.28, 130.02, 129.43, 129.41, 128.03, 128.01, 127.15, 127.01, 126.92, 126.77, 119.38, 118.99, 116.81, 116.65, 113.27, 67.69, 64.64, 20.68, 14.59, 14.54.

ESI-HRMS: [M+H⁺] calculated for C₂₈H₂₅Cl₂N₂O₅⁺: 539.1141 Da, found: 539.1133 m/z.

Elemental analysis: calculated for C₂₈H₂₄Cl₂N₂O₅: C=62.35 %, H=4.48 %, N=5.19 %, found: C=62.35 %, H=4.497 %, N=5.193 %.

5-(4-(2,4-Dichlorobenzoyloxy)-3-ethoxybenzyl)-1-(3,5-dimethylphenyl)-pyrimidine-2,4,6(1H,3H,5H)-trione (PB-2.1)



PB-2 (100 mg, 0.185 mmol) was suspended in ethanol (5 ml) and sodium borohydride (21 mg, 0.556 mmol) was added. The mixture was stirred for 45 min. Next, 2 M HCl was added until a pH 2 was reached. The reaction mixture was concentrated *in vacuo* and water (5 ml) was added. Further, the mixture was extracted 3 times with ethyl acetate (10 ml). Organic phases combined and dried with Na₂SO₄. Solvents were removed and the obtained greasy residue was dried in high vacuum to furnish **PB-2.1** as a colorless oil.

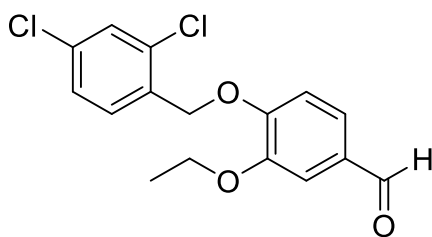
Yield: 82 mg (82 %)

¹H NMR (500 MHz, Chloroform-*d*) δ [ppm] = 7.98 (s, 1H), 7.53 (d, *J* = 8.3 Hz, 1H), 7.40 (s, 1H), 7.05 (s, 1H), 6.82 (d, *J* = 7.9 Hz, 1H), 6.72 (s, 1H), 6.69 (d, *J* = 8.6 Hz, 1H), 6.51 (s, 2H), 5.18 (s, 2H), 4.02 (q, *J* = 7.5 Hz, 2H), 3.86 (s, 1H), 3.55 – 3.46 (m, 2H), 2.31 (s, 6H), 1.43 (q, *J* = 6.6, 5.3 Hz, 3H).

¹³C NMR (126 MHz, Chloroform-*d*) δ [ppm] = 168.73, 167.87, 149.50, 149.32, 147.85, 139.44, 134.10, 133.75, 133.09, 132.95, 131.40, 129.59, 129.22, 128.95, 127.47, 125.87, 121.88, 115.30, 115.06, 68.10, 64.74, 50.87, 36.84, 21.33, 14.99.

ESI-HRMS: [M+H⁺] calculated for C₂₈H₂₇Cl₂N₂O₅⁺: 541.1297 Da, found: 541.1290 m/z.

Elemental analysis: calculated for C₂₈H₂₆Cl₂N₂O₅: C=62.12 %, H=4.84 %, N=5.17 %, found: C=62.28 %, H=4.885 %, N=5.266 %.

4-(2,4-Dichlorobenzyloxy)-3-ethoxybenzaldehyde (PB-2.2)

3-Ethoxy-4-hydroxybenzaldehyde (866 mg, 5.21 mmol) was dissolved in DMF (25 ml). Potassium carbonate (1440 mg, 10.42 mmol) was added to the solution and stirred for 1 h at room temperature. Next, 1-chloromethyl-2,4-dichloro-benzene (730 μ l, 5.21 mmol) was added to the reaction mixture and heated for 5 h at 45 °C. The suspension was stirred overnight at room temperature, extracted with ethyl acetate (100 ml), washed with brine (50 ml) and water (50 ml). Organic phases were combined and dried with Na₂SO₄. Solvent was removed by evaporation and the semi-solid residue was dried in high vacuum to furnish product **PB-2.2**.

Yield: 1.66 g (99 %)

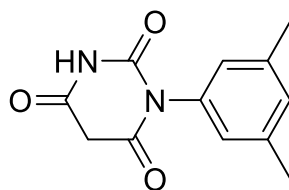
Melting point: 105 °C

¹H NMR (500 MHz, DMSO-*d*₆) δ [ppm] = 9.86 (d, *J* = 17.2 Hz, 1H), 7.67 (d, *J* = 18.0 Hz, 1H), 7.61 (d, *J* = 8.3 Hz, 1H), 7.54 (d, *J* = 9.2 Hz, 1H), 7.50 (d, *J* = 10.4 Hz, 1H), 7.43 (s, 1H), 7.26 (d, *J* = 8.1 Hz, 1H), 5.24 (d, *J* = 16.9 Hz, 2H), 4.10 (td, *J* = 15.4, 14.2, 7.6 Hz, 2H), 1.34 (p, *J* = 9.4, 8.8 Hz, 3H).

¹³C NMR (126 MHz, DMSO-*d*₆) δ [ppm] = 191.41, 152.84, 148.65, 133.64, 133.46, 133.08, 131.07, 130.28, 128.94, 127.61, 125.52, 113.25, 111.38, 67.04, 64.02, 14.55.

ESI-HRMS: [M+H⁺] calculated for C₁₆H₁₅Cl₂O₃⁺: 325.0398 Da, found: 325.0396 m/z.

Elemental analysis: calculated for C₁₆H₁₄Cl₂O₃: C=59.10 %, H=4.34 %, found: C=59.75 %, H=4.34 %.

1-(3,5-Dimethylphenyl)-pyrimidine-2,4,6-(1H,3H,5H)-trione (PB-2.3)

Sodium metal (287 mg, 12.5 mmol) was dissolved in absolute ethanol (15 ml). Next, N-(3,5-dimethylphenyl)-urea (821 mg, 5 mmol) and diethyl malonate (915 μ l, 6 mmol) were added to the sodium ethoxide solution, and the reaction mixture was stirred at room temperature for about 10 min until a clear solution was formed. The mixture was heated under reflux for 6 h, and then it was stirred over night at room temperature. The solvent was removed by evaporation and water (15 ml) was added to residue. Further, 2 M HCl was added dropwise until pH 1-2 was reached and the solution was stirred for 0.5 h. The obtained white crystals of **PB-2.3** were filtered off, washed with water, and dried in high vacuum.

Yield: 1.07 g (92 %)

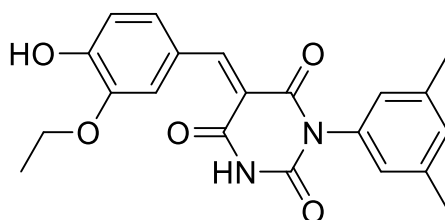
Melting point: 219-220 °C

$^1\text{H NMR}$ (500 MHz, DMSO- d_6) δ [ppm] = 11.46 (s, 1H), 7.04 (s, 1H), 6.83 (s, 2H), 3.71 (s, 2H), 2.25 (s, 6H).

$^{13}\text{C NMR}$ (126 MHz, DMSO- d_6) δ [ppm] = 166.75, 166.67, 151.55, 137.97, 134.85, 129.72, 126.39, 40.29, 20.68.

ESI-HRMS: $[\text{M}+\text{H}^+]$ calculated for $\text{C}_{12}\text{H}_{13}\text{N}_2\text{O}_3^+$: 233.0926 Da, found: 233.0927 m/z.

Elemental analysis: calculated for $\text{C}_{12}\text{H}_{12}\text{N}_2\text{O}_3$: N=12.06 %, C=62.06 %, H=5.21 %, found: N=11.13 %, C=58.30 %, H=5.31 %.

(E/Z)-1-(3,5-Dimethylphenyl)-5-(3-ethoxy-4-hydroxybenzylidene)-pyrimidine-2,4,6(1H,3H,5H)-trione (PB-2.4)

3-Ethoxy-4-hydroxybenzaldehyde (44.6 mg, 0.27 mmol) was dissolved in ethanol (5 ml) and **PB-2.3** (58.1 mg, 0.25 mmol) was added to the solution. Next, the mixture was heated for 5 h under reflux and cooled down to room temperature, then stirred overnight at room temperature. Yellow crystals were filtered off and washed with diethyl ether and ethanol. Finally, crystals were dried in high vacuum to furnish product **PB-2.4**.

Yield: 75 mg (79 %)

Melting point: 251 °C

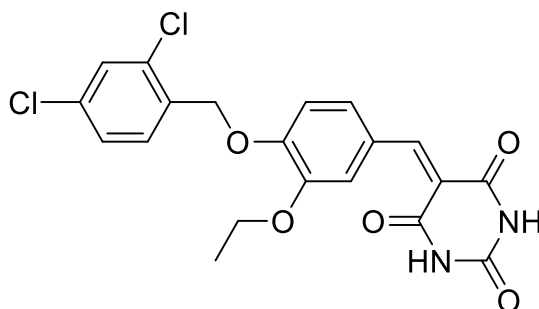
¹H NMR (500 MHz, DMSO-*d*₆) δ [ppm] = 11.56, 11.45 (2s, 1H), 10.51, 10.47 (2s, 1H), 8.41 (d, *J* = 97.3 Hz, 1H), 8.20 (d, *J* = 17.5 Hz, 1H), 7.89 – 7.87 (m, 1H), 7.04 (s, 1H), 6.90 (t, *J* = 9.0 Hz, 3H), 4.13 – 3.99 (2q, 2H), 2.30 (s, 6H), 1.40 – 1.30 (2t, 3H).

¹³C NMR (126 MHz, DMSO-*d*₆) δ [ppm] = 164.41, 162.32, 153.98, 150.75, 146.72, 142.86, 138.47, 136.10, 130.19, 127.25, 127.09, 120.00, 119.43, 115.99, 114.89, 64.48, 21.28, 15.16.

ESI-HRMS: [M+H⁺] calculated for C₂₁H₂₁N₂O₅⁺: 381.1450 Da, found: 381.1445 m/z.

Elemental analysis: calculated for C₂₁H₂₀N₂O₅: C=66.31 %, H=5.30 %, N=7.36 %, found: C=66.43 %, H=5.327 %, N=7.366 %.

5-(4-(2,4-Dichlorobenzoyloxy)-3-ethoxybenzylidene)-pyrimidine-2,4,6(1H,3H,5H)-trione (PB-2.5)



PB-2.2 (84.8 mg, 0.26 mmol) was dissolved in ethanol (5 ml) and pyrimidine-2,4,6-(1H,3H,5H)-trione (35.5 mg, 0.277 mmol) was added. The mixture was heated for 2 h under reflux and cooled down to room temperature. Yellow crystals were filtered and washed with diethylether and ethanol. Finally, crystals were dried in high vacuum to furnish product **PB-2.5**.

Yield: 88 mg (78 %)

Melting point: 253 °C

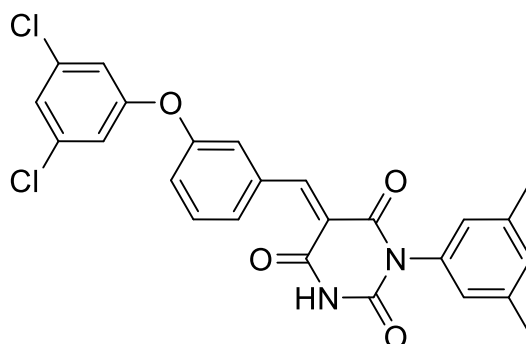
¹H NMR (500 MHz, DMF-*d*₇) δ [ppm] = 11.39, 11.26 (2s, 2H), 8.55 (s, 1H), 8.37 (s, 1H), 7.93 (d, *J* = 8.6 Hz, 1H), 7.75 (d, *J* = 9.0 Hz, 1H), 7.70 (s, 1H), 7.55 (d, *J* = 9.1 Hz, 1H), 7.33, 7.31 (2s, 1H), 5.38 (s, 2H), 4.25 – 4.12 (m, 2H), 1.47 – 1.33 (m, 3H).

¹³C NMR (126 MHz, DMF-*d*₇) δ [ppm] = 164.36, 162.78, 155.97, 153.14, 150.62, 148.23, 134.43, 134.17, 133.83, 131.68, 131.59, 129.40, 128.01, 126.79, 119.01, 116.18, 113.23, 67.67, 64.60, 14.56.

ESI-HRMS: [M+H⁺] calculated for C₂₀H₁₇Cl₂N₂O₅⁺: 435.0515 Da, found: 435.0540 m/z.

Elemental analysis: calculated for C₂₀H₁₆Cl₂N₂O₅: C=55.19 %, H=3.71 %, N=6.44 %, found: C=55.24 %, H=3.745 %, N=6.968 %.

(E/Z)-5-(3-(3,5-Dichlorophenoxy)-benzylidene)-1-(3,5-dimethylphenyl)-pyrimidine-2,4,6-(1H,3H,5H)-trione (PB-2.6)



3-(3,5-Dichlorophenoxy)-benzaldehyde (67.6 mg, 0.253 mmol) and **PB-2.3** were dissolved in absolute ethanol (10 ml). The reaction mixture was heated under reflux for 3 h and cooled down to room temperature. Concentrated reaction mixture (2-3 ml) was heated again under reflux for 6 h and stirred overnight at room temperature. Crystals of product **PB-2.6** were obtained by filtration, washed with diethylether and were dried under vacuum.

Yield: 50 mg (41 %)

Melting point: 230 °C

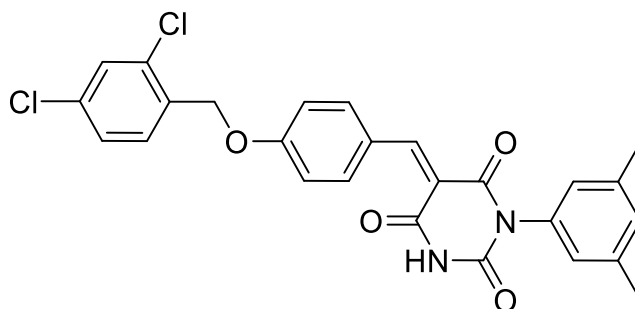
¹H NMR (500 MHz, DMSO-*d*₆) δ [ppm] = 11.74, 11.58 (2s, 1H), 8.38, 8.38 (2s, 1H), 7.94 – 7.88 (m, 1H), 7.82 – 7.75 (m, 1H), 7.59 – 7.47 (m, 1H), 7.36 (d, *J* = 31.5 Hz, 1H), 7.32 – 7.24 (m, 1H), 7.11 (s, 1H), 7.06 – 6.99 (m, 2H), 6.89 (s, 2H), 2.29, 2.27 (2s, 6H).

¹³C NMR (126 MHz, DMSO-*d*₆) δ [ppm] = 160.90, 160.73, 158.26, 154.37, 154.12, 153.73, 153.57, 150.22, 150.11, 137.95, 137.86, 135.21, 135.00, 134.96, 134.90, 130.06, 129.94, 129.76, 129.62, 129.51, 129.21, 126.47, 126.38, 123.16, 123.09, 123.02, 120.63, 120.54, 117.09, 116.88, 20.69, 20.68.

ESI-HRMS: [M+H⁺] calculated for C₂₅H₁₉Cl₂N₂O₄⁺: 481.0722 Da, found: 481.0713 m/z.

Elemental analysis: calculated for C₂₅H₁₈Cl₂N₂O₄: C=62.38 %, H=3.77 %, N=5.82 %, found: C=62.67 %, H=3.837 %, N=5.823 %.

(E/Z)-5-(4-((2,4-Dichlorobenzyl)-oxy)-benzylidene)-1-(3,5-dimethylphenyl)-pyrimidine-2,4,6-(1H,3H,5H)-trione (PB-2.8)



4-((2,4-Dichlorobenzyl)-oxy)-benzaldehyde (72.7 mg, 0.259 mmol) was dissolved in absolute ethanol (10 ml) and **PB-2.3** (60.5 mg, 0.260 mmol) was added to the solution. The mixture was heated under reflux for 5 h and cooled down to room temperature. The suspension was stirred overnight. Yellow crystals were obtained by filtration and washed with ethanol and diethylether. In the end, crystals of product **PB-2.8** were dried in vacuo.

Yield: 87 mg (68 %)

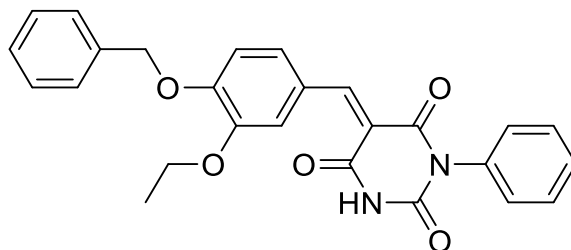
¹H NMR (500 MHz, DMF-*d*₇) δ [ppm] = 11.66, 11.57 (2s, 1H), 8.53 – 8.37 (m, 3H), 7.81 – 7.67 (m, 2H), 7.54 (s, 1H), 7.27(d, *J* = 9.9 Hz, 1H), 7.22 (d, *J* = 8.0 Hz, 1H), 7.08 (s, 1H), 7.04 (s, 2H), 5.38 – 5.35 (q, 2H), 2.34 (s, 6H).

¹³C NMR (126 MHz, DMF-*d*₇) δ [ppm] = 164.19, 163.32, 162.89, 161.84, 156.09, 155.65, 150.84, 138.61, 137.93, 137.87, 136.30, 136.04, 134.40, 133.64, 131.86, 129.99, 129.49, 128.05, 127.16, 127.00, 116.88, 114.98, 67.28, 20.67.

ESI-HRMS: [M+H⁺] calculated for C₂₆H₂₁Cl₂N₂O₄⁺: 495.0878 Da, found: 495.0874 m/z.

Elemental analysis: calculated for C₂₆H₂₀Cl₂N₂O₄: C=63.04 %, H=4.07 %, N=5.66 %, found: C=63.20 %, H=4.078 %, N=5.738 %.

(E/Z)-5-(4-(Benzyloxy)-3-ethoxybenzylidene)-1-phenylpyrimidine-2,4,6(1H,3H,5H)-trione (PB-2.10)



In a solution of 4-(benzyloxy)-3-ethoxybenzaldehyde (128 mg, 0.5 mmol) in ethanol (20 ml) 1-phenylpyrimidine-2,4,6(1H,3H,5H)-trione (102 mg, 0.5 mmol) was added. The mixture was stirred for overnight at room temperature. Crystals were collected by filtration, washed with ethanol and diethylether, and dried under vacuum.

Yield: 139 mg (63 %)

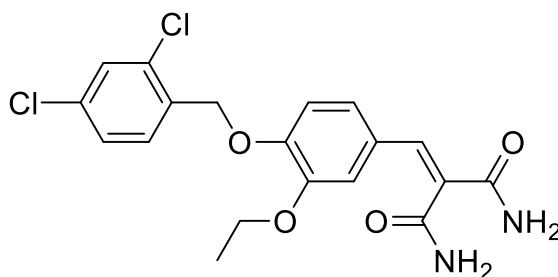
Melting point: 220 °C

¹H NMR (500 MHz, DMF-*d*₇) δ [ppm] = 11.66, 11.55 (2s, 1H), 8.45, 8.22 (2s, 1H), 7.98 – 7.93 (m, 1H), 7.58 – 7.37 (m, 10H), 7.32 – 7.26 (m, 2H), 5.35, 5.32 (2s, 2H), 4.24 – 4.07 (2q, 2H), 1.43 – 1.32 (2t, 3H).

¹³C NMR (126 MHz, DMF-*d*₇) δ [ppm] = 164.18, 156.72, 156.20, 153.74, 150.58, 148.11, 137.03, 136.42, 131.93, 131.42, 129.57, 129.42, 128.95, 128.91, 128.70, 128.69, 128.40, 128.25, 128.02, 127.97, 126.28, 126.13, 119.23, 118.79, 116.07, 112.98, 112.93, 70.55, 70.51, 64.46, 64.41, 14.44, 14.40.

ESI-HRMS: [M+H⁺] calculated for C₂₆H₂₃N₂O₅⁺: 443.1607 Da, found: 443.1599 m/z.

Elemental analysis: calculated for C₂₆H₂₂N₂O₅: C=70.58 %, H=5.01 %, N=6.33 %, found: C=70.73 %, H=5.077 %, N=6.397 %.

2-(4-(2,4-Dichlorobenzoyloxy)-3-ethoxybenzylidene)-malonamide (PB-2.12)

Under nitrogen atmosphere, **PB-2.2** (88.9 mg, 0.273 mmol) and malonamide (30.7 mg, 0.300 mmol) was suspended in toluene (5 ml) in presence of molecular sieves (3 Å). Next, piperidine (27.2 μ l, 0.273 mmol) and glacial acetic acid (15.5 μ l, 0.273 mmol) were added to reaction mixture and was heated under reflux for 5 h, then cooled down to room temperature. Ethyl acetate (10 ml) was added to the reaction mixture and precipitates were formed, which were filtered and washed with ethyl acetate. Combined organic phases were evaporated and product **PB-2.12** was purified by MPLC (DCM / Methanol, 99:1 to 80:20).

Yield: 14 mg (13 %)

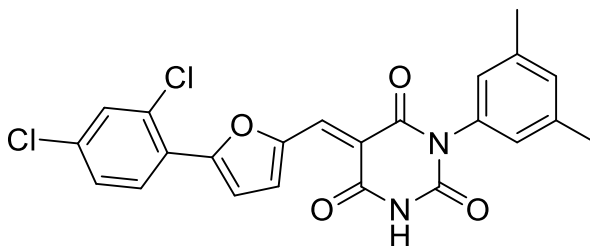
$^1\text{H NMR}$ (500 MHz, DMSO- d_6) δ [ppm] = 7.82 (s, 1H), 7.70(s, 1H), 7.60 (d, J = 8.9 Hz, 1H), 7.50 – 7.47 (m, 2H), 7.29 (s, 1H), 7.23 (s, 2H), 7.13 – 7.04 (m,3H), 5.18 (s, 2H), 4.03 – 3.99 (m, 2H), 1.35 – 1.30 (m, 3H).

$^{13}\text{C NMR}$ (126 MHz, DMSO- d_6) δ [ppm] = 169.60, 165.80, 148.62, 147.98, 134.06, 133.56, 133.47, 133.40, 131.45, 131.09, 128.90, 127.53, 123.17, 119.41, 114.20, 113.90, 66.99, 63.92, 14.64.

ESI-HRMS: $[\text{M}+\text{H}^+]$ calculated for $\text{C}_{19}\text{H}_{19}\text{Cl}_2\text{N}_2\text{O}_4^+$: 409.0722 Da, found: 409.0718 m/z.

Elemental analysis: calculated for $\text{C}_{19}\text{H}_{18}\text{Cl}_2\text{N}_2\text{O}_4$: C=55.76 %, H=4.43 %, N=6.84 %, found: C=55.97 %, H=4.699 %, N=6.921 %.

(E/Z)-5-((5-(2,4-Dichlorophenyl)-furan-2-yl)-methylene)-1-(3,5-dimethylphenyl)-pyrimidine-2,4,6(1H,3H,5H)-trione (PB-3)



5-(2,4-Dichlorophenyl)-furan-2-carbaldehyde (60.3 mg, 0.25 mmol) and **PB-2.3** (58.1 mg, 0.25 mmol) were suspended in ethanol (10 ml). The suspension was heated under reflux for 4 h and cooled down to room temperature. Yellow crystals were collected by filtration, washed with ethanol and diethylether, and dried in vacuo to furnish product **PB-2.3**.

Yield: 89 mg (78 %)

Melting point: 291 °C

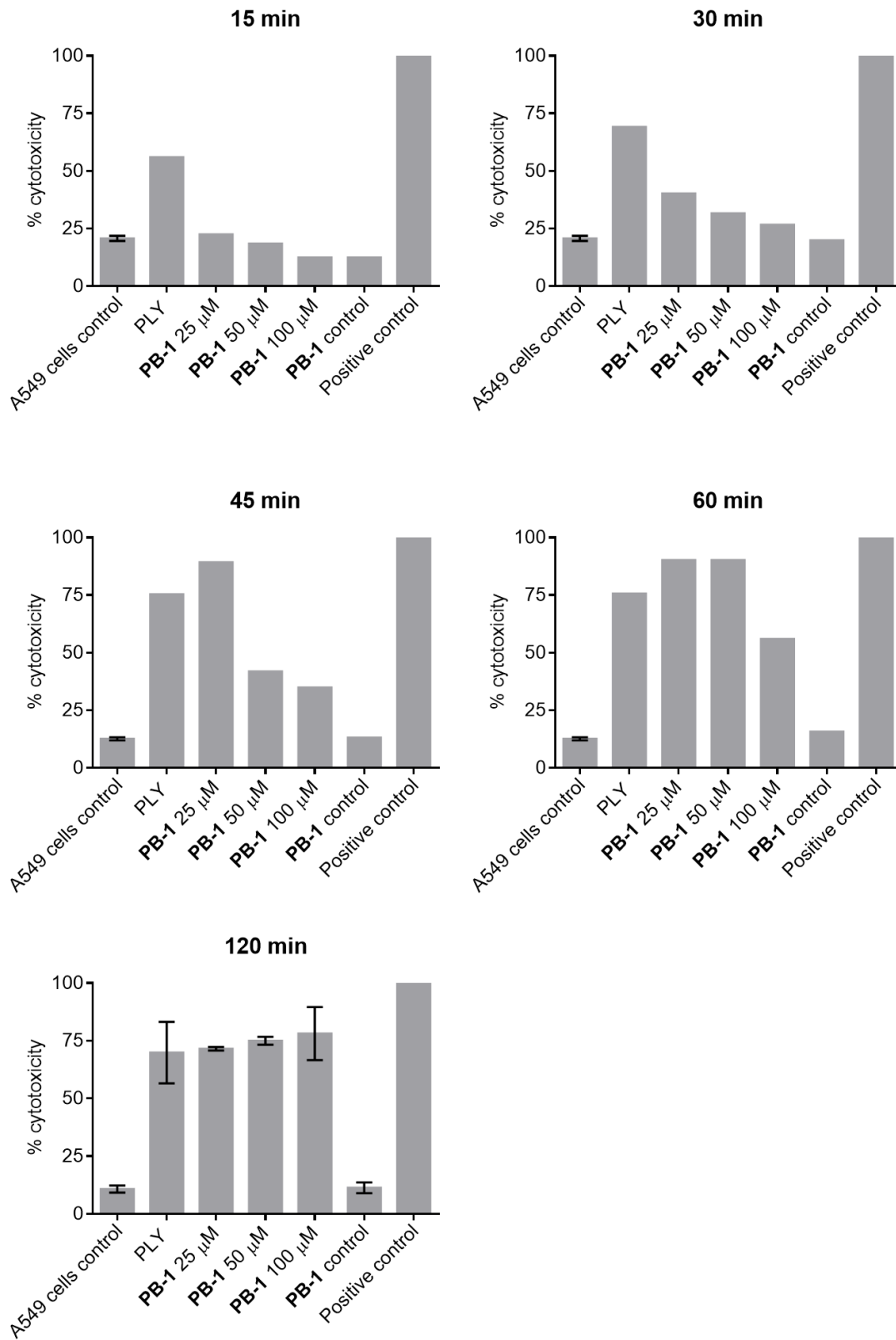
¹H NMR (500 MHz, DMF-*d*₇) δ [ppm] = 11.74 – 11.70 (m, 1H), 8.71 – 8.53 (q, 1H), 8.29 (d, *J* = 24.9 Hz, 1H), 8.21 – 8.15 (m, 1H), 7.82 (s, 1H), 7.70 – 7.55 (m, 2H), 7.10 – 7.04 (m, 3H), 2.35, 2.33 (2s, 6H).

¹³C NMR (126 MHz, DMF-*d*₇) δ [ppm] = 163.57, 162.72, 155.70, 150.79, 138.67, 137.30, 136.99, 136.18, 135.83, 135.54, 132.02, 131.04, 130.84, 130.11, 128.61, 127.07, 126.58, 116.43, 114.59, 20.68.

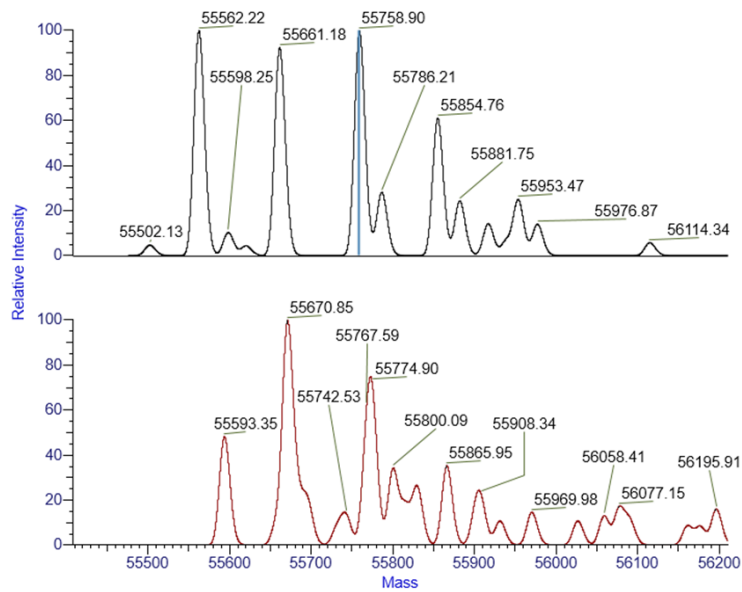
ESI-HRMS: [M+H⁺] calculated for C₂₃H₁₇Cl₂N₂O₄⁺: 455.0565 Da, found: 455.0556 m/z.

Elemental analysis: calculated for C₂₃H₁₆Cl₂N₂O₄: C=60.68 %, H=3.54 %, N=6.15 %, found: C=60.80 %, H=3.577 %, N=6.173 %.

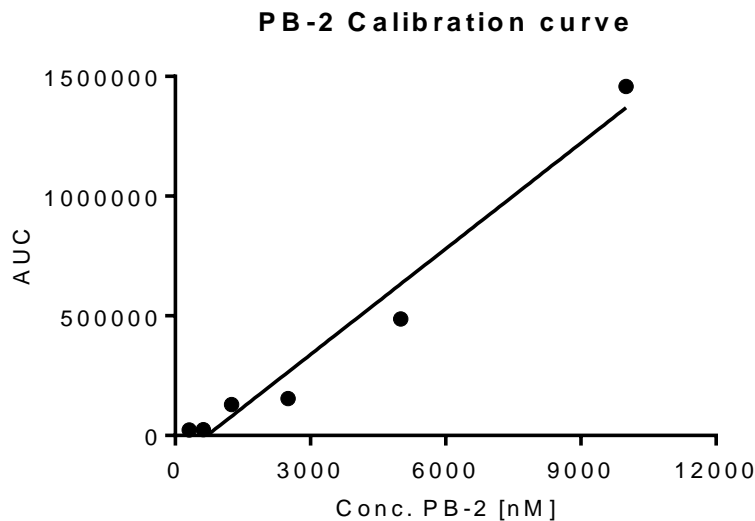
3.2. Supplementary Information



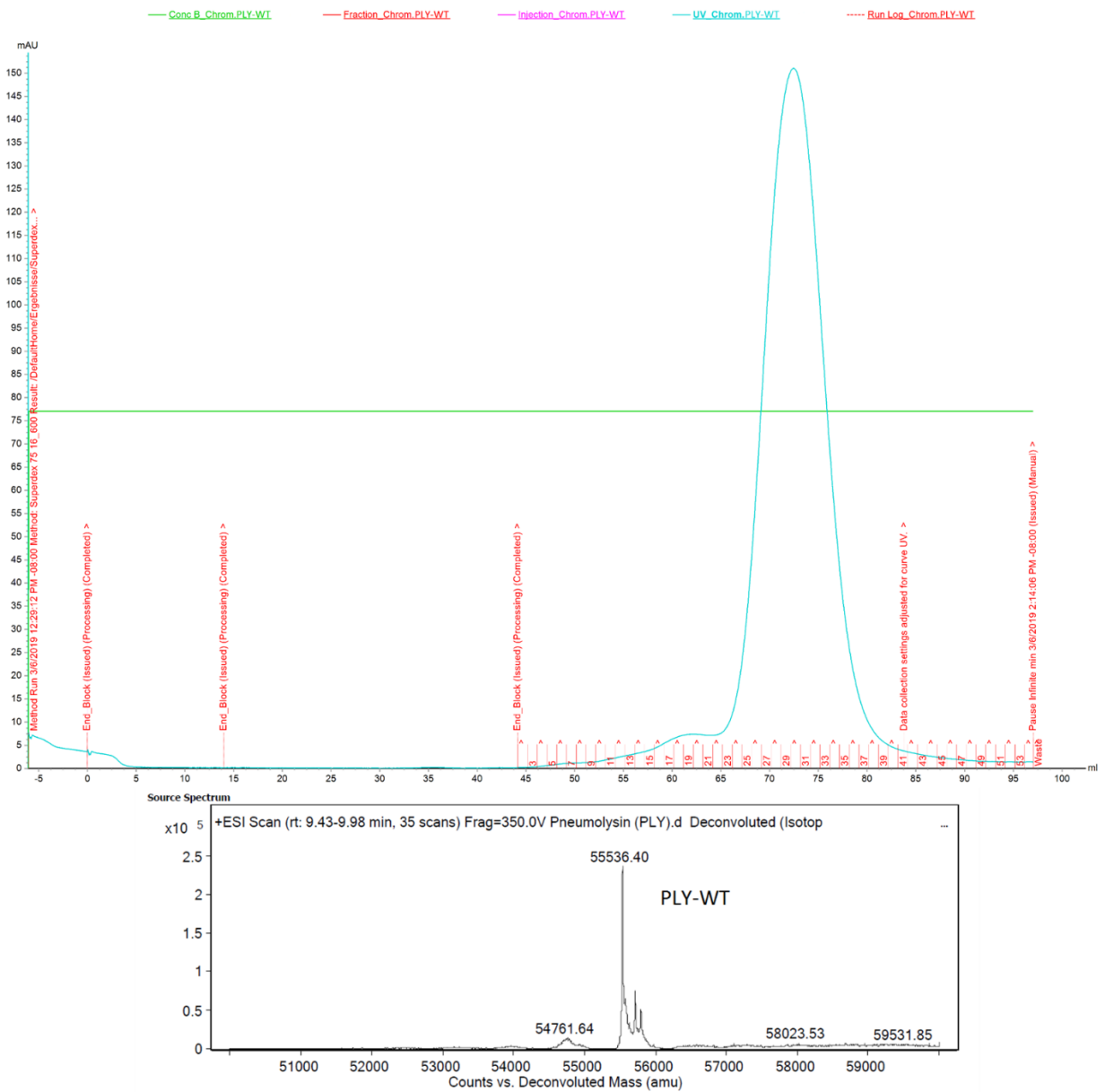
Supplementary Figure 1. Time dependent inhibition by **PB-1** in LDH assays after addition of Tween 20.



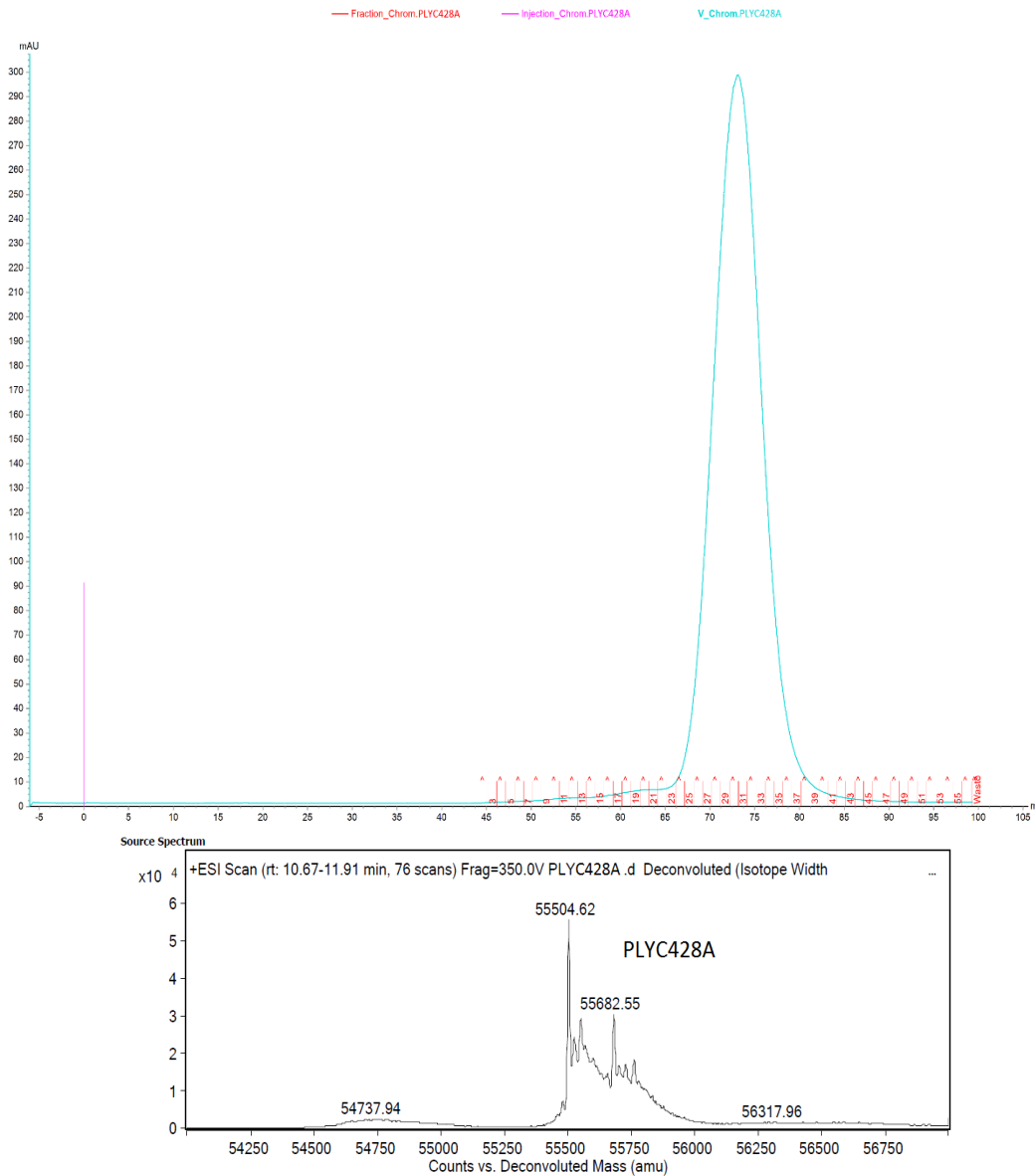
Supplementary Figure 2. MS spectra of PLY-C428A (top) and PLY-WT (bottom) under native MS conditions. Proteins showed numerous additional masses peaks, representing the binding of MOPS buffer salts, ammonium acetate buffer salts, and glycerol, respectively (data here are one of $n = 3$).



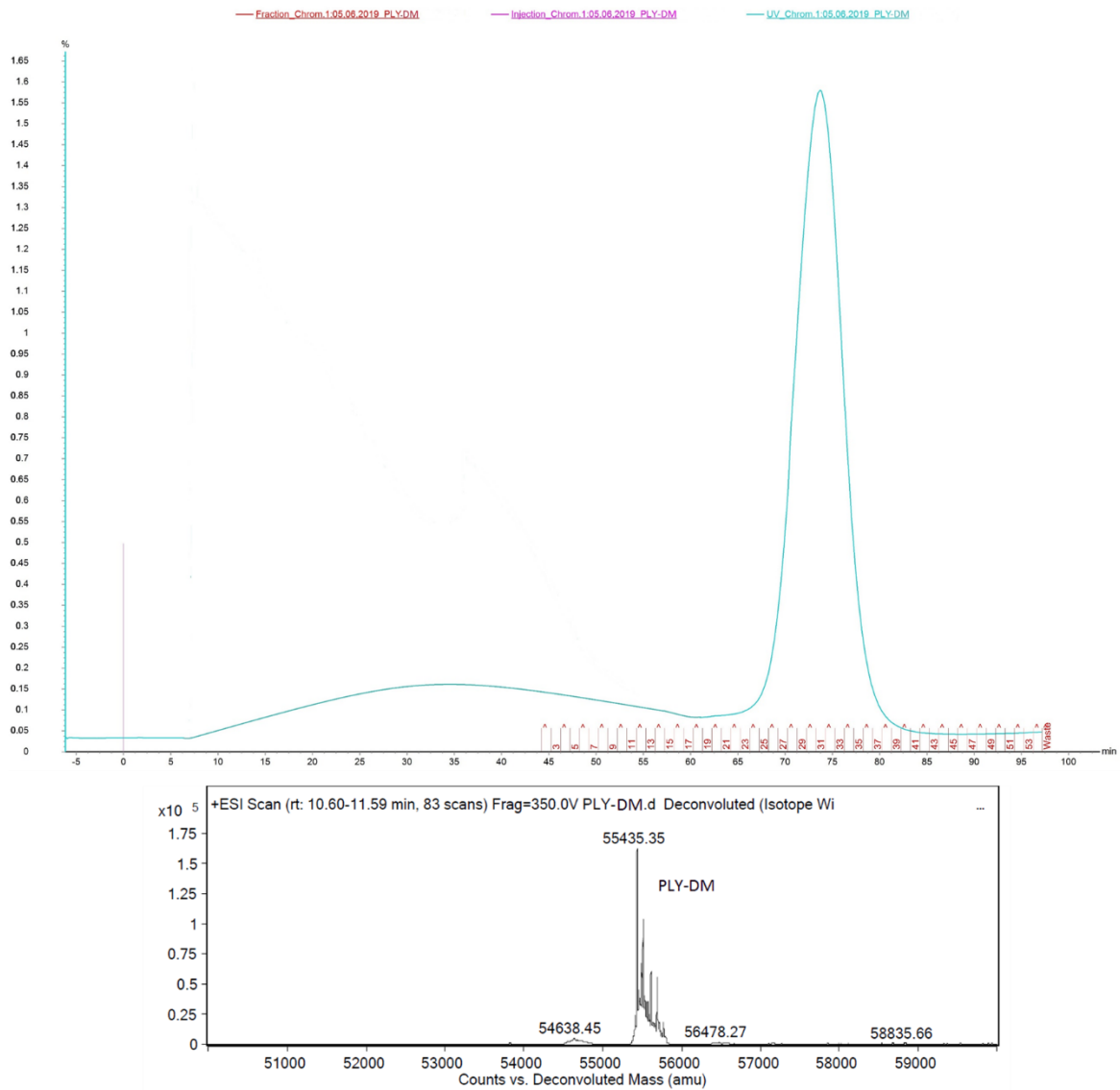
Supplementary Figure 3. The calibration curve of PB-2, the curve is not fitting because of degradation of PB-2.



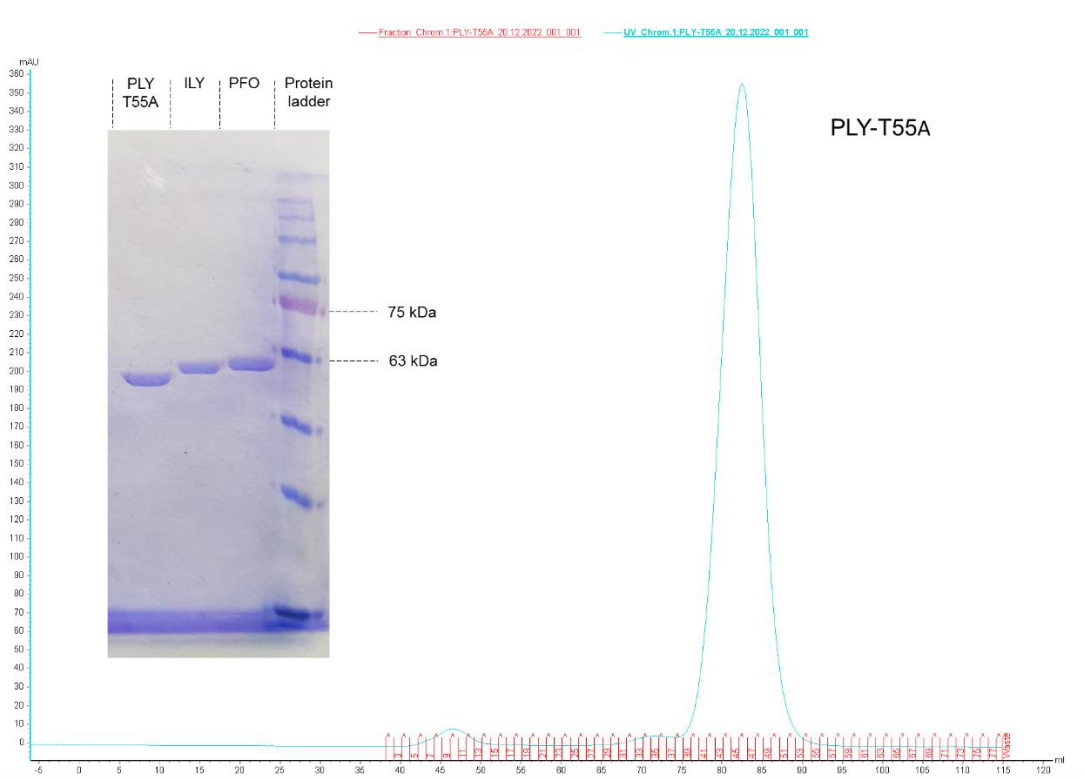
Supplementary Figure 4. Size exclusion chromatogram of recombinant pneumolysin (PLY) on HiLoad 16/600 Superdex 75 pg column and deconvoluted protein mass spectrum displaying the protein mass peak.



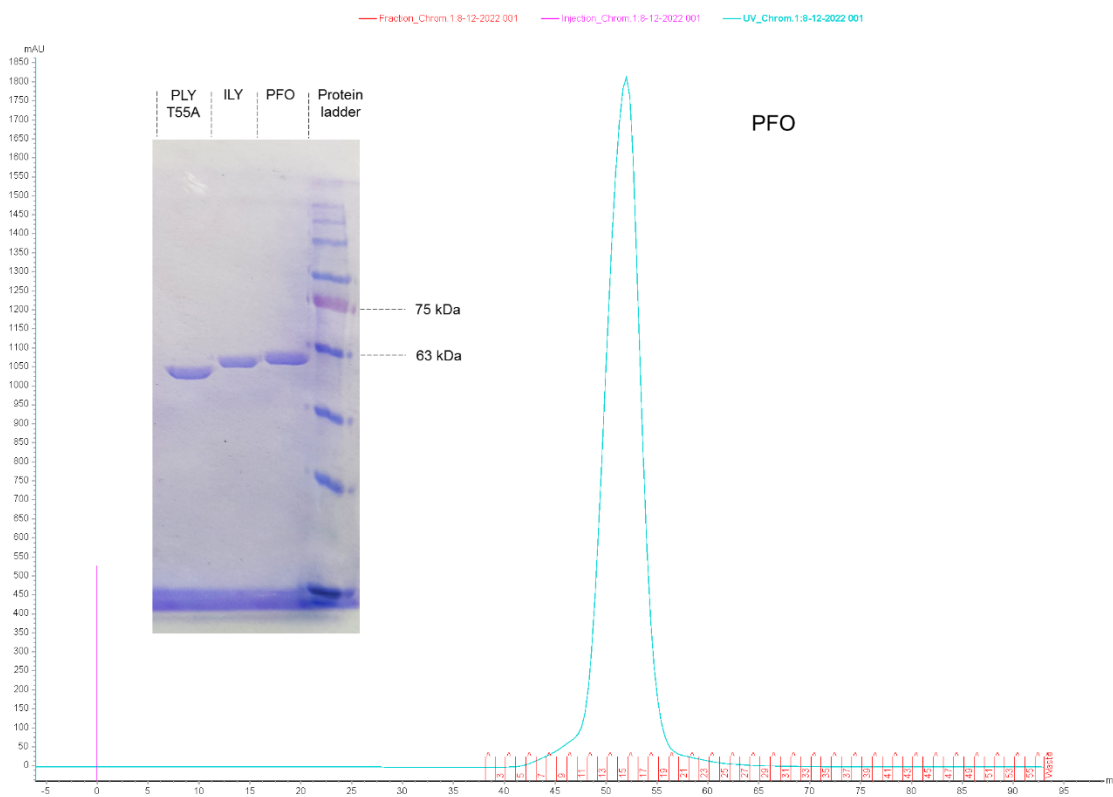
Supplementary Figure 5. Size exclusion chromatogram of PLY-C428A on HiLoad 16/600 Superdex 75 pg column and deconvoluted protein mass spectrum displaying the protein mass peak.



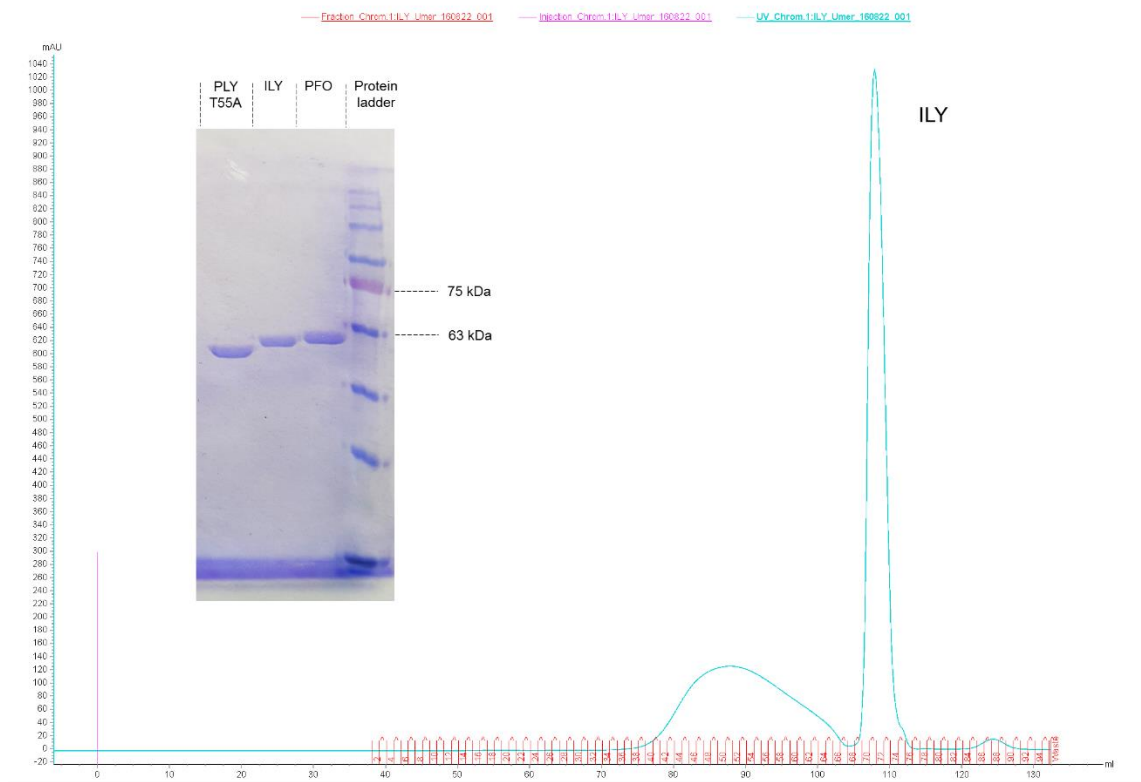
Supplementary Figure 6. Size exclusion chromatogram of pneumolysin double mutant (PLY-DM) on HiLoad 16/600 Superdex 75 pg column and deconvoluted protein mass spectrum displaying the protein mass peak.



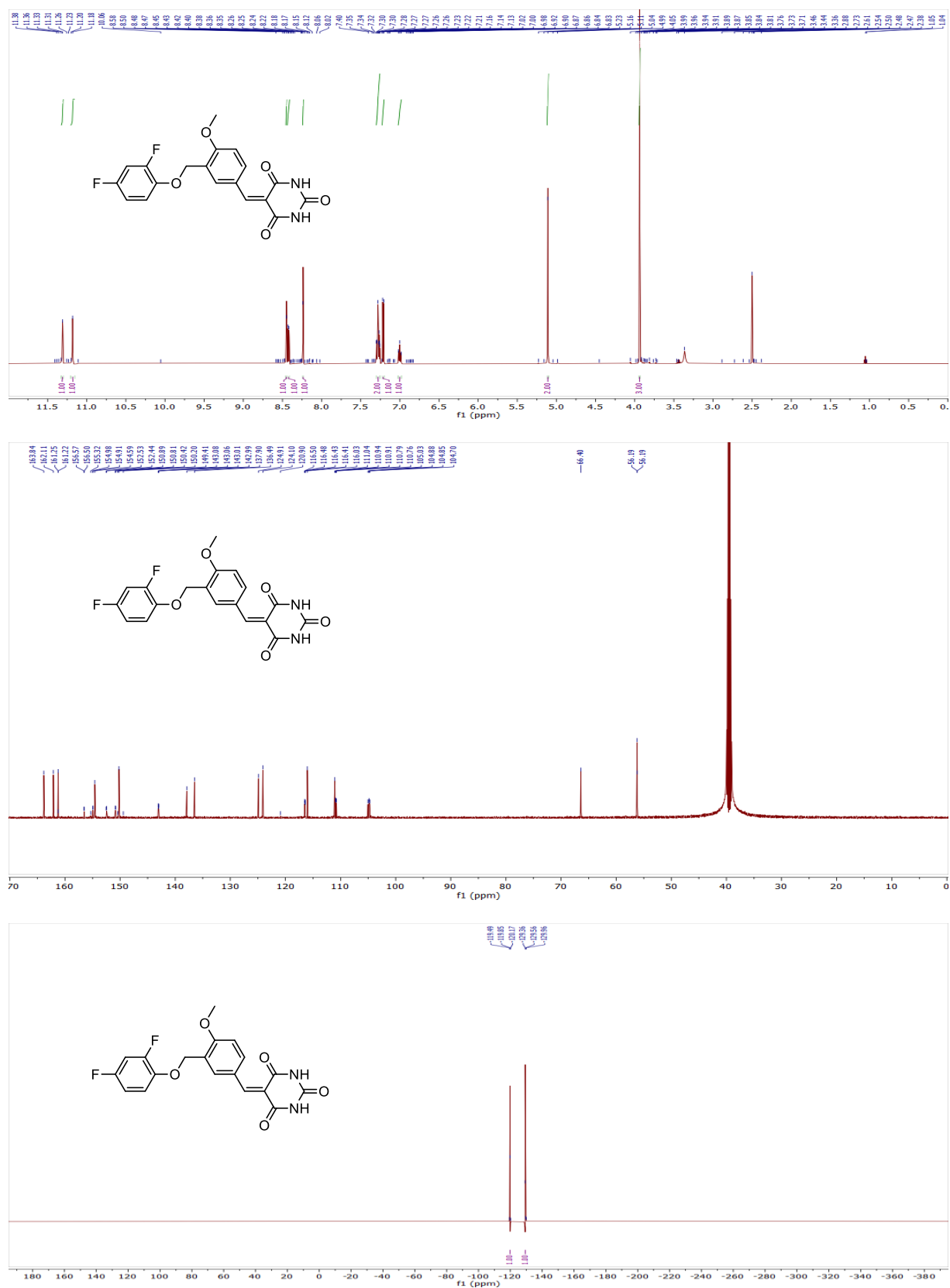
Supplementary Figure 7. Size exclusion chromatogram of PLY-T55A on HiLoad 16/600 Superdex 75 pg column and SDS-gel.



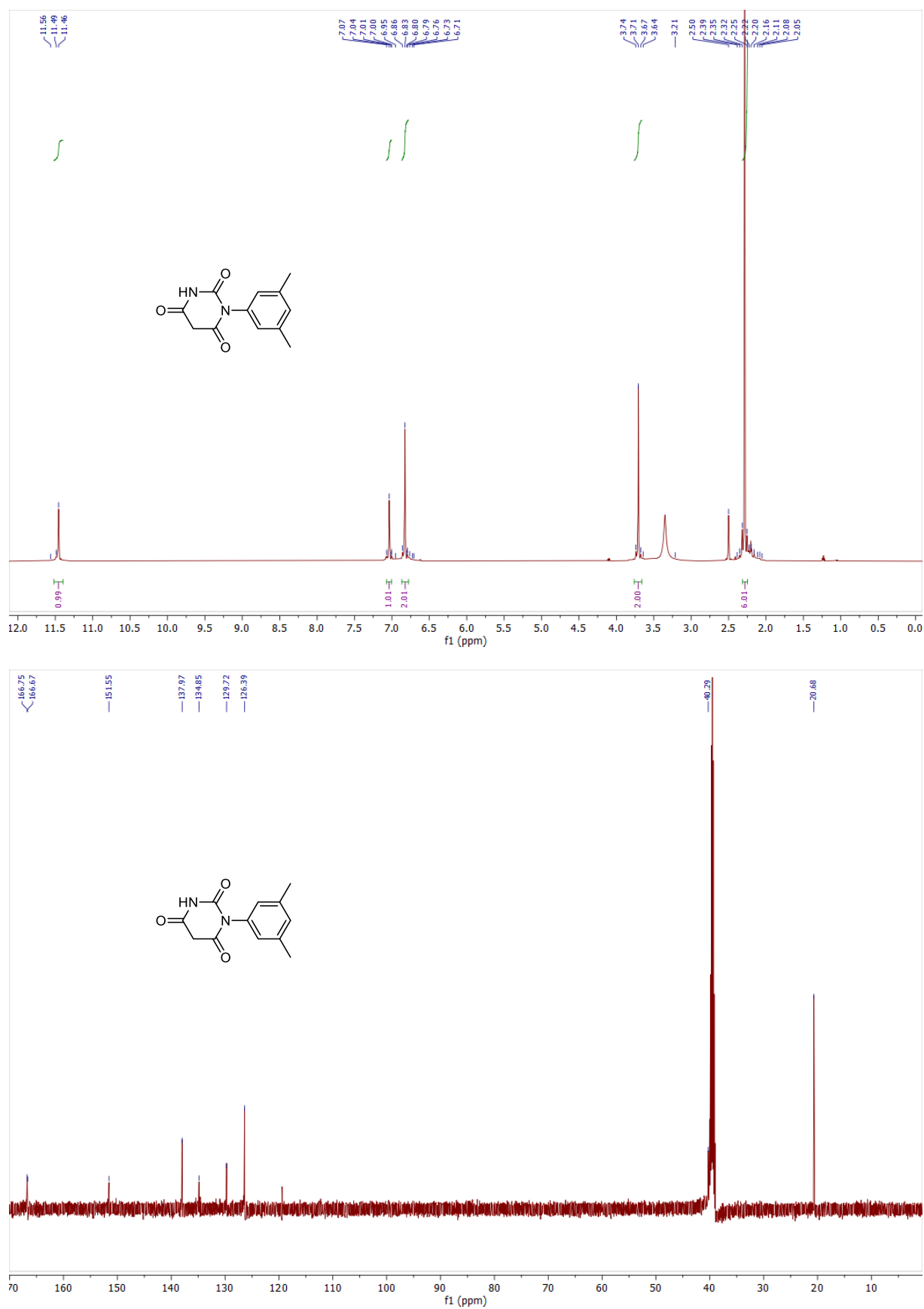
Supplementary Figure 8. Size exclusion chromatogram of perfringolysin on HiLoad 16/600 Superdex 75 pg column and SDS-gel.



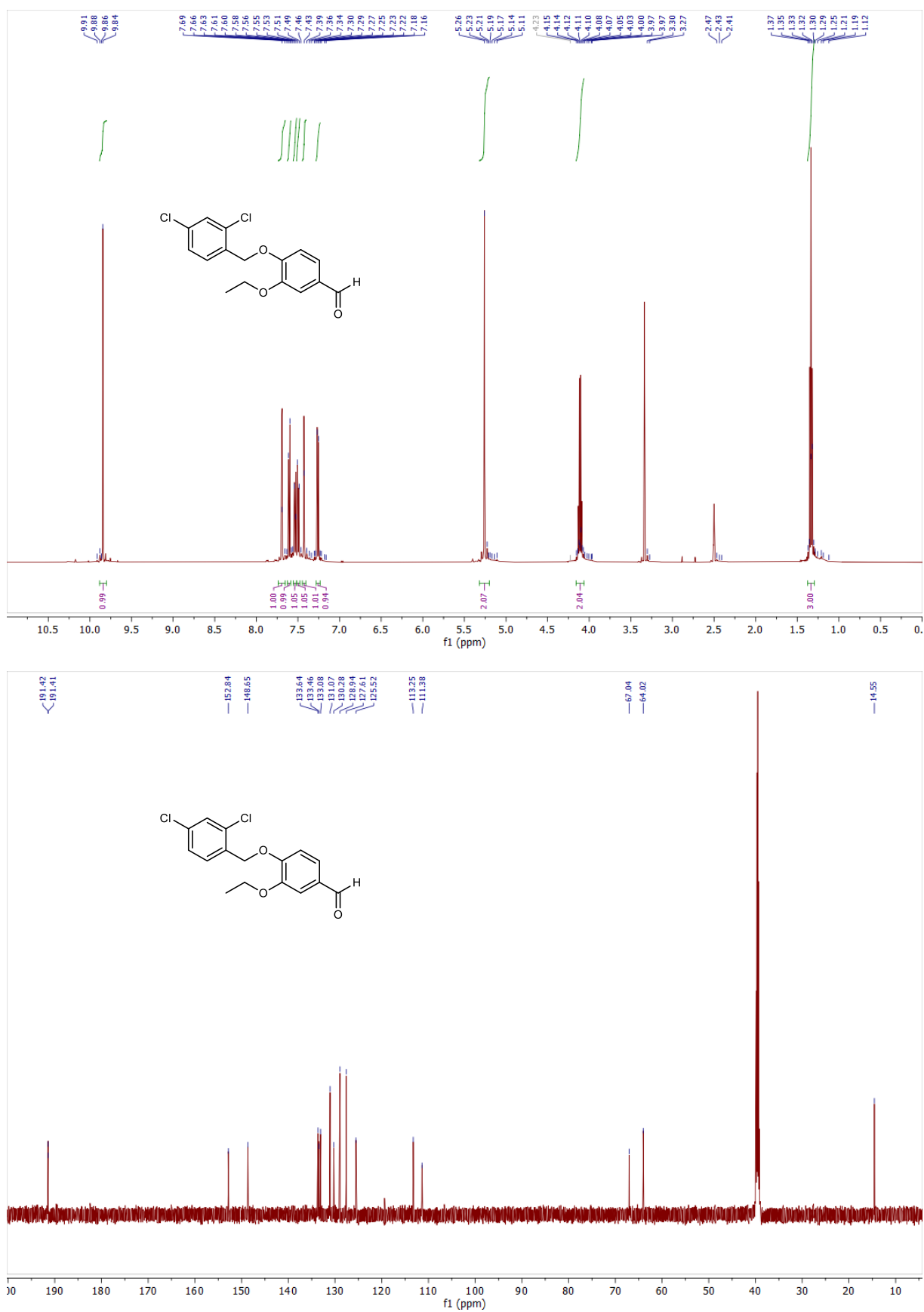
Supplementary Figure 9. Size exclusion chromatogram of intermedilysin on HiLoad 16/600 Superdex 75 pg column and SDS-gel.



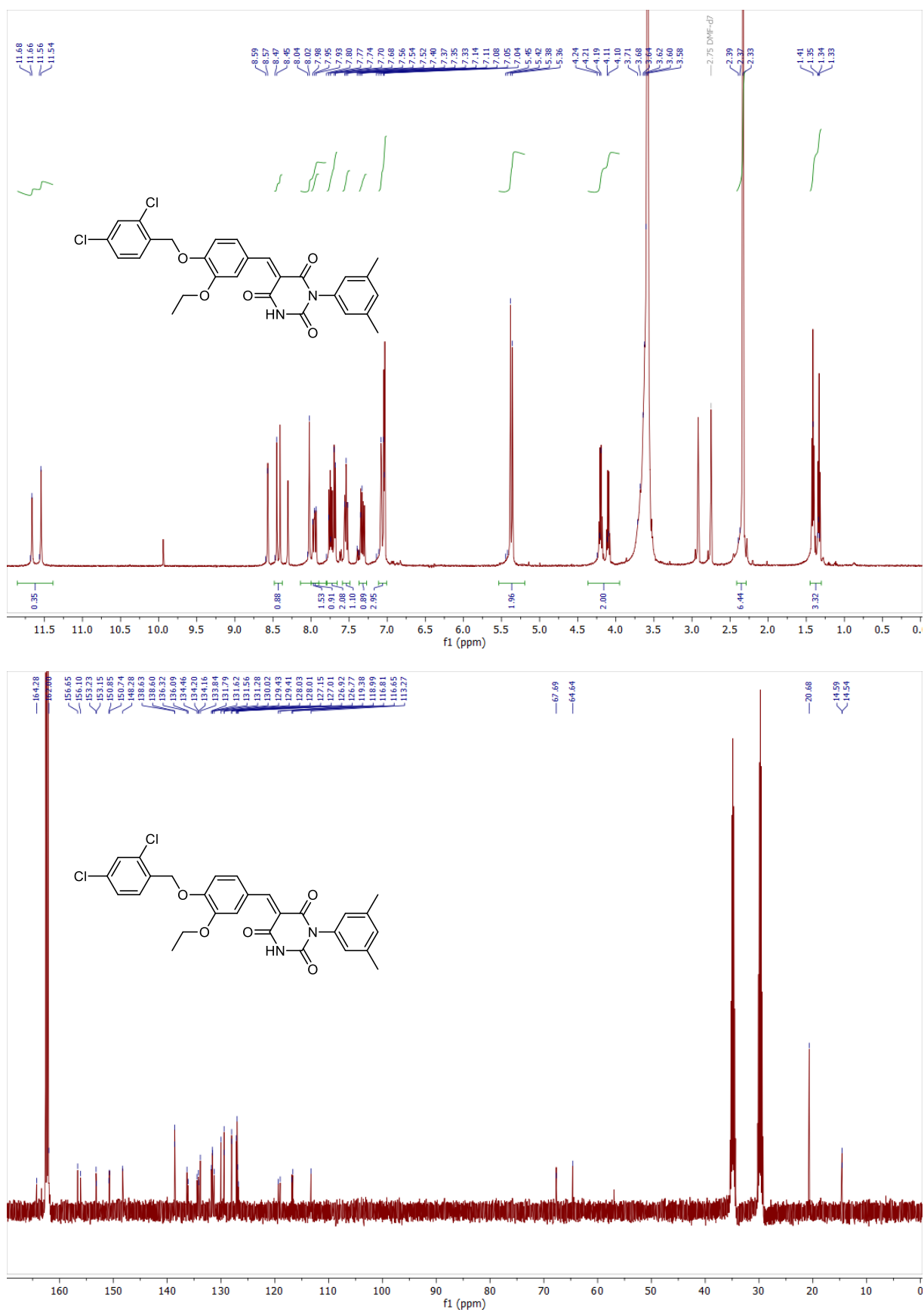
Supplementary Figure 10. $^1\text{H-NMR}$ (600 MHz, DMSO- d_6) (top), $^{13}\text{C-NMR}$ (151 MHz, DMSO- d_6) (middle) and $^{19}\text{F-NMR}$ (565 MHz, DMSO- d_6) (bottom) spectrum of **PB-1**.



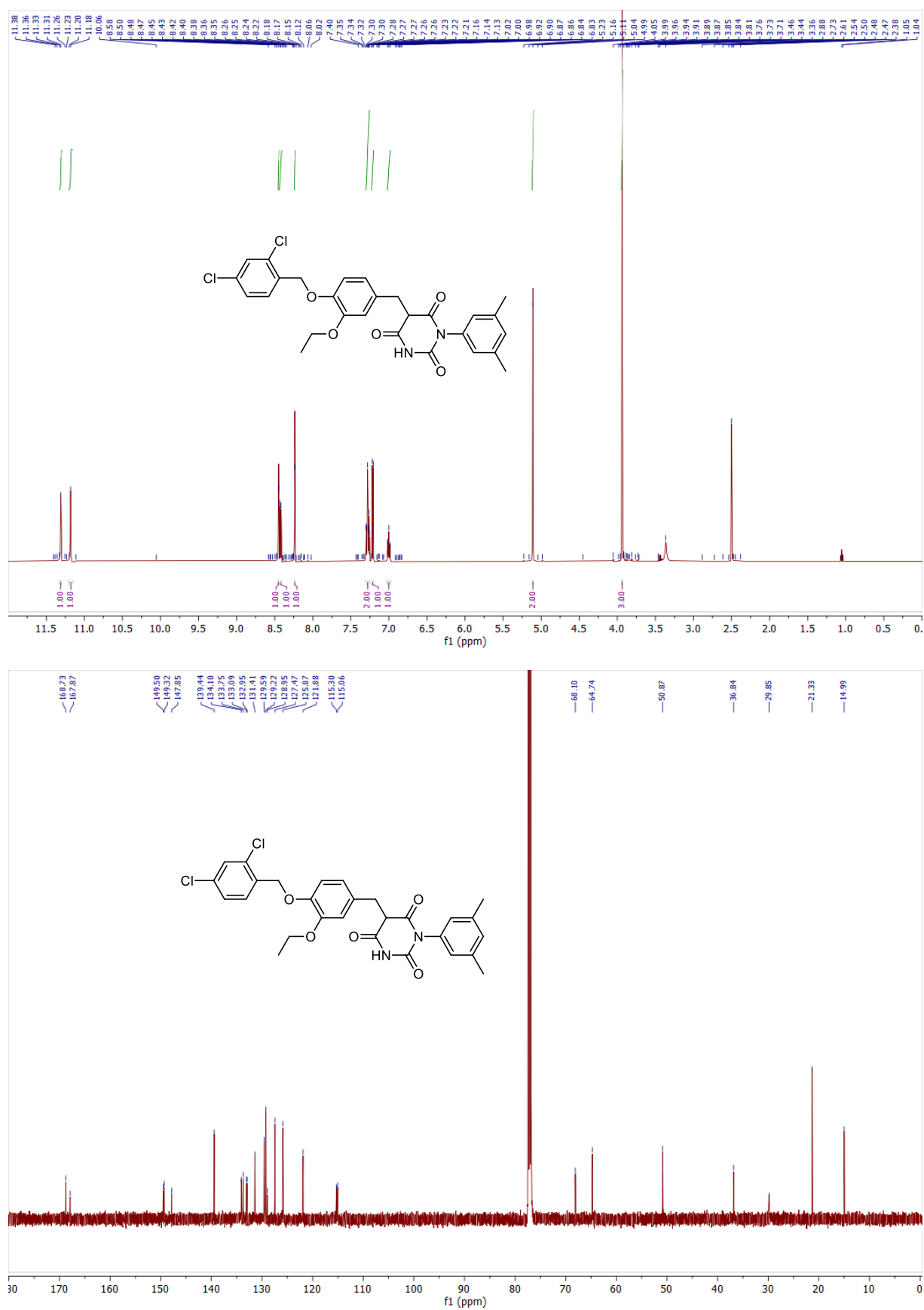
Supplementary Figure 11. ¹H-NMR (500 MHz, DMSO-d₆) and ¹³C-NMR (126 MHz, DMSO-d₆) spectrum of PB-2.3.



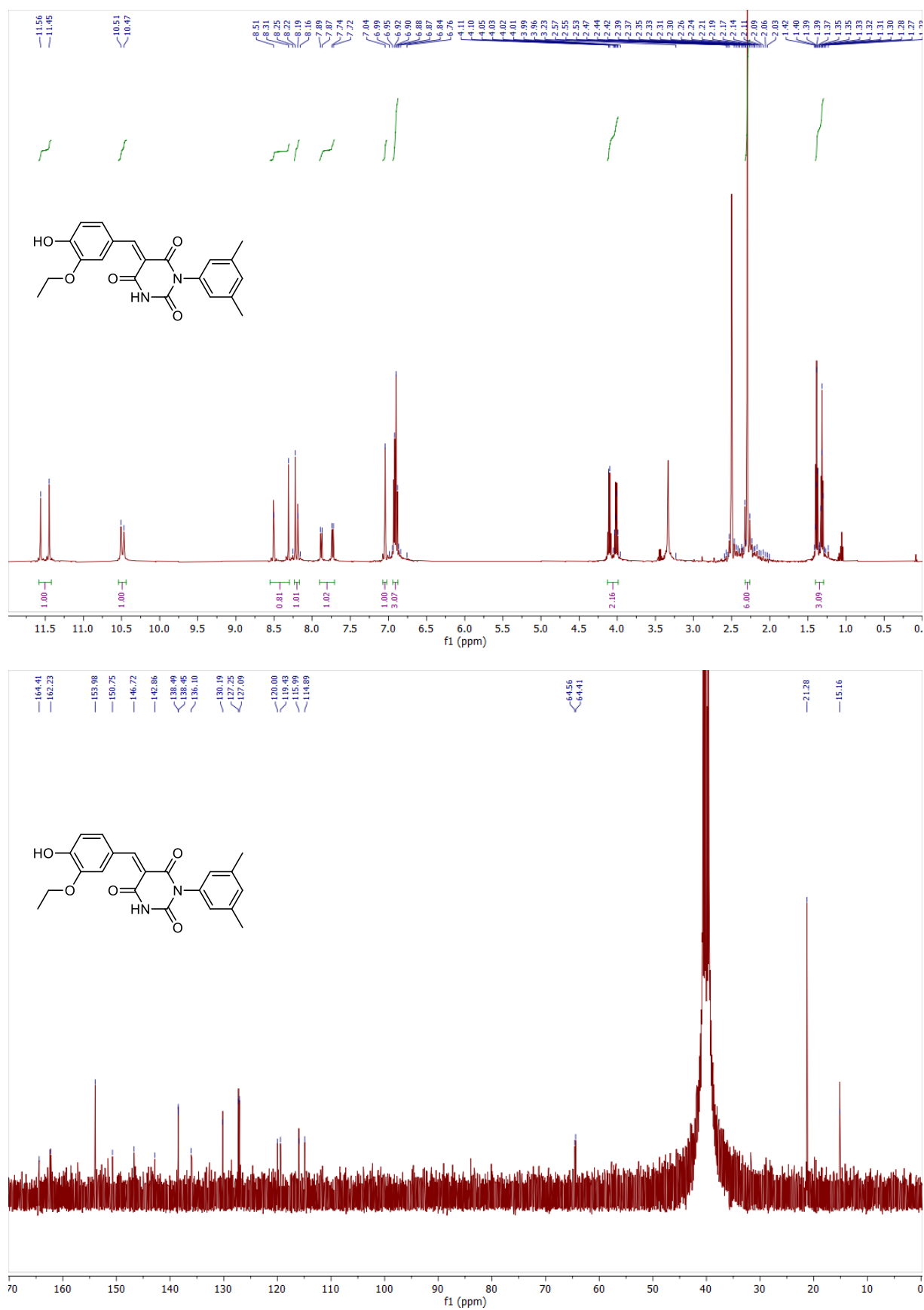
Supplementary Figure 12. $^1\text{H-NMR}$ (500 MHz, DMSO-d_6) and $^{13}\text{C-NMR}$ (126 MHz, DMSO-d_6) spectrum of PB-2.2.



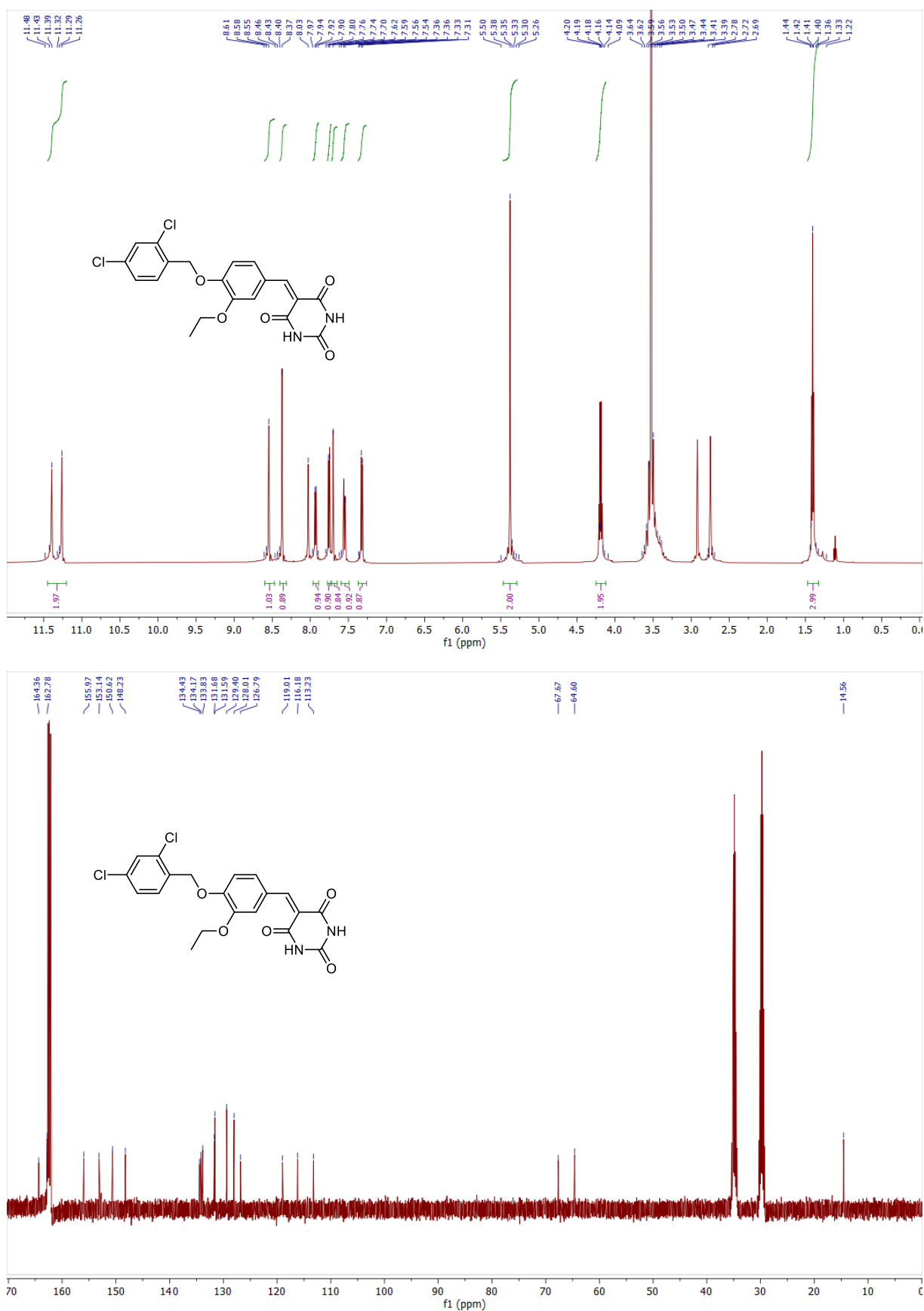
Supplementary Figure 13. ¹H-NMR (500 MHz, DMF-*d*₇) and ¹³C-NMR (126 MHz, DMF-*d*₇) spectrum of PB-2.



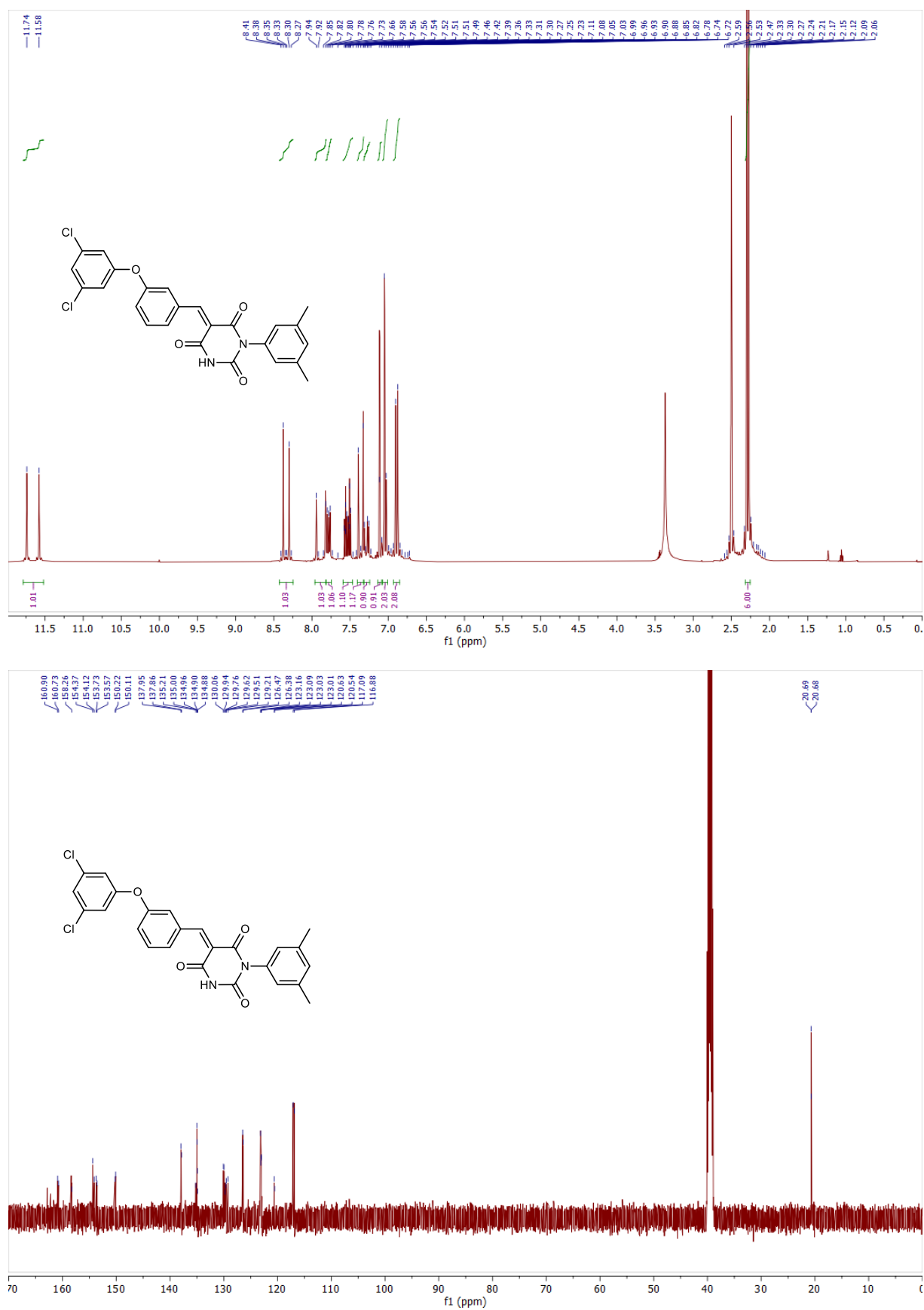
Supplementary Figure 14. $^1\text{H-NMR}$ (500 MHz, Chloroform- d) and $^{13}\text{C-NMR}$ (126 MHz, Chloroform- d) spectrum of **PB-2.1**.



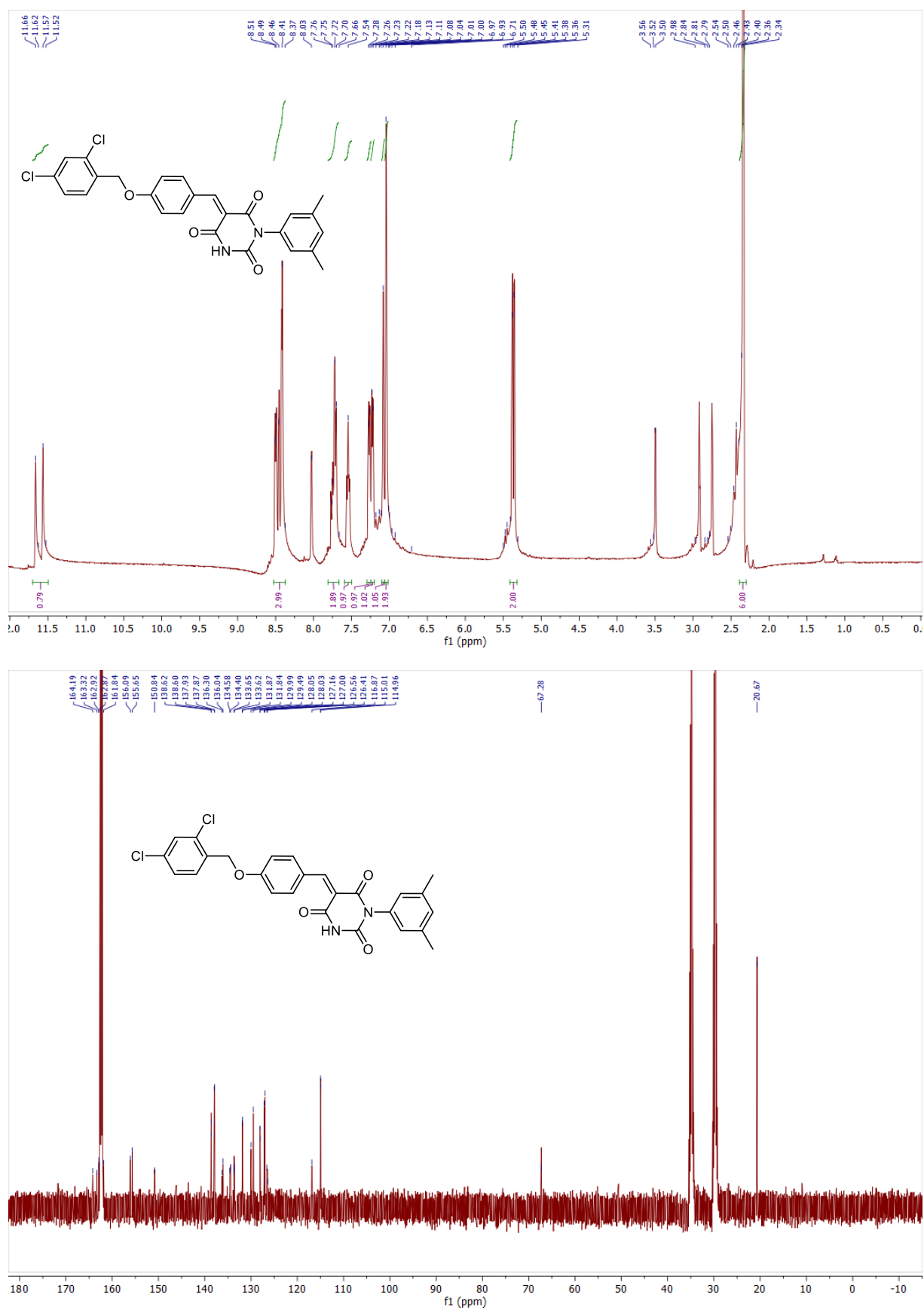
Supplementary Figure 15. ¹H-NMR (500 MHz, DMSO-d₆) and ¹³C-NMR (126 MHz, DMSO-d₆) spectrum of PB-2.4.



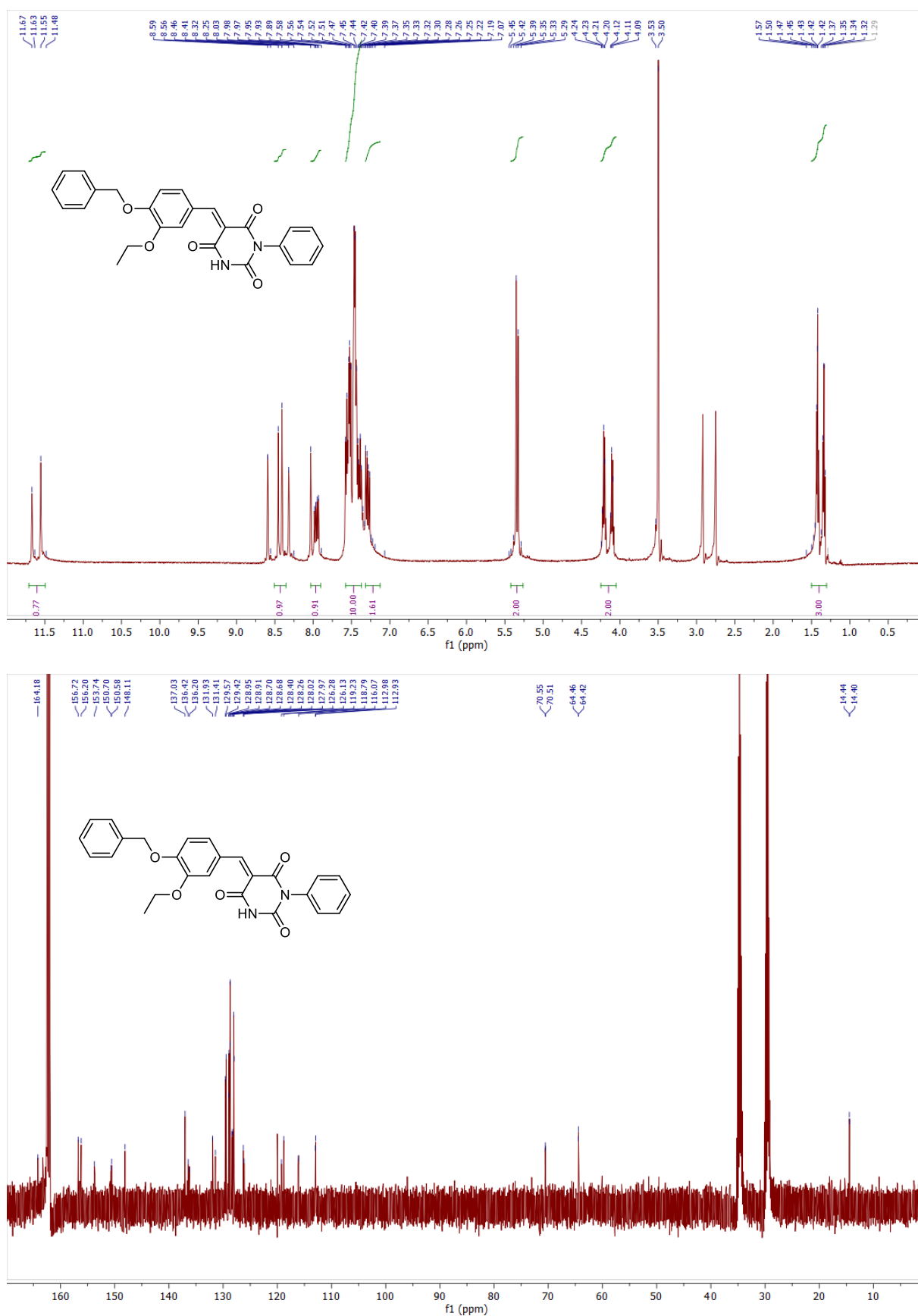
Supplementary Figure 16. $^1\text{H-NMR}$ (500 MHz, DMF-d_7) and $^{13}\text{C-NMR}$ (126 MHz, DMF-d_7) spectrum of **PB-2.5**.



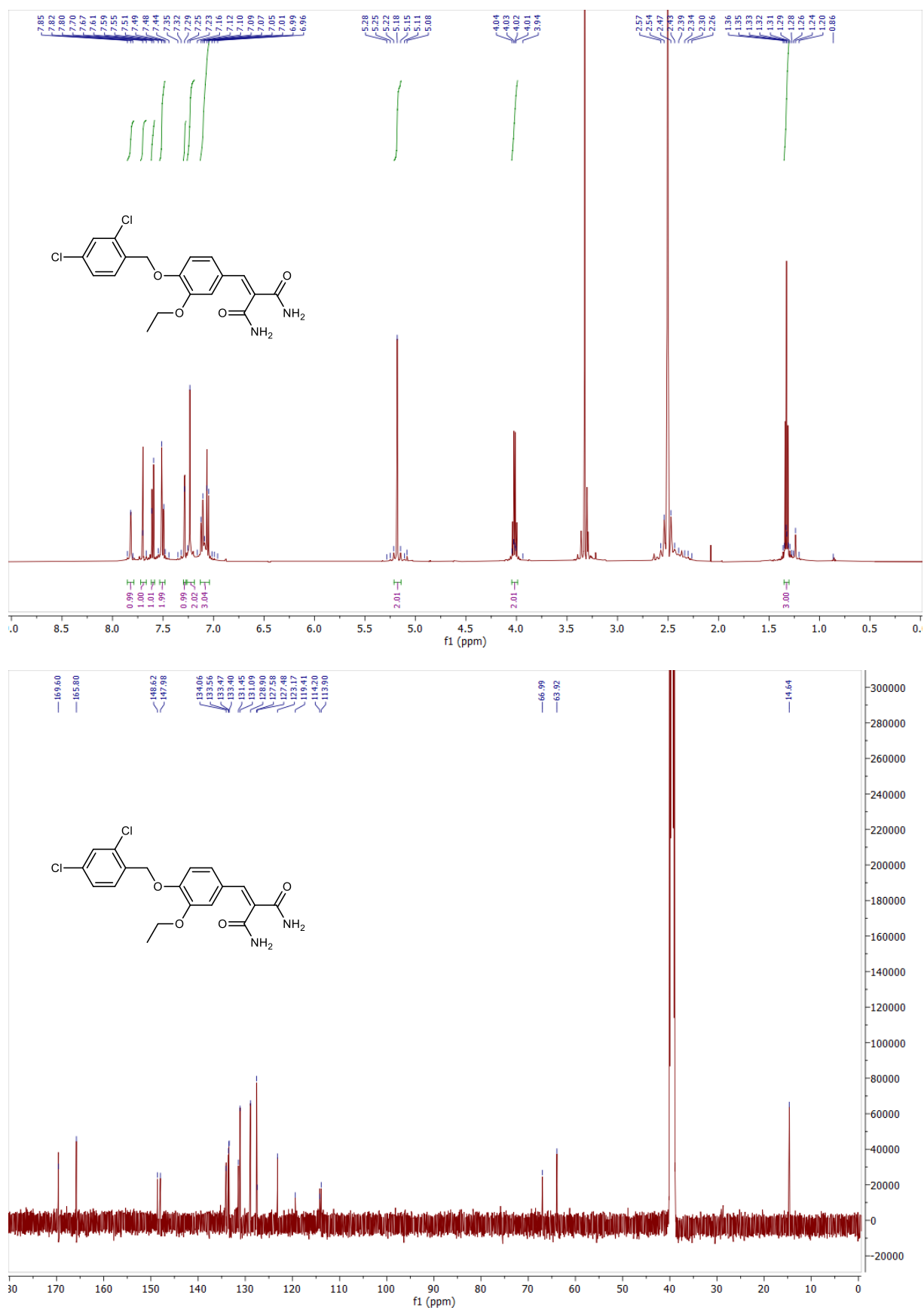
Supplementary Figure 17. $^1\text{H-NMR}$ (500 MHz, DMSO-d_6) and $^{13}\text{C-NMR}$ (126 MHz, DMSO-d_6) spectrum of PB-2.6.



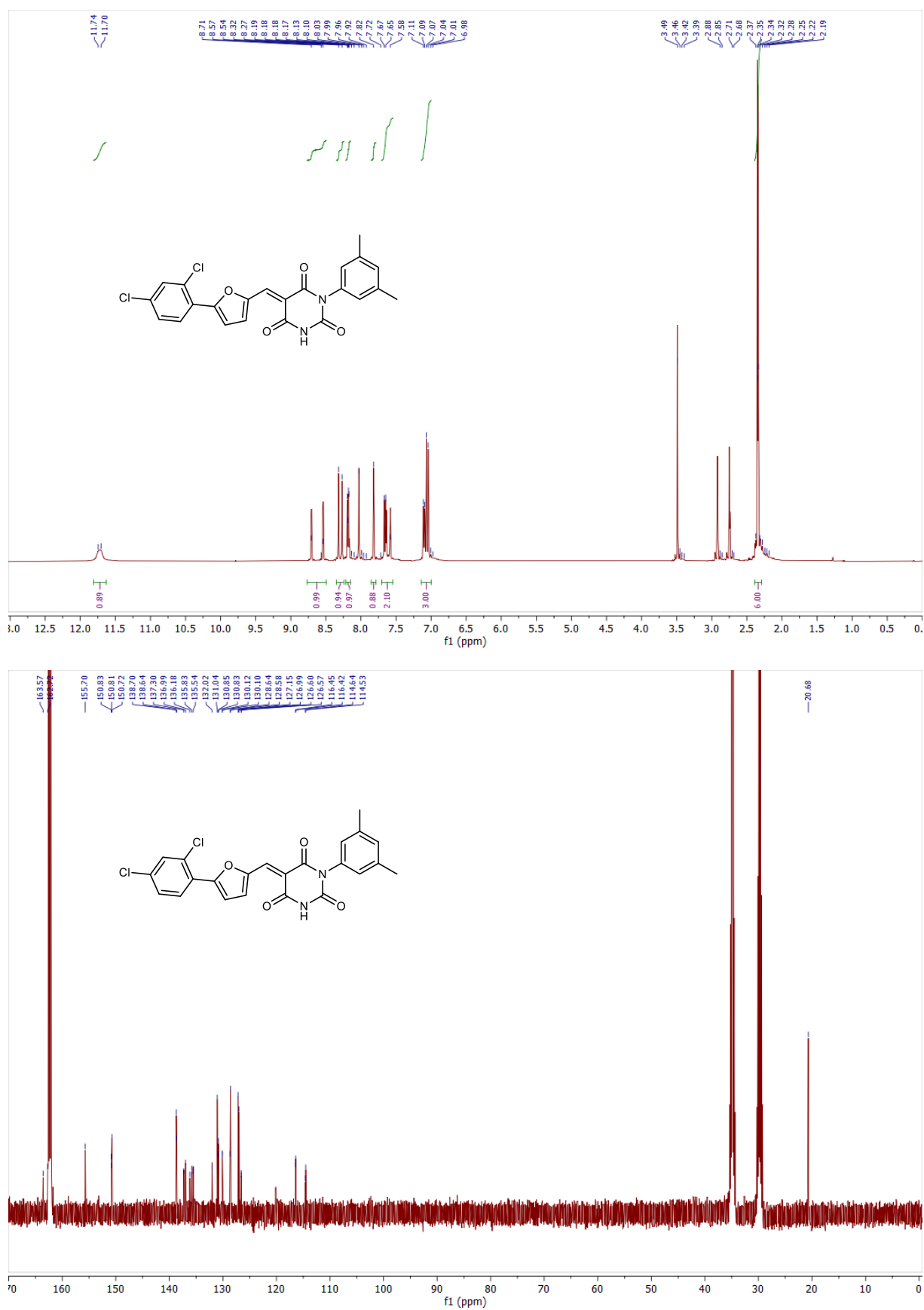
Supplementary Figure 18. $^1\text{H-NMR}$ (500 MHz, DMF-d_7) and $^{13}\text{C-NMR}$ (126 MHz, DMF-d_7) spectrum of PB-2.8.



Supplementary Figure 19. ¹H-NMR (500 MHz, DMF-d₇) and ¹³C-NMR (126 MHz, DMF-d₇) spectrum of PB-2.10.



Supplementary Figure 20. ¹H-NMR (500 MHz, DMSO-d₆) and ¹³C-NMR (126 MHz, DMSO-d₆) spectrum of PB-2.12.



Supplementary Figure 21. $^1\text{H-NMR}$ (500 MHz, DMF-d_7) and $^{13}\text{C-NMR}$ (126 MHz, DMF-d_7) spectrum of PB-3.

3.3. References

- 1 Deamer, D. The Role of Lipid Membranes in Life's Origin. *7*, 5 (2017).
- 2 Bischofberger, M., Iacovache, I. & van der Goot, F. G. Pathogenic pore-forming proteins: function and host response. *Cell host & microbe* **12**, 266-275 (2012).
- 3 Bischofberger, M., Gonzalez, M. R. & van der Goot, F. G. Membrane injury by pore-forming proteins. *Current opinion in cell biology* **21**, 589-595 (2009).
- 4 Separovic, F. *et al.* Sodium ion binding in the gramicidin A channel. Solid-state NMR studies of the tryptophan residues. *Biophys J* **67**, 1495-1500 (1994).
- 5 Morton, C. J., Sani, M.-A., Parker, M. W. & Separovic, F. Cholesterol-Dependent Cytolysins: Membrane and Protein Structural Requirements for Pore Formation. *Chemical Reviews* **119**, 7721-7736 (2019).
- 6 Ehrlich, P. Diskussionsbemerkungen (Crocin und Tetanolysin). *Berliner klinische Wochenschrift*, 273-274 (1898).
- 7 Hewitt, L. F. a. E. W. T. The effect of cholesterol and of sera contaminated with bacteria on the hemolysins produced by haemolytic streptococci. *J. Pathol. Bacteriol.* **49**, 45-51 (1939).
- 8 Heuck, A. P., Moe, P. C. & Johnson, B. B. The cholesterol-dependent cytolysin family of gram-positive bacterial toxins. *Sub-cellular biochemistry* **51**, 551-577 (2010).
- 9 Alouf, J. E., Billington, S. J. & Jost, B. H. in *The Comprehensive Sourcebook of Bacterial Protein Toxins (Third Edition)* (eds Joseph E. Alouf & Michel R. Popoff) 643-658 (Academic Press, 2006).
- 10 Johnstone, B. A. *et al.* Cholesterol-dependent cytolysins: The outstanding questions (2022).
- 11 Ramachandran, R., Heuck, A. P., Tweten, R. K. & Johnson, A. E. . Structural insights into the membrane-anchoring mechanism of a cholesterol-dependent cytolysin. . *Nature Struct. Biol.* **9**, 823–827 (2002).
- 12 Bhattacharjee, P. & Keyel, P. A. Cholesterol-dependent cytolysins impair pro-inflammatory macrophage responses. *Sci Rep* **8**, 6458 (2018).
- 13 Chu, J. *et al.* Cholesterol-dependent cytolysins induce rapid release of mature IL-1beta from murine macrophages in a NLRP3 inflammasome and cathepsin B-dependent manner. *Journal of leukocyte biology* **86**, 1227-1238 (2009).
- 14 Thapa, R., Ray, S. & Keyel, P. A. Interaction of Macrophages and Cholesterol-Dependent Cytolysins: The Impact on Immune Response and Cellular Survival. *Toxins* **12** (2020).
- 15 Tweten, R. K. Cholesterol-dependent cytolysins, a family of versatile pore-forming toxins. *Infect. Immun.* **73**, 6199-6209 (2005).
- 16 Birmingham, C. L. *et al.* *Listeria monocytogenes* evades killing by autophagy during colonization of host cells. *Autophagy* **3**, 442-451 (2007).
- 17 Geoffroy, C., Gaillard, J. L., Alouf, J. E. & Berche, P. Purification, characterization, and toxicity of the sulfhydryl-activated hemolysin listeriolysin O from *Listeria monocytogenes*. *Infection and immunity* **55**, 1641-1646 (1987).
- 18 Kim, S. *et al.* *Listeria monocytogenes* is sensed by the NLRP3 and AIM2 inflammasome. *European journal of immunology* **40**, 1545-1551 (2010).
- 19 Anderson, R. & Feldman, C. Pneumolysin as a potential therapeutic target in severe pneumococcal disease. *J. Infect.* **74**, 527-544 (2017).
- 20 Lucas, R. *et al.* Mini-review: novel therapeutic strategies to blunt actions of pneumolysin in the lungs. *Toxins* **5**, 1244-1260 (2013).
- 21 Nishimoto, A. T., Rosch, J. W. & Tuomanen, E. I. Pneumolysin: Pathogenesis and Therapeutic Target. **11** (2020).
- 22 Köster, S. *et al.* Crystal structure of listeriolysin O reveals molecular details of oligomerization and pore formation. *Nat Commun* **5**, 3690 (2014).
- 23 Lawrence, S. L. *et al.* Crystal structure of *Streptococcus pneumoniae* pneumolysin provides key insights into early steps of pore formation. *Sci Rep* **5**, 14352 (2015).
- 24 Marshall, J. E. *et al.* The Crystal Structure of Pneumolysin at 2.0 Å Resolution Reveals the Molecular Packing of the Pre-pore Complex. *Sci Rep* **5**, 13293 (2015).

- 25 Feil, S. C., Ascher, D. B., Kuiper, M. J., Tweten, R. K. & Parker, M. W. Structural studies of *Streptococcus pyogenes* streptolysin O provide insights into the early steps of membrane penetration. *J Mol Biol* **426**, 785-792 (2014).
- 26 Johnson, S., Brooks, Nicholas J., Smith, Richard A. G., Lea, Susan M. & Bubeck, D. Structural Basis for Recognition of the Pore-Forming Toxin Intermedilysin by Human Complement Receptor CD59. *Cell Reports* **3**, 1369-1377 (2013).
- 27 Lawrence, S. L. *et al.* Structural Basis for Receptor Recognition by the Human CD59-Responsive Cholesterol-Dependent Cytolysins. *Structure (London, England: 1993)* **24**, 1488-1498 (2016).
- 28 van Pee, K. *et al.* CryoEM structures of membrane pore and prepore complex reveal cytolytic mechanism of Pneumolysin. *eLife* **6** (2017).
- 29 Xu, L. *et al.* Crystal structure of cytotoxin protein suilysin from *Streptococcus suis*. *Protein & cell* **1**, 96-105 (2010).
- 30 Johnstone, B. A. *et al.* Cholesterol-dependent cytolysins: The outstanding questions. *IUBMB life* **74**, 1169-1179 (2022).
- 31 Johnson, B. B., Breña, M., Anguita, J. & Heuck, A. P. Mechanistic Insights into the Cholesterol-dependent Binding of Perfringolysin O-based Probes and Cell Membranes. *Sci Rep* **7**, 13793 (2017).
- 32 Farrand, A. J., LaChapelle, S., Hotze, E. M., Johnson, A. E. & Tweten, R. K. Only two amino acids are essential for cytolytic toxin recognition of cholesterol at the membrane surface. *Proceedings of the National Academy of Sciences of the United States of America* **107**, 4341-4346 (2010).
- 33 Park, S. A., Park, Y. S., Bong, S. M. & Lee, K. S. Structure-based functional studies for the cellular recognition and cytolytic mechanism of pneumolysin from *Streptococcus pneumoniae*. *Journal of structural biology* **193**, 132-140 (2016).
- 34 Hughes, T. R. *et al.* Identification of the high affinity binding site in the *Streptococcus intermedius* toxin intermedilysin for its membrane receptor, the human complement regulator CD59. *Molecular immunology* **46**, 1561-1567 (2009).
- 35 Randis, T. M., Kulkarni, R., Aguilar, J. L. & Ratner, A. J. Antibody-based detection and inhibition of vaginolysin, the *Gardnerella vaginalis* cytolysin. *PLoS One* **4**, e5207 (2009).
- 36 Nagamune, H. *et al.* Intermedilysin, a novel cytotoxin specific for human cells secreted by *Streptococcus intermedius* UNS46 isolated from a human liver abscess. *Infection and immunity* **64**, 3093-3100 (1996).
- 37 Dowd, K. J., Farrand, A. J. & Tweten, R. K. The cholesterol-dependent cytolysin signature motif: a critical element in the allosteric pathway that couples membrane binding to pore assembly. *PLoS Pathog.* **8**, e1002787 (2012).
- 38 Dal Peraro, M. & van der Goot, F. G. Pore-forming toxins: ancient, but never really out of fashion. *Nature reviews. Microbiology* **14**, 77-92 (2016).
- 39 Li, Y. *et al.* Structural Basis of the Pore-Forming Toxin/Membrane Interaction. *Toxins* **13** (2021).
- 40 Los, F. C., Randis, T. M., Aroian, R. V. & Ratner, A. J. Role of pore-forming toxins in bacterial infectious diseases. *Microbiology and molecular biology reviews: MMBR* **77**, 173-207 (2013).
- 41 Li, H. *et al.* Insights into structure and activity of natural compound inhibitors of pneumolysin. *Sci Rep* **7**, 42015 (2017).
- 42 Tilley, S. J., Orlova, E. V., Gilbert, R. J., Andrew, P. W. & Saibil, H. R. Structural basis of pore formation by the bacterial toxin pneumolysin. *Cell* **121**, 247-256 (2005).
- 43 Ramachandran, R., Tweten, R. K. & Johnson, A. E. Membrane-dependent conformational changes initiate cholesterol-dependent cytolysin oligomerization and intersubunit beta-strand alignment. *Nature structural & molecular biology* **11**, 697-705 (2004).
- 44 Soltani, C. E., Hotze, E. M., Johnson, A. E. & Tweten, R. K. Specific protein-membrane contacts are required for prepore and pore assembly by a cholesterol-dependent cytolysin. *The Journal of biological chemistry* **282**, 15709-15716 (2007).

- 45 Hotze, E. M. *et al.* Monomer-monomer interactions propagate structural transitions necessary for pore formation by the cholesterol-dependent cytolysins. *The Journal of biological chemistry* **287**, 24534-24543 (2012).
- 46 Hotze, E. M. *et al.* Monomer-monomer interactions drive the prepore to pore conversion of a beta-barrel-forming cholesterol-dependent cytolysin. *The Journal of biological chemistry* **277**, 11597-11605 (2002).
- 47 Ramachandran, R., Tweten, R. K. & Johnson, A. E. The domains of a cholesterol-dependent cytolysin undergo a major FRET-detected rearrangement during pore formation. *Proceedings of the National Academy of Sciences of the United States of America* **102**, 7139-7144 (2005).
- 48 Wade, K. R. *et al.* An intermolecular electrostatic interaction controls the prepore-to-pore transition in a cholesterol-dependent cytolysin. *Proceedings of the National Academy of Sciences of the United States of America* **112**, 2204-2209, (2015).
- 49 van Pee, K., Mulvihill, E., Müller, D. J. & Yildiz, Ö. Unraveling the Pore-Forming Steps of Pneumolysin from *Streptococcus pneumoniae*. *Nano Letters* **16**, 7915-7924 (2016).
- 50 Bonev, B., Gilbert, R. & Watts, A. Structural investigations of pneumolysin/lipid complexes. *Molecular membrane biology* **17**, 229-235 (2000).
- 51 Bonev, B. B., Gilbert, R. J., Andrew, P. W., Byron, O. & Watts, A. Structural analysis of the protein/lipid complexes associated with pore formation by the bacterial toxin pneumolysin. *The Journal of biological chemistry* **276**, 5714-5719 (2001).
- 52 Leung, C. *et al.* Stepwise visualization of membrane pore formation by suliyisin, a bacterial cholesterol-dependent cytolysin. *eLife* **3**, e04247 (2014).
- 53 Asmuth, D. M. *et al.* Effects of *Clostridium perfringens* recombinant and crude phospholipase C and theta-toxin on rabbit hemodynamic parameters. *The Journal of infectious diseases* **172**, 1317-1323 (1995).
- 54 Bryant, A. E. *et al.* *Clostridium perfringens* invasiveness is enhanced by effects of theta toxin upon PMNL structure and function: the roles of leukocytotoxicity and expression of CD11/CD18 adherence glycoprotein. *FEMS immunology and medical microbiology* **7**, 321-336 (1993).
- 55 Stavru, F., Bouillaud, F., Sartori, A., Ricquier, D. & Cossart, P. *Listeria monocytogenes* transiently alters mitochondrial dynamics during infection. *Proceedings of the National Academy of Sciences of the United States of America* **108**, 3612-3617(2011).
- 56 Brooks, L. R. K. & Mias, G. I. *Streptococcus pneumoniae*'s Virulence and Host Immunity: Aging, Diagnostics, and Prevention. *Frontiers in Immunology* **9** (2018).
- 57 Habib, M., Porter, B. D. & Satzke, C. Capsular Serotyping of *Streptococcus pneumoniae* Using the Quellung Reaction. *J Vis Exp*, 51208 (2014).
- 58 Weckel, A. *et al.* *Streptococcus pyogenes* infects human endometrium by limiting the innate immune response. *The Journal of clinical investigation* **131** (2021).
- 59 Weiser, J. N., Ferreira, D. M. & Paton, J. C. *Streptococcus pneumoniae*: transmission, colonization and invasion. *Nature reviews. Microbiology* **16**, 355-367 (2018).
- 60 Limbago, B. P., V.; Weinrick, B.; Scott, J.R. Role of streptolysin O in a mouse model of invasive group A streptococcal disease. *Infect. Immun.* **68**, 6384-6390 (2000).
- 61 Mitsui, K. *et al.* Chemokine production by rat macrophages stimulated with streptolysin O from *Streptococcus pyogenes*. *Microbiology and immunology* **46**, 37-45 (2002).
- 62 Rayner, C. F. *et al.* Interaction of pneumolysin-sufficient and -deficient isogenic variants of *Streptococcus pneumoniae* with human respiratory mucosa. *Infection and immunity* **63**, 442-447 (1995).
- 63 Sanders, M. E. *et al.* A comparison of pneumolysin activity and concentration in vitro and in vivo in a rabbit endophthalmitis model. *Clinical ophthalmology (Auckland, N.Z.)* **2**, 793-800 (2008).
- 64 Jones, S. & Portnoy, D. A. Characterization of *Listeria monocytogenes* pathogenesis in a strain expressing perfringolysin O in place of listeriolysin O. *Infection and immunity* **62**, 5608-5613 (1994).
- 65 McNeil, P. L. & Terasaki, M. Coping with the inevitable: how cells repair a torn surface membrane. *Nature cell biology* **3**, E124-129 (2001).

- 66 Flexner, S. & Noguchi, H. THE INFLUENCE OF COLLOIDS UPON THE DIFFUSION OF HÆMOLYSINS. *Journal of Experimental Medicine* **8**, 547-563 (1906).
- 67 Keyel, P. A. *et al.* Streptolysin O clearance through sequestration into blebs that bud passively from the plasma membrane. *Journal of cell science* **124**, 2414-2423 (2011).
- 68 Tanigawa, T., Suzuki, J., Ueta, T., Katsumoto, T. & Tanaka, Y. Different Sensitivity to Streptolysin-O of Cells in Macrophage Lineage. **40**, 81-84 (1996).
- 69 Mosser, E. M. & Rest, R. F. The Bacillus anthracis cholesterol-dependent cytolysin, Anthrolysin O, kills human neutrophils, monocytes and macrophages. *BMC Microbiology* **6**, 56 (2006).
- 70 Domon, H. *et al.* Streptococcus pneumoniae disrupts pulmonary immune defence via elastase release following pneumolysin-dependent neutrophil lysis. *Sci Rep* **6**, 38013 (2016).
- 71 Babiychuk, E. B. & Draeger, A. Defying death: Cellular survival strategies following plasmalemmal injury by bacterial toxins. *Seminars in Cell & Developmental Biology* **45**, 39-47 (2015).
- 72 Brito, C., Cabanes, D., Sarmiento Mesquita, F. & Sousa, S. Mechanisms protecting host cells against bacterial pore-forming toxins. *Cellular and molecular life sciences: CMLS* **76**, 1319-1339 (2019).
- 73 Cooper, S. T. & McNeil, P. L. Membrane Repair: Mechanisms and Pathophysiology. **95**, 1205-1240 (2015).
- 74 Idone, V. *et al.* Repair of injured plasma membrane by rapid Ca²⁺-dependent endocytosis. *The Journal of cell biology* **180**, 905-914 (2008).
- 75 Cooper, S. T. & McNeil, P. L. Membrane Repair: Mechanisms and Pathophysiology. *Physiological reviews* **95**, 1205-1240 (2015).
- 76 Demonbreun, A. R. *et al.* An actin-dependent annexin complex mediates plasma membrane repair in muscle. *The Journal of cell biology* **213**, 705-718, doi:10.1083/jcb.201512022 (2016).
- 77 Wolfmeier, H. *et al.* Ca²⁺-dependent repair of pneumolysin pores: A new paradigm for host cellular defense against bacterial pore-forming toxins. *Biochimica et Biophysica Acta (BBA) - Molecular Cell Research* **1853**, 2045-2054(2015).
- 78 Babiychuk, E. B., Monastyrskaya, K. & Draeger, A. Fluorescent Annexin A1 Reveals Dynamics of Ceramide Platforms in Living Cells. **9**, 1757-1775 (2008).
- 79 Romero, M. *et al.* Intrinsic repair protects cells from pore-forming toxins by microvesicle shedding. *Cell death and differentiation* **24**, 798-808 (2017).
- 80 Babiychuk, E. B., Monastyrskaya, K., Potez, S. & Draeger, A. Blebbing confers resistance against cell lysis. *Cell death and differentiation* **18**, 80-89 (2011).
- 81 Xie, M. & Low, M. G. Streptolysin-O induces release of glycosylphosphatidylinositol-anchored alkaline phosphatase from ROS cells by vesiculation independently of phospholipase action. *Biochemical Journal* **305**, 529-537 (1995).
- 82 Wolfmeier, H. *et al.* Active release of pneumolysin prepores and pores by mammalian cells undergoing a Streptococcus pneumoniae attack. *Biochimica et Biophysica Acta (BBA) - General Subjects* **1860**, 2498-2509 (2016).
- 83 Ray, S., Thapa, R. & Keyel, P. A. Multiple Parameters Beyond Lipid Binding Affinity Drive Cytotoxicity of Cholesterol-Dependent Cytolysins. **11**, 1 (2019).
- 84 Carrero, J. A., Calderon, B. & Unanue, E. R. Listeriolysin O from *Listeria monocytogenes* is a lymphocyte apoptogenic molecule. *Journal of immunology (Baltimore, Md.: 1950)* **172**, 4866-4874 (2004).
- 85 Braun, J. S. *et al.* Pneumococcal pneumolysin and H₂O₂ mediate brain cell apoptosis during meningitis. *The Journal of clinical investigation* **109**, 19-27 (2002).
- 86 Broz, P. & Dixit, V. M. Inflammasomes: mechanism of assembly, regulation and signalling. *Nature reviews. Immunology* **16**, 407-420 (2016).
- 87 Braun, J. S. *et al.* Pneumolysin causes neuronal cell death through mitochondrial damage. *Infection and immunity* **75**, 4245-4254 (2007).
- 88 Goldmann, O., Sastalla, I., Wos-Oxley, M., Rohde, M. & Medina, E. Streptococcus pyogenes induces oncosis in macrophages through the activation of an inflammatory programmed cell death pathway. *Cellular microbiology* **11**, 138-155(2009).

- 89 Nerlich, A. *et al.* Pneumolysin induced mitochondrial dysfunction leads to release of mitochondrial DNA. *Sci Rep* **8**, 182 (2018).
- 90 Chen, H. D. *et al.* HLH-30/TFEB-mediated autophagy functions in a cell-autonomous manner for epithelium intrinsic cellular defense against bacterial pore-forming toxin in *C. elegans*. *Autophagy* **13**, 371-385 (2017).
- 91 Braicu, C. *et al.* A Comprehensive Review on MAPK: A Promising Therapeutic Target in Cancer. *Cancers* **11** (2019).
- 92 Kloft, N. *et al.* Pore-forming toxins activate MAPK p38 by causing loss of cellular potassium. *Biochemical and biophysical research communications* **385**, 503-506 (2009).
- 93 Ratner, A. J. *et al.* Epithelial cells are sensitive detectors of bacterial pore-forming toxins. *The Journal of biological chemistry* **281** (2006).
- 94 Popova, T. G. *et al.* Acceleration of epithelial cell syndecan-1 shedding by anthrax hemolytic virulence factors. *BMC Microbiology* **6**, 8(2006).
- 95 Stringaris, A. K. *et al.* Neurotoxicity of Pneumolysin, a Major Pneumococcal Virulence Factor, Involves Calcium Influx and Depends on Activation of p38 Mitogen-Activated Protein Kinase. *Neurobiology of Disease* **11**, 355-368 (2002).
- 96 Cabezas, S. *et al.* Damage of eukaryotic cells by the pore-forming toxin sticholysin II: Consequences of the potassium efflux. *Biochimica et Biophysica Acta (BBA) - Biomembranes* **1859**, 982-992 (2017).
- 97 Gelber, S. E., Aguilar, J. L., Lewis, K. L. & Ratner, A. J. Functional and phylogenetic characterization of Vaginolysin, the human-specific cytotoxin from *Gardnerella vaginalis*. *Journal of bacteriology* **190**, 3896-3903 (2008).
- 98 Husmann, M. *et al.* Differential role of p38 mitogen activated protein kinase for cellular recovery from attack by pore-forming *S. aureus* alpha-toxin or streptolysin O. *Biochemical and biophysical research communications* **344**, 1128-1134 (2006).
- 99 Das, R. *et al.* Macrophage migration inhibitory factor promotes clearance of pneumococcal colonization. *Journal of immunology (Baltimore, Md. : 1950)* **193**, 764-772, (2014).
- 100 Lim, J. H. *et al.* Tumor suppressor CYLD regulates acute lung injury in lethal *Streptococcus pneumoniae* infections. *Immunity* **27**, 349-360 (2007).
- 101 Ha, U. H. *et al.* MKP1 regulates the induction of MUC5AC mucin by *Streptococcus pneumoniae* pneumolysin by inhibiting the PAK4-JNK signaling pathway. *The Journal of biological chemistry* **283**, 30624-30631 (2008).
- 102 Tang, P., Sutherland, C. L., Gold, M. R. & Finlay, B. B. *Listeria monocytogenes* Invasion of Epithelial Cells Requires the MEK-1/ERK-2 Mitogen-Activated Protein Kinase Pathway. **66**, 1106-1112 (1998).
- 103 Gonzalez, M. R. *et al.* Pore-forming toxins induce multiple cellular responses promoting survival. **13**, 1026-1043 (2011).
- 104 Weiglein, I. *et al.* *Listeria monocytogenes* infection of HeLa cells results in listeriolysin O-mediated transient activation of the Raf-MEK-MAP kinase pathway. *FEMS microbiology letters* **148**, 189-195 (1997).
- 105 Grootjans, J., Kaser, A., Kaufman, R. J. & Blumberg, R. S. The unfolded protein response in immunity and inflammation. *Nature reviews. Immunology* **16**, 469-484 (2016).
- 106 Pillich, H., Loose, M., Zimmer, K. P. & Chakraborty, T. Activation of the unfolded protein response by *Listeria monocytogenes*. *Cellular microbiology* **14**, 949-964 (2012).
- 107 Alhamdi, Y. *et al.* Circulating Pneumolysin Is a Potent Inducer of Cardiac Injury during Pneumococcal Infection. *PLoS Pathog* **11**, e1004836(2015).
- 108 Sokolov, A. & Radhakrishnan, A. Accessibility of cholesterol in endoplasmic reticulum membranes and activation of SREBP-2 switch abruptly at a common cholesterol threshold. *The Journal of biological chemistry* **285**, 29480-29490 (2010).
- 109 Mesquita, F. S. *et al.* Endoplasmic reticulum chaperone Gp96 controls actomyosin dynamics and protects against pore-forming toxins. *EMBO reports* **18**, 303-318 (2017).
- 110 Malet, J. K. *et al.* Rapid Remodeling of the Host Epithelial Cell Proteome by the Listeriolysin O (LLO) Pore-forming Toxin. *Molecular & cellular proteomics: MCP* **17**, 1627-1636 (2018).

- 111 Ribet, D. *et al.* *Listeria monocytogenes* impairs SUMOylation for efficient infection. *Nature* **464**, 1192-1195 (2010).
- 112 Li, J., Lam, W. W.-I., Lai, T.-w. & Au, S. W.-n. Degradation of nuclear Ubc9 induced by listeriolysin O is dependent on K⁺ efflux. *Biochemical and biophysical research communications* **493**, 1115-1121 (2017).
- 113 Hamon, M. A. *et al.* Histone modifications induced by a family of bacterial toxins. *Proceedings of the National Academy of Sciences of the United States of America* **104**, 13467-13472 (2007).
- 114 Hamon, M. A. & Cossart, P. K⁺ efflux is required for histone H3 dephosphorylation by *Listeria monocytogenes* listeriolysin O and other pore-forming toxins. *Infection and immunity* **79**, 2839-2846 (2011).
- 115 Witzenzath, M. *et al.* The NLRP3 inflammasome is differentially activated by pneumolysin variants and contributes to host defense in pneumococcal pneumonia. *Journal of immunology* **187**, 434-440 (2011).
- 116 Stevens, D. L., Troyer, B. E., Merrick, D. T., Mitten, J. E. & Olson, R. D. Lethal effects and cardiovascular effects of purified alpha- and theta-toxins from *Clostridium perfringens*. *The Journal of infectious diseases* **157**, 272-279 (1988).
- 117 Andersen, B. R. & Van Epps, D. E. Suppression of chemotactic activity of human neutrophils by streptolysin O. *The Journal of infectious diseases* **125**, 353-359 (1972).
- 118 Bryant, A. E. *et al.* Vascular dysfunction and ischemic destruction of tissue in *Streptococcus pyogenes* infection: the role of streptolysin O-induced platelet/neutrophil complexes. *The Journal of infectious diseases* **192**, 1014-1022 (2005).
- 119 Aberdein, J. D., Cole, J., Bewley, M. A., Marriott, H. M. & Dockrell, D. H. Alveolar macrophages in pulmonary host defence the unrecognized role of apoptosis as a mechanism of intracellular bacterial killing. *Clin Exp Immunol* **174**, 193-202 (2013).
- 120 Nishibori, T., Xiong, H., Kawamura, I., Arakawa, M. & Mitsuyama, M. Induction of cytokine gene expression by listeriolysin O and roles of macrophages and NK cells. *Infection and immunity* **64**, 3188-3195 (1996).
- 121 Harder, J. *et al.* Activation of the Nlrp3 inflammasome by *Streptococcus pyogenes* requires streptolysin O and NF-kappa B activation but proceeds independently of TLR signaling and P2X7 receptor. *Journal of immunology (Baltimore, Md.: 1950)* **183**, 5823-5829 (2009).
- 122 Yamamura, K. *et al.* Inflammasome Activation Induced by Perfringolysin O of *Clostridium perfringens* and Its Involvement in the Progression of Gas Gangrene. *Frontiers in microbiology* **10**, 2406 (2019).
- 123 Fatykhova, D. *et al.* Serotype 1 and 8 Pneumococci Evade Sensing by Inflammasomes in Human Lung Tissue. *PLoS One* **10**, e0137108 (2015).
- 124 Hornung, V. *et al.* AIM2 recognizes cytosolic dsDNA and forms a caspase-1-activating inflammasome with ASC. *Nature* **458**, 514-518 (2009).
- 125 Muñoz-Planillo, R. *et al.* K⁺ efflux is the common trigger of NLRP3 inflammasome activation by bacterial toxins and particulate matter. *Immunity* **38**, 1142-1153 (2013).
- 126 Keyel, P. A. How is inflammation initiated? Individual influences of IL-1, IL-18 and HMGB1. *Cytokine* **69**, 136-145 (2014).
- 127 Rathinam, V. A. *et al.* The AIM2 inflammasome is essential for host defense against cytosolic bacteria and DNA viruses. *Nature immunology* **11**, 395-402 (2010).
- 128 Chen, C. J. *et al.* Identification of a key pathway required for the sterile inflammatory response triggered by dying cells. *Nature medicine* **13**, 851-856 (2007).
- 129 Flannagan, R. S., Jaumouillé, V. & Grinstein, S. The cell biology of phagocytosis. *Annual review of pathology* **7**, 61-98 (2012).
- 130 Hara, H. *et al.* Dependency of caspase-1 activation induced in macrophages by *Listeria monocytogenes* on cytolysin, listeriolysin O, after evasion from phagosome into the cytoplasm. *Journal of immunology (Baltimore, Md.: 1950)* **180**, 7859-7868 (2008).
- 131 Portnoy, D. A., Jacks, P. S. & Hinrichs, D. J. Role of hemolysin for the intracellular growth of *Listeria monocytogenes*. *The Journal of experimental medicine* **167**, 1459-1471 (1988).

- 132 Malet, J. K., Cossart, P. & Ribet, D. Alteration of epithelial cell lysosomal integrity induced by bacterial cholesterol-dependent cytolysins. *Cellular microbiology* **19** (2017).
- 133 Bielecki, J., Youngman, P., Connelly, P. & Portnoy, D. A. Bacillus subtilis expressing a haemolysin gene from Listeria monocytogenes can grow in mammalian cells. *Nature* **345**, 175-176 (1990).
- 134 Vadia, S. *et al.* The pore-forming toxin listeriolysin O mediates a novel entry pathway of L. monocytogenes into human hepatocytes. *PLoS Pathog* **7**, e1002356 (2011).
- 135 Portman, J. L., Huang, Q., Reniere, M. L., Iavarone, A. T. & Portnoy, D. A. Activity of the Pore-Forming Virulence Factor Listeriolysin O Is Reversibly Inhibited by Naturally Occurring S-Glutathionylation. *Infection and immunity* **85** (2017).
- 136 Lam, G. Y. *et al.* Listeriolysin O suppresses phospholipase C-mediated activation of the microbicidal NADPH oxidase to promote Listeria monocytogenes infection. *Cell host & microbe* **10**, 627-634 (2011).
- 137 Verherstraeten, S. *et al.* Perfringolysin O: The Underrated Clostridium perfringens Toxin? *Toxins* **7**, 1702-1721 (2015).
- 138 O'Brien, D. K. & Melville, S. B. Effects of Clostridium perfringens alpha-toxin (PLC) and perfringolysin O (PFO) on cytotoxicity to macrophages, on escape from the phagosomes of macrophages, and on persistence of C. perfringens in host tissues. *Infection and immunity* **72**, 5204-5215 (2004).
- 139 Sierig, G., Cywes, C., Wessels, M. R. & Ashbaugh, C. D. Cytotoxic effects of streptolysin o and streptolysin s enhance the virulence of poorly encapsulated group a streptococci. *Infection and immunity* **71**, 446-455 (2003).
- 140 Ofek, I., Bergner-Rabinowitz, S. & Ginsburg, I. Oxygen-stable hemolysins of group A streptococci. 8. Leukotoxic and antiphagocytic effects of streptolysins S and O. *Infection and immunity* **6**, 459-464 (1972).
- 141 Houldsworth, S., Andrew, P. W. & Mitchell, T. J. Pneumolysin stimulates production of tumor necrosis factor alpha and interleukin-1 beta by human mononuclear phagocytes. *Infection and immunity* **62**, 1501-1503 (1994).
- 142 Liu, Y., Defourny, K. A. Y., Smid, E. J. & Abee, T. Gram-Positive Bacterial Extracellular Vesicles and Their Impact on Health and Disease. *Frontiers in microbiology* **9**, 1502 (2018).
- 143 Wang, X., Thompson, C. D., Weidenmaier, C. & Lee, J. C. Release of Staphylococcus aureus extracellular vesicles and their application as a vaccine platform. *Nat Commun* **9**, 1379 (2018).
- 144 Lecuit, M. Understanding how Listeria monocytogenes targets and crosses host barriers. *Clinical microbiology and infection: the official publication of the European Society of Clinical Microbiology and Infectious Diseases* **11**, 430-436 (2005).
- 145 Hackett, S. P. & Stevens, D. L. Streptococcal toxic shock syndrome: synthesis of tumor necrosis factor and interleukin-1 by monocytes stimulated with pyrogenic exotoxin A and streptolysin O. *The Journal of infectious diseases* **165**, 879-885 (1992).
- 146 Stassen, M. *et al.* The streptococcal exotoxin streptolysin O activates mast cells to produce tumor necrosis factor alpha by p38 mitogen-activated protein kinase- and protein kinase C-dependent pathways. *Infection and immunity* **71**, 6171-6177 (2003).
- 147 Littmann, M. *et al.* Streptococcus pneumoniae evades human dendritic cell surveillance by pneumolysin expression. *EMBO molecular medicine* **1**, 211-222, (2009).
- 148 Subramanian, K. *et al.* Pneumolysin binds to the mannose receptor C type 1 (MRC-1) leading to anti-inflammatory responses and enhanced pneumococcal survival. *Nature microbiology* **4**, 62-70 (2019).
- 149 Berry, A. M. Y., J.; Briles, D.E.; Hansman, D.; Paton, J.C. Reduced virulence of a defined pneumolysin-negative mutant of Streptococcus pneumoniae. *Infect. Immun.* **57**, 2037-2042 (1989).
- 150 Fang, R. *et al.* Pneumolysin-Dependent Calpain Activation and Interleukin-1 α Secretion in Macrophages Infected with Streptococcus pneumoniae. *Infection and immunity* **85**, doi:10.1128/iai.00201-17 (2017).

- 151 Harvey, R. M. *et al.* The impact of pneumolysin on the macrophage response to *Streptococcus pneumoniae* is strain-dependent. *PLoS One* **9**, e103625-e103625 (2014).
- 152 Uchiyama, S. *et al.* Streptolysin O Rapidly Impairs Neutrophil Oxidative Burst and Antibacterial Responses to Group A *Streptococcus*. *Front Immunol* **6**, 581 (2015).
- 153 Keyel, P. A., Heid, M. E. & Salter, R. D. Macrophage responses to bacterial toxins: a balance between activation and suppression. *Immunologic Research* **50**, 118-123 (2011).
- 154 Keyel, P. A., Tkacheva, O. A., Larregina, A. T. & Salter, R. D. Coordinate Stimulation of Macrophages by Microparticles and TLR Ligands Induces Foam Cell Formation. *The Journal of Immunology* **189**, 4621-4629 (2012).
- 155 Wolfmeier, H. *et al.* Active release of pneumolysin prepores and pores by mammalian cells undergoing a *Streptococcus pneumoniae* attack. *Biochimica et biophysica acta* **1860**, 2498-2509 (2016).
- 156 Domon, H. *et al.* Mechanism of Macrolide-Induced Inhibition of Pneumolysin Release Involves Impairment of Autolysin Release in Macrolide-Resistant *Streptococcus pneumoniae*. *Antimicrob Agents Chemother* **62**, e00161-00118 (2018).
- 157 Urban-Chmiel, R. *et al.* Antibiotic Resistance in Bacteria-A Review. *Antibiotics (Basel, Switzerland)* **11** (2022).
- 158 Cvitkovitch, D. G., Li, Y.-H. & Ellen, R. P. Quorum sensing and biofilm formation in Streptococcal infections. *The Journal of clinical investigation* **112**, 1626-1632 (2003).
- 159 Geno, K. A. *et al.* Pneumococcal Capsules and Their Types: Past, Present, and Future. *Clinical microbiology reviews* **28**, 871-899 (2015).
- 160 Li, H. *et al.* beta-sitosterol interacts with pneumolysin to prevent *Streptococcus pneumoniae* infection. *Sci Rep* **5**, 17668 (2015).
- 161 Rijneveld, A. W. *et al.* Roles of interleukin-6 and macrophage inflammatory protein-2 in pneumolysin-induced lung inflammation in mice. *The Journal of infectious diseases* **185**, 123-126 (2002).
- 162 Hirst, R. A. *et al.* Effect of pneumolysin on rat brain ciliary function: comparison of brain slices with cultured ependymal cells. *Pediatric research* **47**, 381-384 (2000).
- 163 Mohammed, B. J., Mitchell, T. J., Andrew, P. W., Hirst, R. A. & O'Callaghan, C. The effect of the pneumococcal toxin, pneumolysin on brain ependymal cilia. *Microbial pathogenesis* **27**, 303-309 (1999).
- 164 Zysk, G. *et al.* Pneumolysin is the main inducer of cytotoxicity to brain microvascular endothelial cells caused by *Streptococcus pneumoniae*. *Infection and immunity* **69**, 845-852 (2001).
- 165 Ring, A., Weiser, J. N. & Tuomanen, E. I. Pneumococcal trafficking across the blood-brain barrier. Molecular analysis of a novel bidirectional pathway. *The Journal of clinical investigation* **102**, 347-360 (1998).
- 166 Wellmer, A. *et al.* Decreased virulence of a pneumolysin-deficient strain of *Streptococcus pneumoniae* in murine meningitis. *Infection and immunity* **70**, 6504-6508, doi:10.1128/iai.70.11.6504-6508.2002 (2002).
- 167 Schachern, P. A. *et al.* Viability and Virulence of Pneumolysin, Pneumococcal Surface Protein A, and Pneumolysin/Pneumococcal Surface Protein A Mutants in the Ear. *JAMA Otolaryngology–Head & Neck Surgery* **139**, 937-943 (2013).
- 168 Keller, L. E., Bradshaw, J. L., Pipkins, H. & McDaniel, L. S. Surface Proteins and Pneumolysin of Encapsulated and Nonencapsulated *Streptococcus pneumoniae* Mediate Virulence in a Chinchilla Model of Otitis Media. *Frontiers in cellular and infection microbiology* **6**, 55 (2016).
- 169 Witzenrath, M. *et al.* Role of platelet-activating factor in pneumolysin-induced acute lung injury. *Crit Care Med* **35**, 1756-1762 (2007).
- 170 Nel, J. G. *et al.* Pneumolysin Mediates Platelet Activation In Vitro. *Lung* **194**, 589-593 (2016).
- 171 Witzenrath, M. *et al.* Role of pneumolysin for the development of acute lung injury in pneumococcal pneumonia. *Crit Care Med* **34**, 1947-1954 (2006).
- 172 Feldman, C. *et al.* The effect of *Streptococcus pneumoniae* pneumolysin on human respiratory epithelium in vitro. *Microbial pathogenesis* **9**, 275-284 (1990).

- 173 Mitchell, T. J. & Dalziel, C. E. The biology of pneumolysin. *Sub-cellular biochemistry* **80**, 145-160 (2014).
- 174 Rubins, J. B. *et al.* Dual function of pneumolysin in the early pathogenesis of murine pneumococcal pneumonia. *The Journal of clinical investigation* **95**, 142-150 (1995).
- 175 Brown, A. O. *et al.* Streptococcus pneumoniae translocates into the myocardium and forms unique microlesions that disrupt cardiac function. *PLoS Pathog* **10**, e1004383 (2014).
- 176 Paton, J. C., Rowan-Kelly, B. & Ferrante, A. Activation of human complement by the pneumococcal toxin pneumolysin. **43**, 1085-1087 (1984).
- 177 Mitchell, T. J., Andrew, P. W., Saunders, F. K., Smith, A. N. & Boulnois, G. J. Complement activation and antibody binding by pneumolysin via a region of the toxin homologous to a human acute-phase protein. *Molecular microbiology* **5**, 1883-1888 (1991).
- 178 Cole, J. *et al.* Pneumolysin Is Responsible for Differential Gene Expression and Modifications in the Epigenetic Landscape of Primary Monocyte Derived Macrophages. *Front Immunol* **12**, 573266 (2021).
- 179 Hickey, M. J. *et al.* Molecular and cellular basis of microvascular perfusion deficits induced by Clostridium perfringens and Clostridium septicum. *PLoS Pathog* **4**, e1000045 (2008).
- 180 Pugsley, A. P. The complete general secretory pathway in gram-negative bacteria. *Microbiological reviews* **57**, 50-108 (1993).
- 181 Savinov, S. N. & Heuck, A. P. Interaction of Cholesterol with Perfringolysin O: What Have We Learned from Functional Analysis? *Toxins* **91** (2017).
- 182 Mehdizadeh Gohari, I. *et al.* Pathogenicity and virulence of Clostridium perfringens. *Virulence* **12**, 723-753 (2021).
- 183 Yang, Z. *et al.* Interventions for treating gas gangrene. *The Cochrane database of systematic reviews* **2015**, Cd010577 (2015).
- 184 Bryant, A. E. & Stevens, D. L. Phospholipase C and perfringolysin O from Clostridium perfringens upregulate endothelial cell-leukocyte adherence molecule 1 and intercellular leukocyte adherence molecule 1 expression and induce interleukin-8 synthesis in cultured human umbilical vein endothelial cells. *Infection and immunity* **64**, 358-362 (1996).
- 185 Sakurai, J., Nagahama, M. & Oda, M. Clostridium perfringens alpha-toxin: characterization and mode of action. *Journal of biochemistry* **136**, 569-574 (2004).
- 186 Uzal, F. A. *et al.* Animal models to study the pathogenesis of human and animal Clostridium perfringens infections. *Veterinary microbiology* **179**, 23-33 (2015).
- 187 Awad, M. M., Ellemor, D. M., Boyd, R. L., Emmins, J. J. & Rood, J. I. Synergistic effects of alpha-toxin and perfringolysin O in Clostridium perfringens-mediated gas gangrene. *Infection and immunity* **69**, 7904-7910 (2001).
- 188 Sugahara, T., Takahashi, T., Yamaya, S. & Ohsaka, A. In vitro aggregation of platelets induced by alpha-toxin (phospholipase C) of Clostridium perfringens. *Japanese journal of medical science & biology* **29**, 255-263 (1976).
- 189 Bryant, A. E. *et al.* Clostridium perfringens phospholipase C-induced platelet/leukocyte interactions impede neutrophil diapedesis. *Journal of medical microbiology* **55**, 495-504 (2006).
- 190 Wilson, D. J., Kelly, E. J. & Gucwa, S. Causes of Mortality of Dairy Cattle Diagnosed by Complete Necropsy. **12**, 3001 (2022).
- 191 Verherstraeten, S. *et al.* The synergistic necrohemorrhagic action of Clostridium perfringens perfringolysin and alpha toxin in the bovine intestine and against bovine endothelial cells. *Veterinary Research* **44**, 45 (2013).
- 192 Tran, M. P., Caldwell-McMillan, M., Khalife, W. & Young, V. B. Streptococcus intermedius causing infective endocarditis and abscesses: a report of three cases and review of the literature. *BMC Infectious Diseases* **8**, 154 (2008).
- 193 Geller, A. & Yan, J. The Role of Membrane Bound Complement Regulatory Proteins in Tumor Development and Cancer Immunotherapy. **10** (2019).
- 194 Issa, E., Salloum, T. & Tokajian, S. From Normal Flora to Brain Abscesses: A Review of Streptococcus intermedius. **11** (2020).

- 195 Tomoyasu, T. *et al.* LacR mutations are frequently observed in *Streptococcus intermedius* and are responsible for increased intermedilysin production and virulence. *Infection and immunity* **81**, 3276-3286 (2013).
- 196 Organization, W. H. *Pneumonia*, (2016, September).
- 197 Timmer, A. M. *et al.* Streptolysin O promotes group A *Streptococcus* immune evasion by accelerated macrophage apoptosis. *The Journal of biological chemistry* **284**, 862-871 (2009).
- 198 Li, S., Xu, X., Wei, L., Wang, L. & Lv, Q. Acacetin Alleviates *Listeria monocytogenes* Virulence Both In Vitro and In Vivo via the Inhibition of Listeriolysin O. *Foodborne pathogens and disease* **19**, 115-125 (2022).
- 199 Temple, M. E. & Nahata, M. C. Treatment of listeriosis. *The Annals of pharmacotherapy* **34**, 656-661 (2000).
- 200 Wang, J., Liu, S., Liu, B., Niu, X. & Deng, X. Luteolin Inhibits Listeriolysin O Translation by Directly Targeting the Coding Region of the hly mRNA. *Frontiers in microbiology* **10**, 1496 (2019).
- 201 Barnes, P. J. Glucocorticosteroids: current and future directions. *British journal of pharmacology* **163**, 29-43 (2011).
- 202 Rosch, J. W. *et al.* Statins protect against fulminant pneumococcal infection and cytotoxin toxicity in a mouse model of sickle cell disease. *The Journal of clinical investigation* **120**, 627-635 (2010).
- 203 Feldman, C. & Anderson, R. Community-Acquired Pneumonia: Pathogenesis of Acute Cardiac Events and Potential Adjunctive Therapies. *Chest* **148**, 523-532 (2015).
- 204 Shigematsu, M. *et al.* Leukotriene B(4) receptor type 2 protects against pneumolysin-dependent acute lung injury. *Sci Rep* **6**, 34560 (2016).
- 205 Pagan, F. S. Antibiotics for gram-positive organisms. *British journal of hospital medicine* **25**, 24-27 (1981).
- 206 Zhao, X. *et al.* Shikonin alleviates the biotoxicity produced by pneumococcal pneumolysin. *Life Sci* **177**, 1-7 (2017).
- 207 García-Suárez Mdel, M. *et al.* Protection against pneumococcal pneumonia in mice by monoclonal antibodies to pneumolysin. *Infection and immunity* **72**, 4534-4540, doi:10.1128/iai.72.8.4534-4540.2004 (2004).
- 208 Odotola, A. *et al.* Efficacy of a novel, protein-based pneumococcal vaccine against nasopharyngeal carriage of *Streptococcus pneumoniae* in infants: A phase 2, randomized, controlled, observer-blind study. *Vaccine* **35**, 2531-2542 (2017).
- 209 Henry, B. D. *et al.* Engineered liposomes sequester bacterial exotoxins and protect from severe invasive infections in mice. *Nature biotechnology* **33**, 81-88 (2015).
- 210 Laterre, P.-F. *et al.* CAL02, a novel antitoxin liposomal agent, in severe pneumococcal pneumonia: a first-in-human, double-blind, placebo-controlled, randomised trial. *The Lancet Infectious Diseases* **19**, 620-6303 (2019).
- 211 Quideau, S., Deffieux, D., Douat-Casassus, C. & Pouységou, L. Plant polyphenols: chemical properties, biological activities, and synthesis. *Angewandte Chemie (International ed. in English)* **50**, 586-621 (2011).
- 212 Zhou, Y. *et al.* Natural Polyphenols for Prevention and Treatment of Cancer. *Nutrients* **8** (2016).
- 213 Matsumura, T. *et al.* An anti-perfringolysin O monoclonal antibody cross-reactive with streptolysin O protects against streptococcal toxic shock syndrome. *BMC Research Notes* **13**, 419 (2020).
- 214 Hammitt, L. L. *et al.* Efficacy, safety and immunogenicity of a pneumococcal protein-based vaccine co-administered with 13-valent pneumococcal conjugate vaccine against acute otitis media in young children: A phase IIb randomized study. *Vaccine* **37**, 7482-7492 (2019).
- 215 Li, S. *et al.* Acacetin inhibits *Streptococcus pneumoniae* virulence by targeting pneumolysin. *Journal of Pharmacy and Pharmacology* **72**, 1092-1100 (2020).
- 216 Arzanlou, M. & Bohlooli, S. Inhibition of streptolysin O by allicin - an active component of garlic. *Journal of medical microbiology* **59**, 1044-1049 (2010).

- 217 Liu, S. *et al.* Amentoflavone Attenuates Clostridium perfringens Gas Gangrene by Targeting Alpha-Toxin and Perfringolysin O. *Frontiers in pharmacology* **11**, 179 (2020).
- 218 Zhao, X., Liu, B., Liu, S., Wang, L. & Wang, J. Anticytotoxin Effects of Amentoflavone to Pneumolysin. *Biological & pharmaceutical bulletin* **40**, 61-67 (2017).
- 219 Song, M. *et al.* Apigenin protects mice from pneumococcal pneumonia by inhibiting the cytolytic activity of pneumolysin. *Fitoterapia* **115**, 31-36 (2016).
- 220 Wang, J. *et al.* Novel inhibitor discovery and the conformational analysis of inhibitors of listeriolysin O via protein-ligand modeling. *Sci Rep* **5**, 8864 (2015).
- 221 Escajadillo, T. & Nizet, V. Pharmacological Targeting of Pore-Forming Toxins as Adjunctive Therapy for Invasive Bacterial Infection. **10**, 542 (2018).
- 222 Xu, Y. *et al.* Inhibitory Effect of the Traditional Chinese Medicine Ephedra sinica granules on Streptococcus pneumoniae Pneumolysin. *Biological & pharmaceutical bulletin* **43**, 994-999 (2020).
- 223 Song, M. *et al.* Epigallocatechin gallate inhibits Streptococcus pneumoniae virulence by simultaneously targeting pneumolysin and sortase A. *J Cell Mol Med* **21**, 2586-2598 (2017).
- 224 Wang, J. *et al.* Fisetin inhibits Listeria monocytogenes virulence by interfering with the oligomerization of listeriolysin O. *The Journal of infectious diseases* **211**, 1376-1387 (2015).
- 225 Song, M., Lu, G., Li, M., Deng, X. & Wang, J. Juglone alleviates pneumolysin-induced human alveolar epithelial cell injury via inhibiting the hemolytic activity of pneumolysin. *Antonie Van Leeuwenhoek* **110**, 1069-1075 (2017).
- 226 Wang, G. *et al.* Piceatannol Alleviates Clostridium perfringens Virulence by Inhibiting Perfringolysin O. *Molecules (Basel, Switzerland)* **27** (2022).
- 227 Lv, Q. *et al.* Quercetin, a pneumolysin inhibitor, protects mice against Streptococcus pneumoniae infection. *Microbial pathogenesis* **140**, 103934 (2020).
- 228 Zhang, J. *et al.* Verbascoside Protects Mice from Clostridial Gas Gangrene by Inhibiting the Activity of Alpha Toxin and Perfringolysin O. *Frontiers in microbiology* **11**, 1504 (2020).
- 229 Zhao, X. *et al.* Verbascoside Alleviates Pneumococcal Pneumonia by Reducing Pneumolysin Oligomers. *Mol Pharmacol* **89**, 376-387 (2016).
- 230 Reygaert, W. C. An overview of the antimicrobial resistance mechanisms of bacteria. *AIMS microbiology* **4**, 482-501 (2018).
- 231 Murray, C. J. L. *et al.* Global burden of bacterial antimicrobial resistance in 2019: a systematic analysis. *The Lancet* **399**, 629-655 (2022).
- 232 Rasko, D. A. & Sperandio, V. Anti-virulence strategies to combat bacteria-mediated disease. *Nature Reviews Drug Discovery* **9**, 117-128 (2010).
- 233 Ford, C. A., Hurford, I. M. & Cassat, J. E. Antivirulence Strategies for the Treatment of Staphylococcus aureus Infections: A Mini Review. **11** (2021).
- 234 Fleitas Martínez, O., Cardoso, M. H., Ribeiro, S. M. & Franco, O. L. Recent Advances in Anti-virulence Therapeutic Strategies with a Focus on Dismantling Bacterial Membrane Microdomains, Toxin Neutralization, Quorum-Sensing Interference and Biofilm Inhibition. **9** (2019).
- 235 Bokori-Brown, M. *et al.* Red Blood Cell Susceptibility to Pneumolysin: CORRELATION WITH MEMBRANE BIOCHEMICAL AND PHYSICAL PROPERTIES. *The Journal of biological chemistry* **291**, 10210-10227 (2016).
- 236 Zhang, J. *et al.* Sphingomyelin in erythrocyte membranes increases the total cholesterol content of erythrocyte membranes in patients with acute coronary syndrome. *Coron Artery Dis* **24**, 361-367 (2013).
- 237 Jaegle, M. *et al.* Protein-Templated Fragment Ligations—From Molecular Recognition to Drug Discovery. **56**, 7358-7378 (2017).
- 238 Krishnan, S. *et al.* Design of Reversible, Cysteine-Targeted Michael Acceptors Guided by Kinetic and Computational Analysis. *Journal of the American Chemical Society* **136**, 12624-12630 (2014).
- 239 Zhang, W. *et al.* Replacing the 238th aspartic acid with an arginine impaired the oligomerization activity and inflammation-inducing property of pyolysin. *Virulence* **9**, 1112-1125(2018).

- 240 Oloo, E. O., Yethon, J. A., Ochs, M. M., Carpick, B. & Oomen, R. Structure-guided antigen engineering yields pneumolysin mutants suitable for vaccination against pneumococcal disease. *The Journal of biological chemistry* **286**, 12133-12140 (2011).
- 241 Coan, K. E., Maltby, D. A., Burlingame, A. L. & Shoichet, B. K. Promiscuous aggregate-based inhibitors promote enzyme unfolding. *J Med Chem* **52**, 2067-2075 (2009).
- 242 Tauber, C. *et al.* Chemical Evolution of Antivirals Against Enterovirus D68 through Protein-Templated Knoevenagel Reactions. *Angewandte Chemie (International ed. in English)* **60**, 13294-13301 (2021).
- 243 Barrett, W. C. *et al.* Regulation of PTP1B via glutathionylation of the active site cysteine 215. *Biochemistry* **38**, 6699-6705 (1999).
- 244 Lee, J. *et al.* Crystallographic structure of wild-type SARS-CoV-2 main protease acyl-enzyme intermediate with physiological C-terminal autoprocessing site. *Nature Communications* **11**, 5877 (2020).
- 245 van Montfort, R. L., Congreve, M., Tisi, D., Carr, R. & Jhoti, H. Oxidation state of the active-site cysteine in protein tyrosine phosphatase 1B. *Nature* **423**, 773-777(2003).
- 246 Sekar, R. B. & Periasamy, A. Fluorescence resonance energy transfer (FRET) microscopy imaging of live cell protein localizations. *The Journal of cell biology* **160**, 629-633 (2003).
- 247 Shah, N. B. & Duncan, T. M. Bio-layer interferometry for measuring kinetics of protein-protein interactions and allosteric ligand effects. *J Vis Exp*, e51383 (2014).
- 248 Nirschl, M., Reuter, F. & Vörös, J. Review of Transducer Principles for Label-Free Biomolecular Interaction Analysis. **1**, 70-92 (2011).
- 249 Ghosh, A. K., Samanta, I., Mondal, A. & Liu, W. R. Covalent Inhibition in Drug Discovery. *ChemMedChem* **14**, 889-906 (2019).
- 250 Wartchow, C. A. *et al.* Biosensor-based small molecule fragment screening with bilayer interferometry. *Journal of computer-aided molecular design* **25**, 669-676 (2011).
- 251 Chan, L. L. *et al.* A Method for Identifying Small-Molecule Aggregators Using Photonic Crystal Biosensor Microplates. *JALA (Charlottesville, Va.)* **14**, 348-359 (2009).
- 252 Drücker, P. *et al.* Membrane deformation and layer-by-layer peeling of giant vesicles induced by the pore-forming toxin pneumolysin. *Biomaterials Science* **7**, 3693-3705 (2019).
- 253 Vögele, M. *et al.* Membrane perforation by the pore-forming toxin pneumolysin. *Proceedings of the National Academy of Sciences* **116**, 13352 (2019).
- 254 Klein, R., Nagy, O., Tóthová, C. & Chovanová, F. Clinical and Diagnostic Significance of Lactate Dehydrogenase and Its Isoenzymes in Animals. *Veterinary medicine international* **2020**, 5346483 (2020).
- 255 Eskandani, M., Hamishehkar, H. & Ezzati Nazhad Dolatabadi, J. Cyto/Genotoxicity study of polyoxyethylene (20) sorbitan monolaurate (tween 20). *DNA and cell biology* **32**, 498-503 (2013).
- 256 Martin, N. C. *et al.* The use of phosphate buffered saline for the recovery of cells and spermatozoa from swabs. *Science & justice: journal of the Forensic Science Society* **46**, 179-184 (2006).
- 257 Evans, B. C. *et al.* Ex vivo red blood cell hemolysis assay for the evaluation of pH-responsive endosomolytic agents for cytosolic delivery of biomacromolecular drugs. *J Vis Exp*, e50166-e50166 (2013).
- 258 Kawahara, E., Sako, H., Nomura, S. & Kusuda, R. Properties of Hemolysin Produced by β -Hemolytic *Streptococcus* sp. Isolated from Yellowtail (*Seriola quinqueradiata*). *Fish Pathology* **26**, 177-181 (1991).
- 259 Ravenhill, B. J. *et al.* Quantitative comparative analysis of human erythrocyte surface proteins between individuals from two genetically distinct populations. *Communications Biology* **2**, 350 (2019).